DESIGN AND DISPATCH OPTIMIZATION OF SOLAR POWER PLANTS WITH STORAGE

by

John L. Cox

A thesis submitted to the Faculty and the Board of Trustees of the Colorado School of Mines in partial fulfillment of the requirements for the degree of Doctor of Philosophy (Operations Research with Engineering).

Golden, Colorado

Date ________________________

Signed: ________________________

John L. Cox

Signed: ________________________

Dr. Alexandra M. Newman
Thesis Advisor

Golden, Colorado

Date ________________________

Signed: ________________________

Dr. Alexandra M. Newman
Director, Operations Research with Engineering
Department of Mechanical Engineering

ABSTRACT

Concentrating solar power, when coupled with thermal energy storage, presents a promising path towards utility-scale dispatchable renewable energy. The performance of these plants is a consequence of both the relative sizing of systems and dispatch decisions, which together possess numerous degrees of freedom. In this dissertation, we develop and solve nonlinear, and non-convex optimization models to assist decision makers in the economically-efficient design and dispatch of concentrating and hybrid solar power plants with storage. We first extend a concentrating solar power dispatch optimization model for real-time operations; the resulting revenue-maximizing non-convex mixed-integer, quadradically-constrained program determines a dispatch schedule with sub-hourly time fidelity and considers temperature-dependent power cycle efficiency. We present exact and inexact techniques to improve problem tractability and demonstrate the model's suitability for decision support in a real-time setting. To address design decisions, we then develop an approach to analyze the economic performance of hybrid and single-technology solar power plants, which incorporates optimal dispatch and considers the expected weather and market conditions. We apply formal design-of-experiment sampling and black-box optimization techniques to demonstrate the value of optimal plant sizing, and compare the economic performance of the following designs: (i) photovoltaic-with-battery and, (ii) concentrating solar power with thermal energy storage, in a revenue-maximizing scenario. To investigate the sensitivity of our approach, we consider various weather and market conditions, renewable energy incentives, and plant operating restrictions. Together, our contributions in this dissertation progress a dispatch optimization model, associated solution techniques, and a design optimization approach for concentrating and hybrid solar power plants with storage. We demonstrate an approach for the use of a nonlinear and non-convex optimization for real-time decision support that yields solutions within 3 percent of global optimality in five minutes, show that lifetime plant benefit-to-cost ratio can be improved 6 to 19 percent through optimal sizing, and explore the sensitivity of optimal sizing with respect to several input parameters.

TABLE OF CONTENTS

ABSTRACT . . . iii

LIST OF FIGURES . . . ix

LIST OF TABLES . . . xiii

LIST OF ABBREVIATIONS . . . xvi

ACKNOWLEDGMENTS . . . xvii

DEDICATION . . . xviii

CHAPTER 1 INTRODUCTION . . . 1

CHAPTER 2 ACCEPTED PAPER: REAL-TIME DISPATCH OPTIMIZATION FOR CONCENTRATING SOLAR POWER WITH THERMAL ENERGY STORAGE . . . 3

- 2.1 Introduction . . . 3
- 2.2 Literature Review . . . 5
- 2.3 System Overview and Real-time Dispatch Optimization Model . . . 8
  - 2.3.1 Notation . . . 10
  - 2.3.2 Objective Function and Constraints . . . 15
    - 2.3.2.1 Receiver Operations . . . 16
    - 2.3.2.2 Thermal Energy Storage . . . 20
    - 2.3.2.3 Power Cycle Operations . . . 21
    - 2.3.2.4 Grid Operations . . . 24
    - 2.3.2.5 Variable Bounds . . . 25
  - 2.3.3 Linear Formulation . . . 25
- 2.4 Solution Techniques . . . 26
  - 2.4.1 Exact Problem Modifications . . . 27
  - 2.4.2 Approximate Linear Formulations . . . 27
  - 2.4.3 Inexact Problem Modifications . . . 29
  - 2.4.4 Problem Scaling . . . 30

2.5 Scenario Descriptions and Results 30
    2.5.1 Notional Plant Design 31
    2.5.2 Problem Instances 32
    2.5.3 Solution Times 33
    2.5.4 Example Dispatch Solution 35
    2.5.5 Validation of Inexact Modifications 38
2.6 Conclusions and Future Work 39
2.7 Acknowledgments 39
CHAPTER 3 SUBMITTED PAPER: OPTIMAL SIZING AND DISPATCH OF SOLAR POWER WITH STORAGE 40
3.1 Introduction 40
3.2 Literature Review 42
3.3 Design Evaluation Approach 45
    3.3.1 Design Optimization 46
    3.3.2 Design Objective 51
    3.3.3 Dispatch Optimization 52
3.4 Design Optimization Methodology 54
    3.4.1 Execution Framework 55
    3.4.2 Optimization Approach 55
        3.4.2.1 Sampling Designs 55
        3.4.2.2 Black-Box Optimizers 55
    3.4.3 Dispatch Rolling Horizon 56
3.5 Model Instances and Results 56
    3.5.1 Case Study Parameters 57
        3.5.1.1 Plant Configuration Parameters 57
        3.5.1.2 Dispatch Cost Assumptions 58
        3.5.1.3 Plant Location and Electricity Market 58
    3.5.2 Design Timing Results 60

3.5.3 Design Solutions . . . 61

3.5.4 Dispatch Timing Results . . . 63

3.5.5 Dispatch Solutions . . . 64

3.5.6 Comparison of Plant Designs and Corresponding Dispatch . . . 66

3.6 Conclusions . . . 68

3.7 Acknowledgments . . . 68

CHAPTER 4 SUBMITTED PAPER: PARAMETRIC ANALYSIS ON OPTIMIZED DESIGN OF HYBRID SOLAR POWER PLANTS . . . 70

4.1 Introduction . . . 70

4.2 Literature Review . . . 72

4.3 Methodology . . . 75

4.3.1 Design Objectives . . . 77

4.3.2 Design Optimization Approach . . . 78

4.4 Study Inputs and Data . . . 78

4.4.1 Case Study Parameters . . . 79

4.4.2 Energy Markets . . . 79

4.4.3 Plant Locations . . . 80

4.4.4 Incentive Payments . . . 82

4.5 Results . . . 83

4.5.1 Plant Configuration Parameters . . . 83

4.5.2 Operations Schedule Examples . . . 84

4.5.3 Electricity Market . . . 86

4.5.4 Plant Location . . . 88

4.5.5 Project Budget . . . 90

4.5.6 Grid Interconnect Limit . . . 92

4.5.7 Capacity Credit . . . 93

4.5.8 Hybridization . . . 96

4.5.9 Summary of Results . . . 98

4.6 Conclusions and Future Work 99

4.7 Acknowledgments 100

CHAPTER 5 CONCLUSIONS AND FUTURE WORK 101

REFERENCES 103

APPENDIX A COMPLETE FORMULATION 112

A.1 Receiver Start-up 117

A.2 Receiver Collection Energy Balance 118

A.3 Receiver Shutdown 118

A.4 Receiver Mass Flow Rate 118

A.5 Receiver Outlet Temperature 118

A.6 Receiver Power Balance 118

A.7 Receiver Penalties 119

A.8 Receiver Logic 119

A.9 Thermal Energy Storage 119

A.10 Mass Balance 119

A.11 Energy Balance 119

A.12 Power Cycle Start-up 120

A.13 Power Cycle Thermal Input 120

A.14 Power Cycle Mass Flow Rate 120

A.15 Power Cycle Outlet Temperature 121

A.16 Power Cycle Electric Output 121

A.17 Power Cycle Ramping 121

A.18 Power Cycle Up and Down Times 121

A.19 Power Cycle Penalties 122

A.20 Logic Associated with Power Cycle Modes 122

A.21 Power Cycle Operation Restriction 122

A.22 Grid Operations 122

APPENDIX B PHASED-SOLUTION HEURISTIC 123

APPENDIX C PHASED-SOLUTION HEURISTIC SOLVE TIMES 126

APPENDIX D PLANT EVALUATION ASSUMPTIONS AND CASE STUDY INPUTS 128

APPENDIX E DISPATCH OPTIMIZATION MODEL FORMULATION 129

- E.1 Objective Function and Constraints 132
- E.2 Receiver Operations 135
- E.3 Power Cycle Operations 135
- E.4 Thermal Energy Storage Balance 136
- E.5 PV Field Operations 136
- E.6 Battery Operations 136
- E.7 Grid Operations 136
- E.8 Inter-System Operations 136

APPENDIX F DESIGN OPTIMIZATION MODEL FORMULATION 137

APPENDIX G PLANT EVALUATION ASSUMPTIONS AND CASE STUDY INPUTS 142

APPENDIX H DISPATCH OPTIMIZATION MODEL FORMULATION 143

- H.1 Objective Function and Constraints 146
- H.2 Receiver Operations 149
- H.3 Power Cycle Operations 149
- H.4 Thermal Energy Storage Balance 150
- H.5 PV Field Operations 150
- H.6 Battery Operations 150
- H.7 Grid Operations 150
- H.8 Inter-System Operations 150
- H.9 Dispatch Cost Assumptions 151

APPENDIX I PERMISSIONS 152

LIST OF FIGURES

Figure 2.1 CSP-TES plant configuration (Graphic © NREL). A depiction of a molten salt power tower CSP plant, which consists of a heliostat field, molten salt receiver, thermal energy storage, and a steam Rankine power cycle. Numbers relate the sets of constraints in the mathematical formulation to the plant subsystems they represent. . . . 9

Figure 2.2 Real-time Dispatch Optimization Model Formulation Comparison 10

Figure 2.3 Summary of Solution Techniques Applied to the Real-time Dispatch Optimization Model ($\mathcal{R}$) 26

Figure 2.4 Fraction of power cycle input needed for maximum output with respect to bilinear approximation error. The parameter N represents the number of piece-wise approximation envelopes used. 28

Figure 2.5 Varying Fidelity of Time Periods and Formulation Transition in the Real-Time Dispatch 48-Hour Problem Horizon 32

Figure 2.6 Distribution of solar resource in Clark, Nevada problem instances. 33

Figure 2.7 Price signals considered, constant purchase price agreement (PPA) and California ISO (CAISO) pricing hourly average. 34

Figure 2.8 Example receiver dispatch solution. 37

Figure 2.9 Example power cycle dispatch solution under the CAISO price signal. 38

Figure 2.10 Example power cycle dispatch solution, under the PPA price signal. 38

Figure 3.1 Hybrid CSP-PV with storage plant configuration (Graphic © NREL). A depiction of a molten salt power tower CSP plant with thermal energy storage and a steam Rankine power cycle, co-located with a PV field and battery storage. Colored by the system sizing design variables: CSP solar multiple, TES hours, CSP cycle capacity, PV field DC capacity, and battery hours of storage. 41

Figure 3.2 Flow diagram of the plant evaluation procedure. 46

Figure 3.3 Flow diagram showing the sequence of activities in the design optimization 54

Figure 3.4 Graphical depiction of the rolling planning horizon used in the plant evaluation function. . 56

Figure 3.5 Comparison of direct normal irradiance and electricity prices for Rice, CA in 2020. The left panel compares the hourly average prices over a year-long horizon, while the right panel shows a sorted histogram of the same data (where the sorted solar and price data do not necessarily coincide temporally). 59

Figure 3.6 Heat maps of normalized electricity prices and direct normal irradiance for Rice, CA in 2020. The original data is divided by the multiplier shown in the figure in order to provide sufficient contrast in the heat map. 60

Figure 3.7 Timing study results showing mean evaluation time for the three plant configurations considered, with respect to the number of concurrently-running instances. The computer hardware used has 12 cores and 24 threads. †Work rate is the multiplicative speed-up resulting from concurrent evaluation. 61

Figure 3.8 Benefit-to-cost ratio (BCR) results of sampling 500 CSP-with-TES designs with the baseline and best design found. Designs evaluated during optimization are generally clustered near the best, but are omitted here to emphasize the coverage of sampling. . . . 62

Figure 3.9 Benefit-to-cost ratio (BCR) results of sampling 500 PV-with-battery designs with the baseline and best design found. Designs evaluated during optimization are generally clustered near the best, but are omitted here to emphasize the coverage of sampling. . . . 63

Figure 3.10 Example operations schedule for the PV-with-battery plant, maximizing benefit-to-cost ratio (see Table 3.8 for the plant design). The global horizontal irradiance (GHI) shows the solar resource available for PV generation. Shaded regions and line traces are plotted against the primary (left) axes and the secondary (right) axes, respectively. †Simulated performance is reported over a four-day period in May of 2020. 65

Figure 3.11 Dispatch objective values, the corresponding total direct normal irradiance (DNI) and average electricity price for the 365 48-hour horizon problem instances. The plant design is the baseline single-technology CSP with TES plant shown in Table 3.7. 66

Figure 3.12 Heat map comparison of generation schedules for plants maximizing the benefit-to-cost ratio. 67

Figure 4.1 Hybrid CSP-PV with storage plant configuration (Graphic © NREL). A depiction of a molten salt power tower CSP plant with thermal energy storage and a steam Rankine power cycle, co-located with a PV field and battery storage. Colored by the system sizing design variables: CSP solar multiple, TES hours, CSP cycle capacity, PV field DC capacity, battery hours of storage, and battery power capacity. 71

Figure 4.2 Flow diagram of the plant evaluation procedure. 76

Figure 4.3 Graphical depiction of the rolling planning horizon used in the plant evaluation function. . 76

Figure 4.4 Comparison of electricity prices from the CAISO node in Rice, CA for the 2010 and 2020 calendar years. The left panel depicts the hourly average price, while the right panel shows a price-duration curve of the same data. 80

Figure 4.5 Heat map comparison of electricity prices from the CAISO node in Rice, CA for the 2010 and 2020 calendar years. The white lines indicate the approximate local time of sunrise and sunset. 80

Figure 4.6 Comparison of direct normal irradiance for Rice, CA in 2010 and 2020 and a TMY in N. Chile. The left panel compares the hourly average DNI, while the right panel shows a resource-duration of the same data. 81

Figure 4.7 Heat map comparison of direct normal irradiance for Rice, CA in 2010 and 2020 and a TMY in N. Chile. 81

Figure 4.8 Heat map comparison of the total CAISO renewable generation and net grid load for 2020. The top 100 net load hours are shaded in black. 83

Figure 4.9 Example operations schedule for the CSP-with-TES plant, maximizing benefit-to-cost ratio under the Rice 2020 market and weather conditions (see Table 4.5 for the plant design). The direct normal irradiance (DNI) shows the solar resource available for CSP generation. Shaded regions and line traces are plotted against the primary (left) axes and the secondary (right) axes, respectively. †Simulated performance is reported over a four-day period in June of 2020. 85

Figure 4.10 Example operations schedule for the PV-with-battery plant, maximizing benefit-to-cost ratio under the Rice 2020 market and weather conditions (see Table 4.5 for the plant design). The global horizontal irradiance (GHI) shows the solar resource available for PV generation. Shaded regions and line traces are plotted against the primary (left) axes and the secondary (right) axes, respectively. †Simulated performance is reported over a four-day period in June of 2020. 86

Figure 4.11 Benefit-to-cost ratio (BCR) results of sampling 500 designs with the best BCR and levelized cost of energy (LCOE) designs found, comparing performance under varying electricity markets. Designs evaluated during optimization are generally clustered near the best, but are omitted here to emphasize the coverage of sampling. 87

Figure 4.12 Benefit-to-cost ratio (BCR) results of sampling 500 designs with the best BCR and levelized cost of energy (LCOE) designs found, comparing performance under varying plant location. Designs evaluated during optimization are generally clustered near the best, but are omitted here to emphasize the coverage of sampling. 89

Figure 4.13 Installed cost and benefit-to-cost ratio results of sampling 500 CSP-with-TES designs under the Rice 2010 market and weather conditions. The left panel shows the apparent efficient frontier of installed cost and benefit-to-cost ratio. The right panel shows the position of the efficient designs in the parameter space. 91

Figure 4.14 Comparison of CSP-with-TES designs maximizing the benefit-to-cost ratio and installed cost under varying energy market and plant location. 91

Figure 4.15 Installed cost results of sampling 500 PV-with-battery designs with the best benefit-to-cost ratio and levelized cost of energy designs found, while varying the grid connection limit between 100, 125 and 150 MW. Designs evaluated during optimization are generally clustered near the best, but are omitted here to emphasize the coverage of sampling. 92

Figure 4.16 Benefit-to-cost ratio (BCR) results of sampling 500 CSP-with-TES and PV-with-battery designs with the best benefit-to-cost ratio and levelized cost of energy designs found, with (a) no capacity payment and (b) a $150/kWh per year payment for generation during the top 100 net load hours. Designs evaluated during optimization are generally clustered near the best, but are omitted here to emphasize the coverage of sampling. 94

Figure 4.17 Example operations schedule for the PV-with-battery and CSP-with-TES plants, maximizing benefit-to-cost ratio under the Rice 2020 market and weather conditions with the $150/kWh capacity incentive (see Table 4.8 for the plant designs). Shaded regions and line traces are plotted against the primary (left) axes and the secondary (right) axes, respectively. †Simulated performance is reported over a four-day period in September of 2020, which contains 15 of the 100 peak net load hours. 95

Figure 4.18 Installed cost and benefit-to-cost ratio results of sampling 500 PV-with-battery designs under the Rice 2020 market with a \$150/kWh per year capacity credit. The left panel shows the apparent efficient frontier of capacity credit percent and benefit-to-cost ratio. The right panel shows the position of the efficient designs in the parameter space. 96

Figure 4.19 Benefit-to-cost ratio (BCR) and levelized cost of energy (LCOE) results of sampling 750 hybrid CSP-with-TES and PV designs with the best benefit-to-cost ratio and levelized cost of energy found, with (a) no capacity payment and (b) a \$150/kWh per year payment for generation during the top 100 net load hours. 97

Figure B.1 Diagram of a heuristic approach ($\mathbb{R}$) to solve Real-time Dispatch Optimization Model ($\mathcal{R}$) 123

Figure B.2 Summary of Solution Techniques Applied to the Real-time Dispatch Optimization Model 124

LIST OF TABLES

Table 2.1 Real-time dispatch model, $(\mathcal{R})$, notation. 10

Table 2.2 Real-time dispatch model, $(\mathcal{R})$, additional notation. 29

Table 2.3 Notional CSP with TES plant design. 31

Table 2.4 Estimated CSP with TES operating costs. 32

Table 2.5 Initial Conditions used to develop representative problem instances. 34

Table 2.6 Comparison of tractability for each technique presented. †The number of problem instances for which the solver produces a feasible solution during the five-minute time limit. 35

Table 2.7 Real-Time Dispatch $(\mathcal{R}')$ Timing Study Results. †300-second time limit reached; objective value is reported in thousands of dollars. 36

Table 3.1 Inputs of the design optimization problem, $(\mathcal{D})$. 48

Table 3.2 Notation of the design optimization problem, $(\mathcal{D})$. 48

Table 3.3 Notation for the design objective functions. 51

Table 3.4 Notation involved in the dispatch model, $(\mathcal{H})$, objective. 52

Table 3.5 Case study system sizing variables and simple bounds for each plant configuration considered 57

Table 3.6 Dispatch optimization model cost coefficients (HOPP default values). †The parameter value is scaled with respect to the system size. 58

Table 3.7 Baseline plant designs, used for comparison. 62

Table 3.8 Baseline and best single-technology with storage designs and performance metrics. Green and red percent change values indicate performance improvement and deprovement from the baseline, respectively (where the sign on the change can indicate either an improvement or a deprovement depending on the performance metric). 64

Table 3.9 Dispatch model, $(\mathcal{H})$, 48-hour horizon problem instance sizes, prior to presolve, and average solve performance for each plant configuration. †Time reported by the solver to reach an optimality gap of 0.01% or less. 64

Table 3.10 Plant designs maximizing the benefit-to-cost-ratio. †Indicates a variable is at its lower bound. Bold values indicate a configuration has the best value of a particular performance metric. 68

Table 4.1 Notation used in the benefit-to-cost ratio and levelized cost of energy design objective functions. 77

Table 4.2 Comparison of the distribution of normalized electricity prices for the CAISO node in Rice California in 2010 and 2020 79

Table 4.3 Comparison of total annual solar resource for the three instances of weather conditions used. 82

Table 4.4 System sizing variables and simple bounds for each plant configuration considered 84

Table 4.5 Design variables of plants either maximizing benefit-to-cost-ratio (BCR) or minimizing the levelized cost of energy (LCOE) under the Rice 2010 or 2020 market and weather conditions. † and ‡ indicate a variable is at its lower or upper bound, respectively. Bold values indicate a configuration has the best value of a particular performance metric. . . . 88

Table 4.6 Design variables of plants either maximizing benefit-to-cost-ratio (BCR) or minimizing the levelized cost of energy (LCOE) under the Rice 2010 or N. Chile 2010 weather conditions and Rice 2010 market. †Indicates a variable is at its lower bound. Bold values indicate a configuration has the best value of a particular performance metric. . . . 90

Table 4.7 Design variables of plants either maximizing benefit-to-cost-ratio (BCR) or minimizing the levelized cost of energy (LCOE) under the Rice 2020 market and weather conditions, and varying grid interconnect limit. †Indicates a design variable is at its lower bound. . . . 93

Table 4.8 Design variables of plants maximizing benefit-to-cost-ratio (BCR) under the Rice 2020 market and weather conditions, both with and without a capacity-based incentive. Bold values indicate that a configuration has the best value of a particular performance metric. †Capacity credit percent calculated according to the schedule of operations but not included in plant revenue. 95

Table 4.9 Design characteristics of plants maximizing benefit-to-cost-ratio (BCR) under the Rice 2020 market and weather conditions, both with and without a capacity-based incentive. † and ‡ indicate a variable is at its lower or upper bound, respectively. Bold values indicate a configuration has the best value of a particular performance metric. ††Capacity credit percent calculated according to the schedule of operations but not included in plant revenue. 98

Table 4.10 Summary of input data combinations evaluated in each subsection of Section 4.5, with a concise statement of our conclusions. 99

Table A.1 Real-time dispatch model, ($\mathcal{R}$), remaining notation. 112

Table B.1 Real-time dispatch model, heuristic notation. 124

Table C.1 Real-Time Dispatch Heuristic Approach, ($\mathbb{R}$), Timing Study Results for the PPA price signal. ‡90-second time limit reached in Phase 2; †300-second time limit reached; objective value is reported in thousands of dollars. 126

Table C.2 Real-Time Dispatch Heuristic Approach, ($\mathbb{R}$), Timing Study Results for the CAISO price signal. ‡90-second time limit reached in Phase 2; †300-second time limit reached; objective value is reported in thousands of dollars. 127

Table C.3 Real-Time Dispatch Parallel Timing Study Results. †300-second overall time limit reached; objective value is reported in thousands of dollars; results are bolded for cases in which the heuristic approach ($\mathbb{R}$) achieves the better objective. 127

Table D.1 Molten salt power tower single-owner installation cost parameters used in the CSP system of the plant evaluation procedure 128

Table E.1 Hybrid dispatch model, ($\mathcal{H}$), notation. 129

Table F.2 Inputs of the design optimization problem, ($\mathcal{D}$). 138

Table F.3 Notation of the design optimization problem, ($\mathcal{D}$). 139

Table G.1 Molten salt power tower single-owner installation cost parameters used in the CSP system of the plant evaluation procedure 142

Table H.1 Hybrid dispatch model, ($\mathcal{H}$), notation. 143

Table H.2 Dispatch optimization model cost coefficients (HOPP default values). †The parameter value is scaled with respect to the system size. 151

LIST OF ABBREVIATIONS

Benefit-to-Cost Ratio	BCR
Concentrating Solar Power	CSP
Direct Normal Irradiance	DNI
Global Horizontal Irradiance	GHI
Hybrid Optimization and Performance Platform	HOPP
Levelized Cost of Energy	LCOE
Mixed-integer Linear Program	MILP
Mixed-integer Quadradically Constrained Prgram	MIQCP
National Renewable Energy Laboratory	NREL
Photovoltaic	PV
System Advisor Model	SAM
Thermal Energy Storage	TES

ACKNOWLEDGMENTS

Above all others, thank you to my wife, Nicole, whose endless patience, love, and support for me and our two children made this possible.

Thank you to my advisor, Professor Alexandra Newman, who chose to see my potential to grow into this field of research. You have been a tireless collaborator and mentor throughout, and I am eternally grateful to have had the opportunity to be a part of the Operations Research with Engineering group. Thank you to the members of my committee for your feedback and guidance. Thank you to the Department of Computer and Cyber Sciences at the United States Air Force Academy, and specifically to Col David Caswell, Dr. Steven Hadfield, Lt Col Paul Graham, and Lt Col Jeremy Noel, for your trust and inspiration. I look forward to applying the skills and knowledge I have gained during the remainder of my Air Force career.

For Ash and Rory.

CHAPTER 1

INTRODUCTION

Concentrating solar power (CSP) technology distinguishes itself from photovoltaics (PV) in that it uses mirrors to focus the sun's energy onto a receiver to cause a temperature change in a heat transfer medium. CSP plants can only collect the direct irradiance portion of the sun's energy, unlike PV installations which can generate power using both direct and indirect irradiance. There are four commonly used forms of CSP: dish Sterling, linear Fresnel, parabolic trough, and power tower. We focus on the power tower form of CSP, also called central receiver, as it has several advantages over the other configurations. A power tower CSP plant consists of a large field of mirrors, called heliostats, one or more central receivers sitting atop towers, and, commonly, a thermal energy storage (TES) system. The heliostats focus the sun's light onto the receiver in which the heat transfer medium, usually a molten salt, is pumped in order to collect the thermal energy. The heat transfer fluid can then be stored in a tank or used to generate electricity by way of a steam Rankine turbine. One advantage of CSP over PV is that all forms of CSP pair naturally with TES systems, which are comparatively inexpensive relative to an electro-chemical battery per unit capacity. CSP's disadvantage is its large upfront capital cost, which has limited its implementation in the US.

The penetration of renewable energy in certain utility markets has increased significantly in the last decade, spurred by the decrease in cost-per-Watt capacity of PV panels [1]. The capacity of renewable energy generation at times exceeds grid demand, which depresses energy prices during hours of solar availability. Advancements in the cost and technical maturity of energy storage technologies have made methods for storing this excess renewable energy to meet grid demand at a later time economically feasible. The resulting dispatch flexibility allows renewable energy plants with storage to respond to grid demand by dispatching power to the grid during periods of peak energy price. However, by decoupling energy collection from energy dispatch, it is often not obvious how a plant should be operated to maximize revenue. The economic viability of the plant is a consequence of the dispatch decisions, and, as a result, the optimal design of a solar power plant with storage requires simultaneously considering both the sizing of the plant's systems and how the plant will be operated. This research increases the detail of an existing concentrating solar power plant dispatch optimization model, develops methods for the design optimization of solar energy plants with storage, and explores the sensitivity of optimal sizing with respect to several input parameters. Each effort is conducted in collaboration with the authors listed in the chapters to follow.

Chapter 2 extends an existing concentrating solar power dispatch optimization model for use in real-time operations. "Real-time" solutions require: (i) increased temporal detail within the model; (ii) improved representation of the plant systems to account for operating limitations; and, (iii) methodologies that admit solutions in a timely manner. The contributions of this dissertation writer include: (i) reformulation of existing constraints to account for increased time-fidelity; (ii) reformulation of existing constraints to improve the accuracy of the central receiver and power cycle operating limitations; (iii) the addition of non-linear representations of the receiver, thermal storage, and power cycle; (iv) development of exact and inexact problem modifications to improve model tractability; (v) development of a phased solution heuristic which improves solution time on average; and, (vi) execution of a case study of representative problem instances and the analysis of dispatch solutions and solution times of these instances.

Chapter 3 develops an approach to evaluate the economic performance of hybrid and single-technology solar power plants with storage, incorporating optimal dispatch, and considering the expected market and weather conditions. The contributions of this dissertation writer include: (i) development of an execution framework facilitating concurrent evaluation of plant designs; (ii) identification of leading open-source derivative-free optimization algorithms; (iii) development of an execution scheme that maximizes evaluation throughput and facilitates post-analysis of the parameter space; and, (iv) execution of a small study to demonstrate the value of optimal plant sizing and to compare plant profitability under the imposed weather and market conditions.

Chapter 4 explores the sensitivity of the plant evaluation function, developed in Chapter 3, with respect to several input parameters and assumptions. The contributions of this dissertation writer include the design and execution of a parametric analysis of optimal plant sizing considering: (i) plant configuration and design objective, (ii) the imposed energy market, (iii) weather conditions, (iv) operating assumptions, and (v) the presence of a capacity-based incentive. We present results relevant to renewable energy planners and operators.

This work demonstrates: (i) the suitability of a non-convex nonlinear optimization model for real-time decision support; (ii) a methodology for the economic evaluation and optimal sizing of solar energy plants with storage; and, (iii) an investigation of the sensitivity of plant performance metrics with respect to several input parameters and operational assumptions. We publish open-source software, implementing the plant evaluation and design optimization methods developed in Chapter 3, in collaboration with the National Renewable Energy Laboratory. This software will assist planners in the design and dispatch of solar power plants which are able to meet grid needs with renewable energy.

CHAPTER 2

ACCEPTED PAPER: REAL-TIME DISPATCH OPTIMIZATION FOR CONCENTRATING SOLAR POWER WITH THERMAL ENERGY STORAGE

Modified from a paper accepted to *Optimization and Engineering*.

Reproduced with permission from Springer Nature.

John L. Cox[1,2], William T. Hamilton[3], Alexandra M. Newman[4], Michael J. Wagner[5], Alex J. Zolan[6]

Concentrating solar power (CSP) plants present a promising path towards utility-scale renewable energy. The power tower, or central receiver, configuration can achieve higher operating temperatures than other forms of CSP, and, like all forms of CSP, naturally pairs with comparatively inexpensive thermal energy storage, which allows CSP plants to dispatch electricity according to market price incentives and outside the hours of solar resource availability. Currently, CSP plants commonly include a steam Rankine power cycle and several heat exchange components to generate high-pressure steam using stored thermal energy. The efficiency of the steam Rankine cycle depends on the temperature of the plant's operating fluid, and so is a main concern of plant operators. However, the variable nature of the solar resource and the conservatism with which the receiver is operated prevent perfect control over the receiver outlet temperature. Therefore, during periods of solar variability, collection occurs at lower-than-design temperature.

To support operator decisions in a real-time setting, we develop a revenue-maximizing non-convex mixed-integer, quadradically-constrained program which determines a dispatch schedule with sub-hourly time fidelity and considers temperature-dependent power cycle efficiency. The exact nonlinear formulation proves intractable for real-time decision support. We present exact and inexact techniques to improve problem tractability that include a hybrid nonlinear and linear formulation. Our approach admits solutions within approximately 3% of optimality, on average, within a five-minute time limit, demonstrating its usability for decision support in a real-time setting.

2.1 Introduction

Renewable energy technology has progressed significantly with respect to reductions in cost per Watt capacity [2, 3]. As renewable energy technologies penetrate utility markets, production curtailment arises

---

[1] Graduate student, Colorado School of Mines
[2] Primary researcher and author
[3] Post-Doctoral Researcher, National Renewable Energy Laboratory
[4] Professor, Colorado School of Mines
[5] Assistant Professor, University of Wisconsin-Madison, Department of Mechanical Engineering
[6] Researcher, National Renewable Energy Laboratory

at times when the capacity of solar energy production exceeds grid demand. Improvements to electrical and thermal storage technologies have allowed various forms of solar energy to be stored to meet grid demand when solar resource is not available. The inclusion of energy storage within a renewable energy production system allows these technologies to respond to grid demand, potentially increasing their share of the electricity market, but also presents trade-offs for plant operators attempting to dispatch under supply and demand uncertainty [4, 5].

Concentrating solar power (CSP) uses mirrors to focus the sun's energy to cause an increase in temperature of a heat transfer fluid (HTF). The thermal energy stored in this fluid is then converted to electrical energy, typically with a steam Rankine power cycle. Four primary CSP technologies exist: parabolic trough, linear Fresnel, dish Stirling, and power tower [6]. Each naturally pairs with comparatively inexpensive thermal energy storage (TES), in which the TES medium, most commonly a molten salt [7], is stored in one or more tanks to be used for electricity production at a later time. We focus on the power tower, also referred to as the central receiver, form of CSP, which employs a large field of mirrors, called heliostats, to focus the sun's light onto a receiver sitting atop a tower. The power tower configuration has multiple advantages over the other forms of CSP, but primarily improves the maximum achievable operating temperature of the receiver, thereby allowing it to be paired with more efficient high-temperature power cycles. This feature of power tower CSP presents a promising path toward increased efficiency and reduced cost of a utility-scale solar energy plant [8–10].

The high solar concentration ratios possible in power tower CSP plants enable higher operating temperatures, but also create scenarios in which the receiver can exceed its material's melting temperature. During periods of high solar variability (e.g., due to cloud cover), the receiver can experience potentially damaging changes in thermal flux [11]. Power tower plants adopt some form of temperature-limiting control policy to prevent this damage. These policies often result in reduced receiver operating temperature during periods of solar variability, which, in turn, causes reduced power cycle efficiency.

The combination of the variable solar resource, the capability to defer electricity production, and the efficiency trade-off resulting from the temperature-limiting control policy creates challenging decisions for plant operators competing in the day-ahead utility energy market. The contributions of this chapter entail the extension of an existing mixed-integer, linear programming model which determines the optimal dispatch solution, maximizing plant revenue less estimated operating costs [12]. Specifically, we modify the model to allow real-time decision support by (i) increasing time fidelity in the near-term horizon; (ii) enforcing minimum up- and down-time requirements at the power cycle; (iii) improving the accuracy of the receiver and power cycle start-up processes; and, (iv) using explicit variables to represent mass and temperature of the receiver, storage, and the power cycle. The resulting non-convex mixed-integer, quadratically-constrained program is computationally intractable with respect to supporting real-time decisions. Therefore, we present exact and inexact techniques to improve problem tractability. The addition of decision variables representing mass and temperature of the heat transfer fluid allow the dispatch optimization model to obey temperature-limiting control policies. That is, a primary benefit of incorporating an explicit representation of the mass and temperature is to preclude solutions that could not be executed by a plant. While solutions from a linear model may be appropriate for long-term planning [12], they cannot be used to inform real-time plant operations.

The remainder of the chapter is organized as follows: Section 2.2 reviews literature of previous dispatch optimization methodologies used for CSP with TES, temperature dependence of power cycle efficiency, approximate linear formulations, and solution techniques for non-convex mixed-integer, quadratically-constrained formulations. Section 2.3 provides an overview of CSP plant operations, the key decisions sought by an operator, and a mathematical formulation of the dispatch optimization model. Section 2.4 describes corresponding solution techniques to improve tractability and reduce solution time. Section 2.5 presents a case study that exercises the model over a range of instances developed from a single-plant location and notional energy markets; we include results regarding sample dispatch solutions and solution times. Section 2.6 concludes with a summary and possible extensions of our work.

2.2 Literature Review

Optimization of CSP plant dispatch decisions is an active area of research, with varied approaches, levels of fidelity, and goals. CSP is incorporated into production cost models to assess the technology's potential value to a regional grid. Madaeni et al. [13] and McPherson et al. [14] show that pairing CSP with TES increases its economic viability, while Denholm and Mehos [15] study the paired system's ability to increase overall renewable penetration. Mehos et al. [16] analyze the value of CSP systems with TES on the California regional grid under a scenario with high renewables penetration, and then perform sensitivity analyses in which gas pricing and tax incentives vary; the authors use System Advisor Model (SAM), a multi-technology performance assessment tool developed at NREL [17], to provide plant performance characteristics, and they use the commercial software PLEXOS for unit commitment and generator dispatch decisions. Du et al. [18] and Gao et al. [19] extend existing stochastic unit commitment models described in Zheng et al. [20] to include greater detail of CSP systems with TES which operate differently than existing battery storage models; the former add a look-ahead step to allow for TES management in time periods beyond the planning horizon, while the latter employ chance constraints to address unserved load and curtailed renewable generation. While the works above account for some of the unique properties of CSP paired with TES, the scale of grid-level production cost models limits the level of detail that may be added for CSP systems, such as the interactions between the solar collectors, the TES, and the steam generation system.

Price-taker approaches to dispatch optimization seek profit-maximizing decisions for a single generator or hybrid system, given a pricing signal and plant characteristics as input. Because the grid interactions in this setting are generally limited to pricing and a single transmission limit, a greater level of detail may be applied when modeling operating decisions, and so we adopt a price-taker approach for the contributions we develop; Martinek et al. [21] compare a CSP system's value, revenue, and scheduling decisions when using a price-taker model versus a production cost model. Several works in the literature address the nonlinear and complex nature of CSP operations by employing heuristics to dispatch decisions, such as SAM's that maximizes electrical generation. de Meyer et al. [22] use a collection of four different heuristic policies with a goal of maximizing energy production, plant revenue, or grid value, or minimizing the defocusing of heliostats to assess the impact of each on plant performance and scheduling decisions for a case study in South Africa. Liu et al. [23] develop a hybrid algorithm using both genetic algorithms and particle-swarm optimization to obtain dispatch decisions for CSP-PV hybrid systems quickly, but at the expense of provable optimality.

To our knowledge, the model developed by Wagner et al. [12] includes the highest level of detail in CSP dispatch operations among mathematical programming models that maximize a power tower plant's revenue during the problem horizon, less estimated operations and maintenance costs. Variations on this model have been (i) employed to quantify revenue improvements possible through optimal dispatch [24], (ii) extended to consider hybrid CSP and photovoltaic with TES plant designs [25], (iii) used to demonstrate the importance of accurate off-design power cycle performance [26], (iv) paired with a component failure simulation model to assess the long-term costs of cycling [27], and (v) deployed in an open-source software tool that obtains optimized system designs while accounting for operations and maintenance costs [28]. Yang et al. [29] present a separate mixed-integer, linear programming formulation that obtains profit-maximizing dispatch decisions for CSP systems, and Li et al. [30] extend the model to consider design decisions; however, the dispatch models utilize constant thermal efficiencies for subsystems, instead of the decision-dependent heat losses employed by Wagner et al. [12].

Our primary contribution extends the work in Wagner et al. [12] to include (i) an analytical model of receiver outlet temperature, (ii) an empirical model of the temperature-dependent efficiency of the power cycle, and (iii) a technique that obtains a near-optimal solution to the resulting mixed-integer nonlinear program quickly enough to provide real-time decision support to industry users. Non-convex nonlinear optimization models such as this can present significant tractability issues. Scioletti et al. [31] solve a linear approximation of a nonlinear model to optimize the design and dispatch of a microgrid with diesel generators, PV systems, and batteries installed in a remote location, and Goodall et al. [32] extend the model to account for the battery's capacity fade. In both of these cases, standard linear outer-approximations for the bi-linear terms described in McCormick [33] provide sufficient accuracy, while a heuristic yields high-quality, feasible solutions to the nonlinear model instances. As global optimization methodologies for nonlinear and mixed-integer nonlinear models become more mature and effective, exact nonlinear solutions of these types of models are becoming more common [34]. Ellingwood et al. [35] develop a non-convex mixed-integer, quadratically constrained program to optimize the dispatch of a flexible heat CSP plant with TES, and use a heuristic and genetic algorithm to find a near-optimal dispatch solution. Blackburn et al. [36] optimize a district energy grid with storage using quadratic programming to develop an incumbent solution with which to warm start a mixed-integer nonlinear solver. Dowling et al. [37] solve a CSP system scheduling and control model formulated as a mixed-integer linear program, and coupled with a nonlinear engineering model, via decomposition.

The underlying modeling challenge of energy systems driven by heat is the dependence of the product of interest – electricity, in most cases – on both the temperature and mass flow rate of the heat source. Furthermore, heat source temperature is often constrained in relation to mass flow rate. This condition is most commonly encountered in thermodynamic cycles and heat transfer equipment, including in heating, ventilation, and air-conditioning applications [38], building energy storage [39], in other thermally-powered generators such as natural gas combined cycles [40], coal, or nuclear plants, or in industrial process heat applications. Grid energy storage using a near-reversible thermodynamic cycle is gaining interest. So-called "pumped thermal" energy storage uses electricity from the grid during low-demand time periods to thermally charge media in storage tanks. This media is then used as a thermodynamic reservoir to generate electricity with a power cycle during higher-demand time periods [41]. Decision variables in scheduling the charge or discharge of the fluid must account for the thermal mass of media being charged and the temperature of fluid in the tanks after thermal losses, which become increasingly significant with charge dwell time. In all of these cases, the production rate of the system is dependent on the bi-linear product of two continuous variables, temperature and mass flow rate of the heat source.

We investigate the performance of approximate linear formulations of our model using McCormick envelopes [33], and several piece-wise envelopes [42–45]. Ultimately, we find that these formulations become computationally difficult and possess unacceptable approximation error for our application. Significant advances in methods and software for solving this class of optimization model are ongoing. Among them, we employ a commercial solver utilizing the spatial branch-and-bound method to maintain proof of global optimality and exploit the speed with which the linear sub-problems can be solved [46, 47]; in turn, this methodology can be tailored and applied to energy systems in which heat is explicitly modeled.

2.3 System Overview and Real-time Dispatch Optimization Model

Figure 2.1 depicts a notional CSP plant with TES in the power tower configuration, and relates sets of constraints in our mathematical formulation to the subsystems they represent. The energy flow through the plant can be subdivided into two procedures. In the first, which we call *collection mode*, sunlight is absorbed as heat and transferred to thermal energy storage. The second procedure, which we call *production mode*, deploys the stored thermal energy to generate electricity by transferring the thermal to electrical energy using a turbine and generator with the aid of HTF-to-steam heat exchangers. Specifically, in collection mode, the receiver gathers solar thermal energy from the heliostat field and transfers this energy to the heat transfer fluid pumped through its tubes. The amount of thermal power available to the receiver varies with respect to season, time of day, weather conditions, and the level of dust or other aerosol particles in the atmosphere. During collection, the heat transfer fluid acts as a coolant for the receiver tubing, keeping its temperature within an acceptable range. If the mass flow rate of the heat transfer fluid is too low, the thermal power from the heliostat field can rapidly exceed safe temperature levels for the receiver tubing, damaging or destroying it. To avoid this, plants adopt some form of temperature-limiting control scheme; we consider the most conservative of these schemes, "clear-sky control," in which the receiver mass flow rate is controlled according to the clear-sky solar resource, which is the maximum theoretically possible thermal output of the heliostat field. This control scheme buffers temperatures during periods of varied thermal input, but also reduces the receiver outlet temperature below its design point in these same periods.

In production mode, the power cycle converts thermal energy stored in the HTF into electrical energy, which is used to cover plant operating electrical loads; the excess can be sold to the utility grid. The power cycle physically consists of multiple heat exchangers, steam turbines, a steam condenser, and the associated feedwater components. Power cycle start-up is the process of bringing the heat exchangers gradually up to operating temperature, and ramping the steam turbines to their minimum operating speed. Power cycle standby is modeled as an electrical load in which auxiliary boilers and heat tracing maintain the power cycle component temperatures close to their minimum operating values. Collected energy may be concurrently used in production mode or stored for later use; the presence of TES in this system permits the two modes to run separately, allowing the plant to schedule production to maximize revenue.

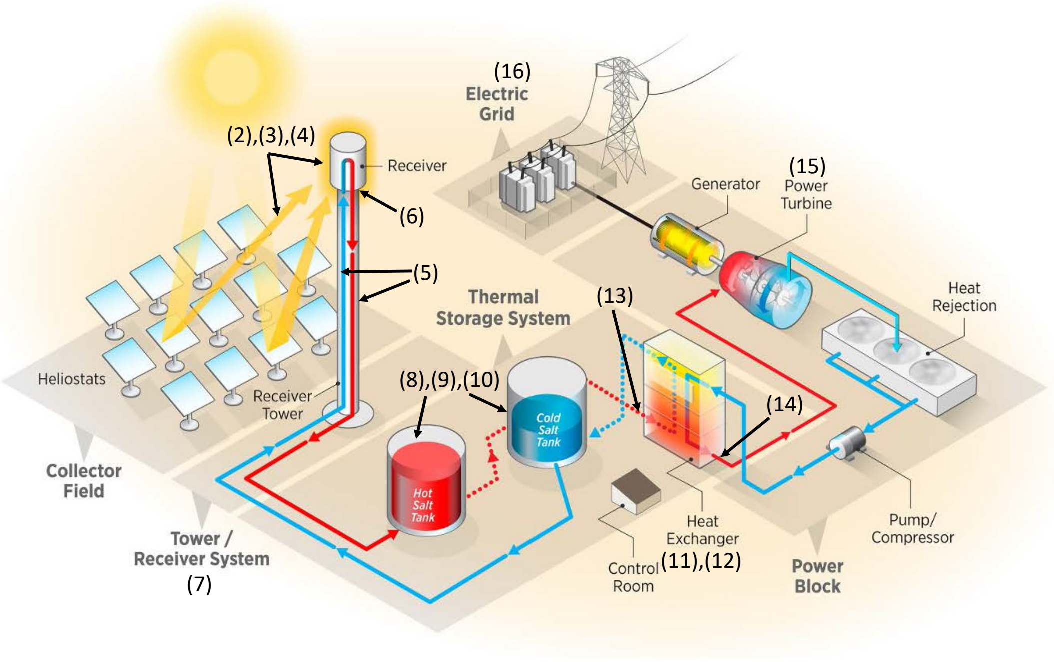

Figure 2.1 CSP-TES plant configuration (Graphic © NREL). A depiction of a molten salt power tower CSP plant, which consists of a heliostat field, molten salt receiver, thermal energy storage, and a steam Rankine power cycle. Numbers relate the sets of constraints in the mathematical formulation to the plant subsystems they represent.

Previous CSP dispatch models [12, 25] represent the thermal energy in storage directly and utilize energy relations to model plant processes, including receiver start-up and operation, thermal energy storage, and cycle start-up and operation. While this yields a linear set of constraints, these relations do not represent energy quality (temperature) trade-offs between receiver collection and power cycle production efficiency [26]. Therefore, we extend the dispatch optimization model ($\mathcal{H}$), presented in Wagner et al. [12], to utilize mass and temperature balance relations for time periods early in the horizon, while retaining the original linear model for time periods further in the future, to improve the quality of the dispatch solutions. Figure 2.2 depicts (a) the plant representation used in ($\mathcal{H}$), and (b) the plant representation used in our model ($\mathcal{R}$), for comparison.

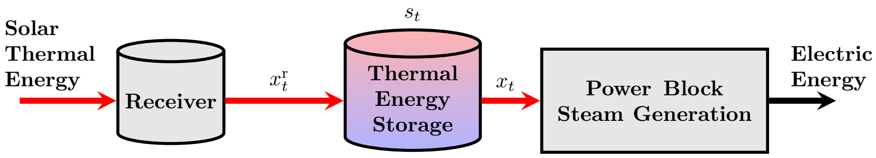

(a) Linear Formulation Plant Representation

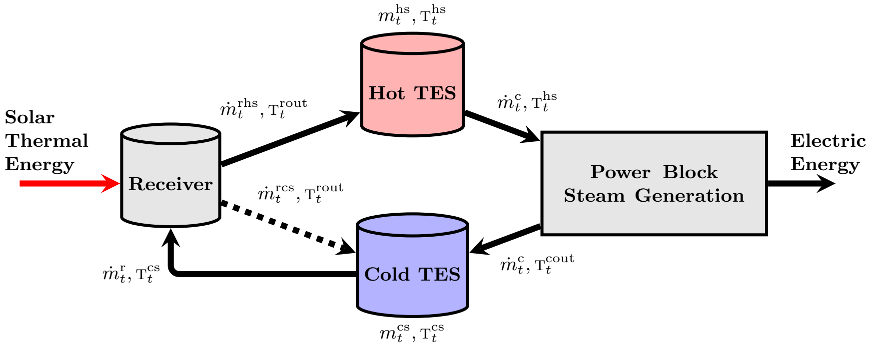

(b) Nonlinear Formulation Plant Representation

Figure 2.2 Real-time Dispatch Optimization Model Formulation Comparison

2.3.1 Notation

The following non-convex, mixed-integer, quadratically-constrained program, $(\mathcal{R})$, requires the initial operational state of the system, the expected cycle conversion efficiency profile as a function of ambient temperature and thermal input, power cycle thermal input and conversion efficiency regressions, pumping power regressions, and the energy price, or tariff profile (Table 2.1). In general, upper-case letters denote parameters while lower-case letters are reserved for variables. We use lower-case letters for indices and upper-case script letters for sets.

Table 2.1 Real-time dispatch model, $(\mathcal{R})$, notation.

Indices and Sets	
$t \in \mathcal{T}^{\mathrm{L}}$	Time periods using the linear formulation
$t \in \mathcal{T}^{\mathrm{N}}$	Time periods using the nonlinear formulation
$t \in \mathcal{T}$	Time periods in the problem horizon; i.e., $\mathcal{T} = \mathcal{T}^{\mathrm{N}} \cup \mathcal{T}^{\mathrm{L}}$, $\mathcal{T}^{\mathrm{N}} \cap \mathcal{T}^{\mathrm{L}} = \emptyset$, and $t < t' \quad \forall\, t \in \mathcal{T}^{\mathrm{N}}, t' \in \mathcal{T}^{\mathrm{L}}$

Time-indexed Parameters		Units
D_t	Time-weighted discount factor in period t; i.e., $D_t = \gamma^t$	-
Δ_t	Duration of period t	h

Table 2.1 Continued.

η_t^{amb}	Cycle efficiency ambient temperature adjustment factor in period t	$\text{kW}_\text{e}/\text{kW}_\text{t}$
F_t	Ratio of available to clear-sky CSP receiver power in period t; i.e., $F_t = \frac{Q_t^{\text{in}}}{Q_t^{\text{cls}}}$	-
L_t^{con}	Normalized condenser parasitic loss in period t	-
P_t	Electricity sale price in period t	$\$/\text{kWh}_\text{e}$
Q_t^{cls}	Theoretical clear-sky thermal power generated by the CSP receiver in period t	kW_t
Q_t^{in}	Available thermal power generated by the CSP receiver in period t	kW_t
W_t^{net}	Maximum net grid transmission in period t	kW_e

Cost Parameters		Units
α	Conversion factor between unitless and monetary values	\$
C^{c}	Operating cost of power cycle	$\$/\text{kWh}_\text{e}$
C^{chsp}	Penalty for power cycle hot start-up per start	\$
C^{csb}	Operating cost of power cycle standby operation	\$/h
C^{csu}	Penalty for power cycle cold start-up per start	\$
$C^{\delta\text{W}}$	Penalty for change in power cycle production	$\$/\text{kW}_\text{e}$
C^{r}	Operating cost of heliostat field and receiver	$\$/\text{kWh}_\text{t}$
C^{rhsp}	Penalty for receiver hot start-up per start	\$
C^{rsu}	Penalty for receiver cold start-up per start	\$
C^{vW}	Penalty for change in power cycle production beyond designed limits	$\$/\text{kW}_\text{e}$
γ	Exponential time weighting factor	-
$\hat{P}$	Average electricity sale price	$\$/\text{kWh}_\text{e}$

CSP Field and Receiver Parameters		Units
D^{rsd}	Time required to complete receiver shutdown	h
D^{rsu}	Minimum time required to complete receiver start-up	h
E^{hs}	Heliostat field start-up or shut down parasitic loss	kWh_e
E^{rsd}	Required energy expended to shut down the receiver	kWh_t
E^{rsu}	Required energy expended to start receiver	kWh_t

Table 2.1 Continued.

$\underline{\dot{M}}^{\text{r}}$	Minimum mass flow rate through the receiver	kg/h
$\overline{\dot{M}}^{\text{r}}$	Maximum mass flow rate through the receiver	kg/h
Q^{rl}	Minimum operational thermal power delivered by receiver	kW_t
Q^{rsb}	Required thermal power for receiver standby	kW_t
Q^{ru}	Allowable power per period for receiver start-up	kW_t
$\bar{T}^{\text{rout}}$	Maximum allowable receiver outlet temperature	$^\circ C$
W^{hco}	Heliostat field communication parasitic draw	kW_e
W^{htf}	Tower piping heat trace full load parasitic draw	kW_e
W^{htp}	Tower piping heat trace part load parasitic draw	kW_e
W^{htr}	Heliostat field tracking parasitic draw	kW_e

Thermal Energy Storage Parameters		Units
C^{p}	Specific heat of the HTF	$\text{kWh}_\text{t}/\text{kg}^\circ C$
E^{u}	Thermal energy storage capacity	kWh_t
$\underline{M}^{\text{cs}}$	Minimum mass of HTF in cold storage	kg
$\overline{M}^{\text{cs}}$	Maximum mass of HTF in cold storage	kg
$\underline{M}^{\text{hs}}$	Minimum mass of HTF in hot storage	kg
$\overline{M}^{\text{hs}}$	Maximum mass of HTF in hot storage	kg
$\underline{T}^{\text{cs}}$	Minimum fluid temperature in cold storage	$^\circ C$
$\bar{T}^{\text{cs}}$	Maximum fluid temperature in cold storage	$^\circ C$
$\underline{T}^{\text{hs}}$	Minimum fluid temperature in hot storage	$^\circ C$
$\bar{T}^{\text{hs}}$	Maximum fluid temperature in hot storage	$^\circ C$

Power Cycle Parameters		Units
α^{b}	Regression intercept for HTF temperature drop across the power cycle	$^\circ C$
α^{T}	Inlet temperature regression coefficient for heat transfer fluid temperature drop across the power cycle	-
α^{m}	Mass flow rate regression coefficient for heat transfer fluid temperature drop across the power cycle	$^\circ C$ h/kg
β^{b}	Regression intercept for power cycle efficiency model	kW_e
β^{T}	Regression coefficients for power cycle efficiency model	$\text{kW}_\text{e}/^\circ C$
β^{m}	Regression coefficients for power cycle efficiency model	$\text{kWh}_\text{e}/\text{kg}$
β^{mT}	Regression coefficients for power cycle efficiency model	$\text{kWh}_\text{e}/^\circ C$ kg

Table 2.1 Continued.

$\overline{\Delta T}^{\mathrm{c}}$	Maximum change in temperature of the heat transfer fluid through the steam generation system	$^\circ C$
E^{c}	Required energy expended to cold start the power cycle	kWh_{t}
E^{w}	Required energy expended to warm start the power cycle	kWh_{t}
η^{D}	Cycle nominal efficiency	$\text{kW}_{\mathsf{e}}/\text{kW}_{\mathsf{t}}$
η^{p}	Slope of linear approximation of power cycle performance curve	$\text{kW}_{\mathsf{e}}/\text{kW}_{\mathsf{t}}$
K^{l}	Slope of minimum thermal input to the power cycle per change in input temperature	$\text{kW}_{\mathsf{t}}/^\circ C$
K^{u}	Slope of maximum thermal input to the power cycle per change in input temperature	$\text{kW}_{\mathsf{t}}/^\circ C$
$\underline{\dot{M}}^{\mathrm{c}}$	Minimum mass flow rate of HTF to the power cycle	kg/h
$\overline{\dot{M}}^{\mathrm{c}}$	Maximum mass flow rate of HTF to the power cycle	kg/h
Q^{c}	Thermal power input during power cycle start-up	kW_{t}
Q^{l}	Minimum operational thermal power input to the power cycle	kW_{t}
Q^{u}	Cycle thermal power capacity	kW_{t}
T^{D}	Design point HTF temperature at the power cycle inlet	$^\circ C$
$\dot{W}^{\mathrm{l}}$	Minimum cycle electric power output	kW_{e}
$\overline{\dot{W}}^{\mathrm{p}}$	Maximum parasitic electrical load	kW_{e}
$\dot{W}^{\mathrm{u}}$	Power cycle electric power rated capacity	kW_{e}
$\dot{W}^{\mathrm{v}^{+}}$	Power cycle ramp-up violation limit	$\text{kW}_{\mathsf{e}}/\text{h}$
$\dot{W}^{\mathrm{v}^{-}}$	Power cycle ramp-down violation limit	$\text{kW}_{\mathsf{e}}/\text{h}$
W^{b}	Power cycle start-up and standby operation parasitic load	kW_{e}
W^{c}	Power cycle operating parasitic load	kW_{e}

Continuous Decision Variables		Units
$\hat{s}$	Discounted thermal energy in storage at the end of the problem horizon	kWh_{t}
s_0	Usable thermal energy at the formulation transition period	kWh_{t}

Table 2.1 Continued.

Time-indexed Continuous Decision Variables		Units
d_t^{rsd}	Receiver shutdown time inventory in period $t \in \mathcal{T}$	h
d_t^{rsu}	Receiver start-up time inventory in period $t \in \mathcal{T}$	h
f_t^{rsd}	Fraction of period used for receiver shutdown in period $t \in \mathcal{T}$	-
f_t^{rsu}	Fraction of period used for receiver start-up in period $t \in \mathcal{T}$	-
p_t^{c}	Power draw of HTF pumps to the power cycle in period $t \in \mathcal{T}$	kW$_\text{e}$
p_t^{fw}	Power draw of feedwater pumps to the power cycle in period $t \in \mathcal{T}$	kW$_\text{e}$
p_t^{r}	Power draw of HTF pumps to the receiver in period $t \in \mathcal{T}$	kW$_\text{e}$
$\dot{m}_t^{\text{c}}$	Mass flow rate of HTF to the cycle in period $t \in \mathcal{T}^{\text{N}}$	kg/h
$\dot{m}_t^{\text{rcs}}$	Mass flow rate of HTF to the receiver directed to cold storage in period $t \in \mathcal{T}^{\text{N}}$	kg/h
$\dot{m}_t^{\text{rhs}}$	Mass flow rate of HTF to the receiver directed to hot storage in period $t \in \mathcal{T}^{\text{N}}$	kg/h
m_t^{cs}	Mass of HTF in cold storage in period $t \in \mathcal{T}^{\text{N}}$	kg
m_t^{hs}	Mass of HTF in hot storage in period $t \in \mathcal{T}^{\text{N}}$	kg
s_t	Usable thermal energy in period $t \in \mathcal{T}^{L}$	kWh$_\text{t}$
T_t^{cout}	Temperature of HTF at the cycle outlet in period $t \in \mathcal{T}^{\text{N}}$	$^\circ C$
T_t^{cs}	Temperature of HTF in cold storage in period $t \in \mathcal{T}^{\text{N}}$	$^\circ C$
T_t^{hs}	Temperature of HTF in hot storage in period $t \in \mathcal{T}^{\text{N}}$	$^\circ C$
T_t^{rout}	Temperature of HTF at the receiver outlet in period $t \in \mathcal{T}^{\text{N}}$	$^\circ C$
u_t^{csu}	Power cycle start-up energy inventory in period $t \in \mathcal{T}$	kWh$_\text{t}$
u_t^{rsu}	Receiver start-up energy inventory in period $t \in \mathcal{T}$	kWh$_\text{t}$
u_t^{rsd}	Receiver shutdown energy inventory in period $t \in \mathcal{T}$	kWh$_\text{t}$
$\dot{w}_t$	Power cycle electricity generation in period $t \in \mathcal{T}$	kW$_\text{e}$
$\dot{w}_t^{\delta+}$	Power cycle ramp-up in period $t \in \mathcal{T}$	kW$_\text{e}$

Table 2.1 Continued.

$\dot{w}_t^{\delta^-}$	Power cycle ramp-down in period $t \in \mathcal{T}$	kW_e
$\dot{w}_t^{\mathrm{p}}$	Electrical power purchased from the grid in period $t \in \mathcal{T}$	kW_e
$\dot{w}_t^{\mathrm{s}}$	Electrical power sold to the grid in period $t \in \mathcal{T}$	kW_e
$\dot{w}_t^{\mathrm{v}^+}$	Power cycle ramp-up beyond designed limit in period $t \in \mathcal{T}$	kW_e
$\dot{w}_t^{\mathrm{v}^-}$	Power cycle ramp-down beyond designed limit in period $t \in \mathcal{T}$	kW_e
x_t	Power cycle thermal power utilization in period $t \in \mathcal{T}^{\mathrm{L}}$	kW_t
x_t^{r}	Thermal power delivered by the receiver in period $t \in \mathcal{T}$	kW_t

Time-indexed Binary Decision Variables	
y_t	1 if cycle is generating electric power in period $t \in \mathcal{T}$; 0 otherwise
y_t^{chsp}	1 if cycle hot start-up penalty is incurred in period $t \in \mathcal{T}$ (from standby); 0 otherwise
y_t^{csb}	1 if cycle is in standby mode in period $t \in \mathcal{T}$; 0 otherwise
y_t^{csdp}	1 if cycle is shutting down in period $t \in \mathcal{T}$; 0 otherwise
y_t^{csu}	1 if cycle is starting up in period $t \in \mathcal{T}$; 0 otherwise
y_t^{csup}	1 if cycle cold start-up penalty is incurred in period $t \in \mathcal{T}$ (from off); 0 otherwise
y_t^{cgb}	1 if cycle begins electric power generation in period $t \in \mathcal{T}$; 0 otherwise
y_t^{r}	1 if receiver is collecting thermal power in period $t \in \mathcal{T}$; 0 otherwise
y_t^{rhsp}	1 if receiver hot start-up penalty is incurred in period $t \in \mathcal{T}$ (from standby); 0 otherwise
y_t^{rsb}	1 if receiver is in standby mode in period $t \in \mathcal{T}$; 0 otherwise
y_t^{rsd}	1 if receiver is shutting down in period $t \in \mathcal{T}$; 0 otherwise
y_t^{rsdp}	1 if receiver completes shut down in period $t \in \mathcal{T}$; 0 otherwise
y_t^{rsu}	1 if receiver is starting up in period $t \in \mathcal{T}$; 0 otherwise
y_t^{rsup}	1 if receiver cold start-up penalty is incurred in period $t \in \mathcal{T}$ (from off); 0 otherwise

2.3.2 Objective Function and Constraints

We maximize plant revenue given as profit from the sale of electricity to the utility grid less the cost of purchases from the grid and estimates of operations and maintenance due to dispatch decisions throughout the time horizon in question. We adopt estimates of costs due to the power cycle dispatch solution as in Kumar et al. [48]. Lesser penalties are introduced to enforce the logic associated with the receiver and power cycle standby and shut down modes. Profit terms in the objective are weighted according to an exponentially diminishing discount factor dependent on the number of periods elapsed; specifically, we adopt the exponential factor used in Hamilton et al. [26]. Cost terms are inversely weighted by this same discount factor. Finally, we add an end-of-model thermal storage incentive which is the discounted value of thermal energy in storage at the end of the problem horizon. This objective mimics that given in Wagner et al. [12], but we state it here for completeness.

Real-time Dispatch Model Objective Function

$$
\begin{aligned}
(\mathcal{R})\quad \text{maximize}\quad & \sum_{t\in\mathcal{T}} \Bigg[D_t \Delta_t P_t \left(\dot{w}_t^{\mathrm{s}} - \dot{w}_t^{\mathrm{p}}\right) \\
& - \frac{1}{D_t} \bigg[\Big(C^{\mathrm{csu}} y_t^{\mathrm{csup}} + C^{\mathrm{chsp}} y_t^{\mathrm{chsp}} + \alpha y_t^{\mathrm{csdp}} \Big) \\
& \quad + \Big(C^{\delta \mathrm{W}} (\dot{w}_t^{\delta^+} + \dot{w}_t^{\delta^-}) + C^{\mathrm{vW}} (\dot{w}_t^{\mathrm{v}^+} + \dot{w}_t^{\mathrm{v}^-}) \Big) \\
& \quad + \Big(C^{\mathrm{rsu}} y_t^{\mathrm{rsup}} + C^{\mathrm{rhsp}} y_t^{\mathrm{rhsp}} + \alpha (y_t^{\mathrm{rsb}} + y_t^{\mathrm{rsdp}}) \Big) \\
& \quad + \Delta_t \left(C^{\mathrm{c}} \dot{w}_t + C^{\mathrm{csb}} y_t^{\mathrm{csb}} + C^{\mathrm{r}} x_t^{\mathrm{r}} \right) \bigg] \Bigg] \\
& + \hat{P} \eta^{\mathrm{D}} \hat{s}
\end{aligned} \tag{2.1}
$$

Constraints having terms indexed in period t-1, but applied to all periods $t \in \mathcal{T}$, use the corresponding initial condition parameter for the decision variable when $t = 1$. All time-indexed decision variables requiring an initial value use the same notation for the parameter as the decision variable indexed in period $t = 0$, e.g., the initial condition for the power cycle operating binary variable y_t is the parameter y_0. Constraints indexed over the set of time periods in $\mathcal{T}^{\mathrm{N}}$ apply only to periods using the nonlinear formulation, while constraints indexed over $\mathcal{T}^{\mathrm{L}}$ apply only to those using the linear formulation. Constraints indexed over $\mathcal{T}$ apply in both formulations. Constraints that either mimic or are largely in the spirit of those already given in Wagner et al. [12] are included in Appendix A; we introduce here only those aspects of the formulation that capture the more detailed temperature and mass balance.

2.3.2.1 Receiver Operations

We represent the clear-sky control scheme in the nonlinear formulation by imposing a lower bound on the mass flow rate to the receiver according to modeled cloudless conditions, but have no natural way to incorporate this effect in the linear formulation. The receiver can be operated in several modes, which we represent as follows:

1. Start-up: Thermal power from the heliostat field is used to gradually raise the temperature of the receiver tubing to its operating temperature. HTF is circulated from the cold storage tank through the receiver, and returned back to cold storage with no increase in the HTF temperature.

2. Collection: Thermal power from the heliostat field collected at the receiver causes a positive change in temperature of the HTF pumped through the receiver. This high temperature fluid is directed to the hot storage tank.

3. Standby: HTF is circulated from cold storage through the receiver to maintain its temperature (in the absence of thermal input from the heliostat field), and returned to the cold storage tank at a lower temperature.

4. Shutdown: Thermal power from the heliostat field is applied to the receiver while the receiver tubing is drained. We do not model the mass of HTF that returns to cold storage in this operating mode.

The following constraints govern receiver operations in each operating mode.

Receiver Start-up

$$d_t^{\mathrm{rsu}} \le d_{t-1}^{\mathrm{rsu}} + \Delta_t f_t^{\mathrm{rsu}} \quad \forall\, t \in \mathcal{T} \tag{2.2a}$$

$$d_t^{\mathrm{rsu}} \le D^{\mathrm{rsu}} y_t^{\mathrm{rsu}} \quad \forall\, t \in \mathcal{T} \tag{2.2b}$$

$$D^{\mathrm{rsu}} y_t^{r} \le d_t^{\mathrm{rsu}} + D^{\mathrm{rsu}} \left(y_{t-1}^{\mathrm{r}} + y_{t-1}^{\mathrm{rsb}} \right) \quad \forall\, t \in \mathcal{T} \tag{2.2c}$$

$$u_t^{\mathrm{rsu}} \le u_{t-1}^{\mathrm{rsu}} + \Delta_t \min \left\{ Q_t^{\mathrm{in}} f_t^{\mathrm{rsu}},\ Q^{\mathrm{ru}} \right\} \quad \forall\, t \in \mathcal{T} \tag{2.2d}$$

$$u_t^{\mathrm{rsu}} \le E^{\mathrm{rsu}} y_t^{\mathrm{rsu}} \quad \forall\, t \in \mathcal{T} \tag{2.2e}$$

$$E^{\mathrm{rsu}} y_t^{r} \le u_t^{\mathrm{rsu}} + E^{\mathrm{rsu}} \left(y_{t-1}^{\mathrm{r}} + y_{t-1}^{\mathrm{rsb}} \right) \quad \forall\, t \in \mathcal{T} \tag{2.2f}$$

$$f_t^{\mathrm{rsu}} \le y_t^{\mathrm{rsu}} \quad \forall\, t \in \mathcal{T} \tag{2.2g}$$

$$f_t^{\mathrm{rsu}} \ge y_t^{\mathrm{rsu}} - y_t^{\mathrm{r}} \quad \forall\, t \in \mathcal{T} \tag{2.2h}$$

Prior to collecting energy, the receiver must complete start-up. Physically, this process involves gradually heating the receiver tubing and HTF to the minimum operating temperature, and requires some level of thermal input from the heliostat field. The duration of this process depends on how thoroughly the receiver was drained of the HTF during previous operations. To represent this dependence, constraints (2.2a)-(2.2c) require a start-up time "inventory" be fulfilled, in addition to the start-up energy "inventory" in constraints (2.2d)-(2.2f). The D^{rsu} parameter defining the time to complete receiver start-up could be set by a plant operator depending on how well the receiver was last drained. We employ a common continuous decision variable in both requirements which represents the fraction of the current period used for the start-up process. This variable is controlled by the start-up and operation binary variables in constraints (2.2g)-(2.2h). The remaining fraction of the last period of start-up may be used for collection.

Receiver Collection Energy Balance

$$x^{\mathrm{r}}_t \leq Q^{\mathrm{in}}_t \min\left\{1 - f^{\mathrm{rsu}}_t,\ y^{\mathrm{r}}_t,\ 1 - f^{\mathrm{rsd}}_t\right\} \quad \forall\, t \in \mathcal{T} \tag{2.3a}$$

$$x^{\mathrm{r}}_t \geq Q^{\mathrm{rl}}\left(y^{\mathrm{r}}_t - f^{\mathrm{rsu}}_t - f^{\mathrm{rsd}}_t\right) \quad \forall\, t \in \mathcal{T} \tag{2.3b}$$

The parameter Q^{in}_t provides an upper bound on the amount of thermal power the receiver can collect in each period, which is reduced by the fraction of the current period used for receiver start-up or shutdown in constraint (2.3a). The receiver operating binary forces the power collected to zero for periods in which the receiver is not operating. Receiver power collection must be greater than its non-zero lower bound Q^{rl} during periods in which it is operating, but we relax this lower bound by the fraction of the period used for receiver start-up or shutdown in constraint (2.3b).

Receiver Shutdown

$$d^{\mathrm{rsd}}_t \leq d^{\mathrm{rsd}}_{t-1} + \Delta_t f^{\mathrm{rsd}}_t \quad \forall\, t \in \mathcal{T} \tag{2.4a}$$

$$d^{\mathrm{rsd}}_t \leq D^{\mathrm{rsd}} y^{\mathrm{rsd}}_t \quad \forall\, t \in \mathcal{T} \tag{2.4b}$$

$$D^{\mathrm{rsd}} y^{\mathrm{rsd}}_t \geq D^{\mathrm{rsd}} y^{\mathrm{rsd}}_{t-1} - d^{\mathrm{rsd}}_{t-1} \quad \forall\, t \in \mathcal{T} \tag{2.4c}$$

$$u^{\mathrm{rsd}}_t \leq u^{\mathrm{rsd}}_{t-1} + \Delta_t Q^{\mathrm{in}}_t f^{\mathrm{rsd}}_t \quad \forall\, t \in \mathcal{T} \tag{2.4d}$$

$$u^{\mathrm{rsd}}_t \leq E^{\mathrm{rsd}} y^{\mathrm{rsd}}_t \quad \forall\, t \in \mathcal{T} \tag{2.4e}$$

$$E^{\mathrm{rsd}} y^{\mathrm{rsd}}_t \geq E^{\mathrm{rsd}} y^{\mathrm{rsd}}_{t-1} - u^{\mathrm{rsd}}_{t-1} \quad \forall\, t \in \mathcal{T} \tag{2.4f}$$

$$f^{\mathrm{rsd}}_t \leq y^{\mathrm{rsd}}_t \quad \forall\, t \in \mathcal{T} \tag{2.4g}$$

$$f^{\mathrm{rsd}}_t \geq y^{\mathrm{rsd}}_t - y^{r}_t \quad \forall\, t \in \mathcal{T} \tag{2.4h}$$

Similar to the receiver start-up process, a receiver shutdown process consists of draining the receiver tubing while thermal energy is applied to the receiver by the heliostat field. We use an analogous formulation of this process having both a time "inventory" in constraints (2.4a)-(2.4c) and an energy "inventory" in constraints (2.4d)-(2.4f). We employ a common continuous decision variable in both requirements which represents the fraction of the current period used for the shutdown process. This variable is controlled by the shutdown and operation binary variables in constraints (2.4g)-(2.4h). The remaining fraction of the first period of shutdown may be used for collection.

Constraints (2.2)-(2.4) apply in all time periods of the problem horizon, and are sufficient to represent receiver operations during periods using the linear formulation. We add the following constraints to model the mass flow rate of HTF pumped through the receiver and the temperature of this fluid at the outlet of the receiver in each time period using the following constraints, a subset of which contain some of the nonlinearities that the model possesses.

Receiver Mass Flow Rate

$$\dot{m}_t^{\mathrm{rcs}} + \dot{m}_t^{\mathrm{rhs}} \leq \overline{\dot{M}}^{\mathrm{r}} \min\left\{1,\ y_t^{\mathrm{rsu}} + y_t^{\mathrm{r}} + y_t^{\mathrm{rsb}}\right\} \quad \forall\ t \in \mathcal{T}^{\mathrm{N}} \tag{2.5a}$$

$$\dot{m}_t^{\mathrm{rcs}} + \dot{m}_t^{\mathrm{rhs}} \geq \underline{\dot{M}}^{\mathrm{r}} \max\left\{f_t^{\mathrm{rsu}},\ y_t^{\mathrm{r}} - f_t^{\mathrm{rsd}} + y_t^{\mathrm{rsb}}\right\} \quad \forall\ t \in \mathcal{T}^{\mathrm{N}} \tag{2.5b}$$

$$\dot{m}_t^{\mathrm{rcs}} \leq \overline{\dot{M}}^{\mathrm{r}} \left(f_t^{\mathrm{rsu}} + y_t^{\mathrm{rsb}}\right) \quad \forall\ t \in \mathcal{T}^{\mathrm{N}} \tag{2.5c}$$

$$\dot{m}_t^{\mathrm{rhs}} \leq \overline{\dot{M}}^{\mathrm{r}} y_t^{\mathrm{r}} \quad \forall\ t \in \mathcal{T}^{\mathrm{N}} \tag{2.5d}$$

Constraint (2.5a) enforces an upper bound on the total mass flow rate through the receiver, while constraint (2.5b) provides the lower bound, depending on the current operating mode. Constraint (2.5c) allows mass flow through the receiver to be directed (back) to cold storage only while the receiver is in start-up or standby modes. Constraint (2.5d) allows mass flow through the receiver to be directed to hot storage only when the receiver is in collection mode. We add constraints (2.5c) and (2.5d) to represent the plant's usual operating procedure, which could be relaxed for cases in which the plant has greater flexibility with respect to receiver operations.

Receiver Outlet Temperature

$$\mathrm{T}_t^{\mathrm{rout}} \leq \bar{T}^{\mathrm{rout}} \min\left\{1,\ y_t^{\mathrm{rsu}} + y_t^{\mathrm{r}} + y_t^{\mathrm{rsb}}\right\} \quad \forall\ t \in \mathcal{T}^{\mathrm{N}} \tag{2.6a}$$

$$\mathrm{T}_t^{\mathrm{rout}} \geq \underline{T}^{\mathrm{cs}} \max\left\{y_t^{\mathrm{rsu}},\ y_t^{\mathrm{r}} + y_t^{\mathrm{rsb}}\right\} \quad \forall\ t \in \mathcal{T}^{\mathrm{N}} \tag{2.6b}$$

Constraint (2.6a) allows the receiver outlet temperature to be non-zero only during periods when the receiver is in start-up, collection, or standby modes. Constraint (2.6b) enforces a lower bound on this temperature under the same operating modes.

Receiver Power Balance

$$x_t^{\mathrm{r}} - Q^{\mathrm{rsb}} y_t^{\mathrm{rsb}} = C^{\mathrm{p}} \left(\dot{m}_t^{\mathrm{rcs}} + \dot{m}_t^{\mathrm{rhs}}\right) \left(\mathrm{T}_t^{\mathrm{rout}} - \mathrm{T}_t^{\mathrm{cs}}\right) \quad \forall\ t \in \mathcal{T}^{\mathrm{N}} \tag{2.7a}$$

$$x_t^{\mathrm{r}} \leq F_t C^{\mathrm{p}} \left(\dot{m}_t^{\mathrm{rcs}} + \dot{m}_t^{\mathrm{rhs}}\right) \left(\bar{T}^{\mathrm{rout}} - \mathrm{T}_t^{\mathrm{cs}}\right) \quad \forall\ t \in \mathcal{T}^{\mathrm{N}} \tag{2.7b}$$

Constraint (2.7a) relates the thermal power collected (or consumed to maintain standby) at the receiver to the corresponding temperature change in the mass flow of HTF through the receiver. Constraint (2.7b) ensures that the mass flow rate through the receiver is sufficient to preclude the receiver outlet temperature from exceeding its upper bound under "clear-sky" conditions. The combination of (2.7a) and (2.7b) guarantee that the receiver never exceeds its maximum outlet temperature, and enforce a reduction in outlet temperature when the “clear-sky” fraction parameter F_t is less than 1.

2.3.2.2 Thermal Energy Storage

The following constraints govern thermal energy storage. The linear formulation directly represents the usable thermal energy in storage by summing contributions from the receiver and outlays to the power cycle. The nonlinear formulation instead represents the mass and bulk temperature of the HTF in the hot and cold storage tanks separately. While temperature gradients can exist in these tanks, we assume that the tanks are constantly stirred reactors, which implies that all mass in the tank is at the bulk temperature.

Initial and Transition Energy

$$s_0 = C^{\mathrm{p}}(m_t^{\mathrm{hs}} - \underline{M}^{\mathrm{hs}})(\mathrm{T}_t^{\mathrm{hs}} - \underline{T}^{\mathrm{cs}}), \qquad t = |\mathcal{T}^{\mathrm{N}}| \tag{2.8a}$$

$$\hat{s} = \gamma^{t+1} s_t, \qquad t = |\mathcal{T}| \tag{2.8b}$$

The initial usable thermal energy in storage is calculated from the mass in and bulk temperature of the hot storage tank as in (2.8a), which uses the initial condition parameters of these values for cases in which the first period of the problem horizon subscribes to the linear formulation. The end-of-problem incentive uses the final value of s_t (as in (2.8b)) for cases in which the last period of the problem is modeled with the linear formulation, or an analogous calculation to (2.8a) when the final period uses the nonlinear formulation. We then discount this level of thermal energy via the same exponentially diminishing factor that appears in the objective.

We do not separate hot and cold storage in this representation, nor is there a representation of the temperature of the HTF holding this energy. The efficiency at which this thermal energy is converted to electrical energy is dependent on this temperature, is commonly referred to as the “quality” of the energy, and is a primary consideration in plant operations.

Mass Balance

$$m_t^{\mathrm{cs}} = m_{t-1}^{\mathrm{cs}} + \Delta_t \left(\dot{m}_t^{\mathrm{c}} - \dot{m}_t^{\mathrm{rhs}}\right) \quad \forall\, t \in \mathcal{T}^{\mathrm{N}} \tag{2.9a}$$

$$m_t^{\mathrm{hs}} = m_{t-1}^{\mathrm{hs}} + \Delta_t \left(\dot{m}_t^{\mathrm{rhs}} - \dot{m}_t^{\mathrm{c}}\right) \quad \forall\, t \in \mathcal{T}^{\mathrm{N}} \tag{2.9b}$$

Constraints (2.9a) and (2.9b) account for the mass of HTF entering and leaving the cold and hot storage tanks, respectively. The mass flow rate of HTF to the receiver directed to the cold tank does not appear in constraint (2.9a), because we model this mass as both leaving and returning to the cold storage tank in the same time period.

Energy Balance

$$m_t^{\text{cs}}\mathrm{T}_t^{\text{cs}} = m_{t-1}^{\text{cs}}\mathrm{T}_{t-1}^{\text{cs}} + \Delta_t\Bigg[\big(\dot{m}_t^{\text{c}}\mathrm{T}_t^{\text{cout}} + \dot{m}_t^{\text{rcs}}\mathrm{T}_t^{\text{rout}}\big) - \big(\dot{m}_t^{\text{rcs}} + \dot{m}_t^{\text{rhs}}\big)\mathrm{T}_t^{\text{cs}}\Bigg] \quad \forall\, t \in \mathcal{T}^{\mathrm{N}} \tag{2.10a}$$

$$m_t^{\text{hs}}\mathrm{T}_t^{\text{hs}} = m_{t-1}^{\text{hs}}\mathrm{T}_{t-1}^{\text{hs}} + \Delta_t\Bigg(\dot{m}_t^{\text{rhs}}\mathrm{T}_t^{\text{rout}} - \dot{m}_t^{\text{c}}\mathrm{T}_t^{\text{hs}}\Bigg) \quad \forall\, t \in \mathcal{T}^{\mathrm{N}} \tag{2.10b}$$

Constraints (2.10a) and (2.10b) enforce energy balance on the cold and hot storage tanks, respectively. Similar to the way in which the previous constraints apply mass balance on the tanks, these energy balance constraints control the bulk temperature of each storage tank.

2.3.2.3 Power Cycle Operations

The power cycle can be operated in several modes, which we represent as follows:

1. Start-up: HTF from the hot storage tank is used to gradually raise the temperature of the power cycle components to their operating temperature, and is returned to the cold storage tank. There is a drop in the HTF temperature corresponding to the allowed thermal power extracted during start-up.

2. Production: HTF from the hot storage tank is used to generate high-pressure, high-temperature steam, which expands through a turbine, which turns a generator producing electrical power. The drop in temperature of the HTF and the efficiency at which the thermal energy is converted into electrical energy are modeled using power cycle performance regressions.

3. Standby: Electric heat tracing and boilers maintain power cycle components above ambient temperature, reducing the time required to complete the start-up procedure.

The following constraints govern power cycle operations.

Power Cycle Start-up

$$u_t^{\mathrm{csu}} \leq u_{t-1}^{\mathrm{csu}} + \Delta_t Q^{\mathrm{c}} y_t^{\mathrm{csu}} + \left(E^{\mathrm{c}} - E^{\mathrm{w}}\right) y_{t-1}^{\mathrm{csb}} \qquad \forall\, t \in \mathcal{T} \tag{2.11a}$$

$$u_t^{\mathrm{csu}} \geq u_{t-1}^{\mathrm{csu}} + \Delta_t Q^{\mathrm{c}} y_t^{\mathrm{csu}} - E^{\mathrm{c}} y_t^{\mathrm{cgb}} \qquad \forall\, t \in \mathcal{T} \tag{2.11b}$$

$$u_t^{\mathrm{csu}} \leq E^{\mathrm{c}} y_t^{\mathrm{csu}} \qquad \forall\, t \in \mathcal{T} \tag{2.11c}$$

$$E^{\mathrm{c}} y_t \leq u_t^{\mathrm{csu}} + E^{\mathrm{c}} y_{t-1} \qquad \forall\, t \in \mathcal{T} \tag{2.11d}$$

$$Q^{\mathrm{c}} y_t^{\mathrm{csu}} \leq C^{\mathrm{p}} \dot{m}_t^{\mathrm{c}} \left(\mathrm{T}_t^{\mathrm{hs}} - \mathrm{T}_t^{\mathrm{cout}}\right) + Q^{\mathrm{u}}(1 - y_t^{\mathrm{csu}}) \qquad \forall\, t \in \mathcal{T}^{\mathrm{N}} \tag{2.11e}$$

$$Q^{\mathrm{c}} y_t^{\mathrm{csu}} \geq C^{\mathrm{p}} \dot{m}_t^{\mathrm{c}} \left(\mathrm{T}_t^{\mathrm{hs}} - \mathrm{T}_t^{\mathrm{cout}}\right) - Q^{\mathrm{u}}(1 - y_t^{\mathrm{csu}}) \qquad \forall\, t \in \mathcal{T}^{\mathrm{N}} \tag{2.11f}$$

Power cycle start-up enforced by constraints (2.11a)-(2.11d) is analogous to receiver start-up, but we only insist on an energy "inventory" requirement to complete power cycle start-up, because this process is not dependent on the variable output of the heliostat field. Constraint (2.11a) includes an energy incentive if the power cycle was in standby mode prior to start-up. This incentive allows the power cycle to start up more quickly for cases in which it was previously in standby mode, and is formulated similarly to warm-start constraints in the unit commitment literature [49]. Constraint (2.11b) enforces a lower bound on the cycle start-up energy "inventory" to prevent prolonging power cycle start-up, which could allow the model to ferry HTF from the hot tank back to the cold tank, and is not an operation mode we consider. For time periods in which we employ the nonlinear formulation, we further impose power balance constraints (2.11e) and (2.11f) to model the temperature drop of the HTF across the power cycle during start-up.

Power Cycle Thermal Input

$$x_t \leq Q^{\mathrm{u}} y_t \qquad \forall\, t \in \mathcal{T}^{\mathrm{L}} \tag{2.12a}$$

$$x_t \leq Q^{\mathrm{u}} - K^{\mathrm{u}} \left(T^{\mathrm{D}} - \mathrm{T}_{t'}^{\mathrm{hs}}\right) \qquad \forall\, t \in \mathcal{T}^{\mathrm{L}}, \quad t' = |\mathcal{T}^{\mathrm{N}}| \tag{2.12b}$$

$$x_t \geq Q^{\mathrm{l}} y_t - K^{\mathrm{l}} \left(T^{\mathrm{D}} - \mathrm{T}_{t'}^{\mathrm{hs}}\right) \qquad \forall\, t \in \mathcal{T}^{\mathrm{L}}, \quad t' = |\mathcal{T}^{\mathrm{N}}| \tag{2.12c}$$

$$\mathrm{T}_t^{\mathrm{hs}} - \mathrm{T}_t^{\mathrm{cout}} \geq \left(\alpha^{\mathrm{b}} + \alpha^{\mathrm{T}} \mathrm{T}_t^{\mathrm{hs}} + \alpha^{\mathrm{m}} \dot{m}_t^{\mathrm{c}}\right) - \overline{\Delta T}^{\mathrm{c}}(1 - y_t) \qquad \forall\, t \in \mathcal{T}^{\mathrm{N}} \tag{2.12d}$$

$$\mathrm{T}_t^{\mathrm{hs}} - \mathrm{T}_t^{\mathrm{cout}} \leq \left(\alpha^{\mathrm{b}} + \alpha^{\mathrm{T}} \mathrm{T}_t^{\mathrm{hs}} + \alpha^{\mathrm{m}} \dot{m}_t^{\mathrm{c}}\right) + \overline{\Delta T}^{\mathrm{c}}(1 - y_t) \qquad \forall\, t \in \mathcal{T}^{\mathrm{N}} \tag{2.12e}$$

Constraints (2.12a)-(2.12c) control the thermal input to the power cycle in periods using the linear formulation. Constraints (2.12b) and (2.12c) reduce the upper and lower bounds, respectively, on thermal input to the power cycle based on a linear function of the bulk temperature of the hot storage tank. These reductions reflect bounds on the mass flow rate input to the power cycle (physically imposed by system pumping limits), and assume a constant hot storage tank bulk temperature over all periods using the linear formulation. Constraints (2.12d)-(2.12e) control the thermal input to the power cycle in periods using the nonlinear formulation. We fit the coefficients used in these constraints to the off-design steam Rankine performance model developed in Hamilton et al. [26], which provides a close fit to the more detailed model and is sufficient for our purposes.

Power Cycle Mass Flow Rate

$$\dot{m}^{\mathrm{c}}_t \leq \overline{\dot{M}}^{\mathrm{c}}(y^{\mathrm{csu}}_t + y_t) \quad \forall\, t \in \mathcal{T}^{\mathrm{N}} \tag{2.13a}$$

$$\dot{m}^{\mathrm{c}}_t \geq \underline{\dot{M}}^{\mathrm{c}} y_t \quad \forall\, t \in \mathcal{T}^{\mathrm{N}} \tag{2.13b}$$

The mass flow rate input to the power cycle is controlled by constraints (2.13a) and (2.13b), which is forced to zero in periods when the power cycle is not in start-up or production modes. Constraint (2.13b) imposes a non-zero lower bound on this mass flow rate during periods of energy production, which is relaxed in periods when the power cycle is in start-up mode.

Power Cycle Outlet Temperature

$$\mathrm{T}^{\mathrm{cout}}_t \leq \overline{T}^{\mathrm{cs}}\left(y_t + y^{\mathrm{csu}}_t\right) \quad \forall\, t \in \mathcal{T}^{\mathrm{N}} \tag{2.14a}$$

$$\mathrm{T}^{\mathrm{cout}}_t \geq \underline{T}^{\mathrm{cs}}\left(y_t + y^{\mathrm{csu}}_t\right) \quad \forall\, t \in \mathcal{T}^{\mathrm{N}} \tag{2.14b}$$

Constraints (2.14a)-(2.14b) control the temperature of HTF at the outlet of the power cycle, forcing it to zero in periods when the power cycle is not either in start-up or production modes, and imposing a non-zero lower bound under either of these operating modes.

Power Cycle Electric Output

$$\dot{w}_t = \frac{\eta^{\mathrm{amb}}_t}{\eta^{\mathrm{D}}}\left[\eta^{\mathrm{p}} x_t + (\dot{W}^{\mathrm{u}} - \eta^{\mathrm{p}} Q^{\mathrm{u}}) y_t\right] \qquad \forall\, t \in \mathcal{T}^{\mathrm{L}} \tag{2.15a}$$

$$\dot{w}_t \leq \frac{\eta^{\mathrm{amb}}_t}{\eta^{\mathrm{D}}}\left[\beta^{\mathrm{b}} + \beta^{\mathrm{T}}\mathrm{T}^{\mathrm{hs}}_t + \beta^{\mathrm{m}}\dot{m}^{\mathrm{c}}_t + \beta^{\mathrm{mT}}\dot{m}^{\mathrm{c}}_t\mathrm{T}^{\mathrm{hs}}_t + \dot{W}^{\mathrm{u}}(1-y_t)\right] \qquad \forall\, t \in \mathcal{T}^{\mathrm{N}} \tag{2.15b}$$

$$\dot{w}_t \geq \frac{\eta^{\mathrm{amb}}_t}{\eta^{\mathrm{D}}}\left[\beta^{\mathrm{b}} + \beta^{\mathrm{T}}\mathrm{T}^{\mathrm{hs}}_t + \beta^{\mathrm{m}}\dot{m}^{\mathrm{c}}_t + \beta^{\mathrm{mT}}\dot{m}^{\mathrm{c}}_t\mathrm{T}^{\mathrm{hs}}_t - \dot{W}^{\mathrm{u}}(1-y_t)\right] \qquad \forall\, t \in \mathcal{T}^{\mathrm{N}} \tag{2.15c}$$

$$\dot{w}_t \leq \dot{W}^{\mathrm{u}}\frac{\eta^{\mathrm{amb}}_t}{\eta^{\mathrm{D}}} y_t \qquad \forall\, t \in \mathcal{T} \tag{2.15d}$$

$$\dot{w}_t \geq \dot{W}^{\mathrm{l}}\frac{\eta^{\mathrm{amb}}_t}{\eta^{\mathrm{D}}} y_t \qquad \forall\, t \in \mathcal{T} \tag{2.15e}$$

Constraints (2.15a), (2.15d), and (2.15e) are sufficient to control the production of electric power in periods using the linear formulation. Constraint (2.15a) enforces a linear model of power cycle efficiency with respect to the level of thermal input. Constraints (2.15d) and (2.15e) enforce non-zero upper and lower bounds, respectively, on power cycle output during periods in which the power cycle is in generation mode. We replace (2.15a) with (2.15b) and (2.15c) in periods during which we employ the nonlinear formulation, which enforces a nonlinear model of power cycle efficiency incorporating both mass flow rate and temperature inputs, as well as the level of thermal energy input. This nonlinear efficiency model is consistent with the linear model in (2.15a) at the design point, but imposes reduced efficiency at lower input temperatures. We fit the coefficients in these constraints to the model developed in Hamilton et al. [26]. We find that a linear regression on this model is not sufficient to capture off-design performance and that the bilinear term in (2.15b) and (2.15c) is needed to accurately represent the temperature dependence of the power cycle.

2.3.2.4 Grid Operations

The following constraints govern electric grid input and output, as well as plant parasitic loads.

Electric Power Sold and Purchased

$$\begin{aligned}
\dot{w}_t^{\mathrm{s}} - \dot{w}_t^{\mathrm{p}} = (1 - L_t^{\mathrm{con}})\dot{w}_t - \Big[& p_t^{\mathrm{r}} + \frac{E^{\mathrm{hs}}}{\Delta_t}(y_t^{\mathrm{rsu}} + 2y_t^{\mathrm{rhsp}} + y_t^{\mathrm{rsdp}}) \\
& + W^{\mathrm{hco}} + W^{\mathrm{htr}}(y_t^{\mathrm{rsu}} + y_t^{\mathrm{r}} + y_t^{\mathrm{rsb}}) \\
& + W^{\mathrm{htp}} y_t^{\mathrm{r}} + W^{\mathrm{htf}}(1 - y_t^{\mathrm{r}}) + p_t^{\mathrm{c}} + p_t^{\mathrm{fw}} \\
& + W^{\mathrm{b}}(y_t^{\mathrm{csu}} + y_t^{\mathrm{csb}}) + W^{\mathrm{c}}(1 - y_t) \Big] \quad \forall\, t \in \mathcal{T} && (2.16\mathrm{a}) \\
\dot{w}_t^{\mathrm{s}} \leq \min\{W_t^{\mathrm{net}} y_t, \dot{w}_t\} \quad \forall\, t \in \mathcal{T} && (2.16\mathrm{b}) \\
\dot{w}_t^{\mathrm{p}} \leq \overline{\dot{W}}^{\mathrm{p}}(1 - y_t) \quad \forall\, t \in \mathcal{T} && (2.16\mathrm{c})
\end{aligned}$$

Constraint (2.16a) accounts for electric production and plant parasitic loads. The electric output of the power cycle is reduced by a multiplicative factor representing the power required to operate the steam condenser portion of the power cycle, which is dependent on ambient temperature and varies with respect to the current time period. Other parasitic loads are then subtracted from this net electric output, including HTF and feedwater pumping power, heliostat and heat trace parasitic load, and the power needed to run auxiliary boilers and heat tracing according to the current power cycle operating state. Constraints (2.16b) and (2.16c) provide upper bounds for the electric power sold and purchased, respectively. Changes to the heliostat tracking fraction incur the electric energy load E^{hs}, which is time-averaged over the duration of the current time period. We include linear models of pumping parasitic loads, which depend on receiver and power cycle thermal input, using the linear formulation. Periods using the nonlinear formulation include piece-wise linear models of pumping parasitic loads, and depend on the mass flow rate input to the receiver or power cycle fit to plant operational data.

2.3.2.5 Variable Bounds

Decision Variable Bounds

Variable bounds are enforced in (2.17a)-(2.17m).

$$d_t^{\text{rsu}}, d_t^{\text{rsd}}, f_t^{\text{rsu}}, f_t^{\text{rsd}}, p_t^{\text{r}}, p_t^{\text{c}}, p_t^{\text{fw}}, u_t^{\text{csu}}, u_t^{\text{rsu}}, u_t^{\text{rsd}} \geq 0 \qquad \forall\, t \in \mathcal{T} \tag{2.17a}$$

$$\dot{w}_t, \dot{w}_t^{\delta^+}, \dot{w}_t^{\delta^-}, \dot{w}_t^{\text{s}}, \dot{w}_t^{\text{p}}, x_t^{\text{r}} \geq 0 \qquad \forall\, t \in \mathcal{T} \tag{2.17b}$$

$$0 \leq \dot{w}_t^{\text{v}^+} \leq \dot{W}^{\text{v}^+} \qquad \forall\, t \in \mathcal{T} \tag{2.17c}$$

$$0 \leq \dot{w}_t^{\text{v}^-} \leq \dot{W}^{\text{v}^-} \qquad \forall\, t \in \mathcal{T} \tag{2.17d}$$

$$0 \leq s_t \leq E^{\text{u}} \qquad \forall\, t \in \mathcal{T}^{\text{L}} \tag{2.17e}$$

$$x_t \geq 0 \qquad \forall\, t \in \mathcal{T}^{\text{L}} \tag{2.17f}$$

$$\dot{m}_t^{\text{c}}, \dot{m}_t^{\text{rcs}}, \dot{m}_t^{\text{rhs}}, \text{T}_t^{\text{cout}}, \text{T}_t^{\text{rout}} \geq 0 \qquad \forall\, t \in \mathcal{T}^{\text{N}} \tag{2.17g}$$

$$\underline{M}^{\text{cs}} \leq m_t^{\text{cs}} \leq \overline{M}^{\text{cs}} \qquad \forall\, t \in \mathcal{T}^{\text{N}} \tag{2.17h}$$

$$\underline{M}^{\text{hs}} \leq m_t^{\text{hs}} \leq \overline{M}^{\text{hs}} \qquad \forall\, t \in \mathcal{T}^{\text{N}} \tag{2.17i}$$

$$\underline{T}^{\text{cs}} \leq \text{T}_t^{\text{cs}} \leq \bar{T}^{\text{cs}} \qquad \forall\, t \in \mathcal{T}^{\text{N}} \tag{2.17j}$$

$$\underline{T}^{\text{hs}} \leq \text{T}_t^{\text{hs}} \leq \bar{T}^{\text{hs}} \qquad \forall\, t \in \mathcal{T}^{\text{N}} \tag{2.17k}$$

$$y_t, y_t^{\text{chsp}}, y_t^{\text{csb}}, y_t^{\text{csdp}}, y_t^{\text{csu}}, y_t^{\text{csup}}, y_t^{\text{cgb}} \in \{0, 1\} \qquad \forall\, t \in \mathcal{T} \tag{2.17l}$$

$$y_t^{r}, y_t^{\text{rhsp}}, y_t^{\text{rsb}}, y_t^{\text{rsd}}, y_t^{\text{rsdp}}, y_t^{\text{rsu}}, y_t^{\text{rsup}} \in \{0, 1\} \qquad \forall\, t \in \mathcal{T} \tag{2.17m}$$

2.3.3 Linear Formulation

We formulate ($\mathcal{R}$) with indexing sets, $\mathcal{T}^{\text{N}}$ and $\mathcal{T}^{\text{L}}$, which differentiate the time periods for which we employ a nonlinear or linear plant representation. If the former set is empty and the latter set contains all time periods in the horizon of interest, the representation reduces to a linear one, which is significantly more tractable than ($\mathcal{R}$). Though this formulation cannot represent the temperature dependence of power cycle efficiency, it can find near-optimal solutions to discrete dispatch decisions (e.g., when to begin cycle start-up). Our solution procedures, presented in §2.4 and Appendix B, take advantage of this feature by solving the linear formulation ($\mathcal{L}$) as an intermediate step towards solving the nonlinear formulation ($\mathcal{R}$).

We define the linear formulation ($\mathcal{L}$) as follows, and use this in Appendix B:

- Sets: $\mathcal{T} = \mathcal{T}^{\text{L}}$ and $\mathcal{T}^{\text{N}} = \emptyset$
- Objective: maximize plant revenue (2.1), (i.e., the objective given in ($\mathcal{R}$))
- Constraints:
    - Receiver operations: constraint groups (2.2), (2.3), (2.4), (A.7), and (A.8)
    - Thermal energy storage: constraint (A.3); note s_0 is a parameter defined by (2.8a)

  - Power cycle: constraints (2.11a)-(2.11d), (2.12a)-(2.12c), (2.15a), (2.15d), and (2.15e); as well as constraint groups (A.17), (A.18), (A.19), and (A.20)
  - Grid operations: constraint group (2.16); note we employ alternate definitions of the pumping parasitic loads in (2.16a)

2.4 Solution Techniques

We consider a 48-hour time horizon owing to standard look-ahead policies. Correspondingly, representative problem instances of ($\mathcal{R}$) possess 6,624 constraints, of which 514 contain quadratic terms, and 2,992 decision variables, of which 2,108 are continuous and 884 are binary, corresponding to using nonlinear constraints for all time periods; that is, $\mathcal{T} = \mathcal{T}^{\mathrm{N}}$ and $\mathcal{T}^{\mathrm{L}} = \emptyset$.

Solving instances of the real-time dispatch problem ($\mathcal{R}$), as described in Section 2.3, is intractable, with relative optimality gaps averaging 10% after twelve hours. However, for the purposes of real-time decision support, we require solution times of no more than five minutes. To increase tractability, we implement three solution-expediting techniques, the first of which does not compromise optimality, the second of which is inexact but consistent with typical operations, and the third of which restricts nonlinear constraints to hold for only a portion of the problem horizon. Figure 2.3 summarizes all problem modifications, and we denote the formulation with these modification ($\mathcal{R}'$). The real-time dispatch optimization model is formulated as a hybrid mixed-integer quadratically constrained program and a mixed-integer linear program, with indexing sets defining the portion of the problem horizon using either the nonlinear or linear constraints. This flexibility allows us to balance the computational difficulty of the problem, enforcing the more accurate nonlinear constraints only in those time periods of most value to plant operators. Appendix B describes a heuristic ($\mathbb{R}$) that improves the optimality gap of solutions on average, during a five-minute time limit.

Exact Modifications

Cuts (2.18a)-(2.18d) improve the simple bounds on variables contained in bilinear terms.

Inexact Modifications

- Discretize values of $\dot{m}^c_t$: add binary decision variables to restrict $\dot{m}^c_t$ to a small number of discrete values.
- Formulate as a hybrid nonlinear-linear model: enforce constraints containing bi-linear terms only in a portion of the problem horizon.

Figure 2.3 Summary of Solution Techniques Applied to the Real-time Dispatch Optimization Model ($\mathcal{R}$)

2.4.1 Exact Problem Modifications

The mixed-integer, quadratically-constrained program solver uses McCormick envelope approximations whose error (and the overall speed of the solver) can be improved by tightening simple bounds. Cuts (2.18a)-(2.18d) are applied to ($\mathcal{R}$) and provide modest improvements in solve times. Tightening bounds on other variables contained in bilinear terms was not found to significantly improve the simple bounds on the variables in question nor provide any significant solve time or error reduction.

Cuts on Variables Contained in Bilinear Terms

$$m_t^{\mathrm{cs}} \leq m_{t-1}^{\mathrm{cs}} + \Delta_t \overline{\dot{M}}^{\mathrm{c}} \quad \forall\, t \in \mathcal{T}^{\mathrm{N}} \tag{2.18a}$$
$$m_t^{\mathrm{cs}} \geq m_{t-1}^{\mathrm{cs}} - \Delta_t \overline{\dot{M}}^{\mathrm{r}} \quad \forall\, t \in \mathcal{T}^{\mathrm{N}} \tag{2.18b}$$
$$m_t^{\mathrm{hs}} \leq m_{t-1}^{\mathrm{hs}} + \Delta_t \overline{\dot{M}}^{\mathrm{r}} \quad \forall\, t \in \mathcal{T}^{\mathrm{N}} \tag{2.18c}$$
$$m_t^{\mathrm{hs}} \geq m_{t-1}^{\mathrm{hs}} - \Delta_t \overline{\dot{M}}^{\mathrm{c}} \quad \forall\, t \in \mathcal{T}^{\mathrm{N}} \tag{2.18d}$$

2.4.2 Approximate Linear Formulations

We investigate the performance of several approximate linear formulations of ($\mathcal{R}$) based on the McCormick approximation envelope [33]. This approach involves substituting bilinear terms with an auxiliary variable and applying linear estimator constraints to this auxiliary variable, allowing it to approximate the actual value of the bilinear term. This approximation becomes exact when either variable contained in the bilinear term is at its upper or lower bound. Error increases as the simple bounds of either variable contained in a bilinear term become looser. Piece-wise approximations mitigate the effects of looser bounds by splitting the approximation envelope into smaller sub-envelopes which individually contain less error than a single envelope. The improved accuracy comes at additional computational expense because these formulations require additional binary decision variables to enforce the representation of the appropriate sub-envelopes.

We present a simple analysis to determine an acceptable level of approximation error in the dispatch solution. Constraints (2.15b) and (2.15c) represent the power cycle off-design efficiency regression developed in Hamilton et al. [26], and control the electrical power produced. Therefore, the bilinear term present in this regression, $\dot{m}_t^{\mathrm{c}}\mathrm{T}_t^{\mathrm{hs}}$, significantly affects the objective function. We estimate acceptable approximation error in this bilinear term by calculating the fraction of power cycle input required to achieve the maximum electrical output. We apply a scaling factor, $(1+\epsilon)$, to the bilinear term to represent a known approximation error, as in equation (2.19a). We then determine the fraction of design-point mass flow input to the cycle required to reach the upper bound of the electrical output. Ideally, this ratio would be 1, but decreases as the approximation error increases, effectively allowing the model to “cheat” the power cycle efficiency constraints by extracting more electrical power than is possible at a certain mass flow rate of input.

Relations Estimating the Impact of Bilinear Approximation Error

$$\dot{w} = \beta^{\mathrm{b}} + \beta^{\mathrm{T}} T^{\mathrm{D}} + \beta^{\mathrm{m}} \dot{m}^{\mathrm{c}} + \beta^{\mathrm{mT}} \dot{m}^{\mathrm{c}} T^{\mathrm{D}} \cdot (1+\epsilon) \tag{2.19a}$$

$$\dot{m}^{\mathrm{c}} = \frac{\dot{W}^{\mathrm{u}} - \beta^{\mathrm{b}} - \beta^{\mathrm{T}} T^{\mathrm{D}}}{\beta^{\mathrm{m}} + \beta^{\mathrm{mT}} T^{\mathrm{D}} \cdot (1+\epsilon)} \tag{2.19b}$$

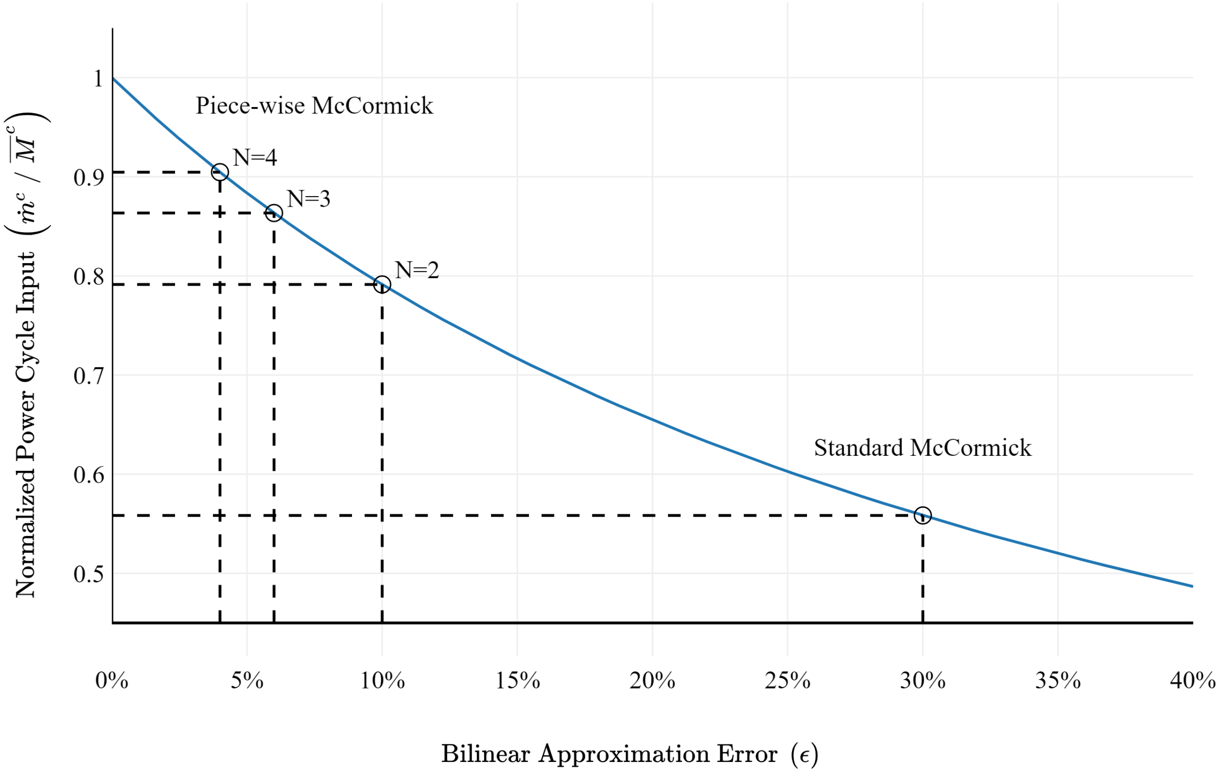

Figure 2.4 Fraction of power cycle input needed for maximum output with respect to bilinear approximation error. The parameter N represents the number of piece-wise approximation envelopes used.

Figure 2.4 depicts the relationship between the bilinear approximation error and the normalized power cycle input required for maximum electrical output. This simple analysis suggests that we could accept approximation error in the range of 5% or less to calculate a solution with 10% approximation error in the power cycle model. We use this relation to judge if an approximate linear formulation produces suitable accuracy. We find that the standard McCormick approximation is computationally efficient but produces a solution with 30% approximation error. Gounaris et al. [42] present many piece-wise approximation envelope formulations for the nonlinear pooling problem and find that their performance is problem-dependent. We implement five of their favored formulations to linearize the bilinear terms in $(\mathcal{R})$, and note that certain formulations are much more computationally tractable than others. However, no versions result in solution times for our instances that are viable in a real-time setting when the number of sub-envelopes exceeds four; on the other hand, four sub-envelopes result in approximately 4% approximation error in the bilinear terms. This 4% approximation error allows for up to 10% error in the power cycle regression. Therefore, we instead solve the exact nonlinear formulation of ($\mathcal{R}$) using the following modifications to reduce the problem size.

2.4.3 Inexact Problem Modifications

We restrict the mass flow rate input to the power cycle, $\dot{m}^{\mathrm{c}}_t$, to a small number of discrete values. This continuous decision variable is contained in two bilinear terms ($\dot{m}^{\mathrm{c}}_t \mathrm{T}^{\mathrm{hs}}_t$ and $\dot{m}^{\mathrm{c}}_t \mathrm{T}^{\mathrm{cout}}_t$), indexed over the periods using the nonlinear formulation, and directly involved in the objective through the electrical output regression constraints (2.15b) and (2.15c). We add binary decision variables to enforce the discrete nature of $\dot{m}^{c}_t$. This modification results in a measurable improvement in problem tractability. (Although it further presents the opportunity to apply exact linearizations of the product of discrete and continuous variables, we find these formulations— which add continuous and binary variables– to be detrimental to problem tractability.) Data show that operators commonly dispatch mass flow rate to the power cycle at a small number of discrete values; however, we do not attempt to prescribe specific values, and instead use evenly spaced values between the minimum and maximum allowable mass flow rate in this analysis.

Table 2.2 Real-time dispatch model, ($\mathcal{R}$), additional notation.

Indices and Sets	
$i \in \mathcal{I}$	Discrete increments of $\dot{m}^{c}_t$

Parameters		Units
$\dot{M}^{\mathrm{csu}}$	Mass flow rate of HTF to the power cycle during start-up	kg/h
$\dot{M}^{\mathrm{c}\Delta}_i$	Increment i of mass flow rate of HTF to the power cycle	kg/h

Binary Variable	
θ_{it}	1 if increment i of mass flow rate to power cycle is used in period t; 0 otherwise

Discretization of Mass Flow Rate to the Power Cycle

$$\dot{m}^{\mathrm{c}}_t = \dot{M}^{\mathrm{csu}} y^{\mathrm{csu}}_t + \underline{\dot{M}}^{\mathrm{c}} y_t + \sum_{i \in \mathcal{I}} \dot{M}^{\mathrm{c}\Delta}_i \theta_{it} \quad \forall\, t \in \mathcal{T}^{\mathrm{N}} \tag{2.20a}$$

$$\theta_{i+1,t} \leq \theta_{it} \quad \forall\, i \in \mathcal{I},\ t \in \mathcal{T}^{\mathrm{N}} \qquad : \ i < |\mathcal{I}| \tag{2.20b}$$

Cut on Binary Variables Used to Discretize $\dot{m}^{\mathrm{c}}_t$

$$\theta_{it} \leq y_t \qquad \forall\, i \in \mathcal{I},\ t \in \mathcal{T}^{\mathrm{N}} \tag{2.21a}$$

We add the binary decision variables θ_{it} and constraints (2.20a)-(2.20b) to restrict $\dot{m}^{\mathrm{c}}_t$ to a small number of discrete values. We find this formulation, which includes a precedence constraint on the added binaries, to be preferable to formulations using a packing constraint. A cut (2.21a) on the added binaries further improves tractability, and relates these new binaries to the existing power cycle binary decision variables.

We then restrict nonlinear constraints to the first 24 hours of the 48-hour problem horizon; that is, $\mathcal{T}^{\mathrm{N}}$ corresponds to the first half of the problem horizon and $\mathcal{T}^{\mathrm{L}}$ to the latter half. This allows the nonlinear constraints to apply only to those time periods which are most important to near-term operator decisions. Representative problem instances of $(\mathcal{R}')$ consisting of 68 time periods and after all inexact modifications, possess 3,144 constraints, of which 338 are quadratic, and 2,928 decision variables, of which 1,868 are continuous and 1,060 are binary. While the number of binary decision variables has increased, the number of quadratic constraints decreases by roughly 35%. Enforcing the nonlinear constraints in only a portion of time periods is an inexact modification; however, this change provides the single most significant improvement in solve time.

2.4.4 Problem Scaling

We find the nonconvex mixed-integer, quadratically-constrained solver to be very sensitive to problem scaling relative to more mature mixed-integer, linear programming solvers. To improve numerical stability, we scale the units of parameters and decision variables to reduce the orders of magnitude between the largest and smallest values. Representative instances of $(\mathcal{R})$ and $(\mathcal{R}')$ have five orders of magnitude between the largest and smallest coefficients after scaling. The original unscaled formulation, which used common engineering units for all parameters, had ten orders of magnitude between the largest and smallest coefficients.

2.5 Scenario Descriptions and Results

The modified real-time dispatch optimization model $(\mathcal{R}')$, is implemented in the AMPL modeling language version 20191223 [50] and solved using Gurobi version 9.5 [51]. A Python wrapper is used to specify plant design parameters, the initial state of the plant, and time-varying parameters before invoking the solver. Upon completion, the dispatch solution is written to an output file, along with the solver log and elapsed wall time. Hardware architecture consists of a Dell Power Edge R610 server with two Intel Xeon x5670s at 2.93 GHz and 192GB RAM, running Ubuntu version 18.04.5. We limit solve time to 300 seconds (which is appropriate for real-time use), specify a minimum relative gap of 1%, and otherwise use the default solver parameters.

2.5.1 Notional Plant Design

We adopt a notional plant design (Table 2.3), which has a nominal generation capacity of 110 MW from a steam Rankine cycle, and approximately 10 hours of thermal storage in a two-tank configuration. We assume that the plant operating fluid is the commonly-used mixture of sodium nitrate and potassium nitrate, which limits the operating temperature to a maximum of 565 $^\circ C$. Table 2.4 lists operating cost parameters, estimated from Kumar et al. [48].

Table 2.3 Notional CSP with TES plant design.

Parameter	Symbol	Units	Value
Receiver:			
Start-up energy	E^{rsu}	MWh_t	141
Minimum start-up time	D^{rsu}	hr	0.75
Maximum (design) thermal input	Q^{ru}	MW_t	565
Minimum thermal input	Q^{rl}	MW_t	141
Maximum outlet temperature	$\bar{T}^{\text{rout}}$	$^\circ C$	565
Maximum mass flow rate	$\overline{\dot{M}}^{\text{r}}$	kg/h	$1.04 \cdot 10^5$
Shutdown energy	E^{rsd}	MWh_t	5
Shutdown time	D^{rsd}	hr	0.5
Thermal energy storage:			
Molten salt specific heat	C^{p}	$\text{kWh}_\text{t}/\text{kg}^\circ C$	1.505
Thermal energy storage capacity	E^{u}	MWh_t	1,100
Minimum mass in storage	$\underline{M}^{\text{cs}}, \underline{M}^{\text{hs}}$	kg	3500
Maximum mass in storage	$\overline{M}^{\text{cs}}, \overline{M}^{\text{hs}}$	Mkg	24
Power cycle:			
Start-up energy consumption	E^{c}	MWh_t	140
Warm start energy consumption	E^{w}	MWh_t	12
Design thermal input	Q^{u}	MW_t	277
Design inlet temperature	$\bar{T}^{\text{D}}$	$^\circ C$	565
Maximum gross output	$\dot{W}^{\text{u}}$	MW_e	110
Maximum mass flow rate	$\overline{\dot{M}}^{\text{c}}$	kg/h	$4.11 \cdot 10^4$
Minimum gross output	$\dot{W}^{\text{l}}$	MW_e	21
Minimum up-time	Y^{u}	h	3
Minimum down-time	Y^{u}	h	8
Standby consumption	W^{b}	MW_e	6.25

2.5.2 Problem Instances

We consider a 48-hour problem horizon with time periods that increase in length after one hour, and again after four hours elapsed, with respect to the beginning of the horizon (see Figure 2.5); smaller time periods (or higher fidelity) thereby exist in the near term, and longer time periods (or coarser fidelity) result in the medium and long term. We adopt a time fidelity roughly consistent with the decision intervals used by plant operators and the availability of weather forecast data, corresponding to 5-minute periods in the first hour, 15-minute periods for the following 3 hours, and hourly periods for the remainder of the problem horizon. In general, the size of each time period can be arbitrarily set by the Δ_t parameters.

Table 2.4 Estimated CSP with TES operating costs.

Operating Costs and Penalties	Symbol	Units	Value
Heliostat field and receiver	C^{r}	$\$/\mathrm{MWh_t}$	3
Receiver cold start-up	C^{rsu}	$\$/\mathrm{start}$	7,000
Power cycle	C^{c}	$\$/\mathrm{MWh_e}$	2
Power cycle cold start-up	C^{csu}	$\$/\mathrm{start}$	10,000
Power cycle change in production	$C^{\delta \mathrm{W}}$	$\$/\Delta\mathrm{MW_e}$	1
Power cycle standby	C^{csb}	$\$/\mathrm{h}$	100

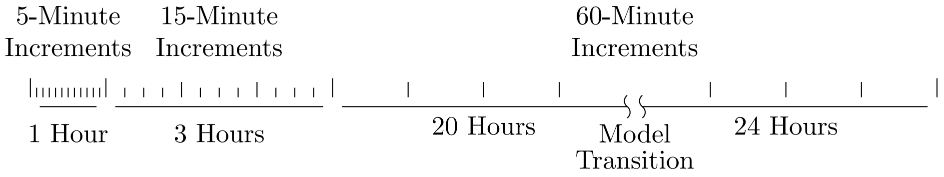

Figure 2.5 Varying Fidelity of Time Periods and Formulation Transition in the Real-Time Dispatch 48-Hour Problem Horizon

We create representative weather condition data relating to solar resource availability and ambient temperature efficiency for seven consecutive days in Clark, Nevada using the SAM Simulation Core software [17, 52]. Time-varying parameters are directly provided by the software, whereas we estimate that the theoretical "clear-sky" resource is equal on all days, and equivalent to the hourly maximum solar resource seen throughout the time period in question. This ensures that for at least some periods in the horizon, the available resource and the theoretical maximum resource match. Figure 2.6 shows the distribution of solar resource for our problem instances and depicts days in Clark (i.e., 1, 3, and 6) that have available solar near the theoretical "clear-sky" maximum; Clark 2 and 4 are somewhat low throughout the solar day; Clark 5 is low at the beginning of the solar day, but recovers towards the end of the day; and Clark 7 is high in the first half but is lower in the second half of the solar day.

We consider two price signals, shown in Figure 2.7: (i) a constant purchase price agreement (PPA) of \$100 / MWh$_e$ during all periods, and (ii) a time-varying price signal taken from an hourly average of California independent system operator (CAISO) pricing. CSP plants operating in the United States have been able to negotiate PPA pricing in their utility markets. These agreements are beneficial because they eliminate variations in pricing due to time of delivery and allow the operators to instead focus on maximizing energy delivered to the grid. As CSP technology matures and becomes more widely adopted in the United States, it is likely that these plants will have to compete in the day-ahead market, where energy prices vary with time of day. Since our model can accommodate time-varying price signals, we include data taken from the California market, which is unique due to the significant penetration of photovoltaic generation. We modify the CAISO price signal data such that the average price for both markets is equal (\$100 / MWh$_e$) to facilitate comparison between problem instances. We assume that power is purchased from the grid at the same price at which it is sold to the grid in each period.

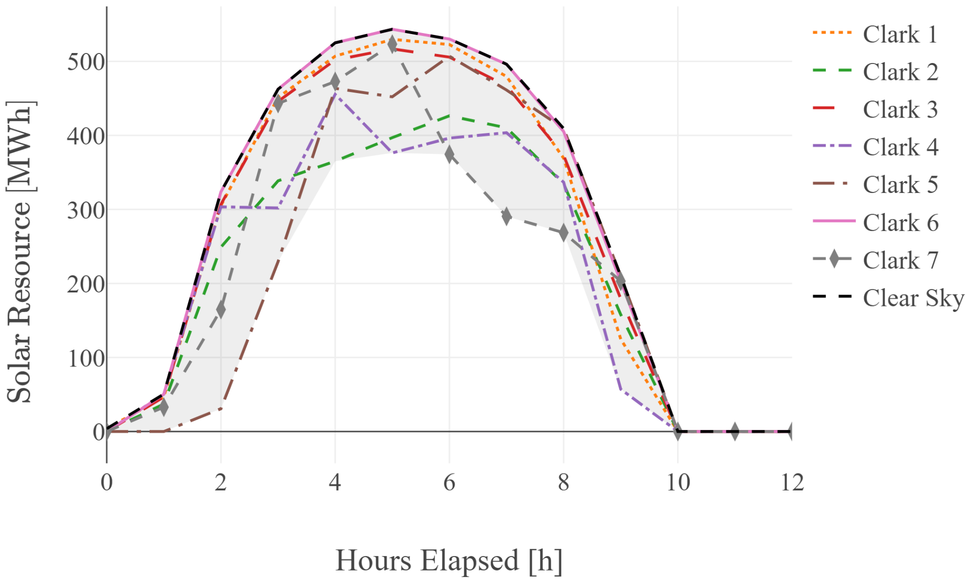

Figure 2.6 Distribution of solar resource in Clark, Nevada problem instances.

2.5.3 Solution Times

We test model solve times over 42 problem instances consisting of the combinations of initial conditions listed in Table 2.5 and time-indexed parameters developed from the weather data provided by the SAM Simulation Core software. The receiver is assumed to begin the day in the “off” mode in all problem instances.

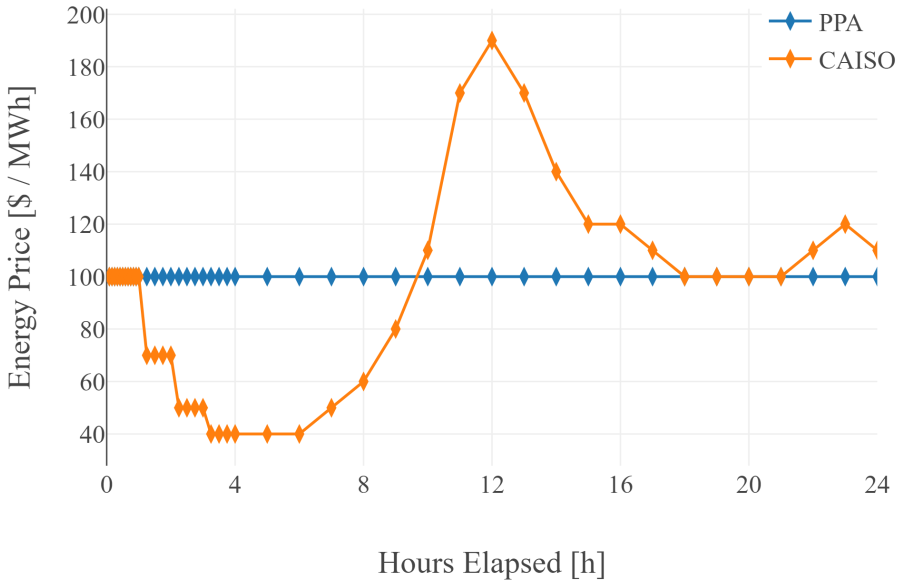

Figure 2.7 Price signals considered, constant purchase price agreement (PPA) and California ISO (CAISO) pricing hourly average.

Table 2.5 Initial Conditions used to develop representative problem instances.

		Baseline	Cycle On Full Tank	Low Temp Tank
Cold Tank	Temp ($^\circ C$)	350	300	300
	Fill (%)	80	10	80
Hot Tank	Temp ($^\circ C$)	550	550	500
	Fill (%)	20	90	20
Power Cycle		standby	minimum output	standby

- Time Indexed Parameters
  - Clark 1-7: Developed from seven days of weather data collected in Clark, Nevada.
  - PPA or CAISO: Price signals assuming either a constant PPA or CAISO hourly average market.

Table 2.6 summaries the benefit to tractability of the exact and inexact modifications presented in Appendix B and Section 2.4. We remove each modification individually to test the improvement provided independently of other modifications. We see steady improvement in the average gap of the problem instances considered, with the exception of the discretization of $\dot{m}^c_t$ for the PPA price signal; in this case, maintaining the variable as continuous (with the other enhancements) provides the best average results, perhaps owing to recent improvements in the solver's ability to handle numerics and in its treatment of the McCormick underestimators. Results for the maximum gap are less clear, possibly due to the solver's heavy reliance on heuristics to produce feasible solutions. We present the number of problem instances solved during the five-minute time limit for completeness, and note that previous versions of the Gurobi solver resulted in far fewer instances solved without the proposed modifications. Given a more challenging model and/or less sophisticated solver, our modifications increase in relevancy.

Table 2.6 Comparison of tractability for each technique presented. †The number of problem instances for which the solver produces a feasible solution during the five-minute time limit.

	PPA Price Signal		
	Solved†	Average Gap	Max Gap
Phased Solve $(\mathcal{L})$-$(\hat{\mathcal{R}})$-$(\mathcal{R}')$	21	1.99 %	5.20 %
$(\mathcal{R}')$ without Phased Solve	21	2.07 %	7.10 %
Drop Mass Cuts (18a)-(18d)	21	2.32 %	7.63 %
Continuous $\dot{m}^c_t$	21	1.48 %	3.77 %
Full Nonlinear Horizon	21	6.41 %	12.82 %
No Scaling	0	-	-

	CAISO Price Signal		
	Solved†	Average Gap	Max Gap
Phased Solve $(\mathcal{L})$-$(\hat{\mathcal{R}})$-$(\mathcal{R}')$	21	4.25 %	11.32 %
$(\mathcal{R}')$ without Phased Solve	21	4.61 %	12.04 %
Drop Mass Cuts (18a)-(18d)	21	4.73 %	12.99 %
Continuous $\dot{m}^c_t$	21	5.08 %	16.04 %
Full Nonlinear Horizon	21	5.61 %	115.81 %
No Scaling	0	-	-

Table 2.7 summarizes solution times and relative gaps resulting from solving the real-time dispatch optimization model $(\mathcal{R}')$ on these 42 instances, having implemented the modifications presented in Section 2.4.3. Solve times average 252 seconds to achieve an average relative gap of approximately 3%. For the problems with greater-than-average gaps, there appears to be difficulty in determining feasible solutions (i.e., slow progress in the lower bound). In select problem instances, there is slow improvement in the upper bound as well.

2.5.4 Example Dispatch Solution

We present the dispatch solution for a problem instance consisting of the Clark 6 solar day and the low-temperature tank initial condition. This solar day has consistently high solar resource, but the hot tank initial temperature is significantly below the design point ($500°C$ versus $565°C$). We choose this solution because it facilitates the discussion of trade-offs in the model's objective. Higher hot storage tank temperature allows for increased efficiency in the power cycle, and our resulting intuition about this problem instance is correct in that the hot tank temperature increases over the course of the problem horizon.

Table 2.7 Real-Time Dispatch ($\mathcal{R}'$) Timing Study Results. †300-second time limit reached; objective value is reported in thousands of dollars.

PPA	Baseline Initial			Cycle On Full Tank			Low Temp Tank		
Price	Time	Obj	Gap	Time	Obj	Gap	Time	Obj	Gap
Clark 1	†	175.4	1.96 %	58 s	222.6	0.89 %	†	155.2	1.51 %
Clark 2	†	155.1	3.62 %	291 s	207.1	1.00 %	†	133.1	4.10 %
Clark 3	†	186.1	4.64 %	74 s	253.9	0.96 %	†	165.7	4.82 %
Clark 4	†	193.6	1.66 %	30 s	238.4	0.67 %	†	172.5	1.61 %
Clark 5	†	175.5	4.85 %	†	233.1	2.32 %	†	155.8	4.14 %
Clark 6	†	175.6	1.52 %	43 s	222.8	0.24 %	†	154.4	1.68 %
Clark 7	†	171.1	2.97 %	201 s	223.6	1.00 %	†	148.8	4.03 %
CAISO	Baseline Initial			Cycle On Full Tank			Low Temp Tank		
Price	Time	Obj	Gap	Time	Obj	Gap	Time	Obj	Gap
Clark 1	†	223.5	2.40 %	236 s	253.4	0.98 %	†	208.2	4.03 %
Clark 2	†	190.3	10.50 %	†	231.5	3.81 %	†	171.3	12.04 %
Clark 3	†	231.6	4.27 %	†	270.1	2.57 %	†	214.2	4.13 %
Clark 4	60 s	242.6	0.19 %	69 s	269.9	0.31 %	†	228.9	1.06 %
Clark 5	†	210.5	6.89 %	†	252.6	3.27 %	†	190.5	10.11 %
Clark 6	†	224.6	1.23 %	63 s	253.5	0.55 %	†	209.5	2.88 %
Clark 7	†	201.0	10.68 %	†	245.4	3.88 %	†	183.1	11.09 %
Max	†	-	10.68 %	†	-	3.88 %	†	-	12.04 %
Average	283 s	-	4.17 %	171 s	-	1.29 %	†	-	4.56 %

Figure 2.8 shows the receiver outlet temperature and mass flow rate during the solar day, where receiver operations for this problem instance are the same under either the PPA or CAISO price signal. The fraction of available solar resource collected is close to 100%, and so is not plotted for clarity. The "clear-sky" control policy, enforced by constraint (2.7b), provides a lower bound on the allowable mass flow rate according to the maximum receiver outlet temperature and "clear-sky" solar resource. We note that the actual mass flow rate to the receiver is very close to this lower bound. Operating the receiver at this mass flow rate means the receiver outlet temperature is very near its maximum achievable value. This is favorable with respect to the objective because the power cycle efficiency improves as the hot storage tank temperature increases, and so the receiver is being operated to maximize the hot storage tank temperature.

Figure 2.9 shows the power cycle output profile and hot tank temperature for the CAISO price signal and the remaining problem parameters as those associated with the dispatch solution in Figure 2.8. After the power cycle completes start-up, it operates near 75% capacity for about an hour before ramping down to minimum output during the periods of less-than-average energy price. This is due to the "duck curve" nature of the CAISO price signal, in which the abundance of photovoltaic generation reduces the price incentive during periods of high solar availability. As the price increases above average, the power cycle ramps to 100% output until the hot storage tank is emptied. The power cycle returns to standby operation until the following day. An important feature of this problem instance is that the plant's hot storage tank is initially at a temperature significantly below its design value. Power cycle operations early in the solar day reduce the total mass at this lower temperature in the hot tank, allowing the hot tank temperature to more quickly recover to its design temperature. Operating at minimum output during the hours of solar availability allows the power cycle to cover the parasitic draw of receiver operations, though the price signal during these periods is less than prices later in the problem horizon.

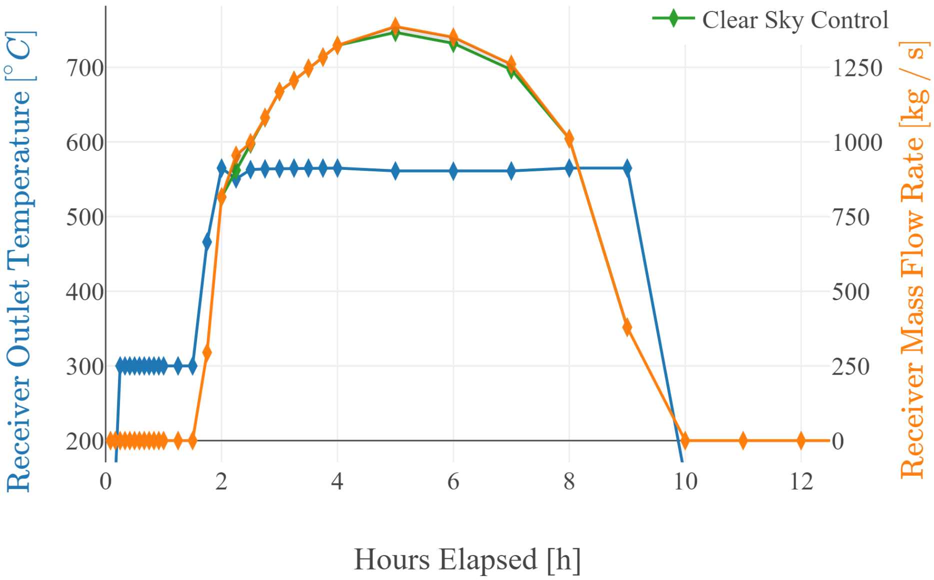

Figure 2.8 Example receiver dispatch solution.

Figure 2.10 shows the power cycle output profile and hot tank temperature for the PPA price signal and the same remaining problem parameters as those corresponding to the solutions shown in Figures 2.8 and 2.9. The power cycle completes start-up about two hours later under the PPA price signal relative to the CAISO price signal, which allows the hot storage tank temperature to begin recovering from its low initial condition before being used at the power cycle. It then ramps to 100% output for five hours before ramping down to near minimum output for the remainder of the day. The long period of near-minimum output in this solution results from the specific parameter values (and assumptions) used in this analysis, which have the following relative magnitudes: Cycle Ramping $<$ Cycle Efficiency $<$ Cycle Standby $<$ Storage Incentive $<$ Profit. Because we assume that energy is purchased from and sold to the grid at the same price, operating the power cycle in cycle standby mode is more expensive than generating power at minimum load. If, however, energy could be purchased from the grid at wholesale price, power cycle standby would price favorably and the power cycle would instead return to standby at the end of the solar day.

We note the following features in both solutions presented here: (i) power cycle operations during the solar day (in the absence of a varying price signal) allow the plant to cover the parasitic loads incurred by receiver operations, (ii) the dispatch model readily follows a varying price signal (sometimes aggressively ramping cycle output to do so), and (iii) power cycle operations at minimum output incur significant efficiency losses, but these losses are less than those incurred from the electric load of cycle standby under our market assumptions.

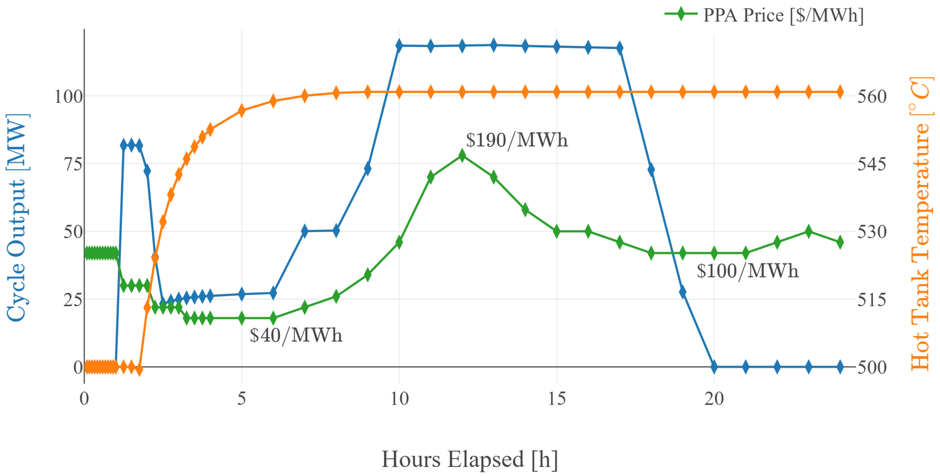

Figure 2.9 Example power cycle dispatch solution under the CAISO price signal.

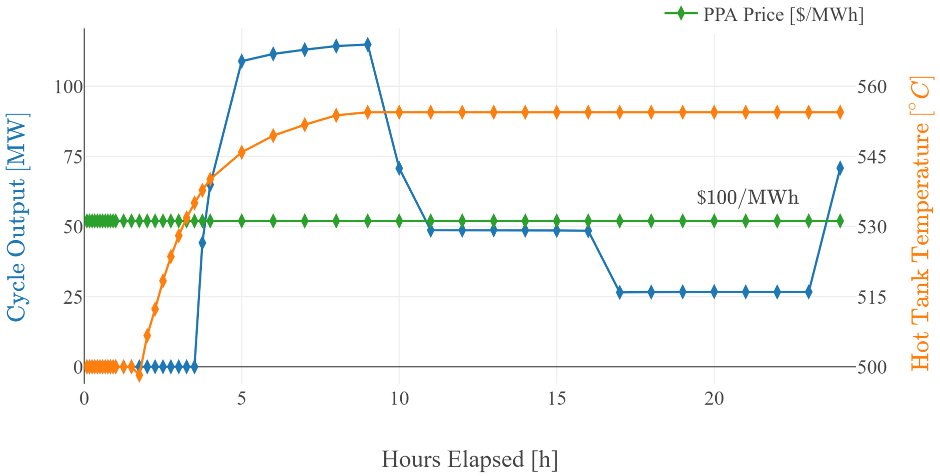

Figure 2.10 Example power cycle dispatch solution, under the PPA price signal.

2.5.5 Validation of Inexact Modifications

We attempt to validate the inexact modifications presented in Section 2.4.3 by solving instances of $(\mathcal{R})$ and corresponding instances of $(\mathcal{R}')$. Ideally, solutions to instances without the changes would be similar to those with the changes, or we could determine a bound on the improvement possible by removing these modifications to the problem. Unfortunately, instances of $(\mathcal{R})$ without these inexact changes could not be solved to a reasonable optimality gap in order to make a comparison.

2.6 Conclusions and Future Work

We extend the CSP with TES dispatch optimization model given in Wagner et al. [12] for real-time decision support. Our contributions include: increasing time fidelity in the near-term portion of the problem horizon; enforcing minimum up- and down-time requirements at the power cycle; improving the accuracy of the receiver and power cycle start-up processes; and formulating mass and temperature representations of the receiver, storage, and power cycle. The resulting non-convex mixed-integer, quadratically-constrained program is computationally intractable with respect to supporting real-time decisions. Therefore, we develop cuts and make realistic approximations to quickly determine near-optimal solutions, i.e., within 3% on average for the instances we test, that can be determined in five minutes or fewer. We present example dispatch solutions of a CSP with TES plant in a notional energy market. More generally, this work demonstrates the potential of solving a non-convex mixed-integer, quadratically-constrained program for the purposes of real-time decision support. Future research efforts might use this model to develop standard policies, allow operators to achieve near-optimal dispatch in the absence of an optimization model, and explore a wider range of problem instances to analyze features impacting plant revenue.

2.7 Acknowledgments

This material is based upon work supported by the U.S. Department of Energy's Office of Energy Efficiency and Renewable Energy (EERE) under the Solar Energy Technologies Office Award Number 34245. This paper was prepared as an account of work sponsored by an agency of the United States Government. Neither the United States Government nor any agency thereof, nor any of their employees, makes any warranty, express or implied, or assumes any legal liability or responsibility for the accuracy, completeness, or usefulness of any information, apparatus, product, or process disclosed, or represents that its use would not infringe on privately owned rights. Reference herein to any specific commercial product, process, or service by trade name, trademark, manufacturer, or otherwise does not necessarily constitute or imply its endorsement, recommendation, or favoring by the United States Government or any agency thereof. The views and opinions of authors expressed herein do not necessarily state or reflect those of the United States Government or any agency thereof.

CHAPTER 3

SUBMITTED PAPER: OPTIMAL SIZING AND DISPATCH OF SOLAR POWER WITH STORAGE

Modified from a paper submitted to *Optimization and Engineering*.

Reproduced with permission from Springer Nature.

John L. Cox[7,8], William T. Hamilton[9], Alexandra M. Newman[10], Janna Martinek[11]

Designers of utility-scale solar plants with storage, seeking to maximize some aspect of plant performance, face multiple challenges. In many geographic locations, there is significant penetration of photovoltaic generation, which depresses energy prices during the hours of solar availability. An energy storage system affords the opportunity to dispatch during higher-priced time periods, but complicates plant design and dispatch decisions. Solar resource variability compounds these challenges, because determining optimal system sizes requires simultaneously considering how the plant will be operated under the imposed market and weather conditions.

We develop an approach to analyze the economic performance of hybrid and single-technology solar power plants, which incorporates optimal dispatch, and considers the expected weather and electricity market conditions. We utilize the System Advisor Model software package to simulate the operation of multiple renewable generation and energy storage technologies, in conjunction with hourly-fidelity generation decisions determined by a revenue-maximizing, mixed-integer linear program. We show that, under our assumed weather and market conditions, the lifetime benefit-to-cost ratio can be improved by 6 to 19 percent, relative to a baseline design without optimizing, and that a concentrating solar power with thermal energy storage design produces significantly more energy per year, but is less profitable under our cost assumptions.

3.1 Introduction

Renewable energy technology has progressed significantly with respect to reductions in cost-per-Watt of capacity [2, 3], in part, motivating interest in the construction of larger renewable energy power plants. The major drawback to the greater prevalence of these plants is that most renewable technologies cannot be dispatched according to grid demand, and instead produce energy only when the resource is available. Cost and capacity improvements to electrical and thermal storage technologies have allowed various forms

---

[7] Graduate student, Colorado School of Mines

[8] Primary researcher and author

[9] Post-Doctoral Researcher, National Renewable Energy Laboratory

[10] Professor, Colorado School of Mines

[11] Researcher, National Renewable Energy Laboratory

of renewable energy to be stored to more flexibly meet demand. The hybridization of renewable energy plants can further improve the availability of renewable energy, and provide greater dispatchable capacity at a lower cost [53–55]. Figure 3.1 depicts a notional CSP and PV hybrid plant with both thermal energy and battery storage.

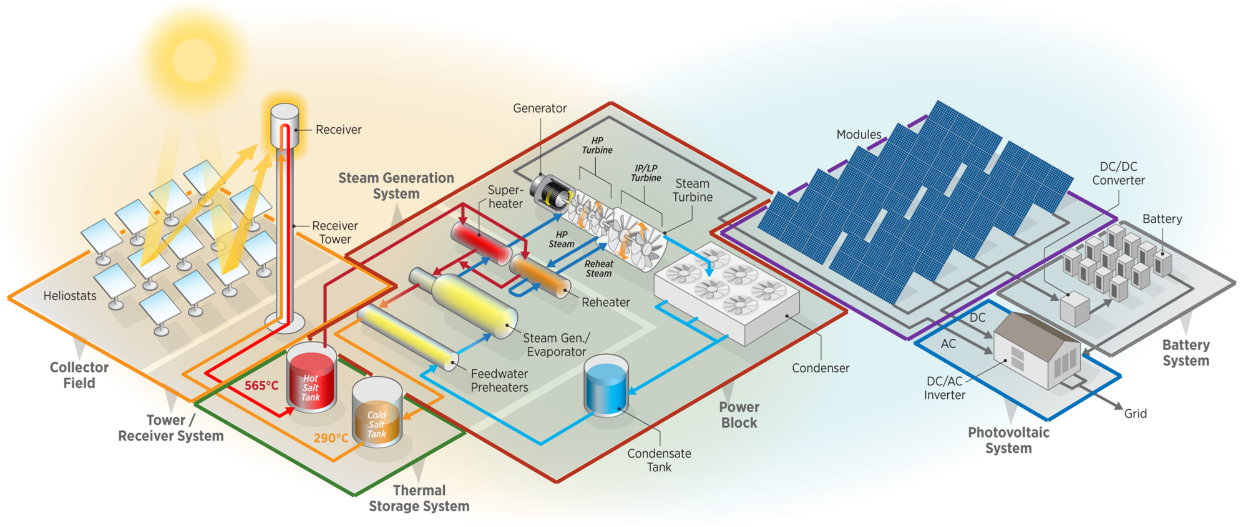

Figure 3.1 Hybrid CSP-PV with storage plant configuration (Graphic © NREL). A depiction of a molten salt power tower CSP plant with thermal energy storage and a steam Rankine power cycle, co-located with a PV field and battery storage. Colored by the system sizing design variables: **CSP solar multiple**, **TES hours**, **CSP cycle capacity**, **PV field DC capacity**, and **battery hours of storage**.

Photovoltaic (PV) panels generate electricity directly, by way of the photovoltaic effect, which can be stored for later use (e.g., in a battery). Concentrating solar power (CSP) uses mirrors to focus the sun's energy to induce an increase in temperature of a heat transfer fluid. The thermal energy stored in this fluid is then converted to electrical energy, typically via a steam Rankine power cycle. Utility companies and governments may provide incentives via time-of-delivery price schedules to generate power at times of the day during which demand is greater or supply is lower. At the time of this writing, PV-generated energy has become sufficiently common in some markets so as to depress energy prices during the solar day, which requires the use of a storage system to dispatch during higher-priced periods. Owing to their collection of thermal, rather than electrical, energy, CSP systems are often coupled with a thermal energy storage system, which improves their annual energy production and potentially provides them with a competitive edge in day-ahead markets. Compared to thermal energy storage, electrochemical battery systems are more expensive per unit capacity, which can make their use for bulk storage, i.e., greater than 8 hours, prohibitively expensive. Utility-scale battery systems are increasing in number and maturity, but are still much less common than PV plants without storage [56, 57].

To evaluate the performance of a plant design under the imposed market and weather conditions, we employ the National Renewable Energy Laboratory's (NREL) System Advisor Model (SAM) to simulate operations. Plant operational decisions are guided by a dispatch optimization model that maximizes plant revenue from energy sales less estimates of operations-and-maintenance costs. We use economic performance metrics of the plant simulation calculated by SAM financial models. This model of plant performance is both complex and implicit, and so we cannot invoke optimization techniques that require convenient mathematical structure and properties (e.g., convexity of the feasible region). Numerous black-box optimization algorithms using various approaches (e.g., surrogate model fitting) are available as open-source software. We focus on algorithms which allow seeding of prior knowledge, for the sake of efficiency.

A concurrent execution framework facilitates sampling and optimizing the plant's design according to the chosen performance metric. The simulation, dispatch, and execution framework are packaged in the Hybrid Optimization and Performance Platform (HOPP) [58]. Designing a solar energy plant with storage is challenging because of the many degrees of freedom that affect the internal and external system interactions and cost-to-performance trade-offs. Therefore, we consider only high-level aspects of the plant design. Overall, we limit design variables to the sizing of plant systems shown in Figure 3.1.

The remainder of this chapter is organized as follows: Section 3.2 provides a literature review of renewable energy technologies, plant performance evaluation, black-box optimization approaches, and a brief overview of sampling techniques. Section 3.3 presents our approach for evaluating hybrid renewable energy plants using the HOPP modeling framework; Section 3.4 describes our design optimization methodology. Section 3.5 presents the results of a study that compares the performance of baseline to optimally sized plants; we present trends seen in this study, dominating plant designs, and representative dispatch solutions. Section 3.6 concludes with a summary and possible extensions of our work.

3.2 Literature Review

At the time of this writing, utility-scale molten salt power tower concentrating solar plants are a relatively new technology with the ability to be coupled with comparatively cost-efficient thermal energy storage [13–15]; a major drawback lies in their high upfront capital cost, though this has been falling in recent years [57]. Jorgenson [59] compares the economic performance of parabolic trough and power tower CSP plants, and Mehos et al. [16] analyze the value of CSP systems with TES on the California regional grid with high renewable penetration; the authors use SAM, a multi-technology performance assessment tool developed at NREL [17], to provide plant performance characteristics, and they use the commercial software package PLEXOS for unit commitment and generator dispatch decisions. Numerous studies point towards the benefits of concentrated solar power when used as part of a hybrid system. Peterseim et al. [60], Pramanik and Ravikrishna [61] and Ju et al. [62] review and analyze CSP hybrid plants, where the hybridization comes in the form of (i) the integration of heat processes, (ii) non-renewable technologies, and (iii) photovoltaics, respectively. Jorgenson et al. [63] present a guide for cost modeling in CSP, while Gonzalo et al. [64] and Rajendran et al. [65] review performance of these systems. Other researchers review historical developments; we refer the reader to Baharoon et al. [66] for general plant construction and development, to Bouhal et al. [67] for analysis specific to Morocco, and to Islam et al. [68] for general international coverage. For a review on the central receiver, or power tower, configuration of concentrating solar power, which we focus on in this work, we refer the reader to Mahdi and Khudheyer [69].

Other researchers have been developing quantitative methodologies to evaluate the efficient design and operation of such plants, most with site-specific case studies in mind. For example, Neber and Lee [70] investigate the design of a solar thermal dish-Brayton system for residential-scale concentrated solar power; the authors propose various system configurations and materials to improve energy conversion efficiency and operating temperature. Farges et al. [71] analyze the design of concentrated solar power plants by estimating annual energy collected and examining specific dates of operation using Monte Carlo sampling. Rady et al. [72] propose a design for a small-scale concentrated solar plant with an organic Rankine cycle, using both parabolic trough and linear Fresnel configurations. They propose an operational strategy that can increase plant efficiency and its corresponding economic value for a study in Egypt. Yan et al. [73] examine the design and implementation of a dish-Stirling configuration, considering aspects such as absorber flux, diameter and focal length of the dish, and installation location. Net power output and efficiency, as measured by a solar-to-electricity ratio, serve as performance parameters. Beegun et al. [74] use SAM to choose a design for a small-scale concentrated solar power hybrid system; design variables include the size of the solar field and the solar multiple, with the goal of maximizing solar-to-electric conversion efficiency. The authors show that their configuration performs more favorably in the summer months for their target user, a textile manufacturing plant in Mauritius. Sezer et al. [75] compute energy and exergy efficiencies for a specific integrated configuration of concentrated solar power and concentrated photovoltaics, in addition to wind; configuration outputs include hydrogen and oxygen, in addition to space heating and cooling, and electricity. Zurita et al. [55] evaluate the economic performance of a hybrid CSP and PV with battery plant according to component sizing and following fixed operation strategies in Chile.

However, these works all analyze a system using a pre-defined set of design specifications and/or operating parameters; none optimizes design and/or operation in any formal sense. By contrast, Starke et al. [76] focus their efforts on plants built in a specific geographic location (the Atacama desert), and, in subsequent work, present a case study of optimizing the design of a CSP and PV hybrid plant in northern

Chile [53]. Bravo and Friedrich [77] optimize a hybrid CSP and PV plant design, with operations controlled by a linear program. The approach we use considers optimal dispatch at hourly time fidelity; Zurita et al. [78] assess the impact of time fidelity on aggregate estimates of plant performance. Yang et al. [29] optimally schedule a CSP-wind hybrid plant with thermal energy storage, and Yang et al. [79] present a novel design optimization methodology of a Brayton-cycle CSP and PV hybrid plant in several locations, where dispatch follows pre-determined load profiles. Zayed et al. [80] optimize the design and operation of a dish-Stirling concentrated solar power system using design variables such as the interception factor; concentrator mirror reflectance; and, receiver absorbance, transmittance and emissivity. Their multi-objective model considers both electric power and efficiency and is solved via a particle swarm methodology; dispatch is not considered.

The dispatchable nature of CSP, when combined with TES, is enticing to markets seeking expanded capacity in periods outside of the hours of solar availability, though investment in CSP plants has been limited to date. A separate line of research examines market incentives for concentrated solar power. Madaeni et al. [81] show that capacity payment incentives can increase the economic value of CSP. Jorgenson et al. [82] explore incentives seeking to expand dispatchable capacity, which may favor CSP. Others have investigated the data and assumptions used in dispatch optimization. Martinek et al. [21] compare CSP plant dispatch and revenue under price-taker and production cost model approaches, and note close agreement. Kahvecioğlu et al. [83] examine the value of conditional weather forecast information in the optimal dispatch of a CSP plant, as well as assigning value to storing energy for use outside the planning horizon.

The implicit nature of the plant evaluation simulation means that we must rely on black-box optimization algorithms. Rios and Sahinidis [84] and, more recently, Larson et al. [85] survey algorithms applicable to this class of problem. Because these algorithms neither guarantee local nor global optimality of a solution, we first execute sampling designs of the parameter space to gain information regarding performance trends in the design space. Dean et al. [86] discuss requirements for effective exploration of the parameter space in computational experiments. Among these, we ensure our samples are *non-collapsing* and *space-filling*, and are sized according to the available computational resources. Our method of evaluating plant performance is deterministic. By utilizing *non-collapsing* sample designs (e.g., Latin Hypercube), we avoid repeated inputs which might provide limited information and waste computational resource. A *space-filling* design avoids neglecting one or more regions of the input space. Among the candidate optimization algorithms, we focus on open-source Python packages that can utilize the results of this sampling. We explore the open source community of Python packages that implement some level of ask-tell interface [87]. This feature allows us to inform the algorithm of the results found during sampling and begin the optimization run using this prior knowledge. Our objective function is well-behaved, appearing to have a single optimal solution in the region of interest. We therefore consider both local and global approaches; conversely, multi-start algorithms appear to be too computationally intense for our purposes though significant progress is being made in this area [88, 89].

Our contributions are (i) a methodology for the evaluation of the performance of a hybrid renewable energy plant design operated according to a revenue-maximizing dispatch schedule; (ii) an execution framework supporting concurrent evaluation of plant designs; and, (iii) a comparison of baseline to optimally-sized plants, and an analysis of their revenue-maximizing operational schedules. We show how system sizing affects plant dispatch and aggregate performance, and compare the relative performance of plant configurations including both single-technology PV and CSP systems with storage as well as a hybrid configuration.

3.3 Design Evaluation Approach

A specific plant design can be evaluated with respect to several metrics. Developers commonly use the levelized cost of energy and benefit-to-cost ratio when comparing design alternatives. We reduce the degrees of freedom in the plant evaluation by only considering high-level system sizing for the variables, whereas lower-level aspects of the plant design are evaluated using the high-level features, or are fixed as parameters. For example, the SolarPILOT™ [90] optimization algorithm sizes the tower and central receiver geometries in the CSP system based on the receiver design point thermal input, while other aspects of the plant design are held constant. We utilize SAM, an open-source software package developed by the NREL, to simulate each generation and storage system included in the specified plant design. At the time of this writing, SAM's graphical user interface does not allow the integration of CSP and PV systems in a single plant, precluding the direct analysis of hybrid systems, i.e., one that co-locates multiple generation technologies in a single plant (as in Figure 3.1). Therefore, we simulate each system individually using the PySAM interface, with operations guided by a dispatch optimization model that considers all plant sub-systems [91]. The dispatch optimization model is a revenue-maximizing, mixed-integer linear program, first developed by Wagner et al. [12] and later extended by Hamilton et al. [25] to include PV and battery sub-systems. The SAM simulation, guided by the dispatch solutions, provides the plant generation schedule, which is used to determine the expected operating costs and revenue of the plant, and, from these, calculates the design objective (e.g., the levelized cost of energy or benefit-to-cost ratio).

Figure 3.2 shows the flow of information in the plant evaluation, where the optimizer determines the values of the design variables and the plant evaluation "black-box" function returns the scalar objective value associated with that specific plant design. Within the plant evaluation function, tasks proceed sequentially, with the outputs of each step given as input to the subsequent steps in the procedure. The design evaluation function begins by receiving the system sizing variable values as input; the SolarPILOT™ algorithm sizes the receiver and heliostat field components of the CSP system (if present in the design); the full plant design is used to initialize the plant simulation in SAM; the plant simulation and dispatch model iterate through the one-year operations simulation; costs and revenue resulting from the schedule of operations are evaluated by a SAM financial model; and outputs from the financial model are used to evaluate the scalar design objective. In addition to being depicted in Figure 3.2, this sequence of tasks is further described in Procedure 3.1. Our approach of connecting the plant simulation and the dispatch model, summarized in Step 4 of Procedure 3.1, is described in greater detail in Sections 3.3.3 and 3.4.3.

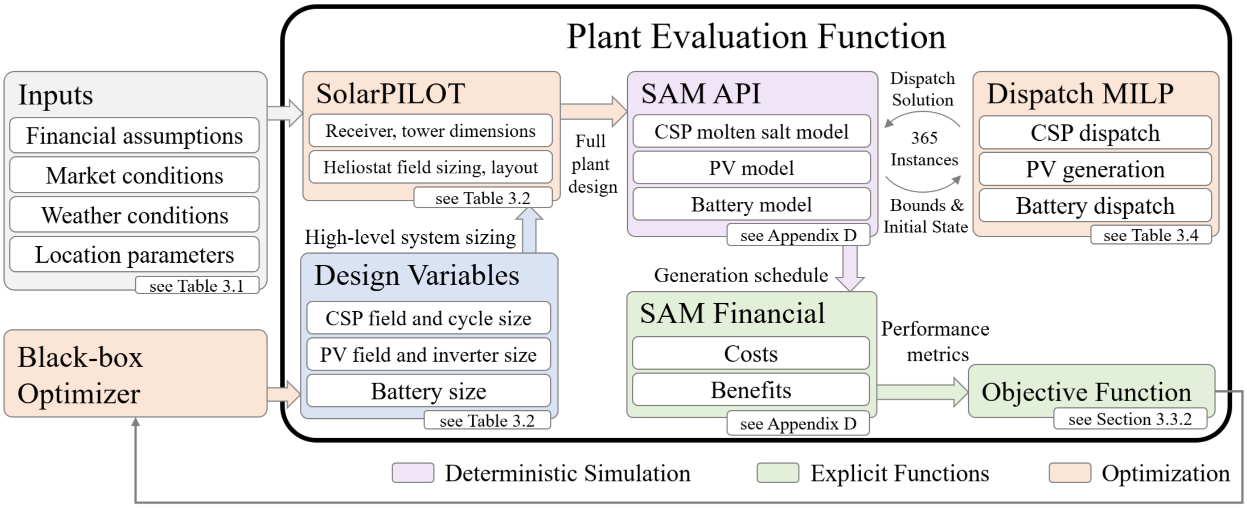

Figure 3.2 Flow diagram of the plant evaluation procedure.

3.3.1 Design Optimization

We seek to optimize the high-level system sizing variables with respect to a scalar performance metric, i.e., the design objective. The plant evaluation procedure is a nonlinear, discrete, constrained, and implicit function of the design variables. As a result, we utilize black-box optimizers, which do not rely on any specific mathematical structure in the evaluation function. The following procedure summarizes the sequence of calculations and software used in evaluating a specific plant design.

Procedure 3.1 Plant Evaluation Function

Step 1: *Inputs* - Collect all parameter values required by the plant evaluation; i.e., financial assumptions, weather and electricity market conditions, location details, and fixed values in the SAM technology models.

Step 2: *Design Variables* - Set the design variable values according to the input given, e.g., from a point in a sampling design or a candidate from an optimization algorithm.

Step 3: *SolarPILOT* - Invoke the SolarPILOT™ optimization algorithm, which determines the receiver, tower, and heliostat field geometry that minimize cost per unit thermal energy generated, while meeting the design point thermal input specified by the provided CSP solar multiple design variable.

Step 4: *Generation Schedule* - Determine a year-long generation schedule at hourly fidelity.

Step 4.1: *Dispatch MILP* - Solve a problem instance of ($\mathcal{H}$) with a 48-hour horizon. Inputs include the plant initial state, weather, and electricity market conditions during the problem horizon.

Step 4.2: *SAM API* - Operate the SAM simulation according to the first 24 hours of the dispatch solution.

Step 4.3: *Repeat* - Document results of the plant simulation, and roll the problem horizon forward 24 hours, repeating Steps 4.1 and 4.2, until a full year has elapsed.

Step 5: *SAM Financial* - Calculate system costs and benefits resulting from the generation schedule. The year-long schedule is repeated for each year in the analysis period after the first. SAM financial models calculate the present value of costs, revenue sources, and the total energy production resulting from the generation schedule.

Step 6: *Objective Function* - Evaluate the design objective function using the outputs of the financial model and plant simulation.

The plant evaluation requires the expected weather conditions and time-of-delivery market pricing at hourly fidelity, as well as the latitude and longitude of the plant site (see Table 3.1). Technology construction, and operations and maintenance costs used in the SAM technology model are summarized in Appendix D, and are the SAM default values at the time of this writing.

Table 3.1 Inputs of the design optimization problem, $(\mathcal{D})$.

Sets	
$\hat{\mathcal{T}}$	Hours in a year

Market Parameters, in time $t \in \hat{\mathcal{T}}$	
Electricity purchase price	$/MWh$_\mathsf{e}$
Electricity sales price	$/MWh$_\mathsf{e}$

Weather Parameters, in time $t \in \hat{\mathcal{T}}$	
Ambient temperature	$^\circ$C
Atmospheric pressure	mbar
Dew point temperature	$^\circ$C
Direct horizontal irradiance	W/m^2
Direct normal irradiance (DNI)	W/m^2
Global horizontal irradiance	W/m^2
Wind speed	m/s

Site Parameters	
Elevation	m
Latitude	degrees
Longitude	degrees

The following constrained and implicit nonlinear program, $(\mathcal{D})$, requires inputs as listed in Table 3.1, and determines high-level system sizing according to the design objective. In general, upper-case letters denote parameters while lower-case letters represent variables. We use lower-case letters for indices and upper-case script letters for sets. Lists of variables are denoted with lower-case bold font symbols. We use the $(\oplus)$ symbol to denote concatenation, e.g., of each 48-hour problem instance over the course of a year $(\mathbf{u} = \mathbf{s}_1 \oplus \mathbf{s}_2 \oplus \cdots \oplus \mathbf{s}_P)$.

Table 3.2 Notation of the design optimization problem, $(\mathcal{D})$.

Sets	
$\mathcal{I}$	Design variables
$\mathcal{J}$	CSP field design attributes evaluated from the design variables
$\mathcal{P}$	48-hour problem instances in a year, i.e., $p \in \{1, \ldots, P\}$
$\mathcal{Q}$	SolarPILOT nonlinear constraints

Table 3.2 Continued.

$\mathcal{R}$	Dispatch MILP linear constraints	
$\mathcal{S}$	SAM simulation nonlinear constraints	
$\mathcal{T}_p$	Hourly periods in problem instance p	

Parameters

C_q, C_r, C_s	Constraint right-hand side constant $q \in \mathcal{Q}$, $r \in \mathcal{R}$, $s \in \mathcal{S}$	-
L_i	Lower bound of design variable $i \in \mathcal{I}$	...
U_i	Upper bound of design variable $i \in \mathcal{I}$	...

Design Variables

$\mathbf{x}$	Design variables; i.e., $\mathbf{x} = (x_1, x_2, \ldots, x_i) \;\; \forall\, i \in \mathcal{I}$	...
Battery Storage		
x_1	Battery capacity, hours of design point output	h
x_2	Battery design point power output, fixed in this study	MW$_\text{e}$
CSP Field and Power Cycle		
x_3	Thermal energy storage capacity, in terms of hours of power cycle design point input	h
x_4	CSP field solar multiple	-
x_5	Power cycle design point output, fixed in this study	MW$_\text{e}$
PV Field		
x_6	Field DC capacity	MW$_\text{e}$

CSP field design attributes, given by SolarPILOT

$\mathbf{y}$	Design attributes; i.e., $\mathbf{y} = (y_1, y_2, \ldots, y_j) \;\; \forall\, j \in \mathcal{J}$	...
y_1	Number of heliostats	-
y_2	Heliostat field layout	-
y_3	Receiver height	m
y_4	Receiver diameter	m
y_5	Tower height	m

Dispatch model outputs and initial conditions

$\mathbf{d}_p$	Dispatch solution for each period $t \in \mathcal{T}_p$ in problem instance p	...

Table 3.2 Continued.

SAM simulation outputs		
$\mathbf{u}$	Year-long generation schedule, i.e., $\mathbf{u} = (\mathbf{s}_1 \oplus \mathbf{s}_2 \oplus \cdots \oplus \mathbf{s}_P)$	...
$\mathbf{s}_p$	Feasible generation schedule during problem instance p	...

Other symbols		
f_r	Linear constraint $r \in \mathcal{R}$	-
$\tilde{f}$	Dispatch optimization model linear objective function	-
g_s, g_q	Nonlinear constraint $s \in \mathcal{S}$, $q \in \mathcal{Q}$	-
$\tilde{g}$	Nonlinear design objective function, evaluated from outputs of the SAM financial model	-
$\hat{g}$	Nonlinear SolarPILOT objective function	-
$\mathbb{S}$	Feasible region of the SAM simulation	-

Design Problem

$$(\mathcal{D}) \qquad \max_{\mathbf{x}} \quad \tilde{g}(\mathbf{u}, \mathbf{x}, \mathbf{y}^\star) \tag{3.1}$$

subject to:

$$\mathbf{y}^\star = \min_{\mathbf{y}} \left\{ \hat{g}(\mathbf{y}) \mid g_q(x_3, x_4, \mathbf{y}) = C_q \quad \forall\, q \in \mathcal{Q} \right\} \tag{3.2}$$

$$\left| \begin{array}{l} \text{Determine } \mathbf{s}_p \text{ for each } p \in \mathcal{P} : \\ \quad \mathbf{d}_p^\star = \max_{\mathbf{d}_p} \left\{ \tilde{f}(\mathbf{d}_p) \mid f_r(\mathbf{d}_p, \mathbf{s}_{p-1}, \mathbf{x}, \mathbf{y}^\star) = C_r \quad \forall\, r \in \mathcal{R} \right\} \\ \quad \mathbb{S} = \left\{ \mathbf{s}_p \mid g_s(\mathbf{d}_p^\star, \mathbf{x}, \mathbf{y}^\star) = C_s \quad \forall\, s \in \mathcal{S} \right\} \end{array} \right| \tag{3.3}$$

$$\mathbf{u} = (\mathbf{s}_1 \oplus \mathbf{s}_2 \oplus \cdots \oplus \mathbf{s}_P) \ \mid \mathbf{s}_p \in \mathbb{S} \quad \forall\, p \in \mathcal{P} \tag{3.4}$$

$$L_i \le x_i \le U_i \quad \forall\, i \in \mathcal{I} \tag{3.5}$$

The design problem, $(\mathcal{D})$, minimizes a scalar objective calculated from the SAM financial model outputs for each year in the project lifetime (3.1), as a function of the design variables (see Section 3.3.2). Equation (3.2) represents the SolarPILOT™ optimization algorithm [90], which gives the detailed CSP heliostat and receiver design that minimize the cost of the CSP system per unit of thermal input to the receiver, while meeting the design-point thermal input required by the plant solar multiple and power cycle input design variables. The procedure in (3.3) determines the schedule of plant operations. For each day of a year, a problem instance with a 48-hour horizon is solved, taking the initial plant state from the last period of SAM output. The SAM simulation has a more detailed representation of the plant than the dispatch formulation, and attempts to follow the first 24 hours of the dispatch solution. Failing this, we take a conservative approach and either derate operations from the dispatch solution or shut down that system to preserve feasibility. The feasible schedules of operations for each day of a year are then concatenated to yield the annual plant generation schedule at hourly fidelity, as in equation (3.4). In equation (3.1) the generation schedule from the first year of operations is assumed to occur in each year of the plant lifetime, with annual discount rates and technology degradation applied after the first, and used to calculate the design objective function. Simple bounds are applied to each of the design variables in constraint (3.5), which are continuous.

3.3.2 Design Objective

The design objective is an explicit function of the cost, revenue, and energy generated in each year of the plant's lifetime and depends on the goals of the plant developer. Investors, building a for-profit plant, are interested in maximizing the return on their investment, reflected by metrics of financial performance. Utility providers, seeking renewable capacity expansion, are interested in minimizing the cost of the added capacity, and so would choose metrics of cost efficiency. We use the benefit-to-cost ratio in this work as it mirrors the revenue-maximizing dispatch objective. Mai et al. [92] provide a more complete discussion of metrics which can be used to evaluate a plant's performance.

Table 3.3 Notation for the design objective functions.

Sets		
$\mathcal{Y}$	Years in the plant lifetime; i.e., $y \in \{0, \ldots, Y\}$	
Select Parameters		**Units**
δ	Annual discount rate	-
Metrics of plant performance, given by the SAM financial model		
b_y	Total revenue (benefits) in year y	\$
k_y	Total costs in year y	\$

The benefit-to-cost ratio is defined as the ratio of the present value of all positive cash flows to all negative cash flows. Positive cash flows include revenue from the sale of electricity, capacity payments, and performance-based incentives. Negative cash flows include construction, financing, tax liability, and operations-and-maintenance costs. Both revenue and costs are discounted each year and accumulated to determine their present values. The ratio of all benefits to all costs represents the expected return to investors as a fraction of the total project cost, where values less than 1 indicate that a design is not profitable, and values greater than 1 indicate a positive return on investment.

$$\text{Benefit-to-Cost Ratio} = \frac{\sum_{y \in \mathcal{Y}} \frac{b_y}{(1+\delta)^y}}{\sum_{y \in \mathcal{Y}} \frac{k_y}{(1+\delta)^y}} \tag{3.6}$$

The benefit-to-cost ratio objective functions yield a scalar value, representing the aggregate expected lifetime performance, rather than plant performance on any specfic day, which is appropriate given the estimated weather and market data [93].

3.3.3 Dispatch Optimization

Wagner et al. [12] develop an optimization model for the dispatch of power tower concentrating solar plants. Constraints enforce operating restrictions of the receiver and power cycle, with binary variables representing the various operational states. Hamilton et al. [25] extend this model to allow for the hybridization of power tower CSP with TES and a PV system either with or without battery storage. We utilize a refinement of the dispatch optimization model, $(\mathcal{H})$, to guide operations of the plant simulation, as in Hamilton et al. [94]. This mixed-integer linear program considers the combined dispatch of energy production and storage technologies, and the solution provides a control policy for the plant at hourly fidelity. Thermal energy is collected at the CSP receiver and can be stored or used immediately to produce electricity at the power cycle. Power collected by the PV field can be sold to the grid, used to charge the battery by returning through the AC bus, or curtailed. We consider a 48-hour problem horizon, which is rolled forward every 24 hours for one year. This approach provides the model with a limited view into future weather and market conditions, which is consistent with the information available to plant operators, and improves tractability compared to solving a monolith with a one-year dispatch horizon. The solution to the dispatch optimization model accounts for interactions between systems; e.g., the total power generated by all systems is at most equal to the grid interconnect limit.

Table 3.4 Notation involved in the dispatch model, $(\mathcal{H})$, objective.

Sets		
$\mathcal{T}$	Time periods in the problem horizon	
Time-indexed Parameters		**Units**
P^s_t, P^p_t	Electricity sale and purchase price in time t	\$/MWh$_\mathrm{e}$
Cost Parameters		**Units**
C^{rec}	CSP field and receiver generation cost	\$/MWh$_\mathrm{t}$
C^{rsu}	Receiver cold start-up fixed cost	\$/start

Table 3.4 Continued.

C^{pc}	Power cycle generation cost	$\$/\text{MWh}_\text{e}$
C^{csu}	Power cycle cold start-up fixed cost	$\$/\text{start}$
$C^{\delta x}$	Change in power cycle thermal input penalty	$\$/\text{MW}_\text{t}$
C^{pv}	Photovoltaic field generation cost	$\$/\text{MWh}_\text{e}$
C^{bc}, C^{bd}	Battery charge, discharge operation cost	$\$/\text{MWh}_\text{e}$
C^{bl}	Battery lifecycle cost	$\$/\text{cycle}$

Miscellaneous Parameters		Units
Δ	Time period duration	hr
ϵ	Small value used in objective for binary logic	$\$$
γ	Exponential time weighting factor	-

Continuous Decision Variables		Units
b^c	Battery cycle count	-
$\dot{e}_t^s, \dot{e}_t^p$	Electricity sold to, or purchased from, the grid in time t	MW_e
$\dot{w}_t$	Power cycle electricity generation at time t	MW_e
$\dot{w}_t^+, \dot{w}_t^-$	Power into and out of the battery at time t	MW_e
x_t^δ	Power cycle change in thermal energy input at time t	MW_t
$\dot{w}_t^{pv}$	Power from the photovoltaic field at time t	MW_e
x_t^r	Thermal power delivered by the receiver at time t	MW_t

Binary Decision Variables		
y_t^{csup}	1 if cycle cold start-up penalty is incurred at time t (from off); 0 otherwise	
y_t^{rsup}	1 if receiver cold start-up penalty is incurred at time t (from off); 0 otherwise	
y_t^g	1 if system is net generating in time period t; 0 otherwise	

The formulation maximizes plant revenue, given as profit from the sale of electricity to the utility grid, less the cost of purchases from the grid and estimates of operations and maintenance due to dispatch decisions. Profit terms in the objective are weighted according to an exponentially diminishing discount factor dependent on the number of periods elapsed, whereas cost terms are discounted according to the inverse of this factor. Cost estimates due to power cycle dispatch are given in Kumar et al. [48]. Lesser penalties enforce logic associated with the receiver and power cycle operating modes. This objective mimics that given in Hamilton et al. [25] and Hamilton et al. [94], but we state it here for completeness and color code the terms according to the scheme presented in Figure 3.1: CSP field and receiver, CSP power cycle, PV field, and battery.

Dispatch Objective

$$
\begin{aligned}
(\mathcal{H}) \quad \max \quad \sum_{t \in \mathcal{T}} \Bigg[& \Delta \left(\gamma^{t} P^{s}_{t} \dot{e}^{s}_{t} - \gamma^{-t} P^{p}_{t} \dot{e}^{p}_{t} \right) - \epsilon y^{g}_{t} \\
& - \gamma^{-t} \left(\Delta C^{rec} x^{r}_{t} + C^{rsu} y^{rsup}_{t} + \Delta C^{pc} \dot{w}_{t} + C^{csu} y^{csup}_{t} + C^{\delta x} x^{\delta}_{t} \right) \\
& - \gamma^{-t} \Delta C^{pv} \dot{w}^{pv}_{t} \\
& - \gamma^{-t} \Delta \left(C^{bc} \dot{w}^{+}_{t} + C^{bd} \dot{w}^{-}_{t} \right) \Bigg] - C^{bl} b^{c}
\end{aligned} \tag{3.7}
$$

The revenue-maximizing dispatch objective is most appropriate in an independent system operator market, where each generator is paid according to the time-of-delivery price [94]. The complete formulation of the dispatch optimization model, $(\mathcal{H})$, is presented in Appendix E.

3.4 Design Optimization Methodology

The plant evaluation procedure is implicit and computationally expensive, so we concurrently execute multiple instances when sampling or optimizing, and tally the results so as to prevent redundant calculations when the same design is invoked by multiple algorithms. We utilize open-source optimization and sampling approaches, and sample prior to optimizing to reduce the overall computational expense (see Figure 3.3).

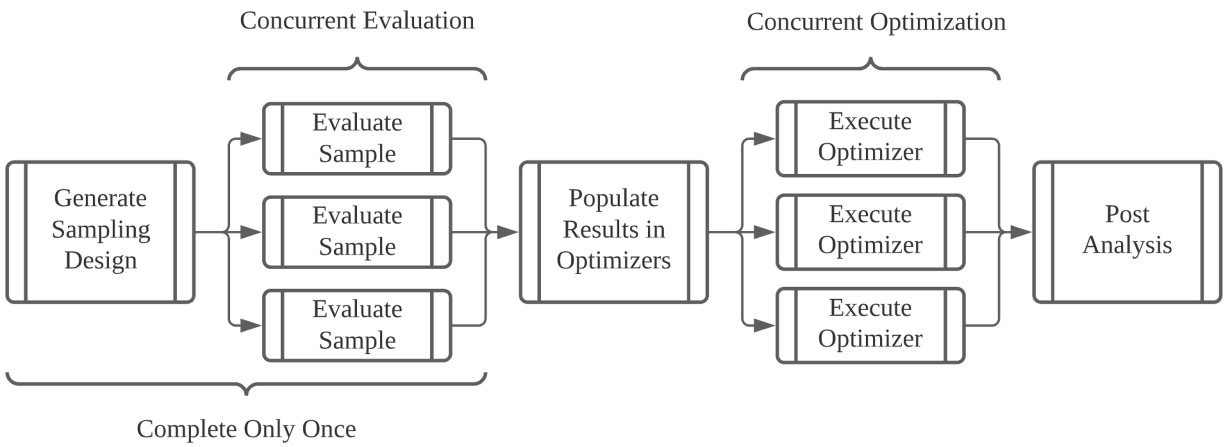

Figure 3.3 Flow diagram showing the sequence of activities in the design optimization

3.4.1 Execution Framework

We develop generic `problem` and `driver` classes to interface between the black-box optimization algorithms and the plant evaluation procedure. The `problem` class wraps the plant evaluation procedure, allowing the collection of information such as the evaluation time and checking if a design exists in the `driver` cache of previous evaluations. The `driver` class holds a first-in-first-out queue of designs to be evaluated and a cache of results. The proposed framework has been implemented in the NREL Hybrid Optimization and Performance Platform (HOPP) Python module [58].

3.4.2 Optimization Approach

Black-box optimization does not guarantee optimality. In order to gain information on general trends (e.g., the region of the parameter space where we expect to find dominating and perhaps optimal designs), we sample the design space prior to optimizing.

3.4.2.1 Sampling Designs

We seek sampling designs with thorough coverage of the parameter space, but limit the number of samples according to the computational resource available. The `idaes` package provides algorithms for sampling designs, though this is not the main purpose of the package [95]. Among these, we select *centroidal Voronoi tessellation* over *Latin hypercube sampling*. Because the objectives we consider are aggregates of annual performance, they vary smoothly over the parameter space; we therefore prefer the roughly equal spacing produced by the former sampling procedure to the more randomly-spaced designs produced by the latter.

3.4.2.2 Black-Box Optimizers

We identify the several Python packages that implement model-based, black-box optimization algorithms in an ask-tell style interface [87]. This interface allows the user to independently “ask” the algorithm to generate the next set of parameters to be evaluated and then “tell” the algorithm the result. Decoupling these actions allows the user to react to these events, which normally occur in a closed loop within the optimization algorithm. We use these features to populate the plant designs and results calculated during sampling. We compare the performance of candidate solvers using fast-running test problems with a similar number of degrees of freedom as the plant evaluation. Among the algorithms tested, we select the `bayesian-optimization` package for its performance under a limited evaluation count [96].

3.4.3 Dispatch Rolling Horizon

A key feature of the plant evaluation function is the control of plant simulation operations according to the dispatch optimization model, ($\mathcal{H}$). We solve the dispatch model on a rolling horizon, where each instance has knowledge of the weather and market condition in the 48-hour horizon it considers. The plant simulation follows the first 24 hours of this solution and is allowed to deviate from the solution by derating operations or shutting systems down, if it encounters infeasibility. The dispatch horizon is then rolled forward 24 hours, with new initial conditions provided by the plant simulation, and this process is repeated for one year. Figure 3.4 depicts the problem horizon and the fixed portion of plant operations for multiple problem instances in the rolling horizon.

Wagner et al. [24] use this approach to demonstrate the value of optimal dispatch in a CSP-with-TES plant. Hamilton et al. [25] follow the same approach when simulating hybrid plants, and show it is computationally efficient relative to solving as a monolith a model containing an annual dispatch horizon. By default, HOPP uses a rolling horizon approach to control the plant simulation according to the dispatch optimization model [94].

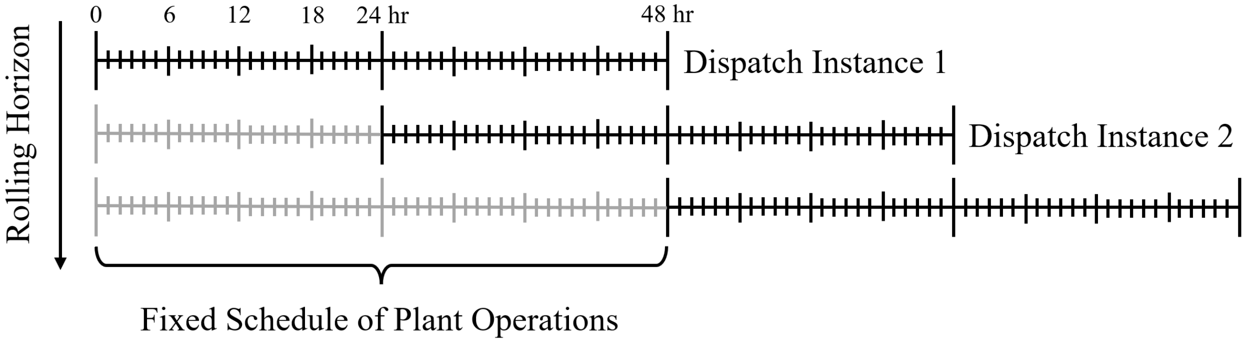

Figure 3.4 Graphical depiction of the rolling planning horizon used in the plant evaluation function.

3.5 Model Instances and Results

We implement the HOPP optimization framework and plant evaluation procedure in Python version 3.8.10 [97], with the dispatch optimization model expressed in Pyomo [98] and solved using Gurobi version 9.5 [51]. We utilize the Gurobi persistent interface to reduce communication time between the modeling language and solver. Hardware architecture consists of a Dell Power Edge R610 server with two Intel Xeon x5670s at 2.93 GHz and 192GB RAM, running Ubuntu version 18.04.5.

3.5.1 Case Study Parameters

We consider three plant configurations, including single-technology (i) CSP with TES, and (ii) PV with battery designs, as well as (iii) a hybrid design consisting of a CSP-with-TES system and a co-located PV field. We do not consider a hybrid configuration with both battery and TES because the cost per unit capacity is significantly lower for TES than for the battery (see Appendix D), and we do not allow uses for the battery other than bulk storage. All evaluations utilize the same weather and electricity market conditions. This study is not intended to be comprehensive, but rather to demonstrate that the HOPP package can show the value of optimal plant sizing. Further, we wish to show the relative performance of single and hybrid designs with storage according to a benefit-to-cost ratio.

3.5.1.1 Plant Configuration Parameters

We fix the sum of all dispatchable generation and the grid connection to be 100 MW, allowing comparisons between plants regardless of configuration. We consider generation from the battery or CSP power cycle systems to be dispatchable, because they can be scheduled according to time-of-delivery prices, and fix the net output of these systems to 100 MW. Power provided by the PV field is not dispatchable, because it cannot be scheduled, and so is not limited except by the grid connection. By limiting the power output of the battery to 100 MW, we do not consider designs having a battery power rating greater than that of the grid connection. Because battery systems charge and discharge at roughly the same power, we are precluding designs which are able to charge faster than they discharge to the grid, which might be advantageous in some markets. However, due to the relative cost of utility-scale battery systems and grid interconnects, it is currently not common for a battery system's power output to be significantly greater than the grid limit, and we consider this to be a reasonable assumption for our study. The grid connection limit also forces the CSP cycle, PV field, and battery to dispatch in periods orthogonal to each other, requiring use of the storage system to avoid curtailment.

Table 3.5 Case study system sizing variables and simple bounds for each plant configuration considered

Design Variable	Units	Lower Bound	Upper Bound
Concentrating Solar Power (CSP) with Thermal Energy Storage (TES)			
Hours of TES	h	4	16
Solar Multiple	-	0.8	3.0
Photovoltaics (PV) with Battery Storage			
Battery Storage	MWh	100	600
Field DC Capacity	MW_e	100	300
Hybrid CSP with TES and PV without Battery Storage			
Field DC Capacity	MW_e	50	300
Hours of TES	h	4	16
Solar Multiple	-	0.8	3.0

Table 3.5 lists design sizing variables and their simple bounds for each of the plant configurations considered. We restrict design variables to the relative size of each technology in the plant (i.e., high-level system sizing), and do not consider variations in connections between plant systems nor variations in individual technology implementations. The PV field utilizes one-axis tracking panels rather than a fixed-tilt system, which Zurita et al. [55] show to be cost efficient, and fixes the DC-to-AC ratio of the inverter to 1.3 (the default value in SAM). The battery chemistry is Lithium Iron Phosphate, with a nominal system voltage of 500V. The CSP system is a central receiver (power tower) design with two-tank molten salt storage and a steam Rankine power cycle. We assume the molten salt to be the commonly-used 60%-to-40% by-weight mixture of sodium nitrate and potassium nitrate, respectively. We apply the standard construction and financing costs in SAM, which includes the 26% federal installation tax credit available at the time of writing in the US. Additional technology parameters and cost assumptions are listed in Appendix A.

3.5.1.2 Dispatch Cost Assumptions

The solution of the dispatch optimization model, ($\mathcal{H}$), is influenced by the relative values of electricity prices and the cost parameters in the objective (3.7). Table 3.6 lists the cost parameters used by the dispatch optimization model, which are the default values in HOPP.

Table 3.6 Dispatch optimization model cost coefficients (HOPP default values). †The parameter value is scaled with respect to the system size.

Operating Costs and Penalties	Symbol	Units	Value
Concentrating Solar Power (CSP) with Thermal Energy Storage (TES)			
CSP field and receiver generation cost	C^{rec}	$\$/\mathrm{MWh_t}$	0.5
Receiver cold start-up fixed cost	C^{rsu}	$\$/\mathrm{MW_t}\cdot\mathrm{start}$	$1.5^\dagger$
Power cycle generation cost	C^{pc}	$\$/\mathrm{MWh_e}$	2.0
Power cycle cold start-up fixed cost	C^{csu}	$\$/\mathrm{MW_e}\cdot\mathrm{start}$	$40.0^\dagger$
Change in power cycle thermal input penalty	$C^{\delta x}$	$\$/\mathrm{MW_t}$	0.5
Photovoltaics (PV) with Battery Storage			
Photovoltaic field generation cost	C^{pv}	$\$/\mathrm{MWh_e}$	1.7
Battery charge, discharge operation cost	C^{bc}, C^{bd}	$\$/\mathrm{MWh_e}$	0.9
Battery lifecycle cost	C^{bl}	$\$/\mathrm{MWh^{dc}}\cdot\mathrm{cycle}$	$26.5^\dagger$

3.5.1.3 Plant Location and Electricity Market

Plant location affects performance through the available solar resource, ambient weather conditions, and site latitude. We consider real-world conditions in Rice California (Rice) that occurred in 2020. This location has both high solar resource and quality data available through the National Solar Radiation Data Base [99]. Solar resource and electricity prices are at times correlated; e.g., periods with very high solar resource may also have high ambient temperature increasing the electricity demand for cooling and energy prices, though this correlation may be reversed in markets with very high PV penetration. To consider these effects, we use electricity prices from the day-ahead energy market in Rice from 2020, which are made available to the public by the California Independent System Operator.

The left panel of Figure 3.5 compares the hourly average direct normal irradiance with the electricity prices; the right panel shows a sorted histogram of the same resource (though the solar resource and prices are not necessarily from the same period in the histogram). Figure 3.6 uses heat maps to compare the direct normal irradiance and the electricity price. The very high prices in August may have been caused by a series of wildfires that occurred across a large area of California in that month [100]. The level of PV penetration in the California market is significant, evident in the pronounced "duck curve" in the left panel of Figure 3.5 and band of lower prices during the solar day in the top panel of Figure 3.6. The depression of prices during the solar day and higher prices in the evening provide an incentive for the plant to utilize the storage system. For additional information on the "duck curve" phenomenon in the CAISO market, see Denholm et al. [1].

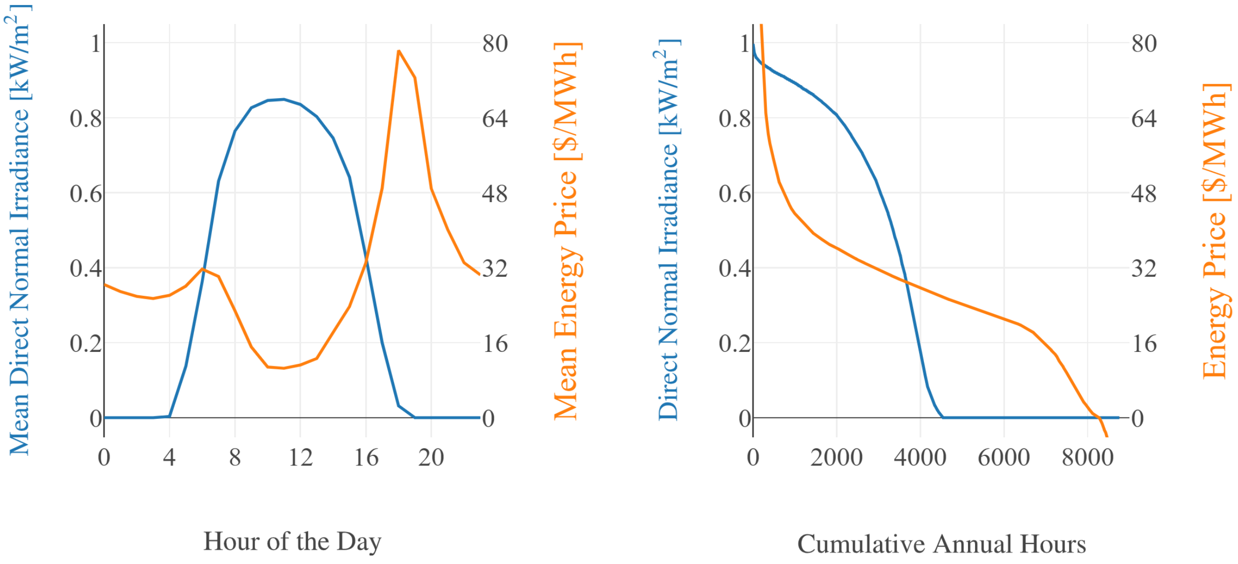

Figure 3.5 Comparison of direct normal irradiance and electricity prices for Rice, CA in 2020. The left panel compares the hourly average prices over a year-long horizon, while the right panel shows a sorted histogram of the same data (where the sorted solar and price data do not necessarily coincide temporally).

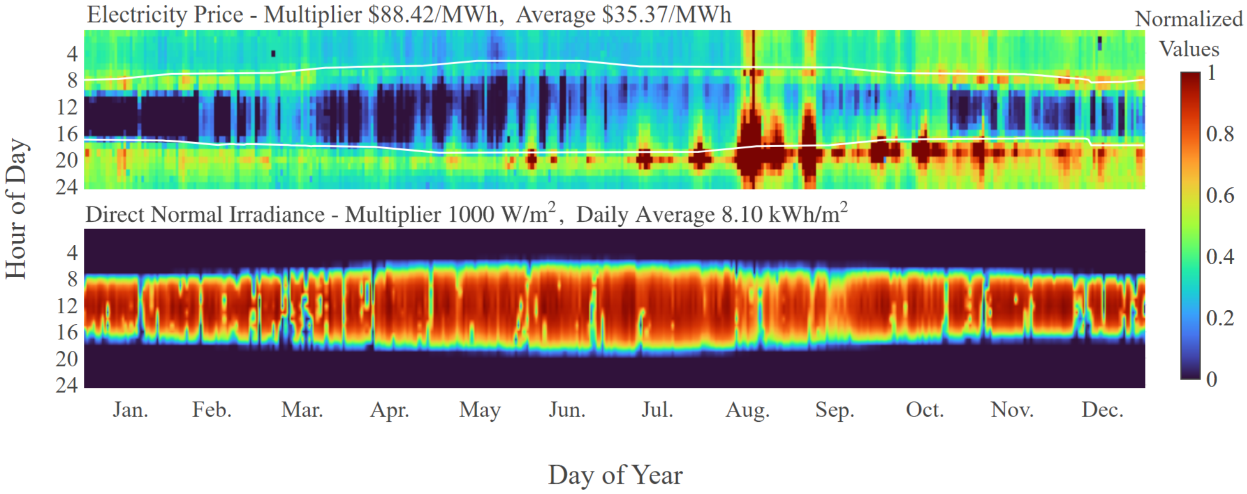

Figure 3.6 Heat maps of normalized electricity prices and direct normal irradiance for Rice, CA in 2020. The original data is divided by the multiplier shown in the figure in order to provide sufficient contrast in the heat map.

3.5.2 Design Timing Results

We investigate the value of concurrent execution by measuring the completion time of the plant evaluation procedure while varying the number of concurrently-running instances. Figure 3.7 shows the mean evaluation time for the three plant configurations considered. We fit a quadratic function of the number of concurrent evaluations to the average completion time and use this fit to estimate the work rate in equation (3.8), where N is the number of concurrent instances and t_N is the average completion time. This ratio is the multiplicative speed-up resulting from N concurrently-running instances. Figure 3.7 shows approximately linear improvement up to 8 concurrent evaluations and continues to improve, with diminishing returns, when running additional concurrent instances.

$$\text{Work rate } (N) = \frac{N \cdot t_N}{t_1} \tag{3.8}$$

The results in Figure 3.7 demonstrate the value of concurrent execution in this setting, where we need to evaluate many computationally expensive tasks which have sequential sub-tasks, each of which are primarily single-threaded. The results in this paper were calculated using 14 concurrent instances of the plant evaluation function, and were completed in approximately one twelfth the total time had they been executed in serial.

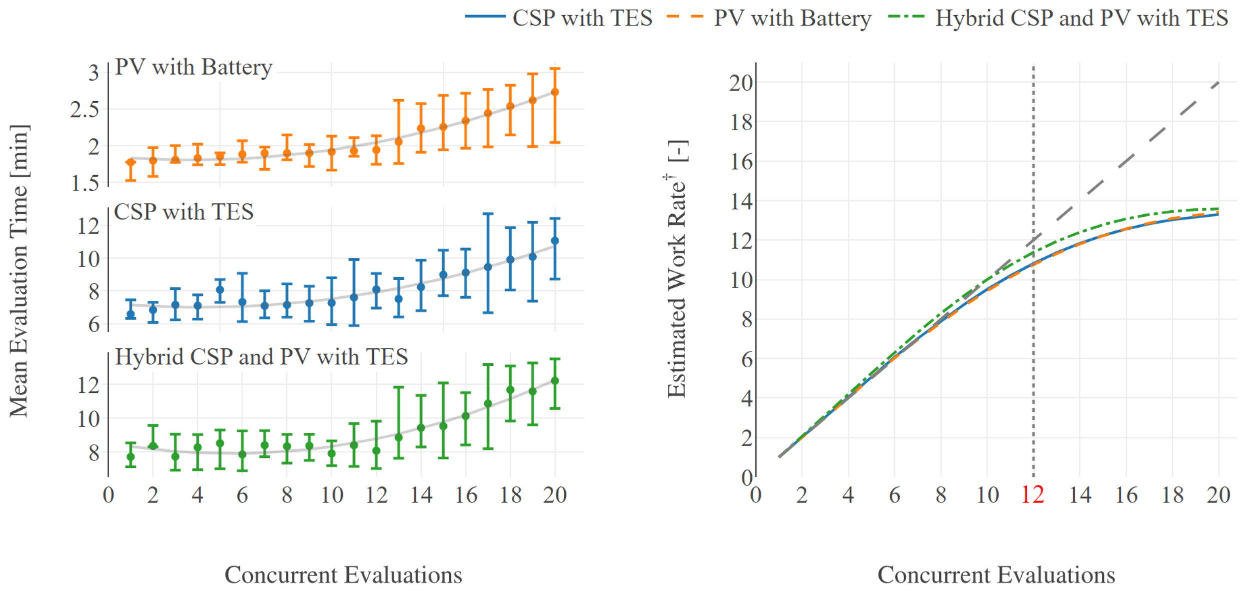

Figure 3.7 Timing study results showing mean evaluation time for the three plant configurations considered, with respect to the number of concurrently-running instances. The computer hardware used has 12 cores and 24 threads. †Work rate is the multiplicative speed-up resulting from concurrent evaluation.

3.5.3 Design Solutions

To demonstrate the value of optimal plant sizing, we fabricate “baseline” single-technology-with-storage designs, shown in Table 3.7, meant to represent plant designs typical at the time of writing. Figure 3.8 plots the baseline CSP-with-TES design with 500 samples of the same configuration, and the design with the greatest benefit-to-cost ratio. We omit designs evaluated by the optimizer in Figure 3.8, which are clustered around the best plant design, to show the coverage of sampling. The Bayesian optimizer is given the results of the 500-design sample, and determines the best plant design by evaluating an additional 30. Results show that plants having a solar multiple between 2.5 and 3.0 and 12 to 16 hours of thermal energy storage achieve the highest benefit-to-cost ratio. We also note that all designs have benefit-to-cost ratios less than 1, indicating they do not provide a positive return on investment. This is a consequence of our cost and revenue assumptions, where we only consider the federal investment tax credit and time-of-delivery price, which are consistent with publicly-available data and may be significantly different than a power purchase agreement that, at the time of writing, are common to utility-scale renewable energy plants and may include electricity prices higher than the open market. The details of these agreements are typically not made available to public. The best-found CSP with TES design increases both the solar multiple and hours of storage from the baseline design and yields a 6.56% improvement in benefit-to-cost ratio.

Table 3.7 Baseline plant designs, used for comparison.

Design Variable	Units	Baseline Value
Baseline CSP with TES Plant		
Hours of TES	h	10
Solar Multiple	-	2.3
Photovoltaics (PV) with Battery Storage		
Battery Storage	MWh	400
DC-to-AC ratio	-	1.2
PV Field DC Capacity	MW_e	300

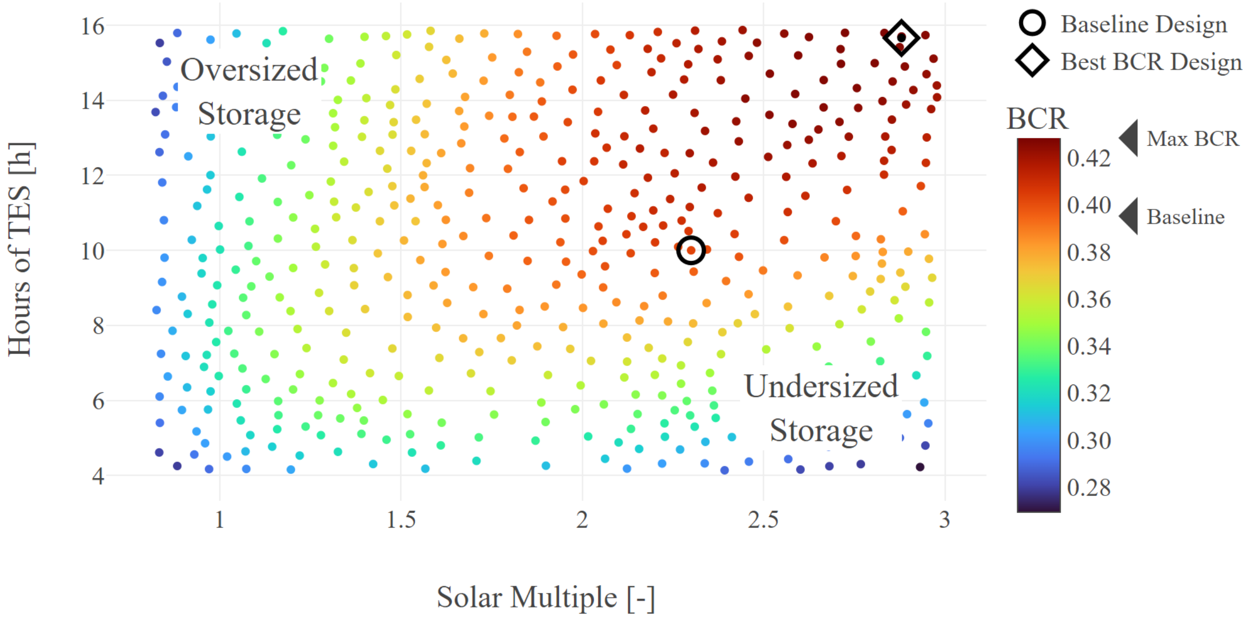

Figure 3.8 Benefit-to-cost ratio (BCR) results of sampling 500 CSP-with-TES designs with the baseline and best design found. Designs evaluated during optimization are generally clustered near the best, but are omitted here to emphasize the coverage of sampling.

Figure 3.9 plots the baseline PV-with-battery design with 500 samples of the same configuration, and the design with the greatest benefit-to-cost ratio. Results show that plants having a PV field DC capacity between 150 and 250 MW with 200 to 400 MWh of battery storage achieve the highest benefit-to-cost ratio. The DC-to-AC ratio of the plant inverter has a minor effect on plant performance, but presently the cost model used by HOPP does not account for changes in inverter cost when changing the DC-to-AC ratio, supporting our decision to fix this aspect of the plant design. Similar to the CSP-with-TES results, no designs are able to achieve a benefit-to-cost ratio greater than 1. The best-found PV-with-battery design decreases both the PV field and battery storage capacity from the baseline and yields a 19.41% improvement in benefit-to-cost ratio (at the cost of reducing annual energy production by 25.22%).

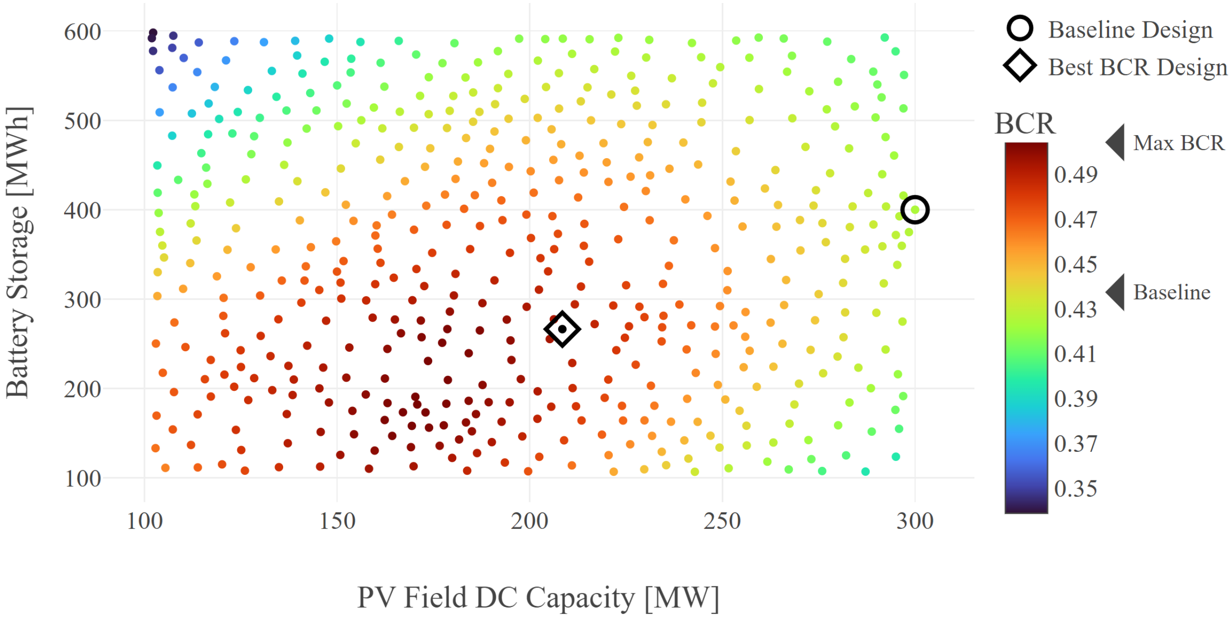

Figure 3.9 Benefit-to-cost ratio (BCR) results of sampling 500 PV-with-battery designs with the baseline and best design found. Designs evaluated during optimization are generally clustered near the best, but are omitted here to emphasize the coverage of sampling.

Table 3.8 compares the baseline single-technology-with-storage designs to the best-found designs and shows the estimated improvement in lifetime benefit-to-cost ratio. Results are dependent on the cost and revenue assumptions used, and would also change if we consider other limitations, e.g., a total plant area restriction, other site limitations, or a total budget constraint. That is, adding design constraints or changing the electricity pricing structure would affect optimal plant sizing. Under our assumptions, we have shown that an increase in lifetime benefit-to-cost ratio of 6 to 19 percent is possible through optimal system sizing. The improvement (Table 3.8) is a result of changes in the installed cost and the schedule of operations, as directed by the dispatch model.

3.5.4 Dispatch Timing Results

The evaluation of each plant design requires solving 365 instances of the dispatch optimization model, each of which converges quickly to a small optimality gap. The systems included in each plant configuration determines the size of the dispatch instances. Table 3.9 shows the number of rows and columns for each of the dispatch problem instances, as well as solver performance averaged over those instances.

Table 3.8 Baseline and best single-technology with storage designs and performance metrics. Green and red percent change values indicate performance improvement and deprovement from the baseline, respectively (where the sign on the change can indicate either an improvement or a deprovement depending on the performance metric).

Design Variable	Units	Baseline	Best-Found	Change
CSP with TES Designs				
Hours of TES	h	10.00	15.15	
Solar Multiple	-	2.30	2.65	
Benefit-to-cost Ratio	-	0.40	0.42	6.52%
Real Levelized Cost of Energy	¢/kWh	8.17	7.54	-7.67%
Annual Energy Production	GWh	470.00	565.58	20.34%
Installed Cost	$M	583.97	669.41	14.63%
Photovoltaics (PV) with Battery Storage				
Battery Storage	MWh	400.00	182.17	
PV Field DC Capacity	$\mathrm{MW_e}$	300.00	170.82	
Benefit-to-cost Ratio	-	0.42	0.50	19.41%
Real Levelized Cost of Energy	¢/kWh	6.45	4.89	-24.17%
Annual Energy Production	GWh	480.62	359.41	-25.22%
Installed Cost	$M	434.84	247.72	-43.03%

Table 3.9 Dispatch model, $(\mathcal{H})$, 48-hour horizon problem instance sizes, prior to presolve, and average solve performance for each plant configuration. †Time reported by the solver to reach an optimality gap of 0.01% or less.

Configuration	PV with battery	CSP with TES	PV and CSP with TES
48-hour dispatch instance sizes, prior to presolve			
Rows	961	2064	2112
Columns	913	1632	1728
Binaries	144	528	528
Average solver performance over 365 48-hour horizon instances			
†Solve Time [sec]	0.01	0.17	0.23
Nodes Explored [-]	1.0	10.7	12.42
Solved at Root Node [%]	100.0	79.7	82.2

3.5.5 Dispatch Solutions

The dispatch solution is revenue-maximizing, and is dependent on the electricity prices and the solar resource available during the problem horizon. Figure 3.10 shows four days of the operations schedule followed by the SAM simulation, as prescribed by the dispatch solution, for the best-found PV-with-battery plant design shown in Table 3.8. We note expected behavior from the dispatch model, which charges the battery using excess PV generation during low-priced periods and dispatches the stored energy during the highest-priced periods.

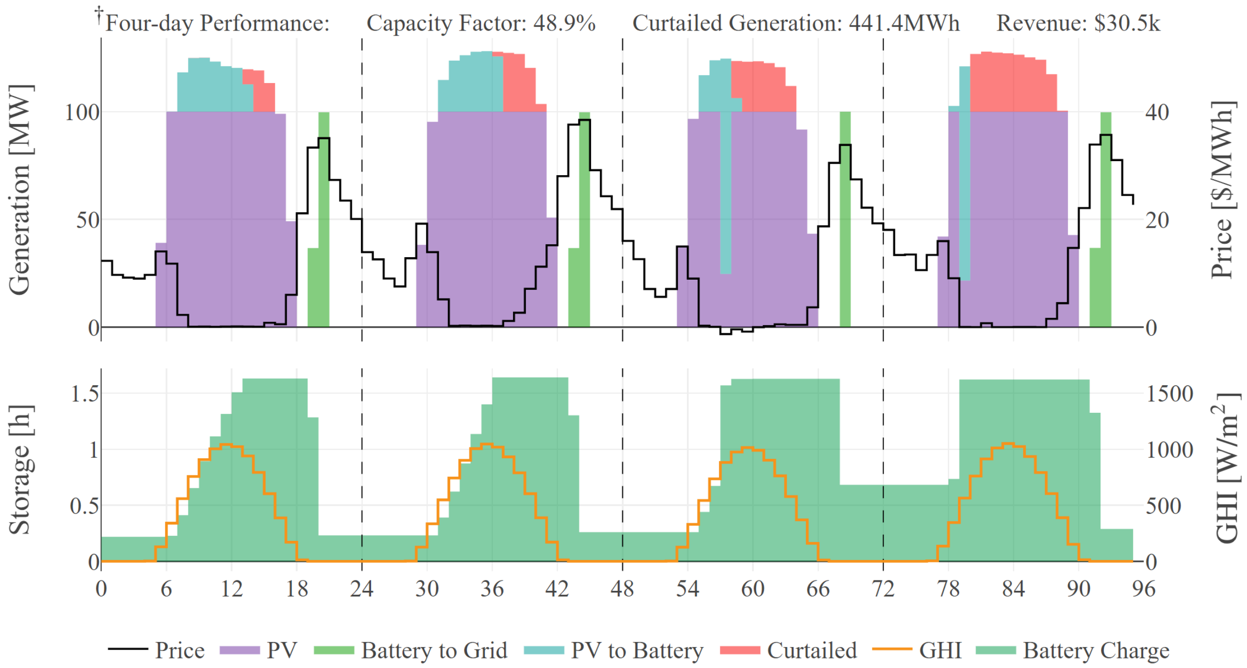

Figure 3.10 Example operations schedule for the PV-with-battery plant, maximizing benefit-to-cost ratio (see Table 3.8 for the plant design). The global horizontal irradiance (GHI) shows the solar resource available for PV generation. Shaded regions and line traces are plotted against the primary (left) axes and the secondary (right) axes, respectively. †Simulated performance is reported over a four-day period in May of 2020.

Figure 3.11 shows dispatch objective values, the corresponding average electricity price, and total direct normal irradiance available during each of the 365 48-hour horizon problem instances, from the baseline CSP with TES design shown in Table 3.8. The results demonstrate the dependence of the objective value on the electricity price and available solar resource. The very high prices in August produce correspondingly high objective values, with approximately 16% of the total annual revenue occurring in the month of August. The distribution of prices over the day, and the very high prices in August are distinguishing features of the market chosen for this study, and the specific market and weather conditions influence optimal sizing through plant operations directed by the dispatch solutions.

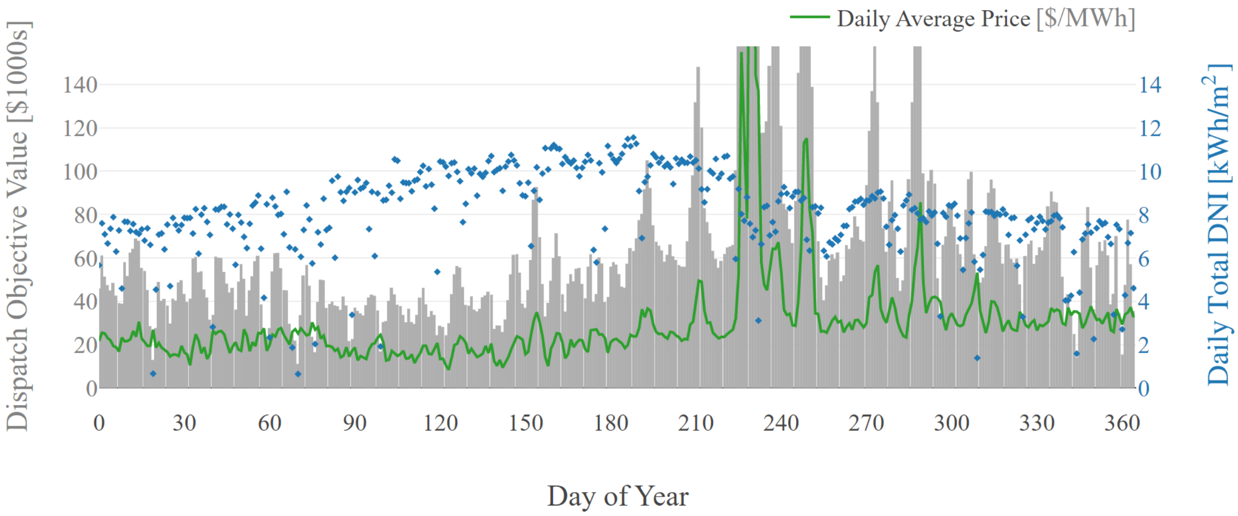

Figure 3.11 Dispatch objective values, the corresponding total direct normal irradiance (DNI) and average electricity price for the 365 48-hour horizon problem instances. The plant design is the baseline single-technology CSP with TES plant shown in Table 3.7.

3.5.6 Comparison of Plant Designs and Corresponding Dispatch

The design objective value is ultimately a result of the plant operational schedule. When maximizing the benefit-to-cost ratio, dominating designs have low installed cost but high revenue from generating power during periods with high time-of-delivery price. Figure 3.12 compares the operational schedules of plant designs maximizing the benefit-to-cost ratio. We consider the best-found (i) PV-with-battery and (ii) CSP-with-TES designs, as well (iii) the hybrid PV and CSP with TES design with the best-found benefit-to-cost ratio. Table 3.10 details these plant designs and shows the relevant performance metrics. The CSP-with-TES designs yield a lower benefit-to-cost ratio than the PV-with-battery design, while the hybrid configuration is somewhat in between, though the PV field capacity is at its lower bound. The advantage of the PV-with-battery design is the installed cost, which is much lower than the designs including a CSP system, but this advantage is mitigated by both the total energy produced and the average price at which energy is dispatched in the CSP-with-TES design's operations. The mean price shown in Figure 3.12 and Table 3.10 is the generation-weighted average price at which energy is sold to the grid. A higher mean dispatch price indicates a design is more responsive to the incentive from the market's time-of-delivery prices.

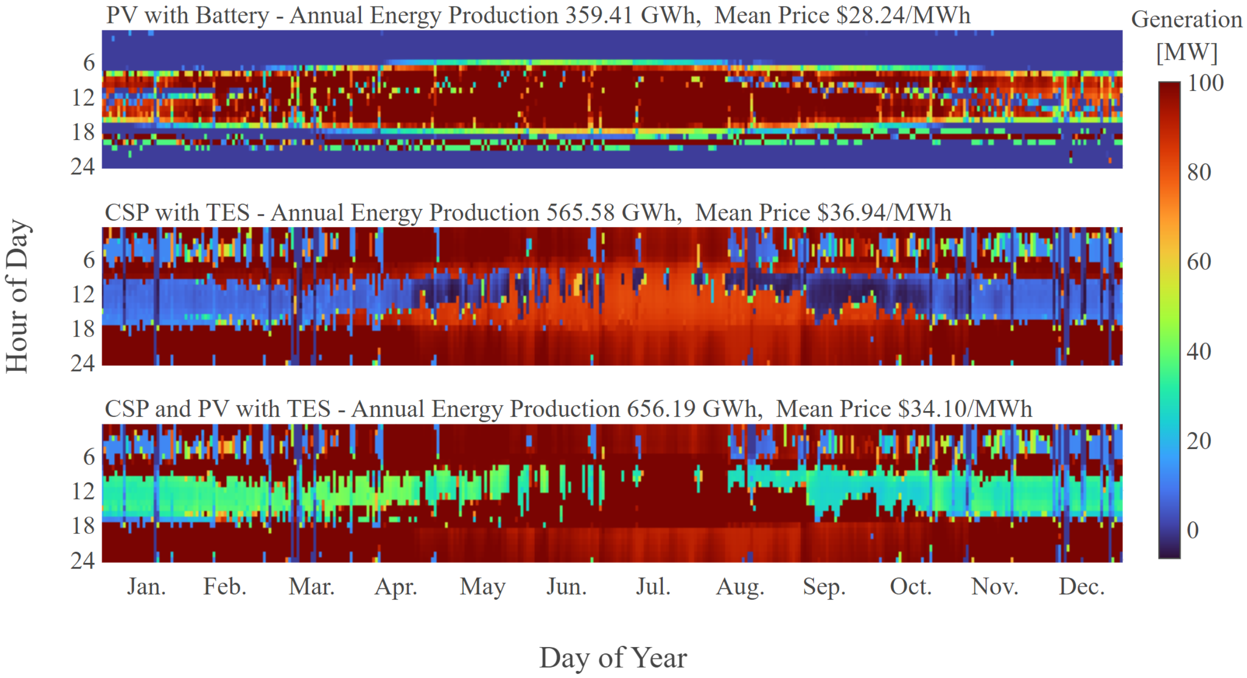

Figure 3.12 Heat map comparison of generation schedules for plants maximizing the benefit-to-cost ratio.

The market chosen for this study favors designs with greater available storage, because the periods with above average time-of-delivery price are outside the hours of solar availability. The single-technology CSP-with-TES design is able to best take advantage of this market, with the middle pane of Figure 3.12 showing consistently high generation in the afternoon and evening hours and less generation during the day when prices are lower. The PV system in the hybrid design actually reduces the average price at which energy is dispatched to the grid, because the PV generation cannot be dispatched according to the market signal. The best-found hybrid design sets the size of the PV field to its lower bound, and so cannot improve the benefit-to-cost ratio much since we force the design to include a PV field of at least 50MW$_{\text{dc}}$ and a CSP power cycle of 100MW$^{\text{e}}$. A different market, such as a constant-price or power purchase agreement, may reverse this result and favor the higher total energy production of the hybrid design.

Table 3.10 Plant designs maximizing the benefit-to-cost-ratio. †Indicates a variable is at its lower bound. Bold values indicate a configuration has the best value of a particular performance metric.

Configuration	PV with battery	CSP with TES	CSP and PV with TES
CSP Cycle Capacity [MW_e]	-	100.00	100.00
Hours of TES [h]	-	15.15	15.12
Solar Multiple [-]	-	2.65	2.65
Field DC Capacity [MW_e]	170.82	-	50.00†
Battery Storage [MWh]	182.17	-	-
Benefit-to-cost Ratio [-]	**0.50**	0.42	0.43
Real Levelized Cost of Energy [¢/kWh]	**4.89**	7.54	6.88
Annual Energy Production [GWh]	359.41	565.58	**656.19**
Installed Cost [$ million]	**247.72**	669.41	721.87
Mean Dispatch Price [$/MWh]	$28.24	**$36.94**	$34.10

3.6 Conclusions

We utilize the NREL HOPP software to simulate operations of hybrid renewable energy plants, controlled according to the dispatch solution of a revenue-maximizing, mixed integer-linear program, as in Hamilton et al. [25] and Hamilton et al. [94]. Our contributions include: a methodology for the evaluation of a hybrid solar plant design operated according to a revenue-maximizing dispatch schedule; development of an execution framework facilitating concurrent execution and central documentation of the plant evaluation procedure; execution of a case study utilizing formal design-of-experiment sampling designs and an open-source, black-box optimization algorithm; and, analysis demonstrating potential improvement in plant performance due to optimal system sizing. Our approach is implemented in the open-source Hybrid Optimization and Performance Platform Python package [58]. We present example dispatch solutions, optimal plant designs and performance under default cost assumptions, and real-world weather and electricity market conditions. This work demonstrates that, under our cost and revenue assumptions, PV-with-battery plants can achieve higher benefit-to-cost ratios in a revenue-maximizing scenario, but that the addition of a CSP-with-TES system yields significantly higher annual energy production. We also show that plant lifetime benefit-to-cost ratio can be improved 6 to 19 percent through optimal sizing, under the imposed weather and market conditions. Future research efforts might examine the sensitivity of optimal plant sizing based on dispatch and technology assumptions, analyze dispatch strategies for different plant configurations and energy markets, and investigate renewable energy incentive programs.

3.7 Acknowledgments

This work was authored in part by the National Renewable Energy Laboratory, operated by Alliance for Sustainable Energy, LLC, for the U.S. Department of Energy (DOE) under Contract No.

DE-AC36-08GO28308. Funding provided by the U.S. Department of Energy's Office of Energy Efficiency and Renewable Energy under the Solar Energy Technologies Office Award Number 34245. The views expressed in the article do not necessarily represent the views of the DOE or the U.S. Government. The U.S. Government retains and the publisher, by accepting the article for publication, acknowledges that the U.S. Government retains a nonexclusive, paid-up, irrevocable, worldwide license to publish or reproduce the published form of this work, or allow others to do so, for U.S. Government purposes. We thank Dr. Jeffrey Larson of Argonne National Laboratory for his comments and insights on earlier drafts of this paper.

CHAPTER 4

SUBMITTED PAPER: PARAMETRIC ANALYSIS ON OPTIMIZED DESIGN OF HYBRID SOLAR POWER PLANTS

Modified from a paper planned for submission to *Applied Energy*.

John L. Cox[12,13], William T. Hamilton[14], Alexandra M. Newman[15]

There is increasing interest in utility-scale solar power plants with storage which can flexibly dispatch renewable energy to the grid. However, plant design possesses many degrees of freedom and non-obvious trade-offs in performance. Software tools can estimate or optimize the performance of a specific plant configuration under market and weather conditions of interest; the associated cost parameters and operating assumptions strongly influence estimates of plant performance and decisions regarding optimal sizing. We employ the National Renewable Energy Laboratory's Hybrid Optimization and Performance Platform, which incorporates optimal dispatch when evaluating plant performance, and investigate the sensitivity of this approach to weather and market conditions, operating limitations, and the presence of a capacity-based incentive. We demonstrate changes in plant performance and optimal sizing with respect to these inputs and discuss implications. Results show that PV-with-battery designs are more profitable under our assumptions, but that designs including a concentrated solar power (CSP) system produce significantly greater annual energy; and that CSP-with-thermal energy storage designs maximizing the benefit-to-cost ratio have an input-dependent linear relationship between the CSP field solar multiple and the hours of storage as the project budget varies.

4.1 Introduction

The interest in utility-scale dispatchable renewable energy has increased dramatically in the past decade, spurred, in part, by the decrease in cost-per-Watt capacity of photovoltaic (PV) panels [2, 3]. The abundance of PV generation in some markets has caused renewable generation to, at times, exceed grid demand, depressing the price of energy during hours of solar availability [1]. An energy storage system can allow this excess generation to be stored and dispatched to the grid at times of greater demand [101]. The hybridization of multiple renewable generation systems, and one or more storage systems, can potentially decrease the cost of dispatchable renewable energy, but complicate plant design decisions. Figure 4.1

---

[12] Graduate student, Colorado School of Mines
[13] Primary researcher and author
[14] Post-Doctoral Researcher, National Renewable Energy Laboratory
[15] Professor, Colorado School of Mines

depicts a notional concentrating solar power (CSP) and PV hybrid plant with both thermal energy and battery storage, and outlines the system sizing variables we consider in this paper. In this context, we define “hybrid” as a plant which co-locates more than one solar generation technology (e.g., a CSP system and co-located PV field); we do not consider a storage system with a single generation technology (e.g., a PV field and battery) to be a “hybrid” design.

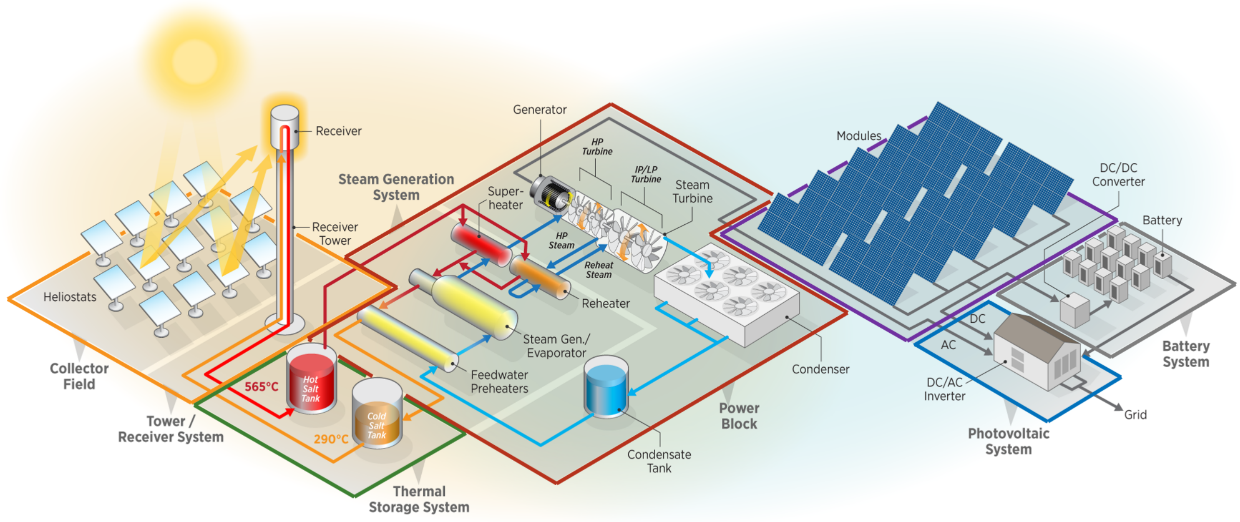

Figure 4.1 Hybrid CSP-PV with storage plant configuration (Graphic © NREL). A depiction of a molten salt power tower CSP plant with thermal energy storage and a steam Rankine power cycle, co-located with a PV field and battery storage. Colored by the system sizing design variables: **CSP solar multiple**, **TES hours**, **CSP cycle capacity**, **PV field DC capacity**, **battery hours of storage**, and **battery power capacity**.

A concentrating solar power plant consists of a field of large articulating mirrors, called heliostats, which focus the sun’s light onto a receiver. A heat transfer fluid is pumped through tubes in the receiver to collect thermal energy, which can then be stored in a tank or used immediately to generate high-pressure and high-temperature steam to operate a Rankine power cycle to yield electricity. Four primary CSP technologies exist: parabolic trough, linear Fresnel, dish Stirling, and power tower [6]. We focus on the power tower, or central receiver, configuration of CSP which can be sized for utility-scale generation and yields a high solar concentration ratio, and allows it to be paired with high-efficiency power cycles and with thermal energy storage (TES), in which the TES medium, most commonly a molten salt [7], is stored in one or more tanks to be used for electricity production at a later time. Photovoltaic panels generate electricity directly, by way of the photovoltaic effect, and can utilize both the direct and diffuse solar irradiance. PV generation can be stored using an electro-chemical battery system, which is comparatively more expensive per unit capacity than a TES, though use of a TES requires the construction of a Rankine power cycle. TES has a further advantage in that it can be charged by pumping the high-temperature fluid into the tank at a much higher rate than that at which the fluid is later discharged, whereas a battery system's maximum rate of charge and typical rate of discharge are the same.

Planners, seeking to optimize the design of a renewable energy plant with storage, face multiple challenges as there are many degrees of freedom in the sizing of plant systems, and cost-performance trade-offs may not be clear between design alternatives. When a design incorporates storage, plant economic performance is ultimately a consequence of dispatch decisions and the installation and operating costs over the plant's lifetime. The National Renewable Energy Laboratory (NREL) Hybrid Optimization and Performance Platform (HOPP) is an open-source Python package intended to support plant design decisions [94, 102]. Software output depends on the imposed weather and market conditions, assumed operating limitations, and numerous installation cost parameters specified by the user. To investigate the sensitivity of plant performance and optimal sizing in HOPP, we execute a sensitivity analysis with respect to the imposed weather and market conditions, plant operating limitations, and the presence of a capacity-based renewable energy incentive. We compare individual plant performance and optimal plant sizing under these scenarios, contrast the schedule of plant operations, and discuss implications of these results for developers of a solar power plant with storage. This study is not meant to be comprehensive, but rather to demonstrate the dependence of plant performance and optimal sizing results on some of the input parameters and assumptions used.

The remainder of the chapter is organized as follows: Section 4.2 provides a literature review of renewable energy technologies and studies of the design and dispatch optimization of hybrid CSP systems. Section 4.3 summarizes the approach to evaluating plant performance in HOPP and describes our methodology for investigating the sensitivity of plant evaluation with respect to the parameters of interest. Section 4.4 details the inputs, assumptions, and design objectives used. Section 4.5 presents results of a study showing the effect of weather and market conditions, operating limitations, and renewable energy incentives on plant performance and optimal sizing. Section 4.6 concludes with a summary and possible extensions of our work.

4.2 Literature Review

The dispatchable nature of CSP, when combined with TES, is enticing to markets seeking expanded renewable capacity in periods outside of the hours of solar availability, though investment in CSP plants has been limited to date. A CSP plant's large upfront cost and complex design relative to those associated with a PV installation, remain drawbacks [57]. Utility-scale battery systems are improving in their technical maturity and cost per unit capacity [57], but thermal energy storage has significantly lower cost per unit capacity. The need for utility-scale dispatchable renewable energy will only increase as PV and wind generation become more common, and making these technologies economically competitive is the goal of several lines of research. For a general history of CSP plant construction and development, see Baharoon et al. [66]; for an international view on CSP, see Islam et al. [68]; and, for a review of the development of CSP technology and its value in electrical systems, see Gauché et al. [103].

We present a flexible approach for the design optimization of solar power plants and their hybrids with storage, which is an active field of research, though typically studies are site-specific or consider a fixed strategy for plant operations. Zurita et al. [55] analyze the economic performance of a hybrid CSP and PV-with-battery storage plant according to component sizing, following a fixed operation strategy in Chile. Starke et al. [76] consider plants operating in the Atacama desert, and optimize the design of a hybrid CSP and PV plant for a site in Northern Chile [53]. Beegun et al. [74] optimize the design of a hybrid CSP system to maximize energy efficiency, with a use case of a textile manufacturing plant in Mauritius; the authors use System Advisor Model to evaluate plant performance, and consider the size of the solar field and the solar multiple as the design variables. Yang et al. [29] utilize a mixed-integer linear program to optimally schedule a CSP-wind hybrid plant with thermal energy storage, and extend this approach to optimize the design of Brayton-cycle hybrid CSP and PV plants in several locations, following pre-determined load profiles [79]. Richter et al. [104] investigate optimal sizing of a CSP-PV hybrid plant and its dependence on the plant's operating strategy. Mata-Torres et al. [105] simulate and optimally size a hybrid CSP and PV plant with a multi-effect distillation plant and show the dependence of sizing on several design factors. Guo et al. [106] consider a hybrid PV and wind configuration with either TES or a battery system and optimize system sizing to minimize the levelized cost of energy. Bravo and Friedrich [77] optimize a hybrid CSP and PV plant design, with operations controlled by a linear program. Iaquaniello et al. [107] propose a CSP and diesel generator hybrid system for a remote system, and show that the hybrid system is comparable to a conventional diesel generator while reducing emissions. Goel et al. [108] analyze the performance of PV panels integrated into a CSP parabolic trough receiver and note that annual production of the hybrid system can be 30% greater than the original design. Liu et al. [23] consider a CSP and PV hybrid configuration in which generation from both systems can be stored in a thermal energy system, and optimize sizing and the operational strategy to minimize the levelized cost of energy. Liu et al. [109] optimize the sizing of hybrid PV and CSP plants with either TES or a battery system and an electric heater according to the levelized cost of energy and system reliability. Aguilar-Jiménez et al. [110] analyze the economic performance of a CSP and PV hybrid system for an isolated community and note that the hybrid configuration dominates a single-technology solution as the load demand increases. Petrollese and Cocco [111] optimize the sizing of a hybrid linear Fresnel CSP and PV design with both TES and storage following a fixed operations in two locations.

A key feature of our approach is the use of a dispatch optimization model to guide plant operations. We consider a plant in an independent system operator market, where the primary goal is to maximize revenue, and so utilize a revenue-maximizing dispatch objective function, though in another market a different objective might be more appropriate [94]. Wagner et al. [12] develop a detailed CSP dispatch optimization model, maximizing a plant's revenue during the problem horizon, and considering operations and maintenance costs due to dispatch decisions. This model has been (i) used to quantify the improvement in long-term plant revenue due to optimal dispatch decisions [24], (ii) extended to guide operations of a hybrid CSP-with-TES and PV-with-battery plant [25], (iii) employed to investigate dispatch decision dependence on the model's representation of power cycle efficiency [26], (iv) coupled with a simulation of component failures to analyze operations and maintenance costs resulting from optimal dispatch decisions [27], and (v) deployed in an open-source software tool that obtains optimized system designs while accounting for operations and maintenance costs [28]. Most recently, this model was used to explore the interdependence of system sizing, upfront capital costs, and lifetime operations and maintenance costs in a CSP-with-TES plant [112]. We utilize a version of this model developed in Hamilton et al. [25], and, subsequently, refined to consider hybrid CSP-with-TES and PV-with-battery dispatch [94]. We utilize this dispatch optimization model, as implemented in the Hybrid Optimization and Performance Platform NREL [58].

Dispatch optimization for CSP system is an active area of research, with various approaches and levels of fidelity used. Yang et al. [29] develop a mixed-integer, linear program that yields a profit-maximizing schedule for a CSP plant, and Li et al. [30] utilize this model to simultaneously consider design decisions; however, the power cycle efficiency model used in the dispatch formulation assumes constant thermal efficiency, whereas the model developed by Wagner et al. [12] is decision-dependent. We use an implementation of the dispatch optimization model, which determines a schedule of plant operations at hourly fidelity. Zurita et al. [78] assess the impact of fidelity of the dispatch optimization model to guide plant operations, and show the dependency of aggregate estimates of plant performance. Solar uncertainty is sometimes incorporated in CSP dispatch optimization. Stochastic unit commitment models developed in Zheng et al. [20] are extended by Du et al. [18] to account for TES storage level beyond the planning horizon and Gao et al. [19] to constrain the chance of unmet load and curtailed generation. While these works account for some of the unique properties of CSP-with-TES operations, they limit the detail of the specifics of CSP operations, such as the interactions between the solar collectors, the TES, and the steam generation system. Others have explored different optimization perspectives. A production cost model approach considers an entire-grid perspective and seeks to minimize cost or emissions while meeting grid demand, while a price-taker approach considers decisions for a single plant with the associated operational detail. We adopt a price-taker perspective and assume a plant's generation does not affect market conditions. Martinek et al. [21] consider several optimization perspectives, include price-taker and production cost model, and compare the value and dispatch decisions of a CSP system under these perspectives. Several works in the literature address the nonlinear and complex nature of CSP operations by employing heuristics to guide dispatch decisions, such as System Advisor Model's approach that maximizes electrical generation [113]. de Meyer et al. [22] use a collection of four different heuristic policies each with a goals of maximizing energy production, plant revenue, grid value, or minimizing the defocusing of heliostats to assess the impact of each operation policy on plant performance and scheduling decisions in South Africa. Liu et al. [23] develop a hybrid algorithm using both genetic algorithms and particle-swarm optimization to obtain dispatch decisions for CSP-PV hybrid systems quickly, but at the expense of provable optimality. The operating temperature of the CSP receiver and the resulting efficiency of the Rankine power cycle is a central concern in plant operations, which Cox et al. [114] incorporate in a nonlinear dispatch optimization model, but we find including these effects to be intractable for design optimization. None of these works explores the sensitivity of optimal system sizing with respect to input parameters in a setting that incorporates optimal dispatch.

Cox et al. [102] present a design evaluation and optimization approach used in the HOPP software, results considering a specific plant location and energy market, as well as a more comprehensive review of plant evaluation techniques. In this chapter, we focus on exploring the sensitivity of this approach with respect to a selection of inputs, and present conclusions relevant to renewable energy developers. Our contributions include a study of plant performance and optimal sizing as evaluated by the HOPP software considering: (i) multiple plant configurations, locations, and electricity markets; (ii) varying grid interconnect and total generation capacity; and, (iii) the presence of capacity-based renewable energy incentive payments. We explore changes in plant performance and optimal sizing with respect to these inputs and identify trends relevant to renewable energy developers.

4.3 Methodology

We optimize plant design using the HOPP software framework within the context of six degrees of freedom (see Figure 4.1): (i) CSP field solar multiple, (ii) hours of thermal energy storage, (iii) CSP power cycle capacity, (iv) PV field DC capacity, (v) battery storage capacity, and (vi) battery power capacity. With respect to a given plant design, the System Advisor Model (SAM) simulates plant operations and an explicit optimization model prescribes dispatch decisions (see Figure 4.2).

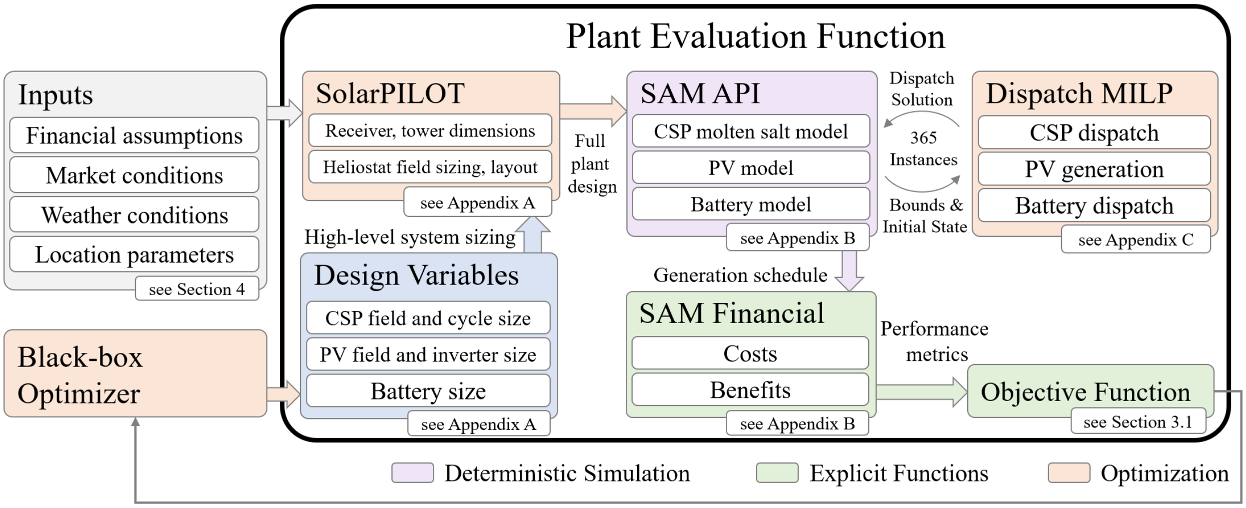

Figure 4.2 Flow diagram of the plant evaluation procedure.

With respect to corresponding dispatch operations, each problem instance considers 48 hours at hourly fidelity; the model has perfect knowledge of the weather and market conditions during the planning horizon, which is consistent with the knowledge available to plant operators, ignoring uncertainty in weather forecasts (see Figure 4.3). The plant simulation attempts to follow the first 24 hours of each dispatch solution, but reduces generation or shuts systems down if an infeasibility is encountered. If the dispatch solution includes curtailment of solar energy collection by the CSP heliostat field, the simulation will operate the power cycle and receiver so as to avoid curtailment, which may result in CSP generation during low-priced periods (see hours 36 through 40 in Figure 4.9). This policy enforces that both CSP heliostat field and PV field maximize the collection of solar energy, and that generation during periods of negative energy price affect both technologies.

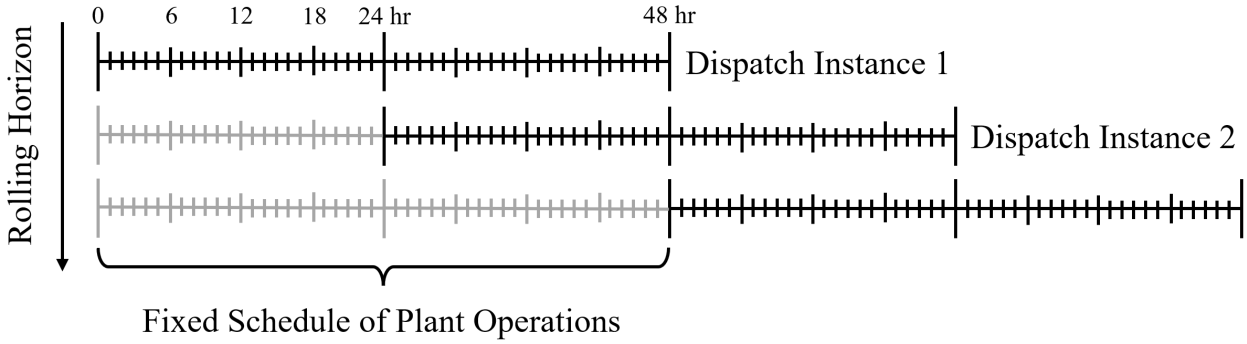

Figure 4.3 Graphical depiction of the rolling planning horizon used in the plant evaluation function.

Guiding the plant simulation according to solutions of the dispatch model has (i) estimated the value of optimal dispatch of a CSP-with-TES plant [12], (ii) evaluated the performance of a hybrid CSP and PV design [25], and (iii) is the default in HOPP [94]. We point the reader to Hamilton et al. [94] and Cox et al. [102] for a more comprehensive discussion. For completeness, we present a mathematical formulation of the design optimization problem and the dispatch optimization model in Appendices F and H, respectively, which are taken from Cox et al. [102].

4.3.1 Design Objectives

The design objective is a scalar metric of performance over the plant's lifetime, calculated from the total energy, revenue, and costs estimated by the plant simulation. We consider the levelized cost of energy and the benefit-to-cost ratio (Mai et al. [92], Hamilton et al. [94] and Cox et al. [102]). Table 4.1 lists notation.

Table 4.1 Notation used in the benefit-to-cost ratio and levelized cost of energy design objective functions.

Sets		
$\mathcal{Y}$	Years in the plant lifetime; i.e., $y \in \{0, \ldots, Y\}$	
Select Parameters		**Units**
δ	Annual discount rate	-
Metrics of plant performance, given by the financial model		**Units**
b_y	Total revenue (benefits) in year y	\$
k_y	Total costs in year y	\$
w_y	Annual energy production	MWh$_\mathsf{e}$

Levelized Cost of Energy

Government-owned utility providers or micro-grid operators may seek the most cost-efficient design, and so use a metric such as the levelized cost of energy. The quotient of the total present value of all costs to the present value of all energy generated yields the lifecycle cost per unit of energy produced by the system, and is known as the levelized cost of energy. The costs include all negative cash flows, as in the benefit-to-cost ratio, and energy production is the total lifetime production of the plant sent to the grid after accounting for all parasitic loads. Both cost and energy are discounted annually to determine their present values. The levelized cost of energy is suitable for identifying the more cost efficient option between plant designs with the same nameplate capacity, as each technology may scale differently with respect to cost and generation capacity.

$$\text{Levelized Cost of Energy} = \frac{\sum_{y\in\mathcal{Y}} \frac{k_y}{(1+\delta)^y}}{\sum_{y\in\mathcal{Y}} \frac{w_y}{(1+\delta)^y}} \tag{4.1}$$

Benefit-to-Cost Ratio

The benefit-to-cost ratio is the ratio of the present value of lifetime plant revenue to costs. Plant revenue includes all positive cash flows from energy sales, tax credits, and capacity incentive payments. Plant costs include installation, financing, and operations and maintenance. Revenue and cost are discounted in out years, where values greater than 1 indicate a design yields a positive return on investment over the lifetime of the plant.

$$\text{Benefit-to-Cost Ratio} = \frac{\sum_{y \in \mathcal{Y}} \frac{b_y}{(1+\delta)^y}}{\sum_{y \in \mathcal{Y}} \frac{k_y}{(1+\delta)^y}} \tag{4.2}$$

Other Metrics of Plant Performance

In addition to these metrics, we report other aspects of plant performance and describe them here for completeness. Annual energy production (AEP) is the total of energy sold to the grid by the plant, accounting for parasitic loads, in its first year of operations. The capacity factor is the ratio of annual energy production to the capacity of the grid interconnect. Installed cost is the total cost of plant installation. The mean energy price is the average price at which a plant sells energy to the grid, where higher values indicate a plant is able to target higher-priced periods which, depending on the market, may occur outside the hours of solar availability.

4.3.2 Design Optimization Approach

The plant evaluation function is nonlinear, implicit, discrete, and computationally expensive. To optimize the design of a plant, we utilize a “black-box” optimization algorithm, which is a tool of choice when convenient mathematical structure is absent. Because these algorithms cannot guarantee global optimality, we sample the solution space thoroughly, after which we “warm start” the optimization algorithm using these results. The sampling and optimization procedures are executed using the `problem` and `driver` classes in HOPP, which facilitate concurrent execution of the plant evaluation. Our approach to design optimization focuses on thorough sampling of the parameter space, and utilizes concurrent execution to reduce the overall computational time.

4.4 Study Inputs and Data

We use Python version 3.8.10 [97] for the HOPP optimization framework and plant evaluation procedure implementation; the dispatch optimization model is written in Pyomo [98] and solved with Gurobi version 9.5 [51] using its persistent interface to increase communication efficiency between the modeling language and solver. We utilize *centroidal Voronoi tessellation* samples for even coverage of the solution space, which the `idaes` Python package implements [95]. The `bayesian-optimization` Python package optimizes the plant designs [96]. Computer hardware consists of a Dell Power Edge R610 server with two Intel Xeon x5670s at 2.93 GHz and 192GB RAM running Ubuntu version 18.04.5.

4.4.1 Case Study Parameters

We execute a study considering two instances of energy markets and three instances of weather data from two locations. For plant revenue, we include the 26% investment tax credit, time-of-delivery pricing, and a capacity-based incentive in some cases. This study is meant to provide select examples of optimal sizing dependence that are relevant to contemporary developers of solar-power-with-storage plant designs.

4.4.2 Energy Markets

Electricity prices affect the dispatch solution through energy purchase and sales price parameters. We select two instances a decade apart of day-ahead market data from the California independent system operator (CAISO) node in Rice, CA where each includes real-world prices at hourly fidelity for one year. The instances chosen have similar average prices ($35/MWh in 2010 and $30/MWh in 2020), but pronounced differences in their hourly average profiles (see Figure 4.4). Prices in 2010 show some variation over the day, between weekdays and weekends, and throughout the year, but are roughly constant when compared to the 2020 prices, see Figure 4.5. The level of PV penetration in the CAISO market increased dramatically over the ten years from 2010 to 2020 [1], which is evident by the pronounced "duck curve" seen in the left panel of Figure 4.4 and band of lower prices during the solar day in Figure 4.5. These differences serve to highlight optimal plant sizing dependence on the price signal, where the Rice 2020 market provides a greater incentive for storage capacity due to the higher-priced periods outside the hours of solar availability. Table 4.2 shows normalized quartiles; we note the close agreement in the median and upper quartiles for the two years, but a vastly higher maximum price in the 2020 data. Figure 4.5 shows the higher-priced periods generally occur between 6 and 11pm in the Rice 2020 market, and a spike in prices in August of 2020, which may have been caused by a series of wildfires that occurred across a large area of California in that month [100].

Table 4.2 Comparison of the distribution of normalized electricity prices for the CAISO node in Rice California in 2010 and 2020

	Average	Minimum	Lower Qtr	Median	Upper Qtr	Maximum
Rice 2010 [$/MWh]	35.37	-10.26	29.04	34.98	41.60	109.37
Rice 2020 [$/MWh]	30.54	-47.36	18.97	26.25	35.33	1,435.43

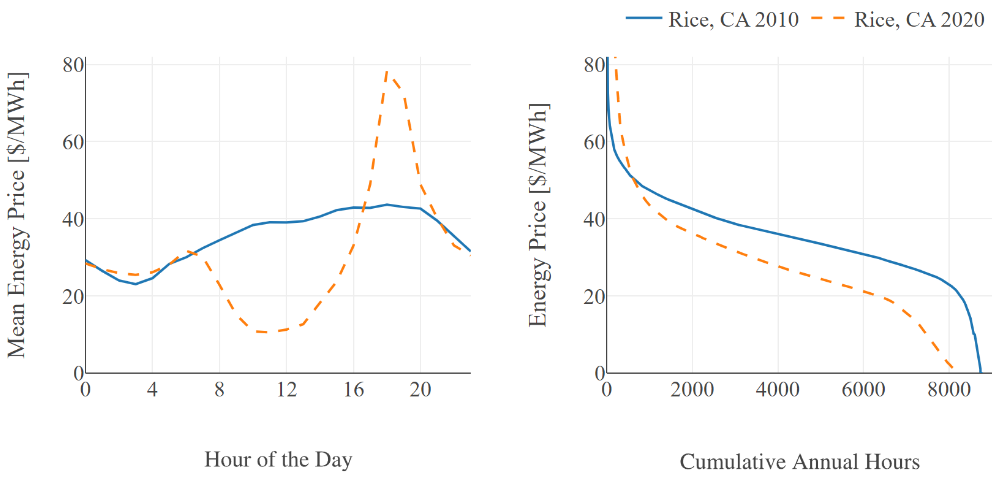

Figure 4.4 Comparison of electricity prices from the CAISO node in Rice, CA for the 2010 and 2020 calendar years. The left panel depicts the hourly average price, while the right panel shows a price-duration curve of the same data.

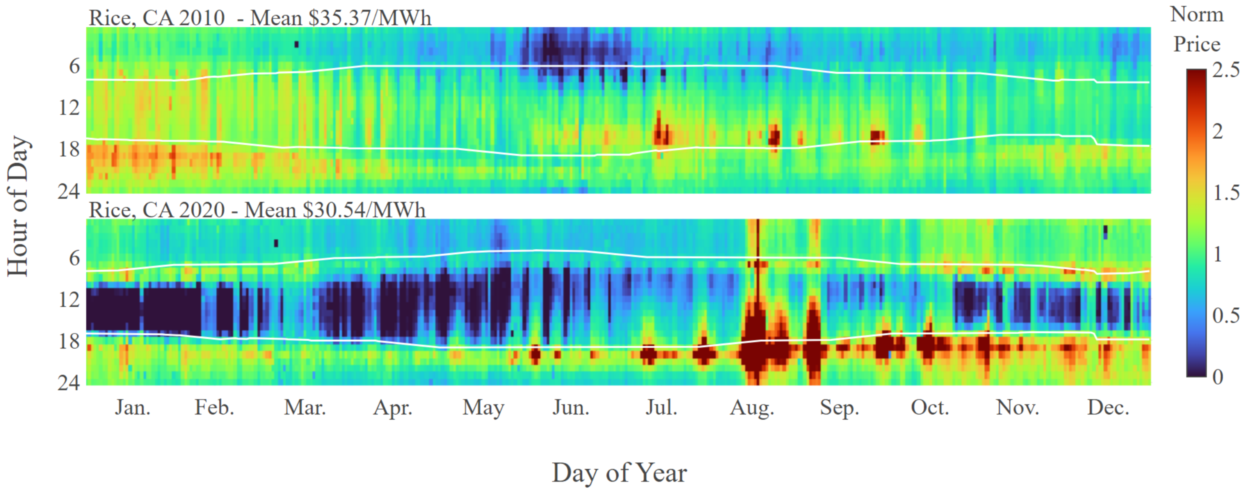

Figure 4.5 Heat map comparison of electricity prices from the CAISO node in Rice, CA for the 2010 and 2020 calendar years. The white lines indicate the approximate local time of sunrise and sunset.

4.4.3 Plant Locations

The plant location affects plant performance through the available solar resource, ambient weather conditions, and site latitude. We include two sites in this study: Rice California (Rice) and Northern Chile (N. Chile). Both locations have high solar resource and data available through the National Solar Radiation Data Base [99]. Solar resource and electricity prices may be positively correlated; however, markets in geographical areas with an abundance of PV may exhibit the opposite relationship. Where possible, we use weather conditions that correspond to the electricity prices in the same period. We include two instances of weather conditions for the Rice location (2010 and 2020), corresponding to the two instances of market data used in that location, and consisting of solar resource and ambient conditions at hourly fidelity for one year. Unfortunately, we do not have access to analogous pricing in the N. Chile location, and so utilize a typical meteorological year (TMY) for the weather conditions and market data from the Rice location in 2010. Because the N. Chile location is in the southern hemisphere, we offset the energy market data by six months from that shown in Figure 4.5 for consistency.

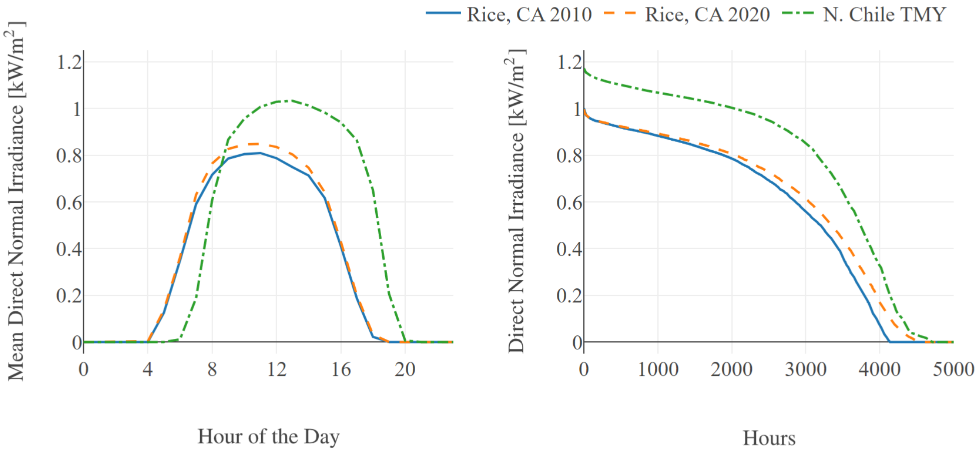

Figure 4.6 Comparison of direct normal irradiance for Rice, CA in 2010 and 2020 and a TMY in N. Chile. The left panel compares the hourly average DNI, while the right panel shows a resource-duration of the same data.

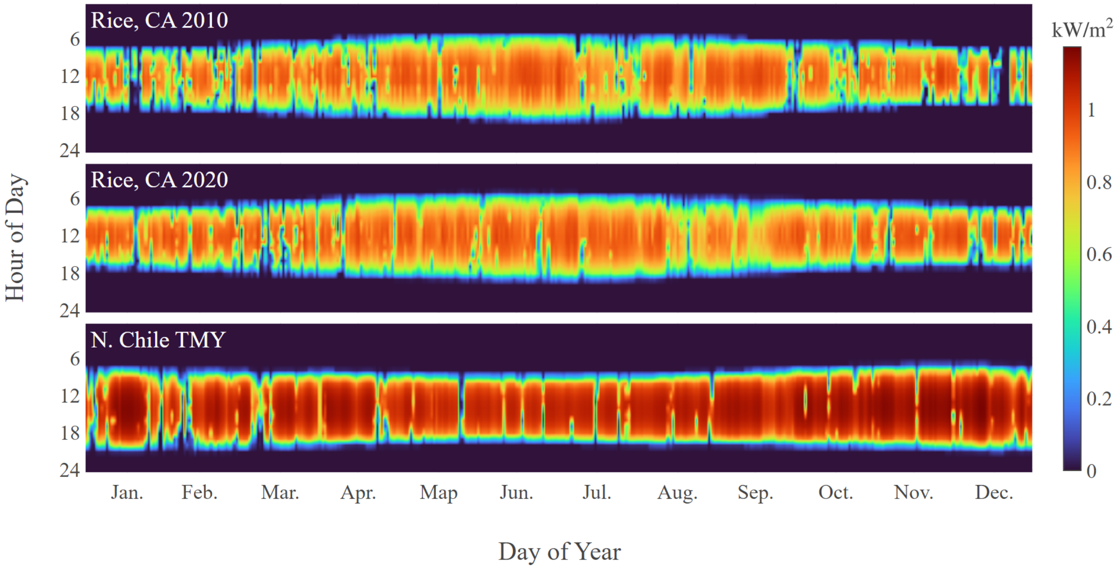

Figure 4.7 Heat map comparison of direct normal irradiance for Rice, CA in 2010 and 2020 and a TMY in N. Chile.

The left panel of Figure 4.6 compares the hourly average direct normal irradiance (DNI) for the three instances of weather data used; the right panel shows a resource-duration curve of the same data. Direct normal irradiance affects generation of both the CSP and PV source, though the PV system can also generate power from diffuse irradiance. The hourly resources of both years in Rice are roughly equal, while the resource in N. Chile is consistently higher due to the reduced atmospheric attenuation at that location. Figure 4.7 compares the three instances of weather data; there is a rough equivalence between the two years of data from Rice, and a higher occurrence of low-irradiance solar days in December of 2010, which were a result of record-setting snow and rainfall [115]. Table 4.3 compares the aggregate solar resource in the three instances of weather data used. We note the significant increase in the direct normal irradiance portion of the solar resource and a more moderate increase in the global horizontal irradiance in N. Chile compared to the conditions in Rice, which favors CSP generation.

Table 4.3 Comparison of total annual solar resource for the three instances of weather conditions used.

	Global Horizontal $\mathrm{kWh/m^2}$	Direct Normal $\mathrm{kWh/m^2}$	Diffuse Horizontal $\mathrm{kWh/m^2}$
Rice 2010	2,159.5	2,798.0	466.3
Rice 2020	2,207.7	2,958.8	448.1
N. Chile TMY	2,730.4	3,782.1	353.4

4.4.4 Incentive Payments

Governments and utilities offer various incentives to encourage investment in renewable energy; an investment tax credit can serve as a reduction in the tax liability of the operating entity, implemented as a percentage of the system installation cost. This credit can be spread over multiple years for cases in which the tax liability is insufficient to receive the benefit of the incentive in a single year. As a result, the SAM financial model treats the investment tax credit as a payment, and does not reduce the benefit according to the estimated tax liability of the project. We include a 26% investment tax credit for all designs in this paper, which is applicable in the U.S. at the time of this writing.

Another approach, meant to target an increase in dispatchable capacity, is the provision of capacity payments, i.e., annual payments to the plant for energy produced during a subset of periods, as defined by the utility. The rules of a capacity payment vary widely, as do methods of estimating them for a specific plant design [81, 116, 117]. We consider a definition of the capacity payment, as in Jorgenson et al. [82] and Hamilton et al. [94], which is a payment each year for energy produced in the periods of peak net load. We assume that these payments do not account for the state of storage in these periods and only apply to actual generation in the top 100 net load hours, at a price of \$150 / kWh per year. Figure 4.8 shows a heat map of renewable generation and grid net load for the CAISO market in 2020. The top 100 net load hours are shaded in black, and mainly occur between 6 and 11 pm in the months of August through October.

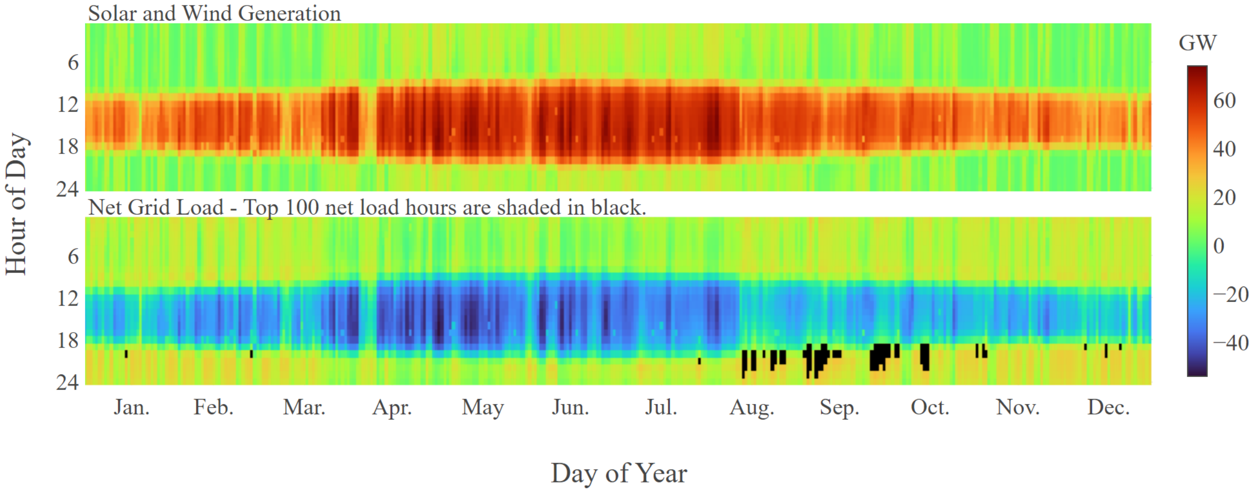

Figure 4.8 Heat map comparison of the total CAISO renewable generation and net grid load for 2020. The top 100 net load hours are shaded in black.

We assume the capacity payments are determined ex post facto by the utility; therefore, the dispatch optimization model has no knowledge of the periods on which these payments are based and so there is no direct incentive for producing during these periods in the schedule of operations, other than the time-of-delivery prices. A comparison of the periods of peak net load in Figure 4.8 and the periods of highest energy price in Figure 4.5, shows that grid net load is somewhat correlated to energy price, which provides a direct incentive for generation during these periods in the revenue-maximizing dispatch objective.

4.5 Results

We consider four plant configurations, including single-technology (i) CSP-with-TES, and (ii) PV-with-battery designs, as well as hybrid (iii) CSP-with-TES and a co-located PV field, and (iv) CSP-with-TES and PV-with-battery. We optimize sizing according either to the benefit-to-cost ratio or to the levelized cost of energy, and execute a study varying (i) plant location, (ii) electricity market, (iii) the grid connection limit, and (iv) the presence of a capacity-based incentive payment, to demonstrate the plant performance and optimal sizing dependence on these inputs. Section 4.5.9 summarizes the combinations of input parameters evaluated and our conclusions from each of Sections 4.5.3 through 4.5.8.

4.5.1 Plant Configuration Parameters

We limit the grid connection and fix dispatchable generation capacity to 100 MW in all but the hybrid CSP-with-TES and PV-with-battery configuration, allowing comparisons between the different plant configurations. The grid connection limit forces the CSP cycle, PV field, and battery to dispatch in periods orthogonal to each other. In Section 4.5.6, we relax the assumed 100 MW grid connection limit to show its effect on plant performance and optimal sizing in PV-with-battery designs. In the hybrid CSP-with-TES and PV-with-battery configuration we fix the power cycle capacity at 100 MW and allow the battery power capacity to vary.

Table 4.4 System sizing variables and simple bounds for each plant configuration considered

Design Variable	Units	Lower Bound	Upper Bound
Concentrating Solar Power (CSP) with Thermal Energy Storage (TES)			
Hours of TES	h	4	16
Solar Multiple	-	0.8	3.0
Photovoltaics (PV) with Battery Storage			
Battery Storage	MWh	1	600
PV Field DC Capacity	MW$_\mathrm{e}$	100	300
Hybrid CSP with TES and PV without Battery Storage			
PV Field DC Capacity	MW$_\mathrm{e}$	1	300
Hours of TES	h	4	16
Solar Multiple	-	0.8	3.0
Hybrid CSP with TES and PV with Battery Storage			
Battery Storage	MWh	1	600
Battery Power	MW$_\mathrm{e}$	1	100
PV Field DC Capacity	MW$_\mathrm{e}$	1	300
Hours of TES	h	4	16
Solar Multiple	-	0.8	3.0

Table 4.4 lists design sizing variables and their simple bounds for each of the plant configurations considered. All other aspects of plant design are fixed, unless otherwise stated. In all configurations, the PV system utilizes single-axis tracking panels and the inverter DC-to-AC ratio is fixed to the default value in SAM, 1.3. When included, the battery nominal voltage is 500V, utilizes a lithium iron phosphate chemistry, and is only allowed to charge using PV generation. The CSP system is configured as a power tower, is paired with a two-tank TES system, and uses a 60%-to-40% by-weight mixture of sodium nitrate and potassium nitrate for the heat transfer and storage fluid. All financing and installation cost parameters are the default values used in SAM at the time of this writing. Additional technology parameters and costs are listed in Appendix G.

4.5.2 Operations Schedule Examples

Plant performance is a result of both the market and weather conditions and the schedule of operations, guided by the dispatch model solutions. In all cases, we consider a revenue-maximizing dispatch objective, consistent with the benefit-to-cost ratio design objective and representative of the way in which a plant would be operated in an independent-system-operator market. Figure 4.9 shows four days of the schedule of plant operations for the CSP-with-TES design with the best benefit-to-cost ratio under the Rice 2020 market and weather conditions. Plant systems behave as expected, collecting solar energy during the day and dispatching energy to the grid during the highest-priced periods. We note the high capacity factor of this design, which we evaluate based on the 100 MW grid connection limit, and low amount of curtailed generation. CSP generation in hours 36 to 40 of Figure 4.9 demonstrates the operational policy to minimize solar energy curtailment. In these hours, the CSP cycle is operated to allow solar energy collection, which would not otherwise be possible since the TES system is at capacity. Generation during these low-priced hours has a neutral effect on the benefit-to-cost ratio of this design, but improves the levelized cost of energy.

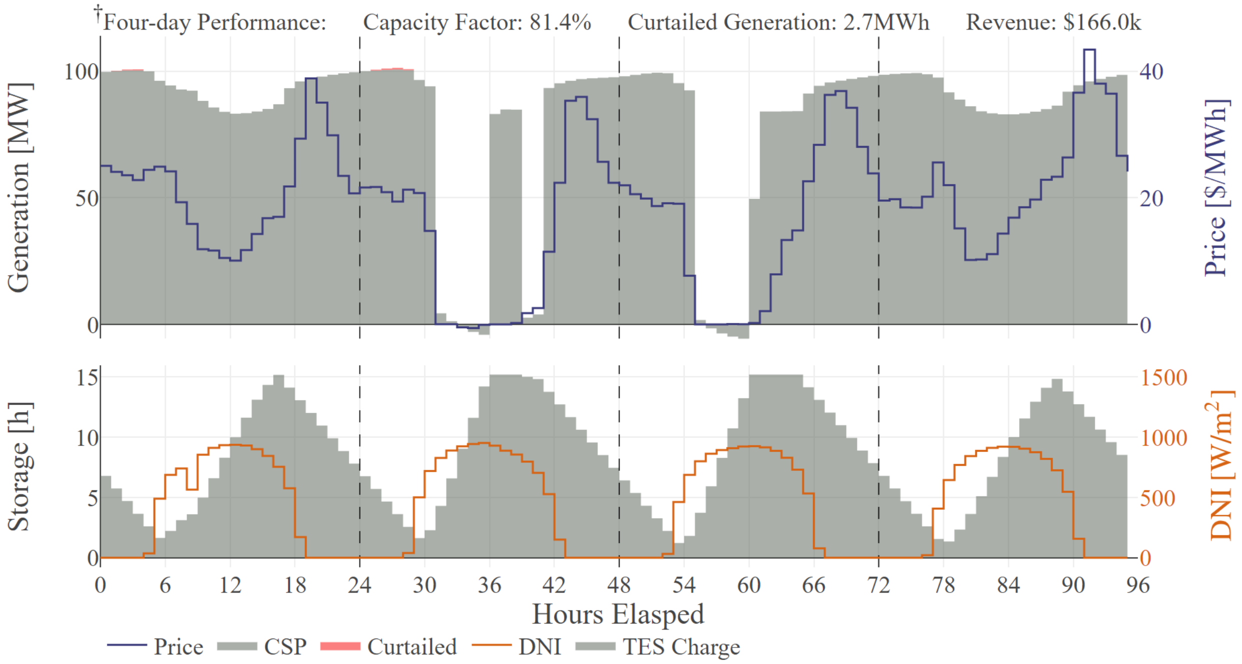

Figure 4.9 Example operations schedule for the CSP-with-TES plant, maximizing benefit-to-cost ratio under the Rice 2020 market and weather conditions (see Table 4.5 for the plant design). The direct normal irradiance (DNI) shows the solar resource available for CSP generation. Shaded regions and line traces are plotted against the primary (left) axes and the secondary (right) axes, respectively. †Simulated performance is reported over a four-day period in June of 2020.

Figure 4.10 shows four days of the schedule of plant operations for the PV-with-battery design with the best benefit-to-cost ratio under the Rice 2020 market and weather conditions. Compared to the CSP-with-TES design, results show significantly lower capacity factor and higher curtailed energy. In this design, the PV field AC capacity (131.4 MW_{ac}) is sized larger than the 100 MW grid connection limit, resulting in curtailed generation. In some periods, energy that would have been curtailed is used to charge the battery and then discharged in higher-priced periods.

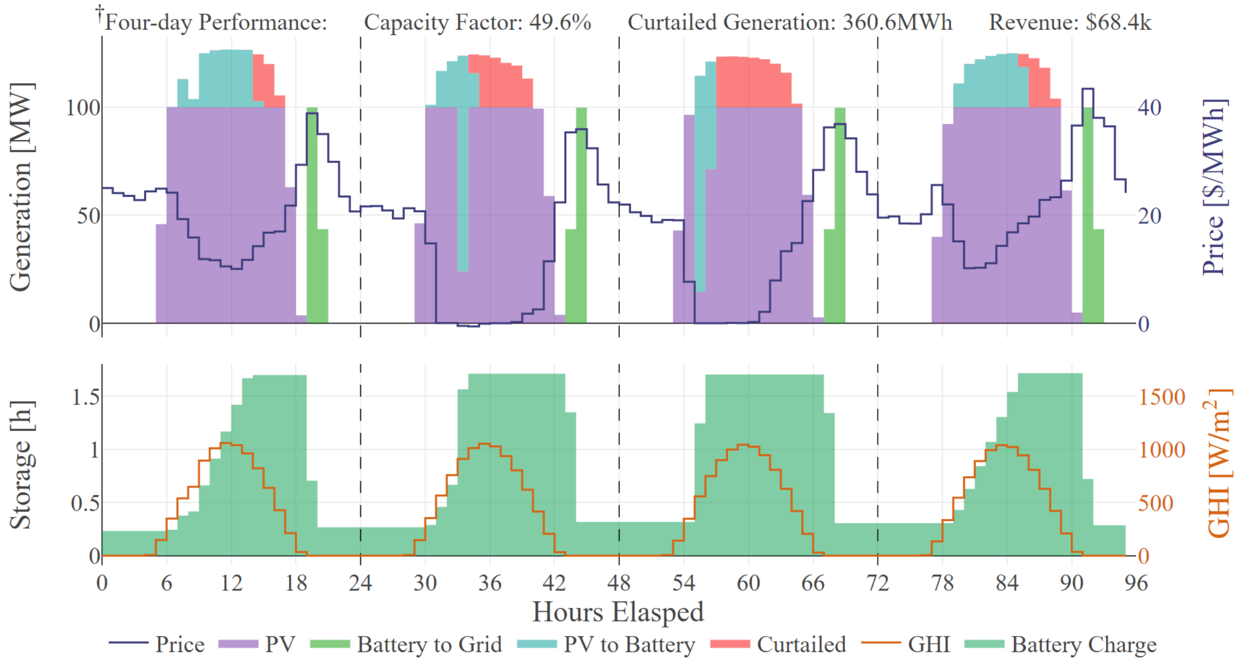

Figure 4.10 Example operations schedule for the PV-with-battery plant, maximizing benefit-to-cost ratio under the Rice 2020 market and weather conditions (see Table 4.5 for the plant design). The global horizontal irradiance (GHI) shows the solar resource available for PV generation. Shaded regions and line traces are plotted against the primary (left) axes and the secondary (right) axes, respectively. †Simulated performance is reported over a four-day period in June of 2020.

4.5.3 Electricity Market

To demonstrate the effect of the electricity market, we consider the two single-technology designs under the Rice 2010 and 2020 market and weather conditions. Figure 4.11 plots the designs optimizing either the benefit-to-cost ratio or the levelized cost of energy with 500 samples of the same configuration. We omit designs evaluated by the optimizer in Figure 4.11, which are clustered around the best plant design, to emphasize the coverage of sampling. Benefit-to-cost ratios are uniformly less than one, indicating that no design provides a positive return on investment. This is a consequence of the cost and revenue parameters used, which do not account for a purchase price agreement that would provide greater revenue than the day-ahead market.

Results under the Rice 2010 conditions show little difference between designs maximizing the benefit-to-cost ratio or minimizing the levelized cost of energy, which is a consequence of the roughly constant time-of-delivery prices in this market. CSP-with-TES designs with 12 to 16 hours of storage and a solar multiple of 2.5 to 3.0 perform well under either design objective, with the solar multiple pushed to its upper bound. PV-with-battery designs with the minimum amount, 1 MWh, of battery storage and 125 to 175 MW of PV capacity perform well under these market and weather conditions. The difference in storage capacity between the configurations serves to highlight differences in the PV-with-battery and CSP-with-TES systems. The battery operates as an arbitrage device, in which the system can take the current market price or pay a round-trip efficiency penalty to dispatch energy in the future at a higher price, while the TES system acts as an energy buffer (by design) between solar energy harvesting and electricity generation. This limitation of the battery system, combined with the roughly constant energy price in the Rice 2010 market, provides no incentive for battery storage capacity under either objective.

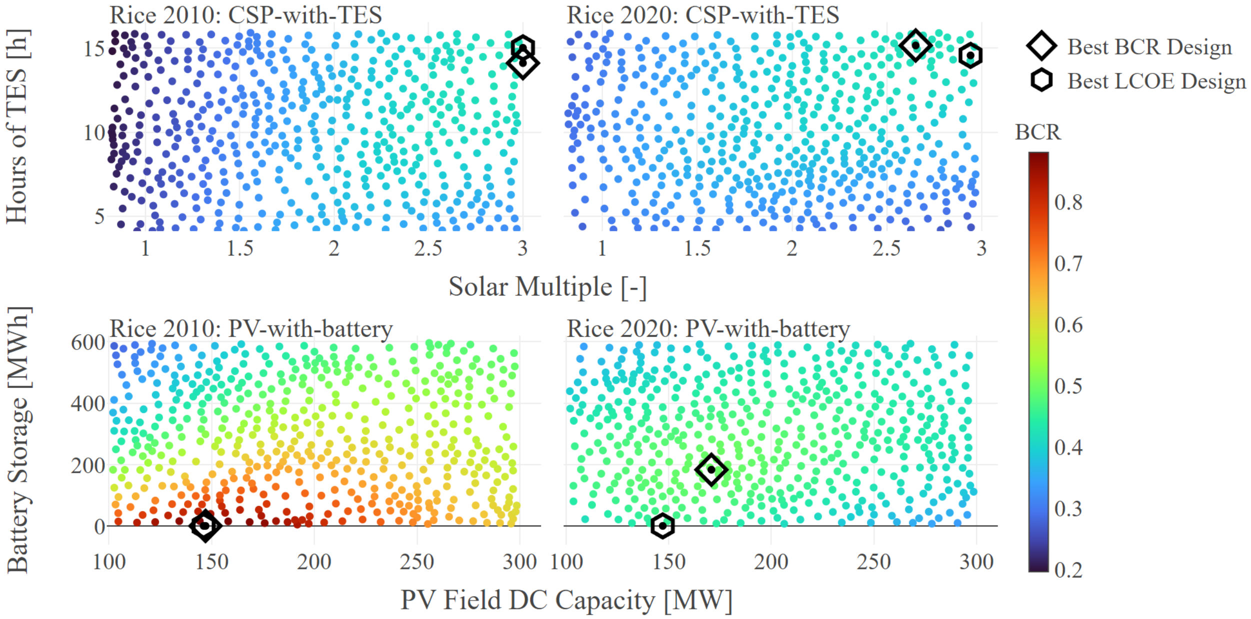

Figure 4.11 Benefit-to-cost ratio (BCR) results of sampling 500 designs with the best BCR and levelized cost of energy (LCOE) designs found, comparing performance under varying electricity markets. Designs evaluated during optimization are generally clustered near the best, but are omitted here to emphasize the coverage of sampling.

Results under the Rice 2020 conditions show greater variation in designs due to the greater incentive for storage this market provides. The plant design in the PV-with-battery configuration minimizing the levelized cost of energy is roughly the same in the Rice 2010 and 2020 results. The PV-with-battery design maximizing the benefit-to-cost ratio adds some battery storage capacity, because there are some opportunities to charge during low-priced periods and discharge in higher-priced periods afforded in this market. The CSP-with-TES design maximizing the benefit-to-cost ratio reduces the size of the solar field, compared to that under the Rice 2010 conditions, because the system is targeting generation during a smaller subset of higher-priced periods. Table 4.5 lists design variable values for the plants either maximizing the benefit-to-cost ratio or minimizing the levelized cost of energy under the Rice 2010 or 2020 conditions. We again note the close agreement in the best-found designs under the Rice 2010 conditions regardless of objective, whereas the Rice 2020 market provides a greater incentive for storage under the benefit-to-cost ratio objective.

Table 4.5 Design variables of plants either maximizing benefit-to-cost-ratio (BCR) or minimizing the levelized cost of energy (LCOE) under the Rice 2010 or 2020 market and weather conditions. † and ‡ indicate a variable is at its lower or upper bound, respectively. Bold values indicate a configuration has the best value of a particular performance metric.

Configuration	CSP-with-TES	CSP-with-TES	PV-with-battery	PV-with-battery
Design Objective	BCR	LCOE	BCR	LCOE
Rice 2010 market and weather				
Hours of TES [h]	14.10	15.01	-	-
Solar Multiple [-]	$3.00^{\ddagger}$	$3.00^{\ddagger}$	-	-
PV Field DC Capacity [MW$_\text{e}$]	-	-	147.10	146.17
Battery Storage [MWh]	-	-	$1.00^{\dagger}$	$1.00^{\dagger}$
BCR [-]	0.42	0.42	**0.91**	**0.91**
LCOE [¢/kWh]	7.45	7.44	**3.51**	**3.51**
AEP [GWh]	602.00	**607.41**	306.67	305.31
Capacity Factor [%]	68.72	**69.34**	35.01	34.85
Installed Cost [$ million]	713.22	719.36	181.30	**180.32**
Rice 2020 market and weather				
Hours of TES [h]	15.15	14.56	-	-
Solar Multiple [-]	2.65	2.94	-	-
PV Field DC Capacity [MW$_\text{e}$]	-	-	170.83	147.11
Battery Storage [MWh]	-	-	183.70	$1.00^{\dagger}$
BCR [-]	0.42	0.42	**0.50**	0.45
LCOE [¢/kWh]	7.54	7.37	4.90	**3.57**
AEP [GWh]	565.58	**604.60**	359.51	314.08
Capacity Factor [%]	64.56	**69.02**	41.04	35.85
Installed Cost [$ million]	669.41	705.57	248.12	**177.52**

The comparison of optimal sizing under either the Rice 2010 or 2020 market demonstrates that greater PV penetration incentivizes greater storage capacity, but also that the time-of-delivery prices alone are not sufficient to make these designs profitable under our cost assumptions. Results also demonstrate that the levelized cost of energy does not provide an incentive for storage in PV-with-battery designs under any market, because this metric only considers a plant's total energy production and does not consider the time value of energy. However, in CSP-with-TES designs, either objective function provides an incentive for storage, because TES systems cost-effectively increase total energy production.

4.5.4 Plant Location

To explore the effect of plant location, we consider the two single-technology configurations in the Rice and N. Chile locations, both under the Rice 2010 electricity market. The comparatively constant price in this market emphasizes differences due to the solar resource, rather than a combination of effects. Figure 4.12 plots designs optimizing either the benefit-to-cost ratio or levelized cost of energy in each location. Compared to the Rice 2010 results, the best-found designs are smaller in the N. Chile location as a result of the increased solar resource and the fixed 100 MW grid limit imposed on all designs.

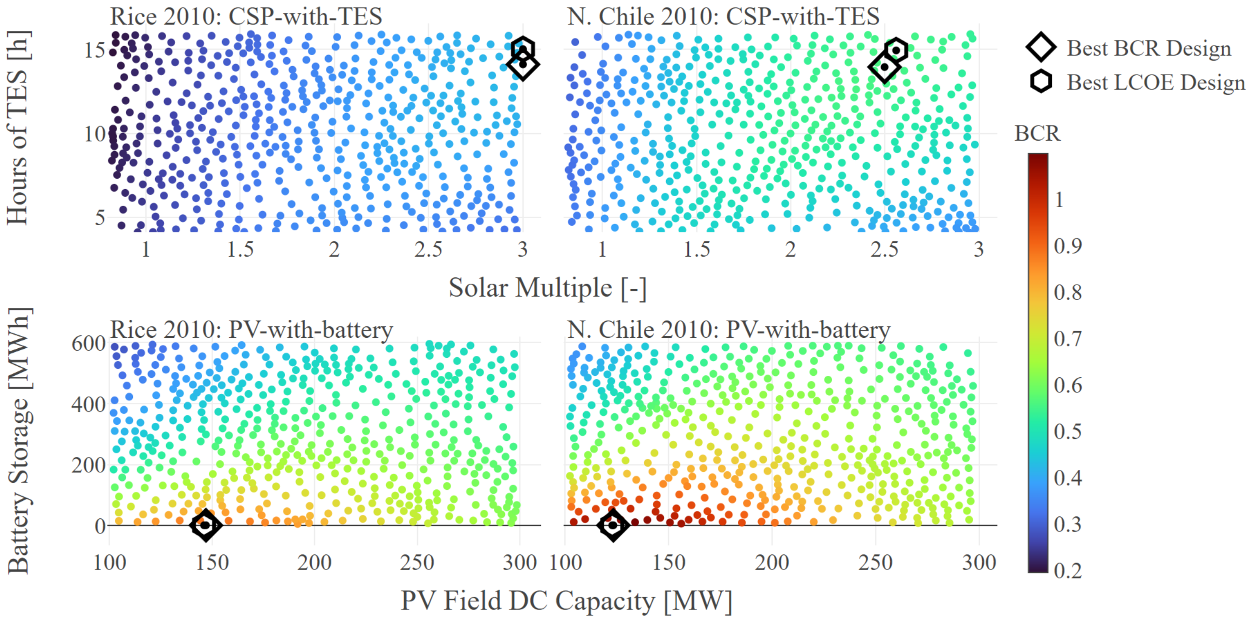

Figure 4.12 Benefit-to-cost ratio (BCR) results of sampling 500 designs with the best BCR and levelized cost of energy (LCOE) designs found, comparing performance under varying plant location. Designs evaluated during optimization are generally clustered near the best, but are omitted here to emphasize the coverage of sampling.

Table 4.6 shows designs of plants either maximizing the benefit-to-cost ratio or minimizing the levelized cost of energy under the combination of N. Chile weather conditions and the Rice 2010 market. We note close agreement in designs for either objective, again owing to the roughly constant price market, in which maximizing energy production (i.e., minimizing levelized cost of energy) is roughly the same as maximizing profit (i.e., maximizing the benefit-to-cost ratio). Results also show an increase in the best-found benefit-to-cost ratio and levelized cost of energy, demonstrating the dependence of plant performance on the available solar resource.

Table 4.6 Design variables of plants either maximizing benefit-to-cost-ratio (BCR) or minimizing the levelized cost of energy (LCOE) under the Rice 2010 or N. Chile 2010 weather conditions and Rice 2010 market. †Indicates a variable is at its lower bound. Bold values indicate a configuration has the best value of a particular performance metric.

Configuration Design Objective	CSP-with-TES BCR	CSP-with-TES LCOE	PV-with-battery BCR	PV-with-battery LCOE
N. Chile 2010 market and weather				
Hours of TES [h]	13.95	14.94	-	-
Solar Multiple [-]	2.50	2.56	-	-
PV Field DC Capacity [$\mathrm{MW_e}$]	-	-	123.37	122.80
Battery Storage [MWh]	-	-	$1.00^{\dagger}$	$1.00^{\dagger}$
BCR [-]	0.56	0.56	**1.13**	**1.13**
LCOE [¢/kWh]	5.67	5.65	**2.88**	**2.88**
AEP [GWh]	730.88	**747.38**	325.47	324.46
Capacity Factor [%]	83.43	**85.32**	37.15	37.04
Installed Cost [$ million]	645.31	661.02	157.64	**157.03**

4.5.5 Project Budget

In Sections 4.5.3 and 4.5.4, we do not consider a constraint on project budget. We investigate trends in the benefit-to-cost ratio with respect to the installed cost of plants using the results of sampling. We filter CSP-with-TES designs having the best benefit-to-cost ratio at a given installed cost from the designs evaluated during sampling. Figure 4.13 shows the apparent Pareto frontier of installed cost and benefit-to-cost ratio found in the results of sampling, and shows these designs in the overall parameter space. The right panel of Figure 4.14 shows that the best-found CSP-with-TES designs at a given installed cost occur in a band across the parameter space, which is dependent on the combination of weather and market conditions imposed and on the cost assumptions used.

We filter designs on the apparent Pareto frontier for each combination of weather and electricity market considered, using the Rice 2010 market and weather conditions as a base case to demonstrate the linear relationship in sizing of CSP-with-TES designs. The left panel of Figure 4.14 illustrates that designs under the Rice 2020 market have greater storage capacity and smaller solar multiples than designs under the Rice 2010 conditions, consistent with the Rice 2020 market providing a greater incentive to dispatch energy in a smaller subset of periods outside of the solar day (i.e., those with the highest time-of-delivery price). The right panel of Figure 4.14 demonstrates that designs in the N. Chile location have a lower solar multiple than those under the Rice 2010 weather conditions, consistent with the greater solar resource in that location and constant grid connection limit of these designs. Generally, these results show that a linear relationship between the solar field size and hours of storage exists and is dependent on the imposed market and weather conditions. A developer interested in a specific site could evaluate the apparent Pareto frontier of installed cost and benefit-to-cost ratio (or some other design objective), and then choose a design that meets their project budget from the dominating designs found.

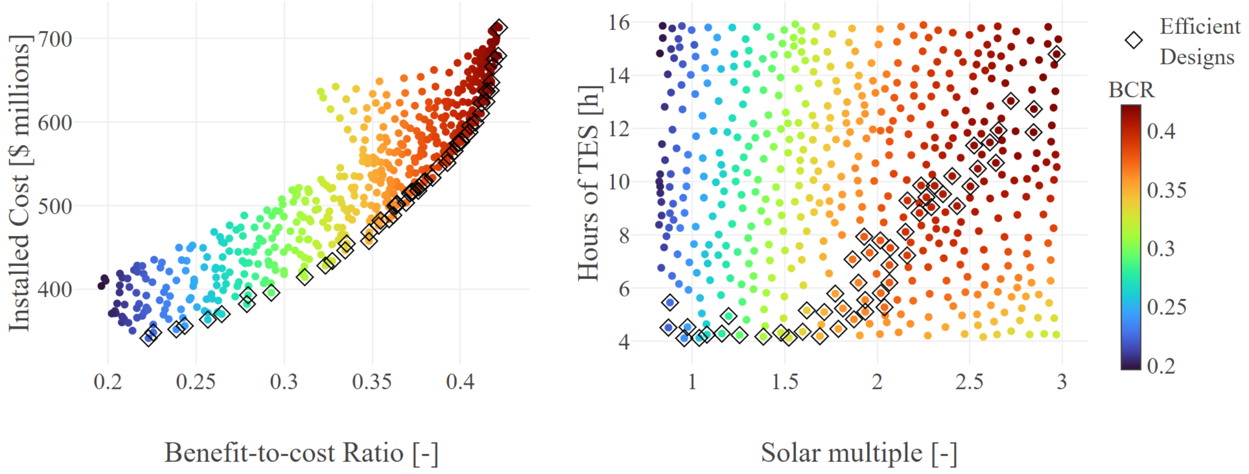

Figure 4.13 Installed cost and benefit-to-cost ratio results of sampling 500 CSP-with-TES designs under the Rice 2010 market and weather conditions. The left panel shows the apparent efficient frontier of installed cost and benefit-to-cost ratio. The right panel shows the position of the efficient designs in the parameter space.

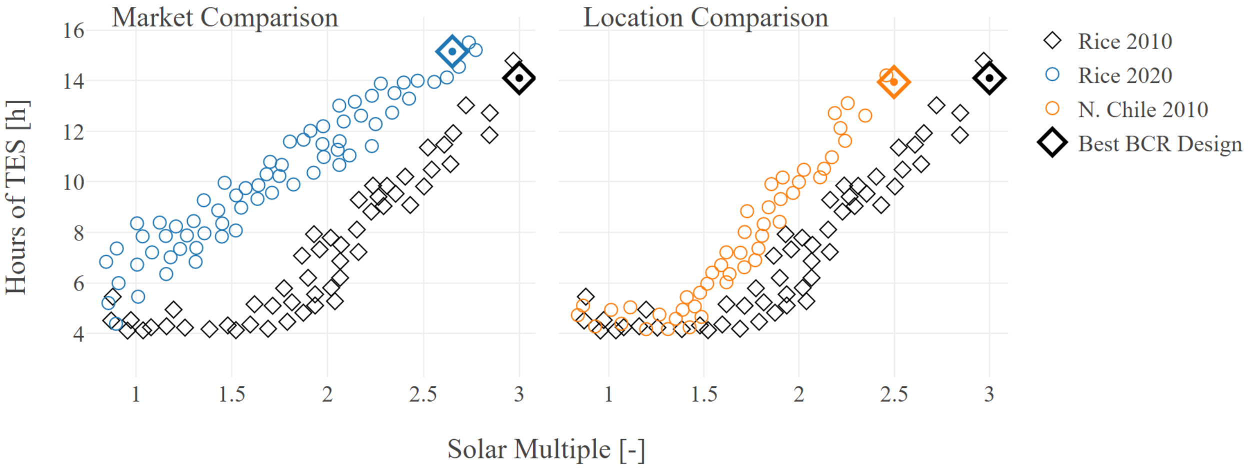

Figure 4.14 Comparison of CSP-with-TES designs maximizing the benefit-to-cost ratio and installed cost under varying energy market and plant location.

The comparison of efficient CSP-with-TES designs demonstrates the dependence of optimal sizing with respect to the imposed market and weather conditions. Further, results show the importance of balancing storage capacity with the CSP field solar multiple for the plant's location, with locations having greater solar resource leading to smaller heliostat fields at the same storage capacity. These relations are not present in PV-with-battery designs, because of the battery system's relatively higher cost per unit capacity.

4.5.6 Grid Interconnect Limit

In Sections 4.5.3 through 4.5.2, we impose a grid interconnect limit of 100 MW. This limit forces PV generation greater than 100 MW to be stored in the battery or curtailed. The best-found PV-with-battery designs in Sections 4.5.3 and 4.5.4 have PV field AC capacities larger than this connection limit, and battery capacities insufficient to capture all curtailed generation. We investigate the effect of the grid interconnect limit on the performance of the PV-with-battery configuration operations by increasing this limit to 125 and then 150 MW, thereby allowing excess PV generation (up to the grid limit) to be sold to the grid at the time-of-delivery price, rather than curtailed. Figure 4.15 shows installed cost results of sampling 500 PV-with-battery designs and the best-found benefit-to-cost ratio and levelized cost of energy designs while varying the grid connection limit. Plants having a larger PV field DC capacity and smaller battery storage capacity dominate as the grid connection limit is increased.

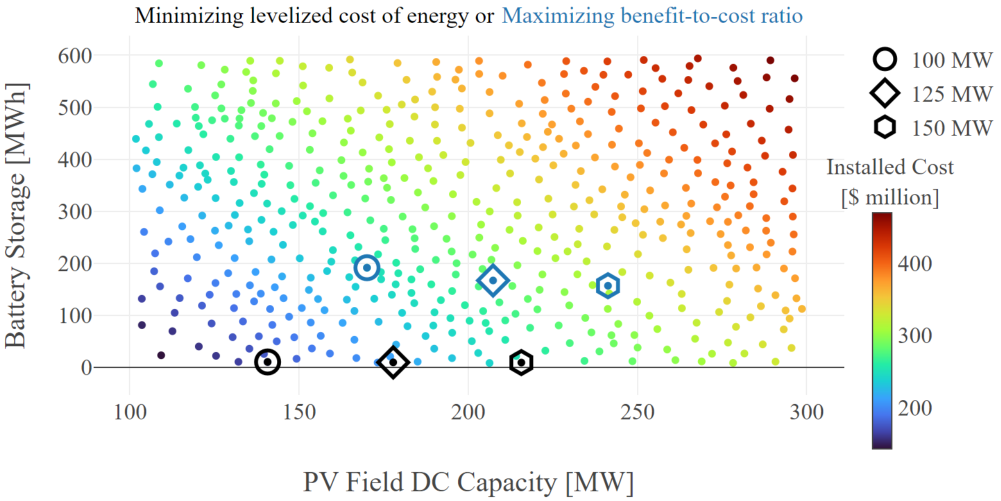

Figure 4.15 Installed cost results of sampling 500 PV-with-battery designs with the best benefit-to-cost ratio and levelized cost of energy designs found, while varying the grid connection limit between 100, 125 and 150 MW. Designs evaluated during optimization are generally clustered near the best, but are omitted here to emphasize the coverage of sampling.

Table 4.7 compares the designs and performance of PV-with-battery plants either maximizing the benefit-to-cost ratio or minimizing the levelized cost of energy. Results show minor improvements in both objective values as the grid connection limit is increased, indicating the Rice 2020 market provides a minor incentive for greater generation during the solar day. We note the PV field AC capacity of these designs all exceed their corresponding grid connection limit (by roughly 30 MW_e and 15 MW_e, respectively for each design objective). Each plant saturates the grid connection over a large portion of the hours of solar availability, resulting in curtailed generation; that is, even as the grid connection limit increases, the best-found PV field capacity also increases and, in each case, the best-found designs curtail 0.71 to 2.24%

of annual generation.

Table 4.7 Design variables of plants either maximizing benefit-to-cost-ratio (BCR) or minimizing the levelized cost of energy (LCOE) under the Rice 2020 market and weather conditions, and varying grid interconnect limit. †Indicates a design variable is at its lower bound.

Grid Limit	100 MW	100 MW	125 MW	125 MW	150 MW	150 MW
Design Objective	BCR	LCOE	BCR	LCOE	BCR	LCOE
Rice 2020 market and weather						
PV Field DC Capacity [$\mathrm{MW_e}$]	170.83	147.11	204.61	181.41	240.02	215.31
Battery Storage [MWh]	183.70	1.00†	157.57	1.00†	149.43	1.00†
PV Field AC Capacity [$\mathrm{MW_e}$]	131.41	113.16	157.39	139.55	184.63	165.62
PV Field AC Overbuilt [$\mathrm{MW_e}$]	31.41	13.16	32.39	14.55	34.63	15.62
BCR [-]	0.50	0.45	0.51	0.47	0.52	0.49
LCOE [¢/kWh]	4.90	3.57	4.32	3.36	4.00	3.21
AEP [GWh]	359.51	314.08	432.56	388.71	508.81	462.52
Capacity Factor [%]	41.04	35.85	39.50	35.50	38.72	35.20
Installed Cost [$ million]	248.12	177.52	277.09	213.51	312.24	249.10
Curtailed [%]	2.24	1.33	1.83	0.96	1.60	0.71

4.5.7 Capacity Credit

Utilities are considering incentivizing investments in utility-scale storage systems. We evaluate a capacity-based payment, as in Hamilton et al. [94], which is paid in addition to the time-of-delivery prices for generation during a subset of periods at a price of $150/kWh per year (taken from Jorgenson et al. [82]). These incentives are targeted to generation during periods of the greatest net grid load, which are often not known to the plant or the utility ahead of time. Figure 4.16 shows the results of sampling 500 CSP-with-TES designs while (a) excluding or (b) including this capacity payment in plant revenue. We note little change in the best-found designs according to the levelized cost of energy objective due to the presence of the capacity payment, as this metric does not consider plant revenue. Designs maximizing the benefit-to-cost ratio change significantly when adding the capacity payment, with the best-found CSP-with-TES design having a significantly smaller heliostat field and storage capacity compared to the best-found design without the capacity payment. The effect of the capacity payment on the CSP-with-TES configuration is to incentivize generation during a smaller subset of periods. The PV-with-battery configuration adds battery storage capacity and shrinks the PV field in response to the capacity payment, consistent with the capacity payment incentivizing generation in a smaller subset of periods. In both configurations, the benefit-to-cost ratio objective seeks a minimum-cost plant with sufficient capacity to be awarded revenue from the capacity payment. We also note that the benefit-to-cost ratio objective is relatively flat over a large range of designs in both configurations, meaning that the result is strongly dependent on the cost parameters, time-of-delivery, and capacity price used.

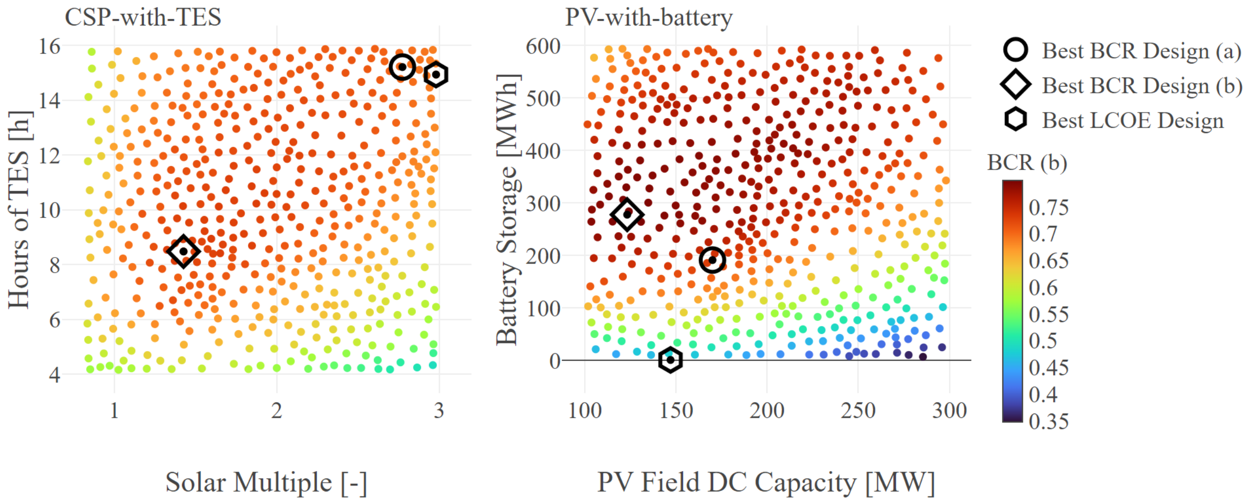

Figure 4.16 Benefit-to-cost ratio (BCR) results of sampling 500 CSP-with-TES and PV-with-battery designs with the best benefit-to-cost ratio and levelized cost of energy designs found, with (a) no capacity payment and (b) a $150/kWh per year payment for generation during the top 100 net load hours. Designs evaluated during optimization are generally clustered near the best, but are omitted here to emphasize the coverage of sampling.

Figure 4.17 shows generation schedules for the best-found designs, which have significantly lower annual energy generation than the best-found designs without the capacity payment. The CSP-with-TES design achieves 91.5% coverage of peak net load hours in the four-day period shown, whereas the PV-with-battery design lacks sufficient battery storage capacity to generate during all peak net load hours, achieving only 41.7% coverage of the hours shown. Because the periods on which the capacity payment is based are opaque to the dispatch optimization model, the schedule of operations of these plants is not affected by the presence of the payment, and is only guided by the time-of-delivery price. We find that the CSP-with-TES design achieves significantly higher coverage of high-net-load periods, though the PV-with-battery design yields a better benefit-to-cost ratio, owing to its lower installed cost.

Table 4.8 shows designs maximizing the benefit-to-cost ratio under the Rice 2020 weather and market conditions either (a) without a capacity payment or (b) with a capacity payment. The best-found benefit-to-cost ratios improve, as expected, since the capacity payment provides an additional source of revenue at no additional cost to the plant. In this scenario, results show that CSP-with-TES designs, sized according to the time-of-delivery price alone, are well positioned to benefit from a capacity-based incentive, while PV-with-battery designs may need additional investment to increase battery capacity to fully benefit from this kind of incentive. Given the similarity of the best-found benefit-to-cost ratios in either configuration, a reduction in CSP costs or an increase in the capacity price, a capacity-based incentive might allow a CSP-with-TES design to be more profitable than a PV-with-battery plant.

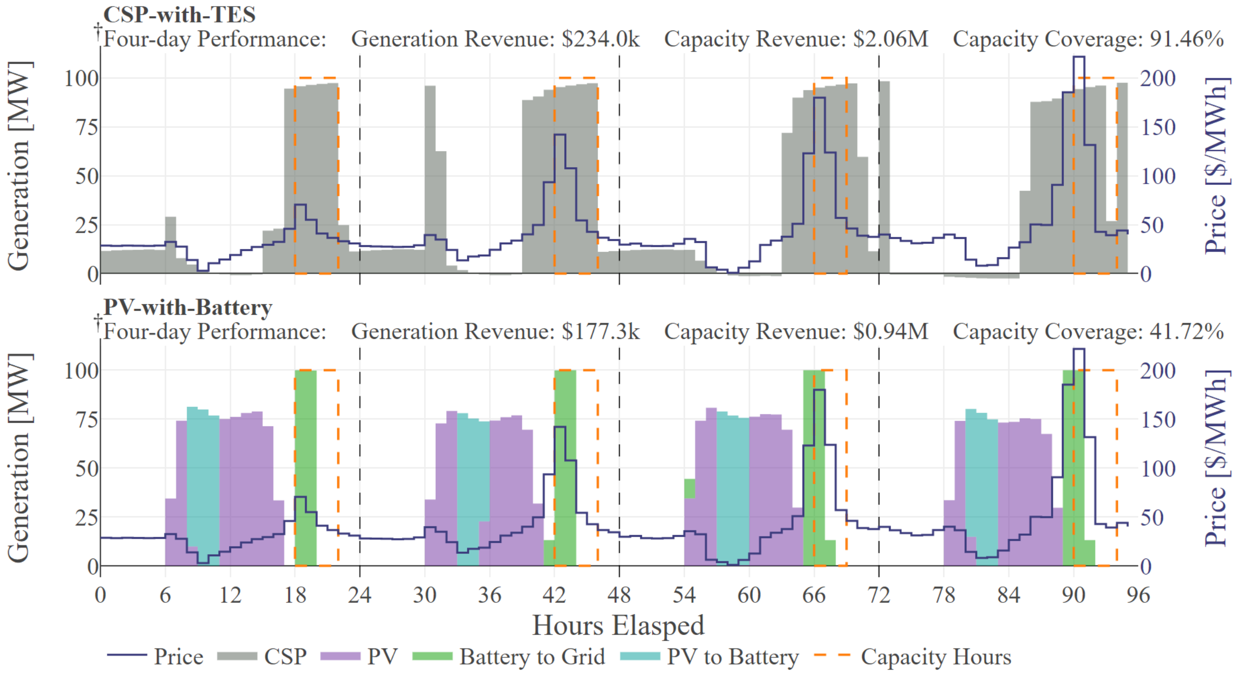

Figure 4.17 Example operations schedule for the PV-with-battery and CSP-with-TES plants, maximizing benefit-to-cost ratio under the Rice 2020 market and weather conditions with the $150/kWh capacity incentive (see Table 4.8 for the plant designs). Shaded regions and line traces are plotted against the primary (left) axes and the secondary (right) axes, respectively. †Simulated performance is reported over a four-day period in September of 2020, which contains 15 of the 100 peak net load hours.

Table 4.8 Design variables of plants maximizing benefit-to-cost-ratio (BCR) under the Rice 2020 market and weather conditions, both with and without a capacity-based incentive. Bold values indicate that a configuration has the best value of a particular performance metric. †Capacity credit percent calculated according to the schedule of operations but not included in plant revenue.

Configuration	CSP-with-TES	CSP-with-TES	PV-with-battery	PV-with-battery
Capacity Credit	(a) without	(b) with	(a) without	(b) with
Rice 2020 market and weather				
Hours of TES [h]	15.15	8.48	-	-
Solar Multiple [-]	2.65	1.43	-	-
Field DC Capacity [MW$_e$]	-	-	170.83	123.35
Battery Storage [MWh]	-	-	183.70	277.69
BCR [-]	0.42	0.73	0.50	**0.80**
LCOE [¢/kWh]	7.54	10.81	**4.90**	6.52
AEP [GWh]	**565.58**	282.28	359.51	264.93
Capacity Factor [%]	**64.56**	32.22	41.04	30.24
Installed Cost [$ million]	669.41	458.54	248.12	**225.83**
Capacity Credit [%]	**93.83**†	89.19	29.53†	42.70

Figure 4.18 shows the apparent Pareto frontier of the capacity credit percent and benefit-to-cost ratio; the capacity credit percent could be doubled from the best-found PV-with-battery design by increasing the size of the PV field and battery storage capacity. As the size of the PV field and battery storage capacity increase, the designs are able to capture additional capacity credit revenue, but under our cost

assumptions, the installed cost of these designs increases at a greater rate; either an increase in the capacity incentive or a decrease in the cost per unit capacity of the battery would shift the optimal sizing. We present these results to demonstrate the effect of a capacity-based incentive on optimal sizing, whereas developers, seeking to maximize revenue gained from a real-world incentive payment, should rely on a more holistic analysis to size plant systems, especially if payments are determined ex post facto or are not available throughout the plant's lifetime.

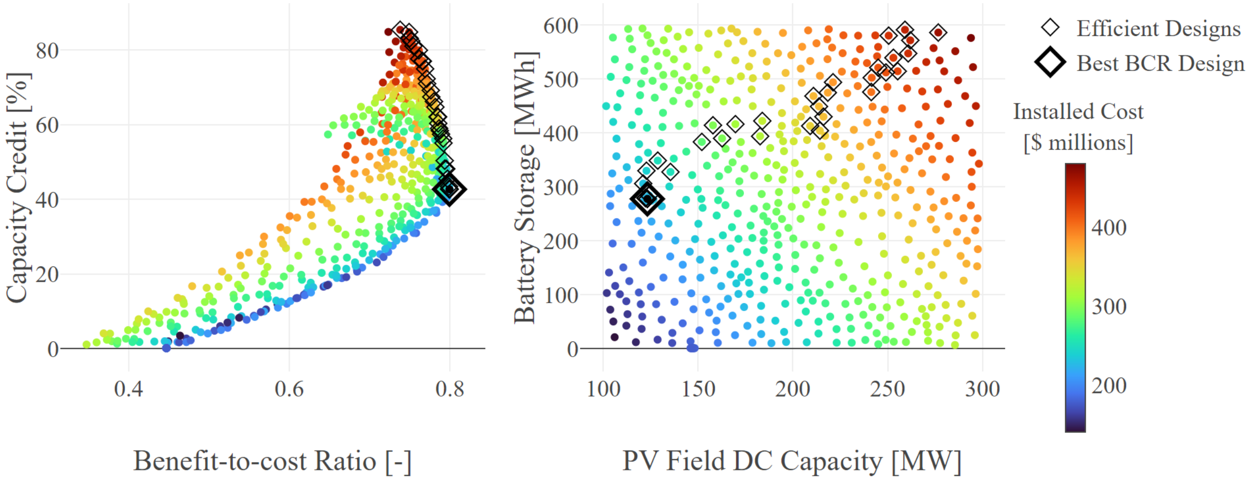

Figure 4.18 Installed cost and benefit-to-cost ratio results of sampling 500 PV-with-battery designs under the Rice 2020 market with a \$150/kWh per year capacity credit. The left panel shows the apparent efficient frontier of capacity credit percent and benefit-to-cost ratio. The right panel shows the position of the efficient designs in the parameter space.

4.5.8 Hybridization

We consider two hybrid plant configurations, the first with a CSP-with-TES system and a co-located PV field, and the second with both a CSP-with-TES and a PV-with-battery system. We approach hybrid configurations from the perspective of adding PV or a PV-with-battery system to an existing CSP-with-TES plant, which theoretically could increase the capacity factor of the plant by coupling the lower-cost PV generation during the solar day with the high-storage-capacity TES for overnight generation. In both hybrid configurations, the CSP power cycle is fixed to 100 MW_e, and so both the hybrid configurations considered are CSP dominant with respect to their performance. Figure 4.19 shows the results of sampling 750 hybrid CSP-with-TES and PV (without a battery) designs under the Rice 2020 conditions, with the designs having the best levelized cost of energy and best benefit-to-cost ratio either (a) without a capacity payment or (b) with a capacity payment identified. We note differences in CSP-with-TES and PV field sizing in these three cases. The design minimizing the levelized cost of energy couples a relatively large CSP-with-TES system having over 13 hours of storage with a 162 $\mathrm{MW_{dc}}$ PV field. The PV field in this design is sized to provide additional capacity during the hours of solar availability. The design maximizing the benefit-to-cost ratio without the capacity credit couples an even larger CSP-with-TES system with a smaller 36 $\mathrm{MW_{dc}}$ PV field. The PV field in this design provides enough energy to cover the parasitic loads of the CSP systems, with additional energy sold to the grid. The design maximizing the benefit-to-cost ratio with the capacity credit has a smaller CSP-with-TES system, consistent with results in Section 4.5.7, and correspondingly smaller PV field.

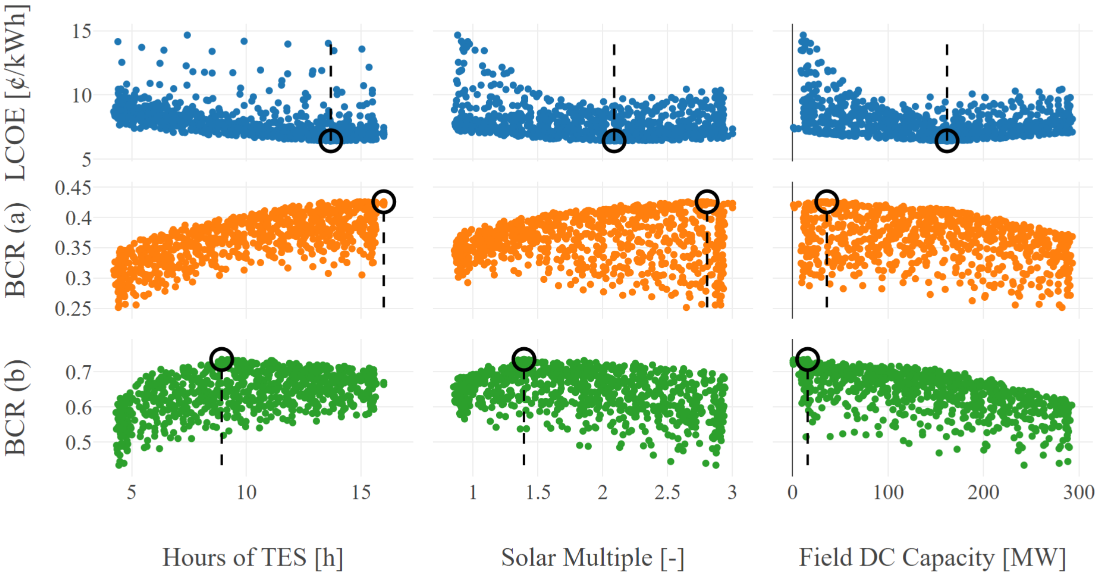

Figure 4.19 Benefit-to-cost ratio (BCR) and levelized cost of energy (LCOE) results of sampling 750 hybrid CSP-with-TES and PV designs with the best benefit-to-cost ratio and levelized cost of energy found, with (a) no capacity payment and (b) a $150/kWh per year payment for generation during the top 100 net load hours.

Table 4.9 shows the variable values of hybrid plant designs either maximizing the benefit-to-cost ratio or the levelized cost of energy. The battery system is sized at its lower bound in each case, when included. This indicates that the battery system does not price favorably under our market and cost assumptions in a hybrid configuration having a 100 MW CSP power cycle. Other uses of the battery system, e.g., rapid-response capacity or frequency control, rather than as bulk storage, would likely affect this result. The two design objectives lead to design using the PV field in two distinct ways: (i) designs minimizing the levelized cost of energy include larger PV fields for additional capacity, while (ii) designs maximizing the benefit-to-cost ratio in a market with significant PV generation primarily use the PV field to cover CSP system parasitic loads.

Table 4.9 Design characteristics of plants maximizing benefit-to-cost-ratio (BCR) under the Rice 2020 market and weather conditions, both with and without a capacity-based incentive. † and ‡ indicate a variable is at its lower or upper bound, respectively. Bold values indicate a configuration has the best value of a particular performance metric. ††Capacity credit percent calculated according to the schedule of operations but not included in plant revenue.

Configuration	CSP-with-TES and PV	CSP-with-TES and PV	CSP-with-TES and PV-with-battery	CSP-with-TES and PV-with-battery
Design Objective	BCR	LCOE	BCR	LCOE
Rice 2020 market and weather				
Hours of TES [h]	16.00‡	13.69	14.35	13.66
Solar Multiple [-]	2.80	2.09	2.56	2.08
Field DC Capacity [MW$_\mathrm{e}$]	35.96	161.86	47.56	164.74
Battery Power [MW]	-	-	1.00†	1.00†
Battery Storage [MWh]	-	-	1.00†	1.00†
BCR [-]	**0.43**	0.41	**0.43**	0.41
LCOE [¢/kWh]	6.96	**6.42**	6.94	6.43
AEP [GWh]	657.78	722.17	635.55	**723.58**
Installed Cost [$ million]	733.58	748.51	**699.80**	750.69
Capacity Credit [%]	93.84††	93.79††	**93.97**††	93.94††
Rice 2020 market and weather with a $150/MWh per year capacity payment				
Hours of TES [h]	8.93	13.18	8.86	13.56
Solar Multiple [-]	1.39	2.06	1.35	2.15
Field DC Capacity [MW$_\mathrm{e}$]	15.92	160.48	15.71	160.33
Battery Power [MW]	-	-	1.00†	1.00†
Battery Storage [MWh]	-	-	1.00†	1.00†
BCR [-]	**0.74**	0.68	0.73	0.67
LCOE [¢/kWh]	10.10	**6.29**	10.15	6.30
AEP [GWh]	309.11	715.07	307.94	**726.47**
Installed Cost [$ million]	**474.23**	749.04	473.97	764.36
Capacity Credit [%]	85.60	89.19	84.84	**89.32**

4.5.9 Summary of Results

Table 4.10 summarizes the input parameter combinations evaluated in each subsection of Section 4.5. Results show that, under our assumptions, PV-with-battery designs are more profitable than CSP-with-TES designs, primarily due to their reduced installation cost. We find the current time-of-delivery prices in the California Independent System Operator market to be insufficient to yield a positive return on investment in any configuration of solar power plant with storage. We also find that CSP field solar multiple and hours of thermal energy storage in CSP-with-TES designs maximizing the benefit-to-cost ratio follow a site- and market-dependent linear relationship as the total project budget varies. A capacity-based incentive, targeted to greater investment in utility-scale storage systems, can benefit both CSP-with-TES and PV-with-battery designs, but are still insufficient to yield a positive return on investment at a price of $150/kWh per year. The hybrid plant configurations we consider, where a PV field is added to a CSP-with-TES plant, utilize the PV field either for additional capacity or to cover parasitic loads.

Table 4.10 Summary of input data combinations evaluated in each subsection of Section 4.5, with a concise statement of our conclusions.

Section	Market	Weather	Configuration	Grid Limit	Conclusions
Section 4.5.3 Energy Market	Rice 2010	Rice 2010	CSP-with-TES	100 MW	- The LCOE objective incentivizes storage in PV-with-battery designs. - Greater PV penetration increases the value of storage in the day-ahead market.
	Rice 2010	Rice 2010	PV-with-battery	100 MW	
	Rice 2020	Rice 2020	CSP-with-TES	100 MW	
	Rice 2020	Rice 2020	PV-with-battery	100 MW	
Section 4.5.4 Plant Location	Rice 2010	Rice 2010	CSP-with-TES	100 MW	- Greater solar resource yields smaller optimal designs under a fixed grid limit. - Optimizing either LCOE or BCR is equivalent in a constant-price market.
	Rice 2010	Rice 2010	PV-with-battery	100 MW	
	Rice 2010	N. Chile TMY	CSP-with-TES	100 MW	
	Rice 2010	N. Chile TMY	PV-with-battery	100 MW	
Section 4.5.5 Project Budget	Rice 2010	Rice 2010	CSP-with-TES	100 MW	- CSP-with-TES designs maximizing benefit-to-cost ratio have an input-dependent linear relation between storage and solar field sizes.
	Rice 2020	Rice 2020	CSP-with-TES	100 MW	
	Rice 2010	N. Chile TMY	CSP-with-TES	100 MW	
Section 4.5.6 Grid Limit	Rice 2020	Rice 2020	PV-with-battery	100 MW	- PV capacity grows with the grid limit. - The best-found design curtails roughly 2% of annual generation under each grid limit.
	Rice 2020	Rice 2020	PV-with-battery	125 MW	
	Rice 2020	Rice 2020	PV-with-battery	150 MW	
Section 4.5.7 Capacity Payment	Rice 2020	Rice 2020	CSP-with-TES	100 MW	- Optimal sizing according to LCOE is not affected by a capacity payment. - CSP-with-TES designs benefit more from a capacity payment than PV-with-battery designs.
	Rice 2020	Rice 2020	PV-with-battery	100 MW	
	$150/kWh	Rice 2020	CSP-with-TES	100 MW	
	$150/kWh	Rice 2020	PV-with-battery	100 MW	
Section 4.5.8 Hybrid Designs	Rice 2020	Rice 2020	Hybrid (no battery)	100 MW	- PV generation can add capacity or cover CSP parasitic loads. - A battery system does not price favorably under our assumptions.
	$150/kWh	Rice 2020		100 MW	
	Rice 2020	Rice 2020	Hybrid (with battery)	100 MW	
	$150/kWh	Rice 2020		100 MW	

4.6 Conclusions and Future Work

We simulate performance of hybrid solar plants with storage, operated according to the dispatch solution of a revenue-maximizing mixed integer-linear program, using NREL's open-source Hybrid Optimization and Performance Platform Python package, as in Hamilton et al. [94] and Cox et al. [102]. Our contributions include: an exploration of optimal sizing sensitivity with respect to (i) the imposed energy market, (ii) weather conditions, (iii) grid interconnect limit, (iv) the presence of a capacity-based incentive, and (v) the design objective. We present trends in optimal plant sizing with respect to several inputs, and include depictions of the schedule of operations of optimally-sized plants. Results show that, under multiple scenarios, a PV-with-battery design is more profitable than a CSP-with-TES design, though the inclusion of a CSP system dramatically increases annual energy production. We also show that both designs can benefit from the presence of a capacity-based incentive, but that, under our assumptions, the decreased installation cost of PV-with-battery designs outweighs the additional dispatch flexibility of CSP-with-TES designs. We demonstrate that cost-efficient CSP-with-TES designs have a roughly linear relationship between the size of their solar field and the hours of thermal energy storage, and that this relationship is energy-market and location dependent. Finally, we show in hybrid configurations that a battery system does not currently price favorably, with the best-found designs setting the battery system at its lower bound. However, the addition of a PV field to a CSP-with-TES plant can improve both the benefit-to-cost ratio and levelized cost of energy. Future research efforts might explore the sensitivity of plant performance and optimal sizing with respect to additional parameters and assumptions in the plant evaluation, explore a method for robust plant sizing across a range of market conditions, consider participation in ancillary service markets, and/or incorporate additional technologies in hybrid configurations.

4.7 Acknowledgments

This work was authored in part by the National Renewable Energy Laboratory, operated by Alliance for Sustainable Energy, LLC, for the U.S. Department of Energy (DOE) under Contract No. DE-AC36-08GO28308. Funding provided by the U.S. Department of Energy's Office of Energy Efficiency and Renewable Energy under the Solar Energy Technologies Office Award Number 34245. The views expressed in the article do not necessarily represent the views of the DOE or the U.S. Government. The U.S. Government retains and the publisher, by accepting the article for publication, acknowledges that the U.S. Government retains a nonexclusive, paid-up, irrevocable, worldwide license to publish or reproduce the published form of this work, or allow others to do so, for U.S. Government purposes.

CHAPTER 5

CONCLUSIONS AND FUTURE WORK

In this dissertation, we develop and solve nonlinear and non-convex optimization problems to support optimal design and dispatch decisions in solar power plants with storage. The total capacity of solar power with storage is limited in the US market at the time of this writing, though these plants present a promising path towards utility-scale renewable energy that can be dispatched according to grid demand. The methods we present can be used to provide decision support to developers and operators of these plants, seeking to improve their profitability.

In Chapter 2, we extend CSP dispatch optimization model for real-time decision support, present exact and inexact modifications to this model to improve tractability, and show that it can be solved to a 3 percent global optimality gap on average in a time suitable for the real-time setting. The formulation we present considers many operating limitations of the receiver and power cycle systems and incorporates a temperature-dependent model of power cycle efficiency. This allows the model to account for temperature-related trade-offs that may occur between receiver and power cycle operations, which are a central issue for plant operators. The modifications we present improve problem tractability, and demonstrate the suitability of a nonlinear and non-convex model for decision support in a real-time setting. Future work in this area might execute a larger study of dispatch instances to develop standard operating policies for use in the absence of an optimization model, explore weather and market features impacting plant revenue, or demonstrate the revenue improvement potential of guiding plant operations according to the solution of this dispatch model.

In Chapter 3, we develop a method for the economic evaluation and optimal sizing of a solar power plant with storage, and demonstrate that the lifetime benefit-to-cost ratio of these plants can be improved 6 to 19 percent compared to a baseline design without optimization. This approach considers optimal dispatch under the imposed market and weather conditions at hourly fidelity when evaluating the economic performance of plant designs. The optimization approach we present improves computational throughput and provides additional information on general trends across the solution space. The software we develop is made publicly available and maintained by the National Renewable Energy Laboratory, to allow plant designers to tailor market and weather scenarios according to their problem of interest. Future work in this area might examine the sensitivity of optimal plant sizing based on additional cost parameters, analyze dispatch strategies for different plant configurations and energy markets, and investigate renewable energy incentive programs.

In Chapter 4, we execute a larger study of market and weather conditions, operating assumptions, and renewable energy incentives to show how our approach for plant economic evaluation is sensitive to these parameters. Results show that under our assumptions, PV-with-battery designs are more profitable than CSP-with-TES designs, but that the inclusion of a CSP system increases annual energy production. We find that CSP-with-TES designs maximizing the benefit-to-cost ratio have an input-dependent linear relationship between the size of their solar field and the hours of thermal energy storage as the project budget varies. Future work in this area might identify critical values of underlying costs that cause each technology to dominate with respect to economic performance, develop a method for robust plant sizing across a range of market conditions, and/or incorporate additional technologies in hybrid configurations.

REFERENCES

[1] Paul Denholm, Matthew O'Connell, Gregory Brinkman, and Jennie Jorgenson. Overgeneration from solar energy in california: A field guide to the duck chart. Technical Report NREL/TP-6A20-65023, 2015.

[2] Paul Denholm, Robert Margolis, Trieu Mai, Greg Brinkman, Easan Drury, Maureen Hand, and Matthew Mowers. Bright future: Solar power as a major contributor to the US grid. *IEEE Power and Energy Magazine*, 11(2):22–32, 2013.

[3] Ran Fu, David J. Feldman, Robert M. Margolis, Michael A. Woodhouse, and Kristen B. Ardani. U.S. Solar Photovoltaic System Cost Benchmark: Q1 2017. Technical Report NREL/TP–6A20-68925, 1390776, September 2017.

[4] Antoni Gil, Marc Medrano, Ingrid Martorell, Ana Lázaro, Pablo Dolado, Belén Zalba, and Luisa F Cabeza. State of the art on high temperature thermal energy storage for power generation. Part 1 — Concepts, materials and modellization. *Renewable and Sustainable Energy Reviews*, 14(1):31–55, 2010.

[5] Christoph Kost, Christoph M. Flath, and Dominik Möst. Concentrating solar power plant investment and operation decisions under different price and support mechanisms. *Energy Policy*, 61:238–248, 2013. ISSN 03014215.

[6] Alexander W. Dowling, Tian Zheng, and Victor M. Zavala. Economic assessment of concentrated solar power technologies: A review. *Renewable and Sustainable Energy Reviews*, 72:1019–1032, 2017. ISSN 1364-0321.

[7] Guruprasad Alva, Lingkun Liu, Xiang Huang, and Guiyin Fang. Thermal energy storage materials and systems for solar energy applications. *Renewable and Sustainable Energy Reviews*, 68:693–706, 2017.

[8] Mark Mehos, Craig Turchi, Judith Vidal, Michael Wagner, Zhiwen Ma, Clifford Ho, William Kolb, Charles Andraka, and Alan Kruizenga. Concentrating solar power Gen3 demonstration roadmap. Technical Report NREL/TP–5500-67464, 1338899, January 2017.

[9] Ming Liu, N.H. Steven Tay, Stuart Bell, Martin Belusko, Rhys Jacob, Geoffrey Will, Wasim Saman, and Frank Bruno. Review on concentrating solar power plants and new developments in high temperature thermal energy storage technologies. *Renewable and Sustainable Energy Reviews*, 53: 1411–1432, 2016. ISSN 1364-0321.

[10] Omar Behar, Abdallah Khellaf, and Kamal Mohammedi. A review of studies on central receiver solar thermal power plants. *Renewable and Sustainable Energy Reviews*, 23:12–39, 2013. ISSN 1364-0321.

[11] Francesco Crespi, Andrea Toscani, Paolo Zani, David Sánchez, and Giampaolo Manzolini. Effect of passing clouds on the dynamic performance of a CSP tower receiver with molten salt heat storage. *Applied Energy*, 229:224–235, 2018. ISSN 0306-2619.

[12] Michael J. Wagner, Alexandra M. Newman, William T. Hamilton, and Robert J. Braun. Optimized dispatch in a first-principles concentrating solar power production model. *Applied Energy*, 203: 959–971, 2017. ISSN 0306-2619.

[13] Seyed Hossein Madaeni, Ramteen Sioshansi, and Paul Denholm. How thermal energy storage enhances the economic viability of concentrating solar power. *Proceedings of the IEEE*, 100(2): 335–347, 2012. ISSN 0018-9219.

[14] Madeleine McPherson, Mark Mehos, and Paul Denholm. Leveraging concentrating solar power plant dispatchability: A review of the impacts of global market structures and policy. *Energy Policy*, 139: 111335, 2020.

[15] Paul Denholm and Mark Mehos. Enabling greater penetration of solar power via the use of CSP with thermal energy storage. *Solar Energy: Application, Economics, and Public Perception*, 99, 2014.

[16] M Mehos, J Jorgenson, P Denholm, and C Turchi. An assessment of the net value of CSP systems integrated with thermal energy storage. *Energy Procedia*, 69:2060–2071, 2015.

[17] Nate Blair. *System Advisor Model, SAM 2014.1.14: General description.* NREL/TP ; 6A20-61019. National Renewable Energy Laboratory, Golden, Colorado, 2014.

[18] Ershun Du, Ning Zhang, Bri-Mathias Hodge, Qin Wang, Zongxiang Lu, Chongqing Kang, Benjamin Kroposki, and Qing Xia. Operation of a high renewable penetrated power system with CSP plants: A look-ahead stochastic unit commitment model. *IEEE Transactions on Power Systems*, 34(1): 140–151, 2018.

[19] Shan Gao, Yiqing Zhang, and Yu Liu. Incorporating concentrating solar power into high renewables penetrated power system: A chance-constrained stochastic unit commitment analysis. *Applied Sciences*, 9(11):2340, 2019.

[20] Qipeng P Zheng, Jianhui Wang, and Andrew L Liu. Stochastic optimization for unit commitment: A review. *IEEE Transactions on Power Systems*, 30(4):1913–1924, 2014.

[21] Janna Martinek, Jennie Jorgenson, Mark Mehos, and Paul Denholm. A comparison of price-taker and production cost models for determining system value, revenue, and scheduling of concentrating solar power plants. *Applied Energy*, 231:854–865, 2018. ISSN 0306-2619.

[22] Oelof AJ de Meyer, Frank Dinter, and Saneshan Govender. Optimisation in operating strategies for concentrating solar power plants. *Renewable Energy Focus*, 30:78–91, 2019.

[23] Hongtao Liu, Rongrong Zhai, Jiaxin Fu, Yulong Wang, and Yongping Yang. Optimization study of thermal-storage PV-CSP integrated system based on GA-PSO algorithm. *Solar Energy*, 184:391–409, 2019.

[24] Michael J. Wagner, William T. Hamilton, Alexandra Newman, Jolyon Dent, Charles Diep, and Robert Braun. Optimizing dispatch for a concentrated solar power tower. *Solar Energy*, 174: 1198–1211, November 2018. ISSN 0038-092X.

[25] William T Hamilton, Mark A Husted, Alexandra M Newman, Robert J Braun, and Michael J Wagner. Dispatch optimization of concentrating solar power with utility-scale photovoltaics. *Optimization and Engineering*, 21(1):335–369, 2020. ISSN 1389-4420.

[26] William T Hamilton, Alexandra M Newman, Michael J Wagner, and Robert J Braun. Off-design performance of molten salt-driven Rankine cycles and its impact on the optimal dispatch of concentrating solar power systems. *Energy Conversion and Management*, 220, 2020. ISSN 0196-8904.

[27] Jesse G. Wales, Alexander J. Zolan, William T. Hamilton, Alexandra M. Newman, and Michael J. Wagner. Using simulation to inform policies derived from a concentrating solar power plant dispatch optimization model. *OR Spectrum*, 2022. Accepted.

[28] Janna Martinek, Michael Wagner, Alexander Zolan, Matthew Boyd, Alexandra Newman, David Morton, Sven Leyffer, and Jeffrey Larson. Design, Analysis, and Operations Toolkit (DAO-Tk). Technical report, National Renewable Energy Laboratory, Golden, CO (United States); Argonne National Laboratory, Argonne, IL (United States), 2019.

[29] Yong Yang, Su Guo, Deyou Liu, Rong Li, and Yinghao Chu. Operation optimization strategy for wind-concentrated solar power hybrid power generation system. *Energy Conversion and Management*, 160:243–250, 2018. ISSN 0196-8904.

[30] Rong Li, Su Guo, Yong Yang, and Deyou Liu. Optimal sizing of wind/concentrated solar plant/electric heater hybrid renewable energy system based on two-stage stochastic programming. *Energy*, 209:118472, 2020.

[31] Michael S Scioletti, Alexandra M Newman, Johanna K Goodman, Alexander J Zolan, and Sven Leyffer. Optimal design and dispatch of a system of diesel generators, photovoltaics and batteries for remote locations. *Optimization and Engineering*, 18(3):755–792, 2017. ISSN 1389-4420.

[32] Gavin Goodall, Michael Scioletti, Alex Zolan, Bharatkumar Suthar, Alexandra Newman, and Paul Kohl. Optimal design and dispatch of a hybrid microgrid system capturing battery fade. *Optimization and Engineering*, 20(1):179–213, 2019. ISSN 1389-4420.

[33] Garth P. McCormick. Computability of global solutions to factorable nonconvex programs: Part I - Convex underestimating problems. *Mathematical Programming*, 10(1):147–175, 1976.

[34] Nikolaos V Sahinidis. Mixed-integer nonlinear programming 2018. *Optimization and Engineering*, 20 (2):301–306, 2019. ISSN 1389-4420.

[35] Kevin Ellingwood, Kasra Mohammadi, and Kody Powell. Dynamic optimization and economic evaluation of flexible heat integration in a hybrid concentrated solar power plant. *Applied Energy*, 276:115513, 2020. ISSN 0306-2619.

[36] Landen Blackburn, Aaron Young, Pratt Rogers, John Hedengren, and Kody Powell. Dynamic optimization of a district energy system with storage using a novel mixed-integer quadratic programming algorithm. *Optimization and Engineering*, 20(2):575–603, 2019. ISSN 1389-4420.

[37] Alexander W Dowling, Tian Zheng, and Victor M Zavala. A decomposition algorithm for simultaneous scheduling and control of CSP systems. *AIChE Journal*, 64(7):2408–2417, 2018.

[38] Farinaz Behrooz, Norman Mariun, Mohammad Hamiruce Marhaban, Mohd Amran Mohd Radzi, and Abdul Rahman Ramli. Review of control techniques for HVAC systems—nonlinearity approaches based on fuzzy cognitive maps. *Energies*, 11(3):495, 2018.

[39] Amy Van Asselt, Douglas T Reindl, and Gregory F Nellis. Policy recommendations for using cool thermal energy storage to increase grid penetration of renewable power sources (1607-rp). *Science and Technology for the Built Environment*, 24(7):759–769, 2018.

[40] Rubén M Montañés, Stefanía Ó GarDarsdóttir, Fredrik Normann, Filip Johnsson, and Lars O Nord. Demonstrating load-change transient performance of a commercial-scale natural gas combined cycle power plant with post-combustion CO_2 capture. *International Journal of Greenhouse Gas Control*, 63:158–174, 2017.

[41] Andreas Olympios, Josh McTigue, Pau Farres Antunez, Alessio Tafone, Alessandro Romagnoli, Yongliang Li, Yulong Ding, Wolf-Dieter Steinmann, Liang Wang, Haisheng Chen, et al. Progress and prospects of thermo-mechanical energy storage–a critical review. *Progress in Energy*, 2021.

[42] C E Gounaris, R Misener, and C A Floudas. Computational comparison of piecewise-linear relaxations for pooling problems. *Industrial & Engineering Chemistry Research*, 48:5742–5766, 2009.

[43] Harsha Nagarajan, Mowen Lu, Emre Yamangil, and Russell Bent. Tightening McCormick relaxations for nonlinear programs via dynamic multivariate partitioning. In *International Conference on Principles and Practice of Constraint Programming*, pages 369–387. Springer, 2016.

[44] Harsha Nagarajan, Mowen Lu, Site Wang, Russell Bent, and Kaarthik Sundar. An adaptive, multivariate partitioning algorithm for global optimization of nonconvex programs. *Journal of Global Optimization*, pages 1–37, 2019. doi: 10.1007/s10898-018-00734-1.

[45] Alexander J Zolan, Michael S Scioletti, David P Morton, and Alexandra M Newman. Decomposing loosely coupled mixed-integer programs for optimal microgrid design. *INFORMS Journal on Computing*, 2021. doi: 10.1287/ijoc.2020.0955.

[46] Francisco Trespalacios and Ignacioè. Grossmann. Review of mixed-integer nonlinear and generalized disjunctive programming methods. *Chemie Ingenieur Technik*, 86(7):991–1012, 2014.

[47] Pietro Belotti, Christian Kirches, Sven Leyffer, Jeff Linderoth, James Luedtke, and Ashutosh Mahajan. Mixed-integer nonlinear optimization. *Acta Numerica*, 22:1–131, 2013. ISSN 0962-4929.

[48] N. Kumar, P. Besuner, S. Lefton, D. Agan, and D. Hilleman. Power plant cycling costs. Technical Report NREL/SR-5500-55433, 1046269, July 2012.

[49] Christos K Simoglou, Pandelis N Biskas, and Anastasios G Bakirtzis. Optimal self-scheduling of a thermal producer in short-term electricity markets by MILP. *IEEE Transactions on Power Systems*, 25(4):1965–1977, 2010. ISSN 0885-8950.

[50] AMPL. *AMPL Version 12.23.19*. AMPL Optimization LLC, 2019.

[51] LLC Gurobi Optimization. Gurobi optimizer reference manual, 2021. URL http://www.gurobi.com.

[52] NREL. System Advisor Model Simulation Core. https://github.com/NREL/ssc, 2021.

[53] Allan R. Starke, José M. Cardemil, Rodrigo Escobar, and Sergio Colle. Multi-objective optimization of hybrid CSP+PV system using genetic algorithm. *Energy*, 147:490–503, 2018. ISSN 0360-5442.

[54] Rongrong Zhai, Ying Chen, Hongtao Liu, Hao Wu, Yongping Yang, and Mohammad O. Hamdan. Optimal design method of a hybrid CSP-PV plant based on genetic algorithm considering the operation strategy. *International Journal of Photoenergy*, 2018, 2018. ISSN 1687529X.

[55] Adriana Zurita, Carlos Mata-Torres, Carlos Valenzuela, Carlos Felbol, José M. Cardemil, Amador M. Guzmán, and Rodrigo A. Escobar. Techno-economic evaluation of a hybrid CSP+PV plant integrated with thermal energy storage and a large-scale battery energy storage system for base generation. *Solar Energy*, 173:1262–1277, 2018. ISSN 0038-092X.

[56] Wesley Cole, A. Will Frazier, and Chad Augustine. Cost Projections for Utility-Scale Battery Storage: 2021 Update. Report, National Renewable Energy Laboratory, NREL/TP-6A20-79236, 2021.

[57] IRENA. Renewable Power Generation Costs in 2020. Report, International Renewable Energy Agency, Abu Dhabi, 2021. URL https://www.irena.org/publications/2021/Jun/Renewable-Power-Costs-in-2020.

[58] NREL. Hybrid optimization and performance platform. https://github.com/NREL/HOPP, 2022.

[59] Jennie Jorgenson. *Estimating the performance and economic value of multiple concentrating solar power technologies in a production cost model.* NREL/TP-6A20-58645. National Renewable Energy Laboratory, 2013.

[60] Juergen H. Peterseim, Stuart White, Amir Tadros, and Udo Hellwig. Concentrating solar power hybrid plants – enabling cost effective synergies. *Renewable Energy*, 67:178–185, 2014. ISSN 0960-1481. Renewable Energy for Sustainable Development and Decarbonisation.

[61] Santanu Pramanik and R.V. Ravikrishna. A review of concentrated solar power hybrid technologies. *Applied Thermal Engineering*, 127:602–637, 2017. ISSN 1359-4311.

[62] Xing Ju, Chao Xu, Yangqing Hu, Xue Han, Gaosheng Wei, and Xiaoze Du. A review on the development of photovoltaic/concentrated solar power (PV-CSP) hybrid systems. *Solar Energy Materials and Solar Cells*, 161:305–327, 2017. ISSN 0927-0248.

[63] Jennie L Jorgenson, Matthew A O'Connell, Paul L Denholm, Janna G Martinek, and Mark S Mehos. A guide to implementing concentrating solar power in production cost models. Technical report, National Renewable Energy Lab, Golden, CO (United States), 2018.

[64] Alfredo Peinado Gonzalo, Alberto Pliego Marugán, and Fausto Pedro García Márquez. A review of the application performances of concentrated solar power systems. *Applied Energy*, 255:113893, 2019.

[65] Duraisamy Ramalingam Rajendran, Esakkimuthu Ganapathy Sundaram, Paulraj Jawahar, Vaithilingam Sivakumar, Omid Mahian, and Evangelos Bellos. Review on influencing parameters in the performance of concentrated solar power collector based on materials, heat transfer fluids and design. *Journal of Thermal Analysis and Calorimetry*, 140(1):33–51, 2020.

[66] Dhyia Aidroos Baharoon, Hasimah Abdul Rahman, Wan Zaidi Wan Omar, and Saeed Obaid Fadhl. Historical development of concentrating solar power technologies to generate clean electricity efficiently–a review. *Renewable and Sustainable Energy Reviews*, 41:996–1027, 2015.

[67] Tarik Bouhal, Y Agrouaz, Tarik Kousksou, A Allouhi, T El Rhafiki, A Jamil, and M Bakkas. Technical feasibility of a sustainable Concentrated Solar Power in Morocco through an energy analysis. *Renewable and Sustainable Energy Reviews*, 81:1087–1095, 2018.

[68] Md Tasbirul Islam, Nazmul Huda, A.B. Abdullah, and R. Saidur. A comprehensive review of state-of-the-art concentrating solar power (CSP) technologies: Current status and research trends. *Renewable and Sustainable Energy Reviews*, 91:987–1018, 2018. ISSN 1364-0321.

[69] Mohanad Salih Mahdi and Ahmed Fakhrey Khudheyer. Central receivers design in concentrated solar thermal power plants: A review. In *IOP Conference Series: Materials Science and Engineering*, volume 1094, page 012018. IOP Publishing, 2021.

[70] Matthew Neber and Hohyun Lee. Design of a high temperature cavity receiver for residential scale concentrated solar power. *Energy*, 47(1):481–487, 2012.

[71] Olivier Farges, Jean-Jacques Bézian, Hélène Bru, Mouna El Hafi, Richard Fournier, and Christophe Spiesser. Life-time integration using Monte Carlo Methods when optimizing the design of concentrated solar power plants. *Solar Energy*, 113:57–62, 2015.

[72] Mohamed Rady, Amr Amin, and Mohamed Ahmed. Conceptual design of small scale multi-generation concentrated solar plant for a medical center in Egypt. *Energy Procedia*, 83: 289–298, 2015.

[73] J Yan, YD Peng, ZR Cheng, FM Liu, and XH Tang. Design and implementation of a 38 kW dish-Stirling concentrated solar power system. In *IOP Conference series: earth and environmental science*, volume 93, page 012052. IOP Publishing, 2017.

[74] Darvesh Beegun, Diksha Juggurnath, M Khalil Elahee, and Abdel Khoodaruth. Design of a concentrated solar power hybrid system for electricity production for a textile manufacturing plant. In *2019 7th International Renewable and Sustainable Energy Conference (IRSEC)*, pages 1–6. IEEE, 2019.

[75] Nurettin Sezer, Yusuf Biçer, and Muammer Koç. Design and analysis of an integrated concentrated solar and wind energy system with storage. *International Journal of Energy Research*, 43(8): 3263–3283, 2019.

[76] Allan R Starke, José M Cardemil, Rodrigo A Escobar, and Sergio Colle. Assessing the performance of hybrid CSP + PV plants in northern Chile. *Solar Energy*, 138:88–97, 2016.

[77] R. Bravo and D. Friedrich. Two-stage optimisation of hybrid solar power plants. *Solar Energy*, 164: 187–199, 2018. ISSN 0038-092X.

[78] Adriana Zurita, Carlos Mata-Torres, José M. Cardemil, and Rodrigo A. Escobar. Assessment of time resolution impact on the modeling of a hybrid CSP-PV plant: A case of study in Chile. *Solar Energy*, 202:553–570, 2020. ISSN 0038-092X.

[79] Jingze Yang, Zhen Yang, and Yuanyuan Duan. Novel design optimization of concentrated solar power plant with S-CO2 Brayton cycle based on annual off-design performance. *Applied Thermal Engineering*, 192:116924, 2021.

[80] Mohamed E Zayed, Jun Zhao, Ammar H Elsheikh, Wenjia Li, and Mohamed Abd Elaziz. Optimal design parameters and performance optimization of thermodynamically balanced dish/stirling concentrated solar power system using multi-objective particle swarm optimization. *Applied Thermal Engineering*, 178:115539, 2020.

[81] Seyed Hossein Madaeni, Ramteen Sioshansi, and Paul Denholm. Estimating the capacity value of concentrating solar power plants with thermal energy storage: A case study of the Southwestern United States. *IEEE Transactions on Power Systems*, 28(2):1205–1215, 2013.

[82] J. Jorgenson, P. Denholm, and M. Mehos. Estimating the value of utility-scale solar technologies in California under a 40% renewable portfolio standard. Technical Report NREL/TP-6A20-61685, 2014.

[83] G Kahvecioğlu, D P Morton, and M J Wagner. Dispatch optimization of a concentrating solar power system under uncertain solar irradiance and energy prices. Technical report, 2021.

[84] Luis Miguel Rios and Nikolaos V Sahinidis. Derivative-free optimization: a review of algorithms and comparison of software implementations. *Journal of global optimization*, 56(3):1247–1293, 2013. ISSN 0925-5001.

[85] Jeffrey Larson, Matt Menickelly, and Stefan M. Wild. Derivative-free optimization methods. *Acta Numerica*, 28:287–404, 2019.

[86] Angela Dean, Daniel Voss, and Danel Draguljić. Computer experiments. In *Springer Texts in Statistics*, pages 765–791. Springer International Publishing, 2017.

[87] Yann Collette, Nikolaus Hansen, Gilles Pujol, Daniel Salazar Aponte, and Rodolphe Le Riche. Object-oriented programming of optimizers - examples in scilab. In *Multidisciplinary Design Optimization in Computational Mechanics*, pages 499–538. John Wiley & Sons, Inc., 2013.

[88] Jeffrey Larson and Stefan M. Wild. A batch, derivative-free algorithm for finding multiple local minima. *Optimization and Engineering*, 17(1):205–228, 2015.

[89] Patricia D. Hough, Tamara G. Kolda, and Virginia J. Torczon. Asynchronous parallel pattern search for nonlinear optimization. *SIAM Journal on Scientific Computing*, 23(1):134–156, 2001.

[90] Michael J Wagner and Tim Wendelin. SolarPILOT: A power tower solar field layout and characterization tool. *Solar Energy*, 171(C):185–196, 2018. ISSN 0038-092X.

[91] NREL. PySAM version 2.2.1., 2021. URL https://github.com/nrel/pysam. Accessed: 2022-03-25.

[92] Trieu Mai, Matthew Mowers, and Kelly Eurek. Competitiveness metrics for electricity system technologies. Technical report, National Renewable Energy Laboratory, NREL/TP-6A20-72549, 2021.

[93] W Short, D J Packey, and T Holt. A manual for the economic evaluation of energy efficiency and renewable energy technologies. Technical Report NREL/TP-462-5173, 1995. URL http://www.nrel.gov/docs/legosti/old/5173.pdf.

[94] William T. Hamilton, Janna Martinek, Paul Denholm, John Cox, and Alexandra Newman. Integrating concentrating solar power technologies into the hybrid optimization and performance platform (HOPP). Technical Report NREL/TBD, 2022. pending.

[95] Andrew Lee, Jaffer H. Ghouse, John C. Eslick, Carl D. Laird, John D. Siirola, Miguel A. Zamarripa, Dan Gunter, John H. Shinn, Alexander W. Dowling, Debangsu Bhattacharyya, Lorenz T. Biegler, Anthony P. Burgard, and David C. Miller. The idaes process modeling framework and model library—flexibility for process simulation and optimization. *Journal of Advanced Manufacturing and Processing*, 3(3), 2021. ISSN 2637-403X.

[96] Fernando Nogueira. Bayesian Optimization: Open source constrained global optimization tool for Python, 2014. URL https://github.com/fmfn/BayesianOptimization.

[97] Python Software Foundation. Python language reference, version 3.8. https://www.python.org/, 2021.

[98] Michael L. Bynum, Gabriel A. Hackebeil, William E. Hart, Carl D. Laird, Bethany L. Nicholson, John D. Siirola, Jean-Paul Watson, and David L. Woodruff. *Pyomo–optimization modeling in Python*, volume 67. Springer Science & Business Media, third edition, 2021.

[99] Manajit Sengupta, Yu Xie, Anthony Lopez, Aron Habte, Galen Maclaurin, and James Shelby. The national solar radiation data base (NSRDB). *Renewable and Sustainable Energy Reviews*, 89:51–60, 2018. ISSN 1364-0321.

[100] Cal Fire. 2020 incident archive, 2020. URL https://www.fire.ca.gov/incidents/2020/. Accessed: 2022-03-25.

[101] Paul Denholm and Maureen Hand. Grid flexibility and storage required to achieve very high penetration of variable renewable electricity. *Energy Policy*, 39(3):1817–1830, 2011. ISSN 0301-4215.

[102] John L. Cox, William T. Hamilton, Alexandra M. Newman, and Janna Martinek. Optimal sizing and dispatch of solar power with storage. *Optimization and Engineering*, TBD(TBD):TBD, 2022.

[103] Paul Gauché, Justine Rudman, Mbalenhle Mabaso, Willem A. Landman, Theodor W. von Backström, and Alan C. Brent. System value and progress of CSP. *Solar Energy*, 152:106–139, 2017. ISSN 0038-092X. Progress in Solar Energy Special Issue: Concentrating Solar Power (CSP).

[104] P. Richter, T. Trimborn, and L. Aldenhoff. Predictive storage strategy for optimal design of hybrid CSP-PV plants with immersion heater. *Solar Energy*, 218:237–250, 2021. ISSN 0038-092X.

[105] Carlos Mata-Torres, Patricia Palenzuela, Diego-César Alarcón-Padilla, Adriana Zurita, José M. Cardemil, and Rodrigo A. Escobar. Multi-objective optimization of a concentrating solar power+photovoltaic+multi-effect distillation plant: Understanding the impact of the solar irradiation and the plant location. *Energy Conversion and Management: X*, 11:100088, sep 2021.

[106] Su Guo, Yi He, Huanjin Pei, and Shuyan Wu. The multi-objective capacity optimization of wind-photovoltaic-thermal energy storage hybrid power system with electric heater. *Solar Energy*, 195:138–149, 2020.

[107] G. Iaquaniello, W. Montanari, and A. Salladini. Standalone CSP-DG system for electrification of remote areas and desalinated water supply. *Solar Energy*, 157:1056–1063, 2017. ISSN 0038-092X.

[108] Nipun Goel, Hannah O'Hern, Matthew Orosz, and Todd Otanicar. Annual simulation of photovoltaic retrofits within existing parabolic trough concentrating solar powerplants. *Solar Energy*, 211:600–612, 2020.

[109] Tianye Liu, Jingze Yang, Zhen Yang, and Yuanyuan Duan. Techno-economic feasibility of solar power plants considering PV/CSP with electrical/thermal energy storage system. *Energy Conversion and Management*, 255:115308, 2022. ISSN 0196-8904.

[110] J.A. Aguilar-Jiménez, N. Velázquez, A. Acuña, R. Cota, E. González, L. González, R. López, and S. Islas. Techno-economic analysis of a hybrid PV-CSP system with thermal energy storage applied to isolated microgrids. *Solar Energy*, 174:55–65, 2018. ISSN 0038-092X.

[111] Mario Petrollese and Daniele Cocco. Optimal design of a hybrid CSP-PV plant for achieving the full dispatchability of solar energy power plants. *Solar Energy*, 137:477–489, 2016. ISSN 0038-092X.

[112] Michael J. Wagner, Alexandra Newman, David Morton, and Sven Leyffer. Concurrent optimization of capital cost and expected o&m. Technical Report NREL/TP-5700-79093, 2 2021.

[113] Nate Blair, Nicholas DiOrio, Janine Freeman, Paul Gilman, Steven Janzou, Ty Neises, and Michael Wagner. NREL/TP ; 6A20-70414. National Renewable Energy Laboratory, 2018.

[114] John L. Cox, William T. Hamilton, Alexandra M. Newman, Michael J. Wagner, and Alex J. Zolan. Real-time dispatch optimization for concentrating solar power with thermal energy storage. *Optimization and Engineering*, 2(9711), Feb 2022.

[115] CNRFC NOAA. Heavy precipitation event California and Nevada December 16 - 23, 2010, 2010. URL https://www.cnrfc.noaa.gov/storm_summaries/dec2010storms.php. Accessed: 2022-03-25.

[116] Paul Denholm and Robert Margolis. The Potential for Energy Storage to Provide Peaking Capacity in California under Increased Penetration of Solar Photovoltaics. Report, National Renewable Energy Laboratory, NREL/TP-6A20-70905, 2018.

[117] Ramteen Sioshansi, Seyed Hossein Madaeni, and Paul Denholm. A dynamic programming approach to estimate the capacity value of energy storage. *IEEE Transactions on Power Systems*, 29(1): 395–403, 2014.

[118] Germán Morales-España, Jesus M. Latorre, and Andres Ramos. Tight and compact MILP formulation of start-up and shut-down ramping in unit commitment. *IEEE Transactions on Power Systems*, 28(2):1288–1296, 2013. ISSN 08858950.

[119] L. L Garver. Power generation scheduling by integer programming-Development of theory. *Transactions of the American Institute of Electrical Engineers. Part 3, Power apparatus and systems*, 81(3):730–734, 1962. ISSN 0097-2460.

[120] Paul Gilman, Steven Janzou, Darice Guittet, Janine Freeman, Nicholas DiOrio, Nathan Blair, Matthew Boyd, Ty Neises, Michael Wagner, USDOE Office of Energy Efficiency, and Renewable Energy. PySAM (Python wrapper for system advisor model "SAM"), 2020.

[121] A Dobos. Pvwatts version 5 manual. Technical Report TP-6A20-62641, 2014. URL http://www.nrel.gov/docs/fy14osti/62641.pdf.

APPENDIX A

COMPLETE FORMULATION

We provide here the complete problem formulation ($\mathcal{R}$), the balance of which does not appear in §2.3 and mimics, to a large extent, the model given in Wagner et al. [12], which is linear, reflecting the assumption that there is no differentiation between the hot and cold sides of the thermal energy storage component of our concentrated solar power tower system. We highlight any additions and modifications to the Wagner et al. [12] formulation in dark blue and light blue, respectively, while the constructs we retain from that formulation remain in black font. We first define the outstanding notation:

Table A.1 Real-time dispatch model, ($\mathcal{R}$), remaining notation.

Time-indexed Parameters		Units
Δ^{e}_t	Cumulative time elapsed at the end of period t; i.e., $\Delta^{\mathrm{e}}_t = \sum_{t'=1}^{t} \Delta_{t'}$	h
$W^{\mathrm{u}^+}_t$	Maximum power production when starting generation in period t	$\mathrm{kW_e/h}$
$W^{\mathrm{u}^-}_t$	Maximum power production in period t when stopping generation in period $t+1$	$\mathrm{kW_e/h}$

Power Cycle Parameters		Units
$\dot{W}^{\delta^+}$	Power cycle ramp-up designed limit	$\mathrm{kW_e/h}$
$\dot{W}^{\delta^-}$	Power cycle ramp-down designed limit	$\mathrm{kW_e/h}$
Y^{d}	Minimum required power cycle down-time	h
Y^{u}	Minimum required power cycle up-time	h

Time-indexed Binary Decision Variables	
y^{cge}_t	1 if cycle stops electric power generation at period $t \in \mathcal{T}$; 0 otherwise

Real-time Dispatch Model Objective Function

$$
\begin{aligned}
(\mathcal{R})\ \ \text{maximize}\quad & \sum_{t\in\mathcal{T}} \Bigg[D_t \Delta_t P_t \left(\dot{w}_t^{\mathrm{s}} - \dot{w}_t^{\mathrm{p}}\right) \\
& - \frac{1}{D_t}\bigg[\Big(C^{\mathrm{csu}} y_t^{\mathrm{csup}} + C^{\mathrm{chsp}} y_t^{\mathrm{chsp}} + \alpha y_t^{\mathrm{csdp}} \Big) \\
& \quad + \Big(C^{\delta\mathrm{W}} (\dot{w}_t^{\delta^+} + \dot{w}_t^{\delta^-}) + C^{\mathrm{vW}} (\dot{w}_t^{\mathrm{v}^+} + \dot{w}_t^{\mathrm{v}^-}) \Big) \\
& \quad + \Big(C^{\mathrm{rsu}} y_t^{\mathrm{rsup}} + C^{\mathrm{rhsp}} y_t^{\mathrm{rhsp}} + \alpha (y_t^{\mathrm{rsb}} + y_t^{\mathrm{rsdp}}) \Big) \\
& \quad + \Delta_t \Big(C^{\mathrm{c}} \dot{w}_t + C^{\mathrm{csb}} y_t^{\mathrm{csb}} + C^{\mathrm{r}} x_t^{\mathrm{r}} \Big) \bigg] \Bigg] \\
& + \hat{P} \eta^{\mathrm{D}} \hat{s}
\end{aligned}
\tag{2.1}
$$

Receiver Start-up, See §A.1

$$d_t^{\mathrm{rsu}} \le d_{t-1}^{\mathrm{rsu}} + \Delta_t f_t^{\mathrm{rsu}} \quad \forall\, t \in \mathcal{T} \tag{2.2a}$$

$$d_t^{\mathrm{rsu}} \le D^{\mathrm{rsu}} y_t^{\mathrm{rsu}} \quad \forall\, t \in \mathcal{T} \tag{2.2b}$$

$$D^{\mathrm{rsu}} y_t^{r} \le d_t^{\mathrm{rsu}} + D^{\mathrm{rsu}} \left(y_{t-1}^{\mathrm{r}} + y_{t-1}^{\mathrm{rsb}} \right) \quad \forall\, t \in \mathcal{T} \tag{2.2c}$$

$$u_t^{\mathrm{rsu}} \le u_{t-1}^{\mathrm{rsu}} + \Delta_t \min \left\{ Q_t^{\mathrm{in}} f_t^{\mathrm{rsu}},\ Q^{\mathrm{ru}} \right\} \quad \forall\, t \in \mathcal{T} \tag{2.2d}$$

$$u_t^{\mathrm{rsu}} \le E^{\mathrm{rsu}} y_t^{\mathrm{rsu}} \quad \forall\, t \in \mathcal{T} \tag{2.2e}$$

$$E^{\mathrm{rsu}} y_t^{r} \le u_t^{\mathrm{rsu}} + E^{\mathrm{rsu}} \left(y_{t-1}^{\mathrm{r}} + y_{t-1}^{\mathrm{rsb}} \right) \quad \forall\, t \in \mathcal{T} \tag{2.2f}$$

$$f_t^{\mathrm{rsu}} \le y_t^{\mathrm{rsu}} \quad \forall\, t \in \mathcal{T} \tag{2.2g}$$

$$f_t^{\mathrm{rsu}} \ge y_t^{\mathrm{rsu}} - y_t^{\mathrm{r}} \quad \forall\, t \in \mathcal{T} \tag{2.2h}$$

Receiver Collection Energy Balance, See §A.2

$$x_t^{\mathrm{r}} \le Q_t^{\mathrm{in}} \min \left\{ 1 - f_t^{\mathrm{rsu}},\ y_t^{\mathrm{r}},\ 1 - f_t^{\mathrm{rsd}} \right\} \quad \forall\, t \in \mathcal{T} \tag{2.3a}$$

$$x_t^{\mathrm{r}} \ge Q^{\mathrm{rl}} \left(y_t^{\mathrm{r}} - f_t^{\mathrm{rsu}} - f_t^{\mathrm{rsd}} \right) \quad \forall\, t \in \mathcal{T} \tag{2.3b}$$

Receiver Shutdown, See §A.3

$$d_t^{\mathrm{rsd}} \le d_{t-1}^{\mathrm{rsd}} + \Delta_t f_t^{\mathrm{rsd}} \quad \forall\, t \in \mathcal{T} \tag{2.4a}$$

$$d_t^{\mathrm{rsd}} \le D^{\mathrm{rsd}} y_t^{\mathrm{rsd}} \quad \forall\, t \in \mathcal{T} \tag{2.4b}$$

$$D^{\mathrm{rsd}} y_t^{\mathrm{rsd}} \ge D^{\mathrm{rsd}} y_{t-1}^{\mathrm{rsd}} - d_{t-1}^{\mathrm{rsd}} \quad \forall\, t \in \mathcal{T} \tag{2.4c}$$

$$u_t^{\mathrm{rsd}} \le u_{t-1}^{\mathrm{rsd}} + \Delta_t Q_t^{\mathrm{in}} f_t^{\mathrm{rsd}} \quad \forall\, t \in \mathcal{T} \tag{2.4d}$$

$$u_t^{\mathrm{rsd}} \le E^{\mathrm{rsd}} y_t^{\mathrm{rsd}} \quad \forall\, t \in \mathcal{T} \tag{2.4e}$$

$$E^{\mathrm{rsd}} y_t^{\mathrm{rsd}} \ge E^{\mathrm{rsd}} y_{t-1}^{\mathrm{rsd}} - u_{t-1}^{\mathrm{rsd}} \quad \forall\, t \in \mathcal{T} \tag{2.4f}$$

$$f_t^{\mathrm{rsd}} \le y_t^{\mathrm{rsd}} \quad \forall\, t \in \mathcal{T} \tag{2.4g}$$

$$f_t^{\mathrm{rsd}} \ge y_t^{\mathrm{rsd}} - y_t^{\mathrm{r}} \quad \forall\, t \in \mathcal{T} \tag{2.4h}$$

Receiver Mass Flow Rate, See §A.4

$$\dot{m}_t^{\text{rcs}} + \dot{m}_t^{\text{rhs}} \leq \overline{\dot{M}}^{\text{r}} \min\left\{1,\ y_t^{\text{rsu}} + y_t^{\text{r}} + y_t^{\text{rsb}}\right\} \quad \forall\, t \in \mathcal{T}^{\text{N}} \tag{2.5a}$$

$$\dot{m}_t^{\text{rcs}} + \dot{m}_t^{\text{rhs}} \geq \underline{\dot{M}}^{\text{r}} \max\left\{f_t^{\text{rsu}},\ y_t^{\text{r}} - f_t^{\text{rsd}} + y_t^{\text{rsb}}\right\} \quad \forall\, t \in \mathcal{T}^{\text{N}} \tag{2.5b}$$

$$\dot{m}_t^{\text{rcs}} \leq \overline{\dot{M}}^{\text{r}} \left(f_t^{\text{rsu}} + y_t^{\text{rsb}}\right) \quad \forall\, t \in \mathcal{T}^{\text{N}} \tag{2.5c}$$

$$\dot{m}_t^{\text{rhs}} \leq \overline{\dot{M}}^{\text{r}} y_t^{\text{r}} \quad \forall\, t \in \mathcal{T}^{\text{N}} \tag{2.5d}$$

Receiver Outlet Temperature, See §A.5

$$\mathrm{T}_t^{\text{rout}} \leq \bar{T}^{\text{rout}} \min\left\{1,\ y_t^{\text{rsu}} + y_t^{\text{r}} + y_t^{\text{rsb}}\right\} \quad \forall\, t \in \mathcal{T}^{\text{N}} \tag{2.6a}$$

$$\mathrm{T}_t^{\text{rout}} \geq \underline{T}^{\text{cs}} \max\left\{y_t^{\text{rsu}},\ y_t^{\text{r}} + y_t^{\text{rsb}}\right\} \quad \forall\, t \in \mathcal{T}^{\text{N}} \tag{2.6b}$$

Receiver Power Balance, See §A.6

$$x_t^{\text{r}} - Q^{\text{rsb}} y_t^{\text{rsb}} = C^{\text{p}} \left(\dot{m}_t^{\text{rcs}} + \dot{m}_t^{\text{rhs}}\right) \left(\mathrm{T}_t^{\text{rout}} - \mathrm{T}_t^{\text{cs}}\right) \quad \forall\, t \in \mathcal{T}^{\text{N}} \tag{2.7a}$$

$$x_t^{\text{r}} \leq F_t C^{\text{p}} \left(\dot{m}_t^{\text{rcs}} + \dot{m}_t^{\text{rhs}}\right) \left(\bar{T}^{\text{rout}} - \mathrm{T}_t^{\text{cs}}\right) \quad \forall\, t \in \mathcal{T}^{\text{N}} \tag{2.7b}$$

Receiver Penalties, See §A.7

$$y_t^{\text{rsup}} \geq y_t^{\text{rsu}} - y_{t-1}^{\text{rsu}} \quad \forall\, t \in \mathcal{T} \tag{A.1a}$$

$$y_t^{\text{rhsp}} \geq y_t^{\text{r}} - \left(1 - y_{t-1}^{\text{rsb}}\right) \quad \forall\, t \in \mathcal{T} \tag{A.1b}$$

$$y_t^{\text{rsdp}} \geq y_{t-1}^{\text{rsd}} - y_t^{\text{rsd}} \quad \forall\, t \in \mathcal{T} \tag{A.1c}$$

Logic Associated with Receiver Modes, See §A.8

$$y_t^{\text{rsu}} + y_t^{\text{rsd}} \leq 1 \quad \forall\, t \in \mathcal{T} : Q_t^{\text{in}} > 0 \tag{A.2a}$$

$$y_t^{\text{rsu}} + y_t^{\text{rsd}} \leq 0 \quad \forall\, t \in \mathcal{T} : Q_t^{\text{in}} = 0 \tag{A.2b}$$

$$y_t^{\text{rsu}} + y_{t-1}^{\text{r}} \leq 1 \quad \forall\, t \in \mathcal{T} \tag{A.2c}$$

$$y_t^{\text{rsu}} + y_{t-1}^{\text{rsb}} \leq 1 \quad \forall\, t \in \mathcal{T} \tag{A.2d}$$

$$y_t^{\text{rsu}} + y_t^{\text{rsb}} + y_t^{\text{rsd}} \leq 1 \quad \forall\, t \in \mathcal{T} \tag{A.2e}$$

$$Q^{\text{rl}} y_t^{\text{r}} \leq Q_t^{\text{in}} \quad \forall\, t \in \mathcal{T} \tag{A.2f}$$

$$y_t^{\text{r}} + y_t^{\text{rsb}} \leq 1 \quad \forall\, t \in \mathcal{T} \tag{A.2g}$$

$$y_t^{\text{rsb}} \leq y_{t-1}^{\text{r}} + y_{t-1}^{\text{rsb}} \quad \forall\, t \in \mathcal{T} \tag{A.2h}$$

$$y_t^{\text{rsd}} \geq (y_t^{\text{r}} - y_{t+1}^{\text{r}}) + (y_t^{\text{rsb}} - y_{t+1}^{\text{rsb}}) \quad \forall\, t \in \mathcal{T} : t < |\mathcal{T}| \tag{A.2i}$$

$$y_t^{\text{r}} + y_{t-1}^{\text{rsd}} \leq 1 \quad \forall\, t \in \mathcal{T} \tag{A.2j}$$

Initial and Transition Energy, See §A.9

$$s_0 = C^{\text{p}}(m_t^{\text{hs}} - \underline{M}^{\text{hs}})(\mathrm{T}_t^{\text{hs}} - \underline{T}^{\text{cs}}), \quad t = |\mathcal{T}^{\text{N}}| \tag{2.8a}$$

$$\hat{s} = \gamma^{t+1} s_t, \quad t = |\mathcal{T}| \tag{2.8b}$$

Mass Balance, See §A.10

$$m_t^{\mathrm{cs}} = m_{t-1}^{\mathrm{cs}} + \Delta_t \left(\dot{m}_t^{\mathrm{c}} - \dot{m}_t^{\mathrm{rhs}} \right) \quad \forall\, t \in \mathcal{T}^{\mathrm{N}} \tag{2.9a}$$

$$m_t^{\mathrm{hs}} = m_{t-1}^{\mathrm{hs}} + \Delta_t \left(\dot{m}_t^{\mathrm{rhs}} - \dot{m}_t^{\mathrm{c}} \right) \quad \forall\, t \in \mathcal{T}^{\mathrm{N}} \tag{2.9b}$$

Energy Balance, See §A.11

$$\begin{aligned} m_t^{\mathrm{cs}} \mathrm{T}_t^{\mathrm{cs}} = m_{t-1}^{\mathrm{cs}} \mathrm{T}_{t-1}^{\mathrm{cs}} + \Delta_t \Big[& (\dot{m}_t^{\mathrm{c}} \mathrm{T}_t^{\mathrm{cout}} + \dot{m}_t^{\mathrm{rcs}} \mathrm{T}_t^{\mathrm{rout}}) \\ & - (\dot{m}_t^{\mathrm{rcs}} + \dot{m}_t^{\mathrm{rhs}}) \mathrm{T}_t^{\mathrm{cs}} \Big] \quad \forall\, t \in \mathcal{T}^{\mathrm{N}} \end{aligned} \tag{2.10a}$$

$$m_t^{\mathrm{hs}} \mathrm{T}_t^{\mathrm{hs}} = m_{t-1}^{\mathrm{hs}} \mathrm{T}_{t-1}^{\mathrm{hs}} + \Delta_t \left(\dot{m}_t^{\mathrm{rhs}} \mathrm{T}_t^{\mathrm{rout}} - \dot{m}_t^{\mathrm{c}} \mathrm{T}_t^{\mathrm{hs}} \right) \quad \forall\, t \in \mathcal{T}^{\mathrm{N}} \tag{2.10b}$$

$$s_t = s_{t-1} + \Delta_t \left[x_t^{\mathrm{r}} - \left(Q^{\mathrm{c}} y_t^{\mathrm{csu}} + x_t + Q^{\mathrm{rsb}} y_t^{\mathrm{rsb}} \right) \right] \quad \forall\, t \in \mathcal{T}^{\mathrm{L}} \tag{A.3}$$

Power Cycle Start-up, See §A.12

$$u_t^{\mathrm{csu}} \leq u_{t-1}^{\mathrm{csu}} + \Delta_t Q^{\mathrm{c}} y_t^{\mathrm{csu}} + \left(E^{\mathrm{c}} - E^{\mathrm{w}} \right) y_{t-1}^{\mathrm{csb}} \quad \forall\, t \in \mathcal{T} \tag{2.11a}$$

$$u_t^{\mathrm{csu}} \geq u_{t-1}^{\mathrm{csu}} + \Delta_t Q^{\mathrm{c}} y_t^{\mathrm{csu}} - E^{\mathrm{c}} y_t^{\mathrm{cgb}} \quad \forall\, t \in \mathcal{T} \tag{2.11b}$$

$$u_t^{\mathrm{csu}} \leq E^{\mathrm{c}} y_t^{\mathrm{csu}} \quad \forall\, t \in \mathcal{T} \tag{2.11c}$$

$$E^{\mathrm{c}} y_t \leq u_t^{\mathrm{csu}} + E^{\mathrm{c}} y_{t-1} \quad \forall\, t \in \mathcal{T} \tag{2.11d}$$

$$Q^{\mathrm{c}} y_t^{\mathrm{csu}} \leq C^{\mathrm{p}} \dot{m}_t^{\mathrm{c}} \left(\mathrm{T}_t^{\mathrm{hs}} - \mathrm{T}_t^{\mathrm{cout}} \right) + Q^{\mathrm{u}} (1 - y_t^{\mathrm{csu}}) \quad \forall\, t \in \mathcal{T}^{\mathrm{N}} \tag{2.11e}$$

$$Q^{\mathrm{c}} y_t^{\mathrm{csu}} \geq C^{\mathrm{p}} \dot{m}_t^{\mathrm{c}} \left(\mathrm{T}_t^{\mathrm{hs}} - \mathrm{T}_t^{\mathrm{cout}} \right) - Q^{\mathrm{u}} (1 - y_t^{\mathrm{csu}}) \quad \forall\, t \in \mathcal{T}^{\mathrm{N}} \tag{2.11f}$$

Power Cycle Thermal Input, See §A.13

$$x_t \leq Q^{\mathrm{u}} y_t \quad \forall\, t \in \mathcal{T}^{\mathrm{L}} \tag{2.12a}$$

$$x_t \leq Q^{\mathrm{u}} - K^{\mathrm{u}} \left(T^{\mathrm{D}} - \mathrm{T}_{t'}^{\mathrm{hs}} \right) \quad \forall\, t \in \mathcal{T}^{\mathrm{L}}, \quad t' = |\mathcal{T}^{\mathrm{N}}| \tag{2.12b}$$

$$x_t \geq Q^{\mathrm{l}} y_t - K^{\mathrm{l}} \left(T^{\mathrm{D}} - \mathrm{T}_{t'}^{\mathrm{hs}} \right) \quad \forall\, t \in \mathcal{T}^{\mathrm{L}}, \quad t' = |\mathcal{T}^{\mathrm{N}}| \tag{2.12c}$$

$$\mathrm{T}_t^{\mathrm{hs}} - \mathrm{T}_t^{\mathrm{cout}} \geq \left(\alpha^{\mathrm{b}} + \alpha^{\mathrm{T}} \mathrm{T}_t^{\mathrm{hs}} + \alpha^{\mathrm{m}} \dot{m}_t^{\mathrm{c}} \right) - \overline{\Delta T}^{\mathrm{c}} (1 - y_t) \quad \forall\, t \in \mathcal{T}^{\mathrm{N}} \tag{2.12d}$$

$$\mathrm{T}_t^{\mathrm{hs}} - \mathrm{T}_t^{\mathrm{cout}} \leq \left(\alpha^{\mathrm{b}} + \alpha^{\mathrm{T}} \mathrm{T}_t^{\mathrm{hs}} + \alpha^{\mathrm{m}} \dot{m}_t^{\mathrm{c}} \right) + \overline{\Delta T}^{\mathrm{c}} (1 - y_t) \quad \forall\, t \in \mathcal{T}^{\mathrm{N}} \tag{2.12e}$$

Power Cycle Mass Flow Rate, See §A.14

$$\dot{m}_t^{\mathrm{c}} \leq \overline{\dot{M}}^{\mathrm{c}} (y_t^{\mathrm{csu}} + y_t) \quad \forall\, t \in \mathcal{T}^{\mathrm{N}} \tag{2.13a}$$

$$\dot{m}_t^{\mathrm{c}} \geq \underline{\dot{M}}^{\mathrm{c}} y_t \quad \forall\, t \in \mathcal{T}^{\mathrm{N}} \tag{2.13b}$$

Power Cycle Outlet Temperature, See §A.15

$$\mathrm{T}_t^{\mathrm{cout}} \leq \overline{T}^{\mathrm{cs}} \left(y_t + y_t^{\mathrm{csu}} \right) \quad \forall\, t \in \mathcal{T}^{\mathrm{N}} \tag{2.14a}$$

$$\mathrm{T}_t^{\mathrm{cout}} \geq \underline{T}^{\mathrm{cs}} \left(y_t + y_t^{\mathrm{csu}} \right) \quad \forall\, t \in \mathcal{T}^{\mathrm{N}} \tag{2.14b}$$

Power Cycle Electric Output, See §A.16

$$\dot{w}_t = \frac{\eta^{\mathrm{amb}}_t}{\eta^{\mathrm{D}}}\left[\eta^{\mathrm{p}} x_t + (\dot{W}^{\mathrm{u}} - \eta^{\mathrm{p}} Q^{\mathrm{u}}) y_t\right] \quad \forall\, t \in \mathcal{T}^{\mathrm{L}} \tag{2.15a}$$

$$\dot{w}_t \le \frac{\eta^{\mathrm{amb}}_t}{\eta^{\mathrm{D}}}\left[\beta^{\mathrm{b}} + \beta^{\mathrm{T}}\mathrm{T}^{\mathrm{hs}}_t + \beta^{\mathrm{m}}\dot{m}^{\mathrm{c}}_t + \beta^{\mathrm{mT}}\dot{m}^{\mathrm{c}}_t\mathrm{T}^{\mathrm{hs}}_t + \dot{W}^{\mathrm{u}}(1 - y_t)\right] \quad \forall\, t \in \mathcal{T}^{\mathrm{N}} \tag{2.15b}$$

$$\dot{w}_t \ge \frac{\eta^{\mathrm{amb}}_t}{\eta^{\mathrm{D}}}\left[\beta^{\mathrm{b}} + \beta^{\mathrm{T}}\mathrm{T}^{\mathrm{hs}}_t + \beta^{\mathrm{m}}\dot{m}^{\mathrm{c}}_t + \beta^{\mathrm{mT}}\dot{m}^{\mathrm{c}}_t\mathrm{T}^{\mathrm{hs}}_t - \dot{W}^{\mathrm{u}}(1 - y_t)\right] \quad \forall\, t \in \mathcal{T}^{\mathrm{N}} \tag{2.15c}$$

$$\dot{w}_t \le \dot{W}^{\mathrm{u}}\frac{\eta^{\mathrm{amb}}_t}{\eta^{\mathrm{D}}} y_t \quad \forall\, t \in \mathcal{T} \tag{2.15d}$$

$$\dot{w}_t \ge \dot{W}^{\mathrm{l}}\frac{\eta^{\mathrm{amb}}_t}{\eta^{\mathrm{D}}} y_t \quad \forall\, t \in \mathcal{T} \tag{2.15e}$$

Power Cycle Ramping, See §A.17

$$\dot{w}^{\delta^+}_t \ge \dot{w}_t - \dot{w}_{t-1} \quad \forall\, t \in \mathcal{T} \tag{A.4a}$$

$$\dot{w}^{\delta^-}_t \ge \dot{w}_{t-1} - \dot{w}_t \quad \forall\, t \in \mathcal{T} \tag{A.4b}$$

$$\dot{w}^{\delta^+}_t - \dot{w}^{\mathrm{v}^+}_t \le \Delta_t\left[\dot{W}^{\delta^+} + \left(\frac{\eta^{\mathrm{amb}}_t}{\eta^{\mathrm{D}}} W^{\mathrm{u}^+}_t - \dot{W}^{\delta^+}\right) y^{\mathrm{cgb}}_t\right] \quad \forall\, t \in \mathcal{T} \tag{A.4c}$$

$$\dot{w}^{\delta^-}_t - \dot{w}^{\mathrm{v}^-}_t \le \Delta_t\left[\dot{W}^{\delta^-} + \left(\frac{\eta^{\mathrm{amb}}_t}{\eta^{\mathrm{D}}} W^{\mathrm{u}^-}_t - \dot{W}^{\delta^-}\right) y^{\mathrm{cge}}_t\right] \quad \forall\, t \in \mathcal{T} \tag{A.4d}$$

Power Cycle Minimum Up-time and Down-time, See §A.18

$$y^{\mathrm{cgb}}_t - y^{\mathrm{cge}}_t = y_t - y_{t-1} \quad \forall\, t \in \mathcal{T} \tag{A.5a}$$

$$\sum_{t' \in \mathcal{T}: 0 \le \Delta^{\mathrm{e}}_t - \Delta^{\mathrm{e}}_{t'} \le Y^{\mathrm{u}}} y^{\mathrm{cgb}}_t \le y_t \quad \forall\, t \in \mathcal{T},\ \Delta^{\mathrm{e}}_t > (Y^{\mathrm{u}} - Y^{\mathrm{u}}_0) y_0 \tag{A.5b}$$

$$\sum_{t' \in \mathcal{T}: 0 \le \Delta^{\mathrm{e}}_t - \Delta^{\mathrm{e}}_{t'} \le Y^{\mathrm{d}}} y^{\mathrm{cge}}_t \le 1 - y_t \quad \forall\, t \in \mathcal{T},\ \Delta^{\mathrm{e}}_t > (Y^{\mathrm{d}} - Y^{\mathrm{d}}_0)(1 - y_0) \tag{A.5c}$$

$$y_t = y_0 \quad \forall\, t \in \mathcal{T},\ \Delta^{\mathrm{e}}_t \le \max\left\{(Y^{\mathrm{u}} - Y^{\mathrm{u}}_0) y_0, (Y^{\mathrm{d}} - Y^{\mathrm{d}}_0)(1 - y_0)\right\} \tag{A.5d}$$

Power Cycle Penalties, See §A.19

$$y^{\mathrm{csup}}_t \ge y^{\mathrm{csu}}_t - (y^{\mathrm{csu}}_{t-1} + y^{\mathrm{csb}}_{t-1}) \quad \forall\, t \in \mathcal{T} \tag{A.6a}$$

$$y^{\mathrm{chsp}}_t \ge y^{\mathrm{csu}}_t - (y^{\mathrm{csu}}_{t-1} + 1 - y^{\mathrm{csb}}_{t-1}) \quad \forall\, t \in \mathcal{T} \tag{A.6b}$$

$$y^{\mathrm{csdp}}_t \ge (y^{\mathrm{csu}}_{t-1} + y_{t-1} + y^{\mathrm{csb}}_{t-1}) - (y^{\mathrm{csu}}_t + y_t + y^{\mathrm{csb}}_t) \quad \forall\, t \in \mathcal{T} \tag{A.6c}$$

Logic Associated with Power Cycle Modes, See §A.20

$$y^{\mathrm{csu}}_t + y_t + y^{\mathrm{csb}}_t \le 1 \quad \forall\, t \in \mathcal{T} \tag{A.7a}$$

$$y^{\mathrm{csu}}_t + y_{t-1} \le 1 \quad \forall\, t \in \mathcal{T} \tag{A.7b}$$

$$y^{\mathrm{csb}}_t \le y_{t-1} + y^{\mathrm{csb}}_{t-1} \quad \forall\, t \in \mathcal{T} \tag{A.7c}$$

Power Cycle Operation Restriction, See §A.21

$$y_t + y_t^{\mathrm{csu}} + y_t^{\mathrm{csb}} = 1 \ \ \forall\, t \in \mathcal{T} \tag{A.8}$$

Electric Power Sold and Purchased, See §A.22

$$\begin{aligned} \dot{w}_t^{\mathrm{s}} - \dot{w}_t^{\mathrm{p}} = (1 - L_t^{\mathrm{con}})\dot{w}_t - \Big[& p_t^{\mathrm{r}} + \frac{E^{\mathrm{hs}}}{\Delta_t}(y_t^{\mathrm{rsu}} + 2y_t^{\mathrm{rhsp}} + y_t^{\mathrm{rsdp}}) \\ & + W^{\mathrm{hco}} + W^{\mathrm{htr}}(y_t^{\mathrm{rsu}} + y_t^{\mathrm{r}} + y_t^{\mathrm{rsb}}) \\ & + W^{\mathrm{htp}} y_t^{\mathrm{r}} + W^{\mathrm{htf}}(1 - y_t^{\mathrm{r}}) + p_t^{\mathrm{c}} + p_t^{\mathrm{fw}} \\ & + W^{\mathrm{b}}(y_t^{\mathrm{csu}} + y_t^{\mathrm{csb}}) + W^{\mathrm{c}}(1 - y_t) \Big] \ \ \forall\, t \in \mathcal{T} \end{aligned} \tag{2.16a}$$

$$\dot{w}_t^{\mathrm{s}} \le \min\{W_t^{\mathrm{net}} y_t, \dot{w}_t\} \ \ \forall\, t \in \mathcal{T} \tag{2.16b}$$

$$\dot{w}_t^{\mathrm{p}} \le \overline{\dot{W}}^{\mathrm{p}}(1 - y_t) \ \ \forall\, t \in \mathcal{T} \tag{2.16c}$$

Additionally, we require:

$$d_t^{\mathrm{rsu}}, d_t^{\mathrm{rsd}}, f_t^{\mathrm{rsu}}, f_t^{\mathrm{rsd}}, p_t^{\mathrm{r}}, p_t^{\mathrm{c}}, p_t^{\mathrm{fw}}, u_t^{\mathrm{csu}}, u_t^{\mathrm{rsu}}, u_t^{\mathrm{rsd}} \ge 0 \ \ \forall\, t \in \mathcal{T} \tag{A.9a}$$

$$\dot{w}_t, \dot{w}_t^{\delta^+}, \dot{w}_t^{\delta^-}, \dot{w}_t^{\mathrm{s}}, \dot{w}_t^{\mathrm{p}}, x_t^{\mathrm{r}} \ge 0 \ \ \forall\, t \in \mathcal{T} \tag{A.9b}$$

$$0 \le \dot{w}_t^{\mathrm{v}^+} \le \dot{W}^{\mathrm{v}^+} \ \ \forall\, t \in \mathcal{T} \tag{A.9c}$$

$$0 \le \dot{w}_t^{\mathrm{v}^-} \le \dot{W}^{\mathrm{v}^-} \ \ \forall\, t \in \mathcal{T} \tag{A.9d}$$

$$0 \le s_t \le E^{\mathrm{u}} \ \ \forall\, t \in \mathcal{T}^{\mathrm{L}} \tag{A.9e}$$

$$x_t \ge 0 \ \ \forall\, t \in \mathcal{T}^{L} \tag{A.9f}$$

$$\dot{m}_t^{\mathrm{c}}, \dot{m}_t^{\mathrm{rcs}}, \dot{m}_t^{\mathrm{rhs}}, \mathrm{T}_t^{\mathrm{cout}}, \mathrm{T}_t^{\mathrm{rout}} \ge 0 \ \ \forall\, t \in \mathcal{T}^{\mathrm{N}} \tag{A.9g}$$

$$\underline{M}^{\mathrm{cs}} \le m_t^{\mathrm{cs}} \le \overline{M}^{\mathrm{cs}} \ \ \forall\, t \in \mathcal{T}^{\mathrm{N}} \tag{A.9h}$$

$$\underline{M}^{\mathrm{hs}} \le m_t^{\mathrm{hs}} \le \overline{M}^{\mathrm{hs}} \ \ \forall\, t \in \mathcal{T}^{\mathrm{N}} \tag{A.9i}$$

$$\underline{T}^{\mathrm{cs}} \le \mathrm{T}_t^{\mathrm{cs}} \le \bar{T}^{\mathrm{cs}} \ \ \forall\, t \in \mathcal{T}^{\mathrm{N}} \tag{A.9j}$$

$$\underline{T}^{\mathrm{hs}} \le \mathrm{T}_t^{\mathrm{hs}} \le \bar{T}^{\mathrm{hs}} \ \ \forall\, t \in \mathcal{T}^{\mathrm{N}} \tag{A.9k}$$

$$y_t, y_t^{\mathrm{cge}}, y_t^{\mathrm{chsp}}, y_t^{\mathrm{csb}}, y_t^{\mathrm{csdp}}, y_t^{\mathrm{csu}}, y_t^{\mathrm{csup}}, y_t^{\mathrm{cgb}} \in \{0, 1\} \ \ \forall\, t \in \mathcal{T} \tag{A.9l}$$

$$y_t^{r}, y_t^{\mathrm{rhsp}}, y_t^{\mathrm{rsb}}, y_t^{\mathrm{rsd}}, y_t^{\mathrm{rsdp}}, y_t^{\mathrm{rsu}}, y_t^{\mathrm{rsup}} \in \{0, 1\} \ \ \forall\, t \in \mathcal{T} \tag{A.9m}$$

We maximize plant revenue given as profit from the sale of electricity to the utility grid less the cost of purchases from the grid and estimates of operations and maintenance due to dispatch decisions throughout the time horizon in question.

A.1 Receiver Start-up

Constraints (2.2a)-(2.2c) require a start-up time "inventory" be fulfilled, in addition to the start-up energy "inventory" in constraints (2.2d)-(2.2f). The D^{rsu} parameter defining the time to complete receiver start-up could be set by a plant operator depending on how well the receiver was last drained. We employ a common continuous decision variable in both requirements which represents the fraction of the current period used for the start-up process. This variable is controlled by the start-up and operation binary variables in constraints (2.2g)-(2.2h). The remaining fraction of the last period of start-up may be used for collection.

A.2 Receiver Collection Energy Balance

The parameter Q_t^{in} provides an upper bound on the amount of thermal power the receiver can collect in each period, which is reduced by the fraction of the current period used for receiver start-up or shutdown in constraint (2.3a). The receiver operating binary forces the power collected to zero for periods in which the receiver is not operating. Receiver power collection must be greater than its non-zero lower bound Q^{rl} during periods in which it is operating, but we relax this lower bound by the fraction of the period used for receiver start-up or shutdown in constraint (2.3b).

A.3 Receiver Shutdown

Similar to the receiver start-up process, a receiver shutdown process consists of draining the receiver tubing while thermal energy is applied to the receiver by the heliostat field. We use an analogous formulation of this process having both a time "inventory" in constraints (2.4a)-(2.4c) and an energy "inventory" in constraints (2.4d)-(2.4f). We employ a common continuous decision variable in both requirements which represents the fraction of the current period used for the shutdown process. This variable is controlled by the shutdown and operation binary variables in constraints (2.4g)-(2.4h). The remaining fraction of the first period of shutdown may be used for collection.

A.4 Receiver Mass Flow Rate

Constraint (2.5a) enforces an upper bound on the total mass flow rate through the receiver, while constraint (2.5b) provides the lower bound, depending on the current operating mode. Constraint (2.5c) allows mass flow through the receiver to be directed (back) to cold storage only while the receiver is in start-up or standby modes. Constraint (2.5d) allows mass flow through the receiver to be directed to hot storage only when the receiver is in collection mode. We add constraints (2.5c) and (2.5d) to represent the plant's usual operating procedure, which could be relaxed for cases in which the plant has greater flexibility with respect to receiver operations.

A.5 Receiver Outlet Temperature

Constraint (2.6a) allows the receiver outlet temperature to be non-zero only during periods when the receiver is in start-up, collection, or standby modes. Constraint (2.6b) enforces a lower bound on this temperature under the same operating modes.

A.6 Receiver Power Balance

Constraint (2.7a) relates the thermal power collected (or consumed to maintain standby) at the receiver to the corresponding temperature change in the mass flow of HTF through the receiver. Constraint (2.7b) ensures that the mass flow rate through the receiver is sufficient to preclude the receiver outlet temperature from exceeding its upper bound under "clear-sky" conditions. The combination of (2.7a) and (2.7b) guarantee that the receiver never exceeds its maximum outlet temperature, and enforce a reduction in outlet temperature when the "clear-sky" fraction parameter F_t is less than 1.

A.7 Receiver Penalties

Constraints (A.1a)-(A.1c) enforce objective penalties for receiver start-up, hot start-up, and shutdown, respectively. These penalties are used to impose estimates of maintenance costs due to these operating decisions in the objective.

A.8 Receiver Logic

Constraints (A.2a) and (A.2b) require that there be non-zero solar resource for the receiver to be in one of the start-up or shutdown modes. Start-up is precluded if the receiver was in the collection or standby modes in the previous period by constraints (A.2c) and (A.2d). Further, constraint (A.2e) applies a packing constraint to preclude the receiver being in more than one of the start-up, standby, or shutdown modes in the same time period. Constraint (A.2f) enforces a lower bound on the available solar resource during periods in which the receiver is in collection mode. Constraint (A.2g) prevents the receiver from simultaneously being in collection and standby modes, though we do allow the receiver to be in start-up or shutdown modes for a portion of a period (relaxed for start-up in constraint (2.2h) or shutdown in constraint (2.4h)) and in collection mode for the remainder of the period. Constraint (A.2i) requires the receiver to enter the shutdown mode when exiting the collection or standby modes, and constraint (A.2j) forces the receiver out of collection mode after entering shutdown. These constraints allow the receiver to be collecting and in shutdown for a single period and solely in the shutdown mode in subsequent periods, until the shutdown process has completed.

A.9 Thermal Energy Storage

The initial usable thermal energy in storage is calculated from the mass in and bulk temperature of the hot storage tank as in (2.8a), which uses the initial condition parameters of these values for cases in which the first period of the problem horizon subscribes to the linear formulation. The end-of-problem incentive uses the final value of s_t (as in (2.8b)) for cases in which the last period of the problem is modeled with the linear formulation, or an analogous calculation to (2.8a) when the final period uses the nonlinear formulation. We then discount this level of thermal energy via the same exponentially diminishing factor that appears in the objective.

A.10 Mass Balance

Constraints (2.9a) and (2.9b) account for the mass of HTF entering and leaving the cold and hot storage tanks, respectively. The mass flow rate of HTF to the receiver directed to the cold tank does not appear in constraint (2.9a), because we model this mass as both leaving and returning to the cold storage tank in the same time period.

A.11 Energy Balance

Constraints (2.10a) and (2.10b) enforce energy balance on the cold and hot storage tanks, respectively. Similar to the way in which the previous constraints apply mass balance on the tanks, these energy balance constraints control the bulk temperature of each storage tank.

Constraint (A.3) accounts for contributions to the usable thermal energy in storage collected at the receiver, and reductions from usable thermal energy to complete power cycle start-up, produce electricity, or maintain the receiver in standby. Constraint (A.3) is sufficient to model thermal energy storage during periods using the linear formulation. We do not separate hot and cold storage in this representation, nor is there a representation of the temperature of the HTF holding this energy. The efficiency at which this thermal energy is converted to electrical energy is dependent on this temperature, is commonly referred to as the "quality" of the energy, and is a primary consideration in plant operations.

A.12 Power Cycle Start-up

Power cycle start-up enforced by constraints (2.11a)-(2.11d) is analogous to receiver start-up, but we only insist on an energy "inventory" requirement to complete power cycle start-up, because this process is not dependent on the variable output of the heliostat field. Constraint (2.11a) includes an energy incentive if the power cycle was in the standby mode prior to start-up. This incentive allows the power cycle to start up more quickly for cases in which it was previously in standby mode, and is formulated similarly to warm-start constraints in the unit commitment literature [49]. Constraint (2.11b) enforces a lower bound on the cycle start-up energy "inventory" to prevent prolonging power cycle start-up, which could allow the model to ferry HTF from the hot tank back to the cold tank, and is not an operation mode we consider. For time periods in which we employ the nonlinear formulation, we further impose power balance constraints (2.11e) and (2.11f) to model the temperature drop of the HTF across the power cycle during start-up.

A.13 Power Cycle Thermal Input

Constraints (2.12a)-(2.12c) control the thermal input to the power cycle in periods using the linear formulation. Constraints (2.12b) and (2.12c) reduce the upper and lower bounds, respectively, on thermal input to the power cycle based on a linear function of the bulk temperature of the hot storage tank. These reductions reflect bounds on the mass flow rate input to the power cycle (physically imposed by system pumping limits), and assume a constant hot storage tank bulk temperature over all periods using the linear formulation. Constraints (2.12d)-(2.12e) control the thermal input to the power cycle in periods using the nonlinear formulation. We fit the coefficients used in these constraints to the off-design steam Rankine performance model developed in Hamilton et al. [26], which provides a close fit to the more detailed model and is sufficient for our purposes.

A.14 Power Cycle Mass Flow Rate

The mass flow rate input to the power cycle is controlled by constraints (2.13a) and (2.13b), which is forced to zero in periods when the power cycle is not in start-up or production mode. Constraint (2.13b) imposes a non-zero lower bound on this mass flow rate during periods of energy production, which is relaxed in periods when the power cycle is in start-up mode.

A.15 Power Cycle Outlet Temperature

Constraints (2.14a)-(2.14b) control the temperature of HTF at the outlet of the power cycle, forcing it to zero in periods when the power cycle is not either in start-up or production modes, and imposing a non-zero lower bound under either of these operating modes.

A.16 Power Cycle Electric Output

Constraints (2.15a), (2.15d), and (2.15e) are sufficient to control the production of electric power in periods using the linear formulation. Constraint (2.15a) enforces a linear model of power cycle efficiency with respect to the level of thermal input. Constraints (2.15d) and (2.15e) enforce non-zero upper and lower bounds, respectively, on power cycle output during periods in which the power cycle is in generation mode. We replace (2.15a) with (2.15b) and (2.15c) in periods during which we employ the nonlinear formulation, which enforces a nonlinear model of power cycle efficiency incorporating both mass flow rate and temperature inputs, as well as the level of thermal energy input. This nonlinear efficiency model is consistent with the linear model in (2.15a) at the design point, but imposes reduced efficiency at lower input temperatures. We fit the coefficients in these constraints to the model developed in Hamilton et al. [26]. We find that a linear regression on this model is not sufficient to capture off-design performance and that the bilinear term in (2.15b) and (2.15c) is needed to accurately represent the temperature dependence of the power cycle.

A.17 Power Cycle Ramping

Constraints (A.4a) and (A.4b) enforce the definition of the positive and negative electric output ramping variables. Constraints (A.4c) and (A.4d) enforce upper bounds on the power cycle output ramping variables, which are reduced if production is started or ended in the current period. These bounds are elasticized by the ramping violation variables $\dot{w}_t^{\mathrm{v}^-}$ and $\dot{w}_t^{\mathrm{v}^+}$, which have greater objective penalties than the ramping variables.

A.18 Power Cycle Up and Down Times

We adopt a formulation of minimum up-time and down-time requirements on the power cycle developed in the unit commitment literature [118, 119], to enforce minimum duration for the power cycle to be in (or out of) generation mode. Constraint (A.5a) relates the operating binary to the start and end generation binaries. Constraint (A.5b) enforces minimum up-time by forcing the operating binary to 1 until the sliding window defined by the minimum up-time parameter no longer contains a non-zero value of the begin-production binary variable. Constraint (A.5c) similarly enforces the minimum down-time. Constraint (A.5d) serves as an initial condition for either minimum up-time or down-time depending on the value of the operating binary initial condition y_0. This formulation allows the integrality of the indicator binary variable y_t^{cgb} and y_t^{cge} to be relaxed to be continuous between 0 and 1.

A.19 Power Cycle Penalties

Constraints (A.6a)-(A.6c) enforce objective penalties for power cycle start-up, hot start-up, and shut down, respectively. These penalty variables are used to enforce estimated maintenance costs in the objective.

A.20 Logic Associated with Power Cycle Modes

Constraints (A.7a)-(A.7c) enforce binary logic on power cycle operations. Constraint (A.7a) requires that the power cycle be in at most one of its operating modes in a single time period. Constraint (A.7b) precludes the cycle being in start-up mode in periods after it was in production mode. Constraint (A.7c) requires that the power cycle be in either production or standby modes in the previous period if it is in standby mode in the current period.

A.21 Power Cycle Operation Restriction

Due to our problem horizon, we expect the power cycle to complete only one or two start-ups, returning to standby operation when not generating power. However, solutions to the dispatch model ($\mathcal{R}$) typically include shutting down the power cycle at the end of the horizon. This contributes to an end-of-horizon effect, because the time required to restart the power cycle after a completed shutdown would be detrimental to plant revenue on the subsequent day. We mitigate this effect by requiring the power cycle to operate either in start-up, generation, or standby modes for the entire problem horizon (see constraint (A.8)). The decision to shut down the power cycle could be made by this formulation, but requires an appropriate end-of-horizon incentive.

A.22 Grid Operations

Constraint (2.16a) accounts for electric production and plant parasitic loads. The electric output of the power cycle is reduced by a multiplicative factor representing the power required to operate the steam condenser portion of the power cycle, which is dependent on ambient temperature and varies with respect to the current time period. Other parasitic loads are then subtracted from this net electric output, including HTF and feedwater pumping power, heliostat and heat trace parasitic load, and the power needed to run auxiliary boilers and heat tracing according to the current power cycle operating state. Constraints (2.16b) and (2.16c) provide upper bounds for the electric power sold and purchased, respectively. Changes to the heliostat tracking fraction incur the electric energy load E^{hs}, which is time-averaged over the duration of the current time period. We include linear models of pumping parasitic loads, which depend on receiver and power cycle thermal input, using the linear formulation. Periods using the nonlinear formulation include piece-wise linear models of pumping parasitic loads, and depend on the mass flow rate input to the receiver or power cycle fit to plant operational data.

APPENDIX B

PHASED-SOLUTION HEURISTIC

We take advantage of the hybrid nature of our formulation by developing a method to quickly obtain a near-optimal solution, which could be used to warm-start the nonlinear solver. Our approach ($\mathbb{R}$), depicted in Figure B.1, consists of solving three separate problems and reduces the time required to find an initial feasible solution in all cases, and improves the relative optimality gap in some instances; correspondingly, this method may obtain solutions of similar or higher quality faster than solving ($\mathcal{R}'$) directly. The non-convex mixed-integer, quadratically-constrained solver we employ uses spatial branch-and-bound, in which approximate linear sub-problems are solved at each node in a tree and the approximation error on the bilinear terms is used to develop new sub-problems. In this approach, the solver might branch on an integer infeasibility or on a bilinear infeasibility. We attempt to separate all binary variables into a Phase 1 problem using the linear formulation ($\mathcal{L}$), and all bilinear terms into a Phase 2 problem with fixed binary variables ($\hat{\mathcal{R}}$), thereby reducing the maximum possible size of the branch-and-bound tree in each problem. This heuristic is applied in addition to all other problem modifications described in Sections 2.4.1 and 2.4.3, as summarized in Figure B.2. We denote the Phase 2 problem, which includes restrictions on ($\mathcal{R}'$) as ($\hat{\mathcal{R}}$).

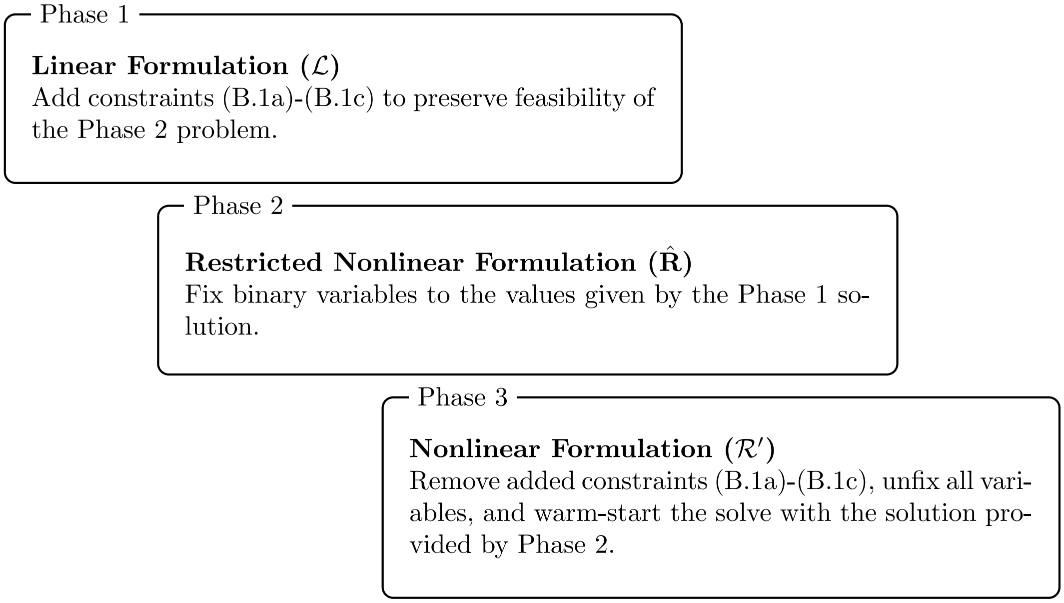

Phase 1

Linear Formulation ($\mathcal{L}$)
Add constraints (B.1a)-(B.1c) to preserve feasibility of the Phase 2 problem.

Phase 2

Restricted Nonlinear Formulation ($\hat{\mathbf{R}}$)
Fix binary variables to the values given by the Phase 1 solution.

Phase 3

Nonlinear Formulation ($\mathcal{R}'$)
Remove added constraints (B.1a)-(B.1c), unfix all variables, and warm-start the solve with the solution provided by Phase 2.

Figure B.1 Diagram of a heuristic approach ($\mathbb{R}$) to solve Real-time Dispatch Optimization Model ($\mathcal{R}$)

Phase 1

The goal of this phase is to quickly determine good values for the binary variables in the Phase 2 problem. We begin by solving the problem using only the linear formulation ($\mathcal{L}$). We add the following constraints to ($\mathcal{L}$), which,

Exact Modifications

Cuts (2.18a)-(2.18d) improve the simple bounds on variables contained in bilinear terms.

Inexact Modifications

- Discretize values of $\dot{m}_t^c$: add binary decision variables to restrict $\dot{m}_t^c$ to a small number of discrete values.
- Formulate as a hybrid nonlinear-linear model: enforce constraints containing bi-linear terms only in a portion of the problem horizon.

Phased Solution Heuristic

- Phase 1: solve the linear formulation ($\mathcal{L}$), with added constraints (B.1a)-(B.1c) to preserve feasibility, to determine values for the binary decision variables.
- Phase 2: apply quadratic constraints, but fix binary decision variables to values found in Phase 1 (formulation ($\hat{\mathcal{R}}$)).
- Phase 3: remove added constraints, unfix all variables, and warm-start the solver with the solution found in Phase 2 (formulation ($\mathcal{R}'$)).

Figure B.2 Summary of Solution Techniques Applied to the Real-time Dispatch Optimization Model

in our testing, ensures the Phase 1 solution is feasible for the Phase 2 problem. Constraint (B.1a) requires the clear-sky fraction parameter, F_t, to be greater than a lower bound, $\underline{F}$, to allow the receiver to be in collection mode. Constraints (B.1b) and (B.1c) enforces a non-zero lower bound and reduced upper bound on the usable thermal energy in storage, respectively.

Table B.1 Real-time dispatch model, heuristic notation.

Parameters		Units
$\underline{F}$	Lower bound on solar resource fraction, in periods that the receiver is collecting thermal power	-
$\underline{s}$	Lower bound on the usable thermal energy in storage	kWh$_\mathrm{t}$
$\bar{s}$	Upper bound on the usable thermal energy in storage	kWh$_\mathrm{t}$

Phase 1 Problem Restrictions

$$\underline{F} y_t^{\mathrm{r}} \le F_t \quad \forall\, t \in \mathcal{T}^{\mathrm{L}} \tag{B.1a}$$
$$s_t \ge \underline{s} \quad \forall\, t \in \mathcal{T}^{\mathrm{L}} \tag{B.1b}$$
$$s_t \le \bar{s} \quad \forall\, t \in \mathcal{T}^{\mathrm{L}} \tag{B.1c}$$

Phase 2

The goal of this phase is to quickly determine a near-optimal solution to the Phase 3 problem. We update indexing sets to impose the use of the nonlinear formulation in the first 24 hours of the problem horizon, with the remainder using the linear formulation (Figure 2.5). Binary variables in the nonlinear portion of the problem, $t \in \mathcal{T}^N$, are fixed to the values given by the Phase 1 solution. We use values of the thermal input to the power cycle, x_t, to fix the binary discretization variables, θ_{it}, which are not present in the Phase 1 problem, but retain some of these binaries in the Phase 2 problem to preserve feasibility. Specifically, if the x_t variable is at its upper bound for the three periods $t \in \{t-1, t, t+1\}$ then we fix $\theta_{it} = 1 \; \forall \; i \in \mathcal{I}$, for the center period t. This is a heuristic approach since it enforces some periods of maximum cycle output while not fixing how the cycle should ramp to maximum output. We denote this problem as $(\hat{\mathcal{R}})$, which is a restriction of $(\mathcal{R}')$, having most binary variables fixed.

Phase 3

We remove all additional constraints (B.1a)-(B.1c), unfix all decision variables, (returning the problem to $(\mathcal{R}')$) and warm-start the solver with the solution to the Phase 2 problem. The goal of this phase is to tighten the global optimality gap. In practice, solving the Phase 2 problem takes only seconds, while solving the Phase 3 problem can require minutes to hours. In some instances, using the Phase 2 solution to warm-start the solver does not improve the overall solve time.

APPENDIX C

PHASED-SOLUTION HEURISTIC SOLVE TIMES

Tables C.1 and C.2 displays solve times on the 42 instances described in Section 2.5.2 using ($\mathbb{R}$). We do not report solve times from Phase 1 problems, as they are uniformly around 1 second. Solving the Phase 2 problem ($\hat{\mathcal{R}}$) to a small gap is significantly more tractable than solving the Phase 3 ($\mathcal{R}'$) problem. However, several instances have significant differences between the best Phase 2 and best Phase 3 objective values. This is due to restrictions imposed by our heuristic in Phase 2, which excise the optimal solution. The results in Table2 C.1 and C.2 exhibit slightly faster solve times and/or gaps, and show minor improvements in 30 of 42 of these problem instances.

Table C.1 Real-Time Dispatch Heuristic Approach, ($\mathbb{R}$), Timing Study Results for the PPA price signal. ‡90-second time limit reached in Phase 2; †300-second time limit reached; objective value is reported in thousands of dollars.

	Phase 2			Phase 3		
PPA Price	Time	Obj	Gap to Phase 3	Time	Obj	Gap
	Baseline Initial					
Clark 1	3 s	171.4	3.09 %	60 s	176.8	0.89 %
Clark 2	‡	131.5	13.27 %	†	151.6	4.82 %
Clark 3	2 s	184.7	0.05 %	†	184.8	5.20 %
Clark 4	8 s	193.2	0.09 %	†	193.4	1.68 %
Clark 5	4 s	167.1	4.40 %	†	174.8	4.67 %
Clark 6	3 s	174.1	0.68 %	†	175.3	1.59 %
Clark 7	2 s	154.5	8.93 %	†	169.7	3.04 %
	Cycle On Full Tank					
Clark 1	5 s	222.8	0.21 %	55 s	223.3	0.07 %
Clark 2	27 s	206.3	0.40 %	75 s	207.1	0.37 %
Clark 3	23 s	254.1	0.68 %	29 s	255.8	0.00 %
Clark 4	22 s	238.4	0.36 %	30 s	239.2	0.16 %
Clark 5	‡	236.0	0.00 %	†	236.0	0.86 %
Clark 6	5 s	221.8	0.46 %	41 s	222.9	0.03 %
Clark 7	25 s	222.8	0.53 %	75 s	224.0	0.31 %
	Low Temp Tank					
Clark 1	7 s	155.5	0.00 %	†	155.5	1.05 %
Clark 2	11 s	126.3	3.94 %	†	131.5	3.96 %
Clark 3	21 s	169.2	0.00 %	†	169.2	2.20 %
Clark 4	‡	172.6	0.00 %	†	172.6	1.51 %
Clark 5	35 s	153.6	0.00 %	†	153.6	5.13 %
Clark 6	1 s	154.6	0.00 %	†	154.6	1.38 %
Clark 7	3 s	143.5	3.53 %	†	148.7	2.97 %

In theory, we could execute both the heuristic approach ($\mathbb{R}$) and a direct solve of the modified problem ($\mathcal{R}'$) in parallel. Table C.3 shows the best results. Rows are bolded for cases in which the heuristic approach ($\mathbb{R}$) achieves the better objective.

Table C.2 Real-Time Dispatch Heuristic Approach, (ℝ), Timing Study Results for the CAISO price signal. ‡90-second time limit reached in Phase 2; †300-second time limit reached; objective value is reported in thousands of dollars.

CAISO Price	Phase 2 Time	Phase 2 Obj	Phase 2 Gap to Phase 3	Phase 3 Time	Phase 3 Obj	Phase 3 Gap
	Baseline Initial					
Clark 1	‡	222.6	0.32 %	†	223.3	2.46 %
Clark 2	‡	-	-	†	189.5	10.86 %
Clark 3	‡	231.5	0.00 %	†	231.5	3.53 %
Clark 4	14 s	238.6	1.64 %	57 s	242.6	0.20 %
Clark 5	‡	214.0	0.00 %	†	214.0	5.21 %
Clark 6	44 s	223.8	0.22 %	†	224.3	1.43 %
Clark 7	‡	198.7	1.86 %	†	202.5	9.41 %
	Cycle On Full Tank					
Clark 1	10 s	252.1	0.52 %	280 s	253.4	0.99 %
Clark 2	‡	231.8	0.03 %	†	231.8	3.57 %
Clark 3	‡	269.9	0.26 %	†	270.6	2.29 %
Clark 4	16 s	267.0	1.04 %	57 s	269.8	0.34 %
Clark 5	‡	250.6	0.94 %	†	252.9	3.04 %
Clark 6	10 s	252.4	0.41 %	70 s	253.4	0.58 %
Clark 7	‡	-	-	†	244.6	4.12 %
	Low Temp Tank					
Clark 1	‡	204.2	2.06 %	†	208.5	3.64 %
Clark 2	‡	-	-	†	171.0	11.32 %
Clark 3	‡	211.4	0.91 %	†	213.3	4.68 %
Clark 4	‡	225.2	1.63 %	†	228.9	1.02 %
Clark 5	‡	194.6	0.00 %	†	194.6	7.13 %
Clark 6	‡	204.6	2.38 %	†	209.6	2.81 %
Clark 7	‡	182.9	0.66 %	†	184.1	10.67 %

Table C.3 Real-Time Dispatch Parallel Timing Study Results. †300-second overall time limit reached; objective value is reported in thousands of dollars; results are bolded for cases in which the heuristic approach (ℝ) achieves the better objective.

PPA	Baseline Initial			Cycle On Full Tank			Low Temp Tank		
Price	Time	Obj	Gap	Time	Obj	Gap	Time	Obj	Gap
Clark 1	†	**176.8**	**0.91 %**	70 s	223.3	0.02 %	†	**155.5**	**1.02 %**
Clark 2	†	153.8	3.33 %	116 s	207.4	0.23 %	†	133.2	2.57 %
Clark 3	†	185.1	5.04 %	67 s	255.8	0.00 %	†	**169.2**	**2.18 %**
Clark 4	†	194.3	1.20 %	75 s	**239.2**	**0.17 %**	†	**172.6**	**1.48 %**
Clark 5	†	**174.8**	**4.68 %**	†	**236.0**	**0.88 %**	†	154.9	4.22 %
Clark 6	†	175.7	1.35 %	62 s	222.9	0.01 %	†	**154.6**	**1.38 %**
Clark 7	†	170.3	2.68 %	132 s	224.2	0.22 %	†	149.8	2.22 %
CAISO	Baseline Initial			Cycle On Full Tank			Low Temp Tank		
Price	Time	Obj	Gap	Time	Obj	Gap	Time	Obj	Gap
Clark 1	†	223.5	2.37 %	236 s	**253.4**	**0.98 %**	†	**208.5**	**3.66 %**
Clark 2	†	190.3	10.40 %	†	**231.8**	**3.58 %**	†	171.3	11.12 %
Clark 3	†	231.6	3.49 %	†	**270.6**	**2.29 %**	†	214.2	4.15 %
Clark 4	60 s	242.6	0.19 %	69 s	269.9	0.30 %	†	**228.9**	**1.03 %**
Clark 5	†	**214.0**	**5.16 %**	†	**252.9**	**3.05 %**	†	**194.6**	**7.14 %**
Clark 6	†	224.6	1.24 %	63 s	253.5	0.53 %	†	**209.6**	**2.80 %**
Clark 7	†	**202.5**	**9.39 %**	†	245.4	3.80 %	†	**184.1**	**10.46 %**
Max	†	-	10.40 %	†	-	3.80 %	†	-	11.12 %
Average	283 s	-	3.67 %	171 s	-	1.15 %	†	-	3.96 %

APPENDIX D

PLANT EVALUATION ASSUMPTIONS AND CASE STUDY INPUTS

The cost assumptions used in this work are the default values in the corresponding PySAM technology model or PySSC simulation. These defaults are intended to represent conservative estimates for the current state of technology and market conditions [91, 120].

Table D.1 presents the molten salt power tower single-owner installation cost parameters used. All parameters are the defaults used in the PySSC molten salt power tower model.

Table D.1 Molten salt power tower single-owner installation cost parameters used in the CSP system of the plant evaluation procedure

Parameter	Value	Units
Site improvement cost	16	$\$/m^2$
Heliostat field cost	140	$\$/m^2$
Tower cost fixed	3	$ million
Tower cost scaling exponent	0.0113	-
Receiver reference cost	103	$ million
Receiver reference area	1571	m^2
Receiver cost scaling exponent	0.7	-
Thermal energy storage cost	22	$\$/kWh_t$
Power cycle cost	1040	$\$/kW_e$
Contingency	7	%
Engineering, procurement and construction; and, owner cost	13	% of direct cost
Total land cost	10	$1000/acre
Sales tax basis	80	%
Sale tax rate	5	%
O&M fixed cost by capacity	66	$/kW-yr
O&M variable cost by generation	3.5	$/MWh
Balance of plant costs	290	$/kW

The PV system uses SAM's PVWatts model. We fix the array type to single axis tracking for all plants, and utilize the default cost assumptions in SAM version 2021.12.2 for all other parameters. HOPP utilizes a simplified model of PV field costs by default, which is based on the \$51.38M installation cost of a benchmark $50MW_{dc}$ field. The PV system cost is linearly scaled by the capacity multiplier $\$973/kW_{dc}$, according to the cost of the benchmark system. For the battery system, we use the SAM default values of \$233.17/kW and \$241.79/kWh for the installation costs. Fixed maintenance costs are \$15/kW-yr, and we assume a default 10-year replacement period for the battery system.

APPENDIX E

DISPATCH OPTIMIZATION MODEL FORMULATION

We provide here the complete problem formulation ($\mathcal{H}$), which is taken from Hamilton et al. [94], and mimics the model given in Hamilton et al. [25]. We first define notation:

Table E.1 Hybrid dispatch model, ($\mathcal{H}$), notation.

Indices and Sets		
$t \in \mathcal{T}$	Time periods in the problem horizon	

CSP Field and Receiver Parameters		Units
C^{rec}	Generation cost for the CSP field and receiver	\$/MWh$_t$
C^{rsu}	Fixed cost for receiver start-up	\$/start
Δ^{l}	Minimum time to start the receiver	hr
Δ^{rs}_t	Estimated fraction of time period t required for receiver start-up	-
E^{hs}	Heliostat field startup or shut down parasitic loss	MWh$_e$
E^{r}	Required energy expended to start receiver	MWh$_t$
L^{r}	Receiver pumping power per unit power produced	MW$_e$/MW$_t$
Q^{in}_t	Available thermal power generated by the CSP heliostat field in period t	MW$_t$
Q^{rl}	Minimum operational thermal power delivered by the receiver	MWh$_t$
Q^{ru}	Allowable power per period for receiver start-up	MWh$_t$
W^{h}	Heliostat field tracking parasitic loss	MW$_e$

Power Cycle Parameters		Units
C^{pc}	Generation cost for power cycle operation	\$/MWh$_e$
C^{csu}	Fixed cost for power cycle start-up	\$/start
$C^{\delta x}$	Penalty for change in power cycle thermal input	\$/ΔMW$_t$
η^{amb}_t	Cycle efficiency ambient temperature adjustment factor in period t	-
η^{c}_t	Normalized condenser parasitic loss in period t	-
E^{c}	Required energy expended to start cycle	MWh$_t$
η^{des}	Cycle nominal efficiency	-

Table E.1 Continued.

η^p	Slope of linear approximation of power cycle performance curve	$\mathrm{MW_e/MW_t}$
L^c	Cycle heat transfer fluid pumping power per unit energy expended	$\mathrm{MW_e/MW_t}$
Q^c	Allowable power per period for cycle start-up	$\mathrm{MW_t}$
Q^l	Minimum operational thermal power input to the cycle	$\mathrm{MW_t}$
Q^u	Maximum operational thermal power input to the cycle	$\mathrm{MW_t}$
W^u	Cycle electric power rated capacity	$\mathrm{MW_e}$

TES and Miscellaneous Parameters		Units
Δ	Time period duration	hr
E^u	Thermal energy storage capacity	$\mathrm{MWh_t}$

PV Field Parameters		Units
C^{pv}	Generation cost of PV field	$\$/\mathrm{MWh_e}$
W_t^{pv}	Available PV (AC) generation in period t	$\mathrm{MW_e}$

Battery Parameters		Units
C^{bc}, C^{bd}	Operating cost of charging and discharging battery	$\$/\mathrm{MWh_e}$
C^{bl}	Lifecycle cost for battery	\$/lifecycle
C^B	Battery manufacturer-specified capacity	$\mathrm{MWh_e}$
η^+, η^-	Charge and discharge efficiency	-
$\underline{P}^B, \bar{P}^B$	Battery minimum and maximum power ratings	$\mathrm{MW_e}$
$\underline{S}^B, \bar{S}^B$	Battery state of charge minimum and maximum operational bounds	-

Grid Parameters		Units
ϵ	Small value used in objective for binary logic	\$
γ	Exponential weighting factor	-
P_t^s, P_t^p	Electricity sale and purchase price in period t	$\$/\mathrm{MWh_e}$
W_t^g, W_t^l	Grid transmission limit for generation and load in period t	$\mathrm{MW_e}$

Table E.1 Continued.

Continuous Decision Variables		Units
b^c	Battery cycle count	-
b_t^{soc}	State of charge of battery in time period t	-
$\dot{e}_t^s, \dot{e}_t^p$	Electricity sold to and purchased from grid in time t	$\mathrm{MW_e}$
s_t	TES reserve quantity in period t	$\mathrm{MWh_t}$
u_t^{rsu}	Receiver start-up energy inventory in period t	$\mathrm{MWh_t}$
x_t^r	Thermal power delivered by the receiver in period t	$\mathrm{MW_t}$
x_t^{rsu}	Receiver start-up power consumption in period t	$\mathrm{MW_t}$
u_t^{csu}	Cycle start-up energy inventory in period t	$\mathrm{MWh_t}$
$\dot{w}_t$	Power cycle electricity generation in period t	$\mathrm{MW_e}$
$\dot{w}_t^+, \dot{w}_t^-$	Power into and out of the battery in period t	$\mathrm{MW_e}$
$\dot{w}_t^l$	Electrical load of CSP system in period t	$\mathrm{MW_e}$
$\dot{w}_t^{pv}$	PV generation in time t	$\mathrm{MW_e}$
$\dot{w}_t^{sg}, \dot{w}_t^{sl}$	System generation and load in time t	$\mathrm{MW_e}$
x_t	Cycle thermal power utilization in period t	$\mathrm{MW_t}$
x_t^δ	Power cycle change in thermal energy input in period t	$\mathrm{MW_t}$

Binary Decision Variables	
y_t	1 if cycle is generating electric power in period t; 0 otherwise
y_t^+, y_t^-	1 if battery is charging or discharging in time period t; 0 otherwise
y_t^{csu}	1 if cycle is starting up in period t; 0 otherwise
y_t^{csup}	1 if cycle cold start-up penalty is incurred at time t (from off); 0 otherwise
y_t^g	1 if system is net generating in time period t; 0 otherwise
y_t^r	1 if receiver is generating “usable” thermal power in period t; 0 otherwise
y_t^{rsu}	1 if receiver is starting up in period t; 0 otherwise
y_t^{rsup}	1 if receiver cold start-up penalty is incurred in period t (from off); 0 otherwise

The following formulation, $(\mathcal{H})$, requires the initial operational state of the system, PV field and receiver energy generation forecasts, the expected cycle conversion efficiency profile as a function of ambient temperature and thermal input, and the energy price or desired load profile depending on the system analysis. Initialization parameters used to set variable values at $t = 0$ follow variable notation and are not included here. Variables and parameters describe energy (thermal $\mathrm{MWh_t}$ or electric $\mathrm{MWh_e}$) states and power flows (thermal $\mathrm{MW_t}$ or electric $\mathrm{MW_e}$) in the system. We use lowercase letters to represent variables and capital letters for parameters. All binary variables are represented with some variant of the letter y.

E.1 Objective Function and Constraints

We present two possible objective functions. The first maximizes revenue less operations and maintenance costs resulting from the dispatch solution, which is appropriate in an independent-system-operator market. The second objective minimizes the cost of following a pre-determined load profile.

Maximize Revenue

$$
\begin{aligned}
(\mathcal{H}_1)\ \ \text{maximize} \quad \sum_{t\in\mathcal{T}} \Bigg[& \Delta\left(\gamma^t P^s_t \dot{e}^s_t - \gamma^{-t} P^p_t \dot{e}^p_t\right) - \epsilon y^g_t \\
& - \gamma^{-t}\left(\Delta C^{rec} x^r_t + C^{rsu} y^{rsup}_t + \Delta C^{pc} \dot{w}_t + C^{csu} y^{csup}_t + C^{\delta x} x^{\delta}_t\right) \\
& - \gamma^{-t} \Delta C^{pv} \dot{w}^{pv}_t \\
& - \gamma^{-t} \Delta \left(C^{bc} \dot{w}^+_t + C^{bd} \dot{w}^-_t\right) \Bigg] - C^{bl} b^c
\end{aligned}
\tag{E.1}
$$

Minimize Cost of a Load Profile

$$
\begin{aligned}
(\mathcal{H}_2)\ \ \text{minimize} \quad \sum_{t\in\mathcal{T}} \Bigg[& \Delta\gamma^t \left(P^s_t \left(W^g_t - \dot{e}^s_t\right) + P^p_t \dot{e}^p_t\right) + \epsilon y^g_t \\
& + \gamma^{t}\left(\Delta C^{rec} x^r_t + C^{rsu} y^{rsup}_t + \Delta C^{pc} \dot{w}_t + C^{csu} y^{csup}_t + C^{\delta x} x^{\delta}_t\right) \\
& + \gamma^{t} \Delta C^{pv} \dot{w}^{pv}_t \\
& + \gamma^{t} \Delta \left(C^{bc} \dot{w}^+_t + C^{bd} \dot{w}^-_t\right) \Bigg] + C^{bl} b^c
\end{aligned}
\tag{E.2}
$$

Constraints having terms indexed in period t-1, but applied to all periods $t \in \mathcal{T}$, use the corresponding initial condition parameter for the decision variable when $t = 1$. All time-indexed decision variables requiring an initial value use the same notation for the parameter as the decision variable indexed in period $t = 0$, e.g., the initial condition for the power cycle operating binary variable y_t is the parameter y_0.

Receiver Operations

Receiver Start-up

$$u_t^{rsu} \le u_{t-1}^{rsu} + \Delta x_t^{rsu} \qquad \forall\, t \in \mathcal{T} \tag{E.3a}$$

$$u_t^{rsu} \le E^r y_t^{rsu} \qquad \forall\, t \in \mathcal{T} \tag{E.3b}$$

$$y_t^r \le \frac{u_t^{rsu}}{E^r} + y_{t-1}^r \qquad \forall\, t \in \mathcal{T} \tag{E.3c}$$

$$y_t^{rsu} + y_{t-1}^r \le 1 \qquad \forall\, t \in \mathcal{T} \tag{E.3d}$$

$$x_t^{rsu} \le Q^{ru} y_t^{rsu} \qquad \forall\, t \in \mathcal{T} \tag{E.3e}$$

$$y_t^{rsu} \le \frac{Q_t^{in}}{Q^{rl}} \qquad \forall\, t \in \mathcal{T} \tag{E.3f}$$

$$y_t^{rsup} \ge y_t^{rsu} - y_{t-1}^{rsu} \qquad \forall\, t \in \mathcal{T} \tag{E.3g}$$

Receiver Supply and Demand

$$x_t^r + x_t^{rsu} \le Q_t^{in} \qquad \forall\, t \in \mathcal{T} \tag{E.4a}$$

$$x_t^r \le Q_t^{in} y_t^r \qquad \forall\, t \in \mathcal{T} \tag{E.4b}$$

$$x_t^r \ge Q^{rl} y_t^r \qquad \forall\, t \in \mathcal{T} \tag{E.4c}$$

$$y_t^r \le \frac{Q_t^{in}}{Q^{rl}} \qquad \forall\, t \in \mathcal{T} \tag{E.4d}$$

Power Cycle Operations

Cycle Start-up

$$u_t^{csu} \le u_{t-1}^{csu} + \Delta Q^c y_t^{csu} \qquad \forall\, t \in \mathcal{T} \tag{E.5a}$$

$$u_t^{csu} \le E^c y_t^{csu} \qquad \forall\, t \in \mathcal{T} \tag{E.5b}$$

$$y_t \le \frac{u_t^{csu}}{E^c} + y_{t-1} \qquad \forall\, t \in \mathcal{T} \tag{E.5c}$$

$$y_t^{csu} + y_{t-1} \le 1 \qquad \forall\, t \in \mathcal{T} \tag{E.5d}$$

$$y_t^{csup} \ge y_t^{csu} - y_{t-1}^{csu} \qquad \forall\, t \in \mathcal{T} \tag{E.5e}$$

Power Supply and Demand

$$x_t + \frac{E^c}{\Delta} y_t^{csu} \le Q^u \qquad \forall\, t \in \mathcal{T} \tag{E.6a}$$

$$x_t \le Q^u y_t \qquad \forall\, t \in \mathcal{T} \tag{E.6b}$$

$$x_t \ge Q^l y_t \qquad \forall\, t \in \mathcal{T} \tag{E.6c}$$

$$\dot{w}_t = \frac{\eta_t^{amb}}{\eta^{des}} [\eta^p x_t + (W^u - \eta^p Q^u) y_t] \qquad \forall\, t \in \mathcal{T} \tag{E.6d}$$

$$x_t^\delta \ge x_t - x_{t-1} \qquad \forall\, t \in \mathcal{T} \tag{E.6e}$$

$$\begin{aligned} \dot{w}_t^l = {} & \eta_t^c \dot{w}_t \\ & + L^r (x_t^r + x_t^{rsu}) + L^c (x_t + Q^c y_t^{csu}) \\ & + W^h y_t^r + \frac{E^{hs}}{\Delta} y_t^{rsu} \qquad \forall\, t \in \mathcal{T} \end{aligned} \tag{E.6f}$$

TES Energy Balance Constraints

$$s_t - s_{t-1} = \Delta[x_t^r - (Q^c y_t^{csu} + x_t)] \qquad \forall\, t \in \mathcal{T} \tag{E.7a}$$

$$s_t \leq E^u \qquad \forall\, t \in \mathcal{T} \tag{E.7b}$$

$$s_{t-1} \geq \Delta \cdot \Delta_t^{rs}[Q^u(-3 + y_t^{rsu} + y_{t-1} + y_t) + x_t] \qquad \forall\, t \in \mathcal{T} \tag{E.7c}$$

PV Constraints

$$\dot{w}_t^{pv} \leq W_t^{pv} \qquad \forall\, t \in \mathcal{T} \tag{E.8a}$$

$$\dot{w}_t^{pv} \geq 0 \qquad \forall\, t \in \mathcal{T} \tag{E.8b}$$

Battery Constraints

$$b_t^{soc} = b_{t-1}^{soc} + \Delta \left(\frac{\eta^+ \cdot \dot{w}_t^+ - \frac{\dot{w}_t^-}{\eta^-}}{C^B} \right) \qquad \forall\, t \in \mathcal{T} \tag{E.9a}$$

$$\underline{S}^B \leq b_t^{soc} \leq \bar{S}^B \qquad \forall\, t \in \mathcal{T} \tag{E.9b}$$

$$\underline{P}^B y_t^- \leq \dot{w}_t^- \leq \bar{P}^B y_t^- \qquad \forall\, t \in \mathcal{T} \tag{E.9c}$$

$$\underline{P}^B y_t^+ \leq \dot{w}_t^+ \leq \bar{P}^B y_t^+ \qquad \forall\, t \in \mathcal{T} \tag{E.9d}$$

$$y_t^+ + y_t^- \leq 1 \qquad \forall\, t \in \mathcal{T} \tag{E.9e}$$

$$b^c \geq \frac{\Delta}{C^B} \sum_{t \in \mathcal{T}} \dot{w}_t^- \tag{E.9f}$$

Grid Constraints

$$\dot{e}_t^s - \dot{e}_t^p = \dot{w}_t^{sg} - \dot{w}_t^{sl} \qquad \forall\, t \in \mathcal{T} \tag{E.10a}$$

$$\dot{e}_t^s \leq W_t^g y_t^g \qquad \forall\, t \in \mathcal{T} \tag{E.10b}$$

$$\dot{e}_t^p \leq W_t^l (1 - y_t^g) \qquad \forall\, t \in \mathcal{T} \tag{E.10c}$$

System Connection Constraints

$$\dot{w}_t^{sg} = \dot{w}_t + \dot{w}_t^{pv} + \dot{w}_t^- \qquad \forall\, t \in \mathcal{T} \tag{E.11a}$$

$$\dot{w}_t^{sl} = \dot{w}_t^l + \dot{w}_t^+ \qquad \forall\, t \in \mathcal{T} \tag{E.11b}$$

$$\dot{w}_t^{sg} \geq \dot{w}_t^+ \qquad \forall\, t \in \mathcal{T} \tag{E.11c}$$

$$\dot{w}_t^{pv} \geq \dot{w}_t^+ \qquad \forall\, t \in \mathcal{T} \tag{E.11d}$$

Decision Variable Bounds

$$s_t,\ u^{csu}_t,\ u^{rsu}_t,\ \dot{w}_t,\ \dot{w}^l_t,\ x_t,\ x^{\delta}_t,\ x^r_t,\ x^{rsu}_t \geq 0 \qquad \forall\ t \in \mathcal{T} \tag{E.12a}$$

$$y_t,\ y^{csu}_t,\ y^{csup}_t,\ y^r_t,\ y^{rsu}_t,\ y^{rsup}_t \in \{0,1\} \qquad \forall\ t \in \mathcal{T} \tag{E.12b}$$

$$b^c,\ b^{soc}_t,\ \dot{w}^+_t,\ \dot{w}^-_t \geq 0 \qquad \forall\ t \in \mathcal{T} \tag{E.12c}$$

$$y^+_t,\ y^-_t \in \{0,1\} \qquad \forall\ t \in \mathcal{T} \tag{E.12d}$$

$$\dot{w}^g_t,\ \dot{w}^l_t,\ \dot{e}^s_t,\ \dot{e}^p_t \geq 0 \qquad \forall\ t \in \mathcal{T} \tag{E.12e}$$

$$y^g_t \in \{0,1\} \qquad \forall\ t \in \mathcal{T} \tag{E.12f}$$

E.2 Receiver Operations

Constraint (E.3a) accounts for receiver start-up energy "inventory," which can assume a positive value during time periods of receiver start-up (Constraint (E.3b)). Power production assumes a positive value only upon completion of a start-up or if the receiver also operates in the time period prior (Constraint (E.3c)). In the latter case, the receiver cannot be starting up in the next time period (Constraint (E.3d)). Ramp-rate limits hold during the start-up procedure (Constraint (E.3e)). The presence of trivial solar resource prevents receiver start-up (Constraint (E.3f)). Constraints (E.3g) ensure that penalties for receiver start-up are incurred.

The parameter Q^{in}_t serves as an upper bound on the thermal power produced by the receiver, from which any energy used for start-up detracts (Constraint (E.4a)). Constraint (E.4b) permits the receiver to generate thermal power only while in power-producing mode. Receiver thermal power generation is subject to a lower bound by Constraint (E.4c). The receiver cannot operate (Constraint (E.4d)) in the absence of thermal power.

E.3 Power Cycle Operations

Constraint (E.5a) accounts for start-up energy "inventory," which can only be positive during time periods in which the cycle is starting up (Constraint (E.5b)). Normal cycle operation can occur upon completion of start-up energy requirements or if the cycle is operating normally (Constraint (E.5c)). In the latter case, the cycle cannot start up in the time period directly following operation (Constraint (E.5d)). Cycle start up penalties are incurred via Constraint (E.5e).

Constraint (E.6a) limits the cycle input thermal power during periods when the cycle is starting up. This is a model approximation to derate power cycle output during startup periods. In reality, the cycle power output is not derated but the total energy production during the time period is reduced due to the time the cycle is starting up during that period. Constraint (E.6b) and Constraint (E.6c) form the upper and lower bounds on the heat input to the power cycle, respectively. The relationship between electrical power and cycle heat input is modeled as a linear function with corrections for ambient temperature effects (Constraint (E.6d)). Constraint (E.6e) measures the positive change in cycle thermal input, i.e., ramping, over time. Constraint (E.6f) calculates the CSP system load depending operational decisions.

E.4 Thermal Energy Storage Balance

Constraint (E.7a) balances energy to and from TES with the charge; a time-scaling parameter Δ reconciles power and energy. Constraint (E.7b) imposes the upper bound to TES charge state. If the power cycle is operating in time periods $t-1$ and t, and if the receiver is starting up in time t, then there must be a sufficient charge level in the TES in time $t-1$ to ensure that the power cycle can operate through its start-up period (Constraint (E.7c)). Constraint (E.7c) uses Q^u as a 'big M' value to make the constraint non-binding when the specific condition is not occurring, i.e., the cycle operating and receiver starting up in the same period. The expected fraction of a time period used for receiver start-up is given by (E.13), if applicable.

$$\Delta_t^{rs} = \min\left\{1, \max\left\{\Delta^l, \frac{E^r}{\max\left\{\epsilon, Q_t^{in}\Delta\right\}}\right\}\right\} \tag{E.13}$$

Constraints (E.7a)-(E.7c) measure TES state of charge via energy flow.

E.5 PV Field Operations

Within the hybrid framework, we assume that PV system has a *take it or leave it* policy in which the hybrid system can take up to the available generation at any time (Constraint (E.8a)) or curtail part or all of the available generation depending other system constraints. Non-negativity is enforced by Constraint (E.8b)

E.6 Battery Operations

Battery state-of-charge must be updated (Constraint (E.9a)), and this quantity is bounded both below and above (Constraint (E.9b)). Power flow into and out of the battery is bounded by Constraints (E.9c) and (E.9d). The battery cannot be charging and discharging simultaneously (Constraint (E.9e)) while Constraint (E.9f) measures battery cycle count similar to what is done in Scioletti et al. [31].

E.7 Grid Operations

Constraint (E.10a) provides an energy balance at the transmission interconnect of the hybrid system. Electricity sales are limited by the transmission limit for generation during periods in which the system is generating net power (Constraint (E.10b)). During periods in which the hybrid system net generation is negative, Constraint (E.10c) limits the load the system can pull from the grid.

E.8 Inter-System Operations

Constraints (E.11a) and (E.11b) enforce energy balance for the grid module on system generation and load, respectively. Constraints (E.11c) and (E.11d) are conditional constraints depending on specific requirements imposed on the hybrid system's battery charging. Constraint (E.11c) limits battery charging to only electricity produced by the hybrid system locally, i.e., the battery cannot be charged by the electric grid. Constraint (E.11d) restricts battery charging to only electricity generated by the PV system. Constraint (E.11d) is more restrictive than Constraint (E.11c); therefore, Constraint (E.11c) can be omitted if Constraint (E.11d) is imposed. Variable bounds are enforced in constraints (E.12a) through (E.12f).

APPENDIX F
DESIGN OPTIMIZATION MODEL FORMULATION

We provide here the complete design optimization formulation taken from Cox et al. [102]. We seek to optimize the high-level system sizing variables with respect to a scalar performance metric, i.e., the design objective. We utilize the revenue-maximizing mixed-integer linear program (MILP), developed in Hamilton et al. [94] and denoted $(\mathcal{H})$ to guide dispatch decisions. The plant evaluation procedure is a nonlinear, discrete, constrained, and implicit function of the design variables. As a result, we utilize black-box optimizers, which do not rely on any specific mathematical structure. The following procedure summarizes the sequence of calculations and software used in evaluating a specific plant design.

Procedure F.1 Plant Evaluation Function

Step 1: *Inputs* - Collect all parameter values required by the plant evaluation; i.e., financial assumptions, weather and electricity market conditions, location details, and fixed values in the SAM technology models.

Step 2: *Design Variables* - Set the design variable values according to the input given, e.g., from a point in a sampling design or a candidate from an optimization algorithm.

Step 3: *SolarPILOT* - Invoke the SolarPILOT™ optimization algorithm, which determines the receiver, tower, and heliostat field geometry that minimize cost per unit thermal energy generated, while meeting the design point thermal input specified by the provided CSP solar multiple design variable.

Step 4: *Generation Schedule* - Determine a year-long generation schedule at hourly fidelity.

Step 4.1: *Dispatch MILP* - Solve a problem instance of $(\mathcal{H})$ with a 48-hour horizon. Inputs include the plant initial state, weather, and electricity market conditions during the problem horizon.

Step 4.2: *SAM API* - Operate the SAM simulation according to the first 24 hours of the dispatch solution.

Step 4.3: *Repeat* - Document results of the plant simulation, and roll the problem horizon forward 24 hours, repeating Steps 4.1 and 4.2, until a full year has elapsed.

Step 5: *SAM Financial* - Calculate system costs and benefits resulting from the generation schedule. The year-long schedule is repeated for each year in the analysis after the first. SAM financial models calculate the present value of costs, revenue sources, and the total energy production resulting from the generation schedule.

Step 6: *Objective Function* - Evaluate the design objective function using the outputs of the financial model and plant simulation.

The plant evaluation requires the expected weather conditions and time-of-delivery market pricing at hourly fidelity, as well as the latitude and longitude of the plant site (see Table F.2). Technology construction, and operations and maintenance costs used in the SAM technology model are summarized in Appendix G, and correspond to the SAM default values at the time of this writing.

Table F.2 Inputs of the design optimization problem, $(\mathcal{D})$.

Sets	
$\hat{\mathcal{T}}$	Hours in a year

Market Parameters, in time $t \in \hat{\mathcal{T}}$	
Electricity purchase price	$\$/\mathrm{MWh_e}$
Electricity sales price	$\$/\mathrm{MWh_e}$

Weather Parameters, in time $t \in \hat{\mathcal{T}}$	
Ambient temperature	°C
Atmospheric pressure	mbar
Dew point temperature	°C
Direct horizontal irradiance	$\mathrm{W/m^2}$
Direct normal irradiance (DNI)	$\mathrm{W/m^2}$
Global horizontal irradiance	$\mathrm{W/m^2}$
Wind speed	m/s

Site Parameters	
Elevation	m
Latitude	degrees
Longitude	degrees

The following constrained and implicit nonlinear program, $(\mathcal{D})$, requires inputs as listed in Table F.2, and determines high-level system sizing according to the design objective. In general, upper-case letters denote parameters while lower-case letters represent variables. We use lower-case letters for indices and upper-case script letters for sets. Lists of variables are denoted with lower-case bold font symbols. We use the $(\oplus)$ symbol to denote concatenation, e.g., of each 48-hour problem instance over the course of a year $(\mathbf{u} = \mathbf{s}_1 \oplus \mathbf{s}_2 \oplus \cdots \oplus \mathbf{s}_P)$.

Table F.3 Notation of the design optimization problem, ($\mathcal{D}$).

Sets	
$\mathcal{I}$	Design variables
$\mathcal{J}$	CSP field design attributes evaluated from the design variables
$\mathcal{P}$	48-hour problem instances in a year, i.e., $p \in \{1, \ldots, P\}$
$\mathcal{Q}$	SolarPILOT nonlinear constraints
$\mathcal{R}$	Dispatch MILP linear constraints
$\mathcal{S}$	SAM simulation nonlinear constraints
$\mathcal{T}_p$	Hourly periods in problem instance p

Parameters		
C_q, C_r, C_s	Constraint right-hand side constant $q \in \mathcal{Q}$, $r \in \mathcal{R}$, $s \in \mathcal{S}$	-
L_i	Lower bound of design variable $i \in \mathcal{I}$	...
U_i	Upper bound of design variable $i \in \mathcal{I}$	...

Design Variables		
$\mathbf{x}$	Design variables; i.e., $\mathbf{x} = (x_1, x_2, \ldots, x_i) \;\; \forall\, i \in \mathcal{I}$	...
Battery Storage		
x_1	Battery capacity, hours of design point output	h
x_2	Battery design point power output	$\mathrm{MW_e}$
CSP Field and Power Cycle		
x_3	Thermal energy storage capacity, in terms of hours of power cycle design point input	h
x_4	CSP field solar multiple	-
x_5	Power cycle design point output	$\mathrm{MW_e}$
PV Field		
x_6	Field DC capacity	$\mathrm{MW_e}$

CSP field design attributes, given by SolarPILOT		
$\mathbf{y}$	Design attributes; i.e., $\mathbf{y} = (y_1, y_2, \ldots, y_j) \;\; \forall\, j \in \mathcal{J}$	...
y_1	Number of heliostats	-
y_2	Heliostat field layout	-
y_3	Receiver height	m
y_4	Receiver diameter	m
y_5	Tower height	m

Table F.3 Continued.

Dispatch model outputs and initial conditions		
$\mathbf{d}_p$	Dispatch solution for each period $t \in \mathcal{T}_p$ in problem instance p	...

SAM simulation outputs		
$\mathbf{u}$	Year-long generation schedule, i.e., $\mathbf{u} = (\mathbf{s}_1 \oplus \mathbf{s}_2 \oplus \cdots \oplus \mathbf{s}_P)$	...
$\mathbf{s}_p$	Feasible generation schedule during problem instance p	...

Other symbols		
f_r	Linear constraint $r \in \mathcal{R}$	-
$\tilde{f}$	Dispatch optimization model linear objective function	-
g_s, g_q	Nonlinear constraint $s \in \mathcal{S}$, $q \in \mathcal{Q}$	-
$\tilde{g}$	Nonlinear design objective function, evaluated from outputs of the SAM financial model	-
$\hat{g}$	Nonlinear SolarPILOT objective function	-
$\mathbb{S}$	Feasible region of the SAM simulation	-

Design Problem

$$(\mathcal{D}) \qquad \max_{\mathbf{x}} \quad \tilde{g}(\mathbf{u}, \mathbf{x}, \mathbf{y}^\star) \tag{F.1}$$

subject to:

$$\mathbf{y}^\star = \min_{\mathbf{y}} \left\{ \hat{g}(\mathbf{y}) \mid g_q(x_3, x_4, \mathbf{y}) = C_q \quad \forall\, q \in \mathcal{Q} \right\} \tag{F.2}$$

$$\left| \begin{array}{l} \text{Determine } \mathbf{s}_p \text{ for each } p \in \mathcal{P}: \\ \quad \mathbf{d}_p^\star = \max_{\mathbf{d}_p} \left\{ \tilde{f}(\mathbf{d}_p) \mid f_r(\mathbf{d}_p, \mathbf{s}_{p-1}, \mathbf{x}, \mathbf{y}^\star) = C_r \quad \forall\, r \in \mathcal{R} \right\} \\ \quad \mathbb{S} = \left\{ \mathbf{s}_p \mid g_s(\mathbf{d}_p^\star, \mathbf{x}, \mathbf{y}^\star) = C_s \quad \forall\, s \in \mathcal{S} \right\} \end{array} \right| \tag{F.3}$$

$$\mathbf{u} = (\mathbf{s}_1 \oplus \mathbf{s}_2 \oplus \cdots \oplus \mathbf{s}_P) \mid \mathbf{s}_p \in \mathbb{S} \quad \forall\, p \in \mathcal{P} \tag{F.4}$$

$$L_i \leq x_i \leq U_i \quad \forall\, i \in \mathcal{I} \tag{F.5}$$

The design problem, $(\mathcal{D})$, minimizes a scalar objective calculated from the SAM financial model outputs for each year in the project lifetime (F.1), as a function of the design variables (see Section 4.3.1). Equation (F.2) represents the SolarPILOT™ optimization algorithm [90], which gives the detailed CSP heliostat and receiver design that minimize the cost of the CSP system per unit of thermal input to the receiver, while meeting the design-point thermal input required by the plant solar multiple and power cycle input design variables. The procedure in (F.3) determines the schedule of plant operations. For each day of a year, a problem instance with a 48-hour horizon is solved, taking the initial plant state from the last period of SAM output. The SAM simulation has a more detailed representation of the plant than the dispatch formulation, and attempts to follow the first 24 hours of the dispatch solution. Failing this, we take a conservative approach and either derate operations from the dispatch solution or shut down that system to preserve feasibility. The feasible schedules of operations for each day of a year are then concatenated to yield the annual plant generation schedule at hourly fidelity, as in equation (F.4). In functional form (F.1) the generation schedule from the first year of operations is assumed to occur in each year of the plant lifetime, with annual discount rates and technology degradation applied after the first, and used to calculate the design objective function. Simple bounds are applied to each of the design variables in constraint (F.5), which are continuous.

APPENDIX G

PLANT EVALUATION ASSUMPTIONS AND CASE STUDY INPUTS

The cost assumptions used in this work are the default values in the corresponding PySAM technology model or PySSC simulation. These defaults are intended to represent conservative estimates for the current state of technology and market conditions [91, 120]. Table G.1 presents the molten salt power tower single-owner installation cost parameters used. All parameters are the defaults used in the PySSC molten salt power tower model.

Table G.1 Molten salt power tower single-owner installation cost parameters used in the CSP system of the plant evaluation procedure

Parameter	Value	Units
Site improvement cost	16	$\$/\mathrm{m}^2$
Heliostat field cost	140	$\$/\mathrm{m}^2$
Fixed tower cost	3	$ million
Tower cost scaling exponent	0.0113	-
Receiver reference cost	103	$ million
Receiver reference area	1571	m^2
Receiver cost scaling exponent	0.7	-
Thermal energy storage cost	22	$\$/\mathrm{kWh}_\mathrm{t}$
Power cycle cost	1040	$\$/\mathrm{kW}_\mathrm{e}$
Contingency	7	%
Procurement, construction, owner cost	13	% of direct cost
Total land cost	10	$1000/acre
Sales tax basis	80	%
Sale tax rate	5	%
Operations and maintenance fixed cost by capacity	66	$/kW-yr
Operations and maintenance variable cost by generation	3.5	$/MWh
Balance of plant costs	290	$/kW

The PV system uses SAM's PVWatts model [121]. We fix the array type to single axis tracking for all plants, and utilize the default cost assumptions in SAM version 2021.12.2 for all other parameters. HOPP utilizes a simplified model of PV field costs by default, which is based on the $51.38M installation cost of a benchmark $50\mathrm{MW}_\mathrm{dc}$ field. The PV system cost is linearly scaled by the capacity multiplier $\$973/\mathrm{kW}_\mathrm{dc}$, according to the cost of the benchmark system. For the battery system, we use the SAM default values of $233.17/kW and $241.79/kWh as the installation costs. Fixed maintenance costs are $15/kW-yr, and we assume a default 10-year replacement period.

APPENDIX H

DISPATCH OPTIMIZATION MODEL FORMULATION

We provide here the complete problem formulation ($\mathcal{H}$), which is taken from Hamilton et al. [94], and mimics the model given in Hamilton et al. [25]. We first define notation:

Table H.1 Hybrid dispatch model, ($\mathcal{H}$), notation.

Indices and Sets		
$t \in \mathcal{T}$	Time periods in the problem horizon	

CSP Field and Receiver Parameters		Units
C^{rec}	Generation cost for the CSP field and receiver	\$/MWh$_\mathsf{t}$
C^{rsu}	Fixed cost for receiver start-up	\$/start
Δ^{l}	Minimum time to start the receiver	hr
Δ^{rs}_{t}	Estimated fraction of time period t required for receiver start-up	-
E^{hs}	Heliostat field startup or shut down parasitic loss	MWh$_\mathsf{e}$
E^{r}	Required energy expended to start receiver	MWh$_\mathsf{t}$
L^{r}	Receiver pumping power per unit power produced	MW$_\mathsf{e}$/MW$_\mathsf{t}$
Q^{in}_{t}	Available thermal power generated by the CSP heliostat field in period t	MW$_\mathsf{t}$
Q^{rl}	Minimum operational thermal power delivered by the receiver	MWh$_\mathsf{t}$
Q^{ru}	Allowable power per period for receiver start-up	MWh$_\mathsf{t}$
W^{h}	Heliostat field tracking parasitic loss	MW$_\mathsf{e}$

Power Cycle Parameters		Units
C^{pc}	Generation cost for power cycle operation	\$/MWh$_\mathsf{e}$
C^{csu}	Fixed cost for power cycle start-up	\$/start
$C^{\delta x}$	Penalty for change in power cycle thermal input	\$/ΔMW$_\mathsf{t}$
η^{amb}_{t}	Cycle efficiency ambient temperature adjustment factor in period t	-
η^{c}_{t}	Normalized condenser parasitic loss in period t	-
E^{c}	Required energy expended to start cycle	MWh$_\mathsf{t}$
η^{des}	Cycle nominal efficiency	-

Table H.1 Continued.

η^p	Slope of linear approximation of power cycle performance curve	$\mathrm{MW_e/MW_t}$
L^c	Cycle heat transfer fluid pumping power per unit energy expended	$\mathrm{MW_e/MW_t}$
Q^c	Allowable power per period for cycle start-up	$\mathrm{MW_t}$
Q^l	Minimum operational thermal power input to the cycle	$\mathrm{MW_t}$
Q^u	Maximum operational thermal power input to the cycle	$\mathrm{MW_t}$
W^u	Cycle electric power rated capacity	$\mathrm{MW_e}$

TES and Miscellaneous Parameters		Units
Δ	Time period duration	hr
E^u	Thermal energy storage capacity	$\mathrm{MWh_t}$

PV Field Parameters		Units
C^{pv}	Generation cost of PV field	$\$/\mathrm{MWh_e}$
W_t^{pv}	Available PV (AC) generation in period t	$\mathrm{MW_e}$

Battery Parameters		Units
C^{bc}, C^{bd}	Operating cost of charging and discharging battery	$\$/\mathrm{MWh_e}$
C^{bl}	Lifecycle cost for battery	\$/lifecycle
C^B	Battery manufacturer-specified capacity	$\mathrm{MWh_e}$
η^+, η^-	Charge and discharge efficiency	-
$\underline{P}^B, \bar{P}^B$	Battery minimum and maximum power ratings	$\mathrm{MW_e}$
$\underline{S}^B, \bar{S}^B$	Battery state of charge minimum and maximum operational bounds	-

Grid Parameters		Units
ϵ	Small value used in objective for binary logic	\$
γ	Exponential weighting factor	-
P_t^s, P_t^p	Electricity sale and purchase price, respectively, in period t	$\$/\mathrm{MWh_e}$
W_t^g, W_t^l	Grid transmission limit for generation and load in period t	$\mathrm{MW_e}$

Table H.1 Continued.

Continuous Decision Variables		Units
b^c	Battery cycle count	-
b_t^{soc}	State of charge of battery in time period t	-
$\dot{e}_t^s, \dot{e}_t^p$	Electricity sold to and purchased from grid in time t	MW_e
s_t	TES reserve quantity in period t	MWh_t
u_t^{rsu}	Receiver start-up energy inventory in period t	MWh_t
x_t^r	Thermal power delivered by the receiver in period t	MW_t
x_t^{rsu}	Receiver start-up power consumption in period t	MW_t
u_t^{csu}	Cycle start-up energy inventory in period t	MWh_t
$\dot{w}_t$	Power cycle electricity generation in period t	MW_e
$\dot{w}_t^+, \dot{w}_t^-$	Power into and out of the battery in period t	MW_e
$\dot{w}_t^l$	Electrical load of CSP system in period t	MW_e
$\dot{w}_t^{pv}$	PV generation in time t	MW_e
$\dot{w}_t^{sg}, \dot{w}_t^{sl}$	System generation and load in time t	MW_e
x_t	Cycle thermal power utilization in period t	MW_t
x_t^δ	Power cycle change in thermal energy input in period t	MW_t

Binary Decision Variables	
y_t	1 if cycle is generating electric power in period t; 0 otherwise
y_t^+, y_t^-	1 if battery is charging or discharging, respectively, in time period t; 0 otherwise
y_t^{csu}	1 if cycle is starting up in period t; 0 otherwise
y_t^{csup}	1 if cycle cold start-up penalty is incurred at time t (from off); 0 otherwise
y_t^g	1 if system is net generating in time period t; 0 otherwise
y_t^r	1 if receiver is generating "usable" thermal power in period t; 0 otherwise
y_t^{rsu}	1 if receiver is starting up in period t; 0 otherwise
y_t^{rsup}	1 if receiver cold start-up penalty is incurred in period t (from off); 0 otherwise

The following formulation, $(\mathcal{H})$, requires the initial operational state of the system, PV field and receiver energy generation forecasts, the expected cycle conversion efficiency profile as a function of ambient temperature and thermal input, and the energy price or desired load profile depending on the system analysis. Initialization parameters used to set variable values at $t = 0$ follow variable notation and are not included here. Variables and parameters describe energy (thermal MWh_t or electric MWh_e) states and power flows (thermal MW_t or electric MW_e) in the system. We use lowercase letters to represent variables and capital letters for parameters. All binary variables are represented with some variant of the letter y.

H.1 Objective Function and Constraints

We present two possible objective functions. The first maximizes revenue less operations and maintenance costs resulting from the dispatch solution, which is appropriate in an independent-system-operator market. The second objective minimizes the cost of following a pre-determined load profile.

Maximize Revenue

$$
\begin{aligned}
(\mathcal{H}_1)\ \ \text{maximize} \quad \sum_{t \in \mathcal{T}} \Bigg[& \Delta \left(\gamma^t P^s_t \dot{e}^s_t - \gamma^{-t} P^p_t \dot{e}^p_t\right) - \epsilon y^g_t \\
& - \gamma^{-t} \left(\Delta C^{rec} x^r_t + C^{rsu} y^{rsup}_t + \Delta C^{pc} \dot{w}_t + C^{csu} y^{csup}_t + C^{\delta x} x^\delta_t\right) \\
& - \gamma^{-t} \Delta C^{pv} \dot{w}^{pv}_t \\
& - \gamma^{-t} \Delta \left(C^{bc} \dot{w}^+_t + C^{bd} \dot{w}^-_t\right) \Bigg] - C^{bl} b^c
\end{aligned} \tag{H.1}
$$

Minimize Cost of a Load Profile

$$
\begin{aligned}
(\mathcal{H}_2)\ \ \text{minimize} \quad \sum_{t \in \mathcal{T}} \Bigg[& \Delta \gamma^t \left(P^s_t \left(W^g_t - \dot{e}^s_t\right) + P^p_t \dot{e}^p_t\right) + \epsilon y^g_t \\
& + \gamma^t \left(\Delta C^{rec} x^r_t + C^{rsu} y^{rsup}_t + \Delta C^{pc} \dot{w}_t + C^{csu} y^{csup}_t + C^{\delta x} x^\delta_t\right) \\
& + \gamma^t \Delta C^{pv} \dot{w}^{pv}_t \\
& + \gamma^t \Delta \left(C^{bc} \dot{w}^+_t + C^{bd} \dot{w}^-_t\right) \Bigg] + C^{bl} b^c
\end{aligned} \tag{H.2}
$$

Constraints having terms indexed in period t-1, but applied to all periods $t \in \mathcal{T}$, use the corresponding initial condition parameter for the decision variable when $t = 1$. All time-indexed decision variables requiring an initial value use the same notation for the parameter as the decision variable indexed in period $t = 0$, e.g., the initial condition for the power cycle operating binary variable y_t is the parameter y_0.

Receiver Operations

Receiver Start-up

$$u_t^{rsu} \leq u_{t-1}^{rsu} + \Delta x_t^{rsu} \qquad \forall\ t \in \mathcal{T} \tag{H.3a}$$

$$u_t^{rsu} \leq E^r y_t^{rsu} \qquad \forall\ t \in \mathcal{T} \tag{H.3b}$$

$$y_t^r \leq \frac{u_t^{rsu}}{E^r} + y_{t-1}^r \qquad \forall\ t \in \mathcal{T} \tag{H.3c}$$

$$y_t^{rsu} + y_{t-1}^r \leq 1 \qquad \forall\ t \in \mathcal{T} \tag{H.3d}$$

$$x_t^{rsu} \leq Q^{ru} y_t^{rsu} \qquad \forall\ t \in \mathcal{T} \tag{H.3e}$$

$$y_t^{rsu} \leq \frac{Q_t^{in}}{Q^{rl}} \qquad \forall\ t \in \mathcal{T} \tag{H.3f}$$

$$y_t^{rsup} \geq y_t^{rsu} - y_{t-1}^{rsu} \qquad \forall\ t \in \mathcal{T} \tag{H.3g}$$

Receiver Supply and Demand

$$x_t^r + x_t^{rsu} \leq Q_t^{in} \qquad \forall\ t \in \mathcal{T} \tag{H.4a}$$

$$x_t^r \leq Q_t^{in} y_t^r \qquad \forall\ t \in \mathcal{T} \tag{H.4b}$$

$$x_t^r \geq Q^{rl} y_t^r \qquad \forall\ t \in \mathcal{T} \tag{H.4c}$$

$$y_t^r \leq \frac{Q_t^{in}}{Q^{rl}} \qquad \forall\ t \in \mathcal{T} \tag{H.4d}$$

Power Cycle Operations

Cycle Start-up

$$u_t^{csu} \leq u_{t-1}^{csu} + \Delta Q^c y_t^{csu} \qquad \forall\ t \in \mathcal{T} \tag{H.5a}$$

$$u_t^{csu} \leq E^c y_t^{csu} \qquad \forall\ t \in \mathcal{T} \tag{H.5b}$$

$$y_t \leq \frac{u_t^{csu}}{E^c} + y_{t-1} \qquad \forall\ t \in \mathcal{T} \tag{H.5c}$$

$$y_t^{csu} + y_{t-1} \leq 1 \qquad \forall\ t \in \mathcal{T} \tag{H.5d}$$

$$y_t^{csup} \geq y_t^{csu} - y_{t-1}^{csu} \qquad \forall\ t \in \mathcal{T} \tag{H.5e}$$

Power Supply and Demand

$$x_t + \frac{E^c}{\Delta} y_t^{csu} \leq Q^u \qquad \forall\ t \in \mathcal{T} \tag{H.6a}$$

$$x_t \leq Q^u y_t \qquad \forall\ t \in \mathcal{T} \tag{H.6b}$$

$$x_t \geq Q^l y_t \qquad \forall\ t \in \mathcal{T} \tag{H.6c}$$

$$\dot{w}_t = \frac{\eta_t^{amb}}{\eta^{des}} [\eta^p x_t + (W^u - \eta^p Q^u) y_t] \qquad \forall\ t \in \mathcal{T} \tag{H.6d}$$

$$x_t^\delta \geq x_t - x_{t-1} \qquad \forall\ t \in \mathcal{T} \tag{H.6e}$$

$$\begin{aligned} \dot{w}_t^l = {} & \eta_t^c \dot{w}_t \\ & + L^r (x_t^r + x_t^{rsu}) + L^c (x_t + Q^c y_t^{csu}) \\ & + W^h y_t^r + \frac{E^{hs}}{\Delta} y_t^{rsu} \end{aligned} \qquad \forall\ t \in \mathcal{T} \tag{H.6f}$$

TES Energy Balance Constraints

$$
\begin{aligned}
s_t - s_{t-1} &= \Delta[x_t^r - (Q^c y_t^{csu} + x_t)] && \forall\, t \in \mathcal{T} && \text{(H.7a)}\\
s_t &\leq E^u && \forall\, t \in \mathcal{T} && \text{(H.7b)}\\
s_{t-1} &\geq \Delta \cdot \Delta_t^{rs}[Q^u(-3 + y_t^{rsu} + y_{t-1} + y_t) + x_t] && \forall\, t \in \mathcal{T} && \text{(H.7c)}
\end{aligned}
$$

PV Constraints

$$
\begin{aligned}
\dot{w}_t^{pv} &\leq W_t^{pv} && \forall\, t \in \mathcal{T} && \text{(H.8a)}\\
\dot{w}_t^{pv} &\geq 0 && \forall\, t \in \mathcal{T} && \text{(H.8b)}
\end{aligned}
$$

Battery Constraints

$$
\begin{aligned}
b_t^{soc} &= b_{t-1}^{soc} + \Delta\left(\frac{\eta^+ \cdot \dot{w}_t^+ - \frac{\dot{w}_t^-}{\eta^-}}{C^B}\right) && \forall\, t \in \mathcal{T} && \text{(H.9a)}\\
\underline{S}^B &\leq b_t^{soc} \leq \bar{S}^B && \forall\, t \in \mathcal{T} && \text{(H.9b)}\\
\underline{P}^B y_t^- &\leq \dot{w}_t^- \leq \bar{P}^B y_t^- && \forall\, t \in \mathcal{T} && \text{(H.9c)}\\
\underline{P}^B y_t^+ &\leq \dot{w}_t^+ \leq \bar{P}^B y_t^+ && \forall\, t \in \mathcal{T} && \text{(H.9d)}\\
y_t^+ + y_t^- &\leq 1 && \forall\, t \in \mathcal{T} && \text{(H.9e)}\\
b^c &\geq \frac{\Delta}{C^B} \sum_{t \in \mathcal{T}} \dot{w}_t^- && && \text{(H.9f)}
\end{aligned}
$$

Grid Constraints

$$
\begin{aligned}
\dot{e}_t^s - \dot{e}_t^p &= \dot{w}_t^{sg} - \dot{w}_t^{sl} && \forall\, t \in \mathcal{T} && \text{(H.10a)}\\
\dot{e}_t^s &\leq W_t^g y_t^g && \forall\, t \in \mathcal{T} && \text{(H.10b)}\\
\dot{e}_t^p &\leq W_t^l (1 - y_t^g) && \forall\, t \in \mathcal{T} && \text{(H.10c)}
\end{aligned}
$$

System Connection Constraints

$$
\begin{aligned}
\dot{w}_t^{sg} &= \dot{w}_t + \dot{w}_t^{pv} + \dot{w}_t^- && \forall\, t \in \mathcal{T} && \text{(H.11a)}\\
\dot{w}_t^{sl} &= \dot{w}_t^l + \dot{w}_t^+ && \forall\, t \in \mathcal{T} && \text{(H.11b)}\\
\dot{w}_t^{sg} &\geq \dot{w}_t^+ && \forall\, t \in \mathcal{T} && \text{(H.11c)}\\
\dot{w}_t^{pv} &\geq \dot{w}_t^+ && \forall\, t \in \mathcal{T} && \text{(H.11d)}
\end{aligned}
$$

Decision Variable Bounds

$$s_t,\ u_t^{csu},\ u_t^{rsu},\ \dot{w}_t,\ \dot{w}_t^{l},\ x_t,\ x_t^{\delta},\ x_t^{r},\ x_t^{rsu} \geq 0 \qquad \forall\ t \in \mathcal{T} \tag{H.12a}$$

$$y_t,\ y_t^{csu},\ y_t^{csup},\ y_t^{r},\ y_t^{rsu},\ y_t^{rsup} \in \{0,1\} \qquad \forall\ t \in \mathcal{T} \tag{H.12b}$$

$$b^c,\ b_t^{soc},\ \dot{w}_t^{+},\ \dot{w}_t^{-} \geq 0 \qquad \forall\ t \in \mathcal{T} \tag{H.12c}$$

$$y_t^{+},\ y_t^{-} \in \{0,1\} \qquad \forall\ t \in \mathcal{T} \tag{H.12d}$$

$$\dot{w}_t^{g},\ \dot{w}_t^{l},\ \dot{e}_t^{s},\ \dot{e}_t^{p} \geq 0 \qquad \forall\ t \in \mathcal{T} \tag{H.12e}$$

$$y_t^{g} \in \{0,1\} \qquad \forall\ t \in \mathcal{T} \tag{H.12f}$$

H.2 Receiver Operations

Constraint (H.3a) accounts for receiver start-up energy "inventory," which can assume a positive value during time periods of receiver start-up (Constraint (H.3b)). Power production assumes a positive value only upon completion of a start-up or if the receiver also operates in the time period prior (Constraint (H.3c)). In the latter case, the receiver cannot be starting up in the next time period (Constraint (H.3d)). Ramp-rate limits hold during the start-up procedure (Constraint (H.3e)). The presence of trivial solar resource prevents receiver start-up (Constraint (H.3f)). Constraints (H.3g) ensure that penalties for receiver start-up are incurred.

The parameter Q_t^{in} serves as an upper bound on the thermal power produced by the receiver, from which any energy used for start-up detracts (Constraint (H.4a)). Constraint (H.4b) permits the receiver to generate thermal power only while in power-producing mode. Receiver thermal power generation is subject to a lower bound by Constraint (H.4c). The receiver cannot operate (Constraint (H.4d)) in the absence of thermal power.

H.3 Power Cycle Operations

Constraint (H.5a) accounts for start-up energy "inventory," which can only be positive during time periods in which the cycle is starting up (Constraint (H.5b)). Normal cycle operation can occur upon completion of start-up energy requirements or if the cycle is operating normally (Constraint (H.5c)). In the latter case, the cycle cannot start up in the time period directly following operation (Constraint (H.5d)). Cycle start up penalties are incurred via Constraint (H.5e).

Constraint (H.6a) limits the cycle input thermal power during periods when the cycle is starting up. This is a model approximation to derate power cycle output during startup periods. In reality, the cycle power output is not derated but the total energy production during the time period is reduced due to the time the cycle is starting up during that period. Constraint (H.6b) and Constraint (H.6c) form the upper and lower bounds on the heat input to the power cycle, respectively. The relationship between electrical power and cycle heat input is modeled as a linear function with corrections for ambient temperature effects (Constraint (H.6d)). Constraint (H.6e) measures the positive change in cycle thermal input, i.e., ramping, over time. Constraint (H.6f) calculates the CSP system load depending operational decisions.

H.4 Thermal Energy Storage Balance

Constraint (H.7a) balances energy to and from TES with the charge; a time-scaling parameter Δ reconciles power and energy. Constraint (H.7b) imposes the upper bound to TES charge state. If the power cycle is operating in time periods $t-1$ and t, and if the receiver is starting up in time t, then there must be a sufficient charge level in the TES in time $t-1$ to ensure that the power cycle can operate through its start-up period (Constraint (H.7c)). Constraint (H.7c) uses Q^u as a 'big M' value to make the constraint non-binding when the specific condition is not occurring, i.e., the cycle operating and receiver starting up in the same period. The expected fraction of a time period used for receiver start-up is given by (H.13), if applicable.

$$\Delta_t^{rs} = \min\left\{1, \max\left\{\Delta^l, \frac{E^r}{\max\left\{\epsilon, Q_t^{in}\Delta\right\}}\right\}\right\} \tag{H.13}$$

Constraints (H.7a)-(H.7c) measure TES state of charge via energy flow.

H.5 PV Field Operations

Within the hybrid framework, we assume that PV system has a *take it or leave it* policy in which the hybrid system can take up to the available generation at any time (Constraint (H.8a)) or curtail part or all of the available generation depending other system constraints. Non-negativity is enforced by Constraint (H.8b)

H.6 Battery Operations

Battery state-of-charge must be updated (Constraint (H.9a)), and this quantity is bounded both below and above (Constraint (H.9b)). Power flow into and out of the battery is bounded by Constraints (H.9c) and (H.9d). The battery cannot be charging and discharging simultaneously (Constraint (H.9e)) while Constraint (H.9f) measures battery cycle count similar to what is done in Scioletti et al. [31].

H.7 Grid Operations

Constraint (H.10a) provides an energy balance at the transmission interconnect of the hybrid system. Electricity sales are limited by transmission for generation during periods in which the system is generating net power (Constraint (H.10b)). During periods in which the hybrid system net generation is negative, Constraint (H.10c) limits the load the system can pull from the grid.

H.8 Inter-System Operations

Constraints (H.11a) and (H.11b) enforce energy balance for the grid module on system generation and load, respectively. Constraints (H.11c) and (H.11d) are conditional constraints depending on specific requirements imposed on the hybrid system's battery charging. Constraint (H.11c) limits battery charging to only electricity produced by the hybrid system locally, i.e., the battery cannot be charged by the electric grid. Constraint (H.11d) restricts battery charging to only electricity generated by the PV system. Constraint (H.11d) is more restrictive than Constraint (H.11c); therefore, Constraint (H.11c) can be omitted if Constraint (H.11d) is imposed. Variable bounds are enforced in constraints (H.12a) through (H.12f).

H.9 Dispatch Cost Assumptions

The solution of the dispatch optimization model is influenced by the relative values of electricity prices and the cost parameters in the objective (H.1). Table H.2 lists the cost parameters used by the dispatch optimization model, which are the default values in HOPP.

Table H.2 Dispatch optimization model cost coefficients (HOPP default values). †The parameter value is scaled with respect to the system size.

Operating Costs and Penalties	Symbol	Units	Value
Concentrating Solar Power (CSP) with Thermal Energy Storage (TES)			
CSP field and receiver generation cost	C^{rec}	\$/MWh$_{\mathsf{t}}$	0.5
Receiver cold start-up fixed cost	C^{rsu}	\$/MW$_{\mathsf{t}}$·start	1.5†
Power cycle generation cost	C^{pc}	\$/MWh$_{\mathsf{e}}$	2.0
Power cycle cold start-up fixed cost	C^{csu}	\$/MW$_{\mathsf{e}}$·start	40.0†
Change in power cycle thermal input penalty	$C^{\delta x}$	\$/MW$_{\mathsf{t}}$	0.5
Photovoltaics (PV) with Battery Storage			
Photovoltaic field generation cost	C^{pv}	\$/MWh$_{\mathsf{e}}$	1.7
Battery charge, discharge operation cost	C^{bc}, C^{bd}	\$/MWh$_{\mathsf{e}}$	0.9
Battery lifecycle cost	C^{bl}	\$/MWh$^{\mathrm{dc}}$·cycle	26.5†

APPENDIX I

PERMISSIONS

Permission to reuse papers accepted and submitted for publication in Optimization and Engineering

Chapters 2 and 3 have been accepted and submitted for publication, respectively, in *Optimization and Engineering*, which is published by Springer Nature Journals. They give blanket permission for reuse in an author's own thesis on their website. See https://www.springer.com/gp/rights-permissions/obtaining-permissions/882, accessed on 13 June 2022, and included in this Appendix as a screenshot image.

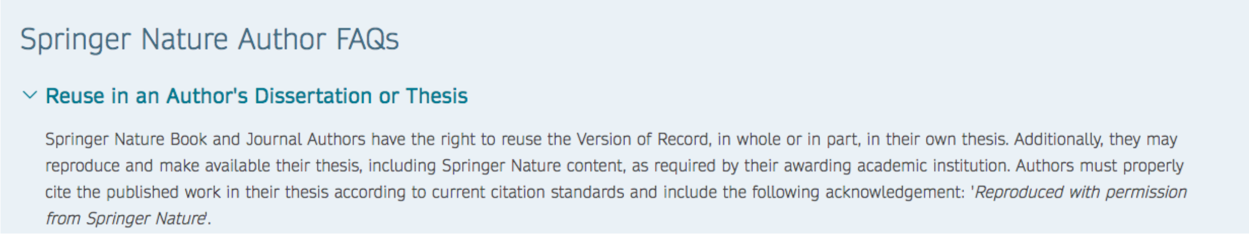

Springer Nature Author FAQs

Reuse in an Author's Dissertation or Thesis

Springer Nature Book and Journal Authors have the right to reuse the Version of Record, in whole or in part, in their own thesis. Additionally, they may reproduce and make available their thesis, including Springer Nature content, as required by their awarding academic institution. Authors must properly cite the published work in their thesis according to current citation standards and include the following acknowledgement: '*Reproduced with permission from Springer Nature*'.

Permission to reuse papers submitted for publication in Solar Energy

Chapter 4 has been submitted for publication in *Solar Energy*, which is published by Elsevier. They give blanket permission for reuse in an author's own thesis on their website. See https://www.elsevier.com/about/policies/copyright/permissions, accessed on 13 June 2022, and included in this Appendix as a screenshot image.

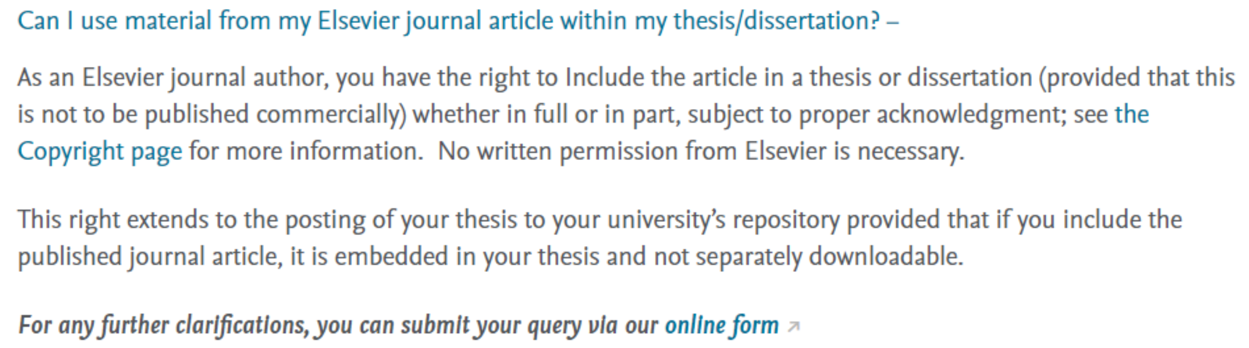

Can I use material from my Elsevier journal article within my thesis/dissertation? –

As an Elsevier journal author, you have the right to Include the article in a thesis or dissertation (provided that this is not to be published commercially) whether in full or in part, subject to proper acknowledgment; see the Copyright page for more information. No written permission from Elsevier is necessary.

This right extends to the posting of your thesis to your university's repository provided that if you include the published journal article, it is embedded in your thesis and not separately downloadable.

For any further clarifications, you can submit your query via our online form

Permission to include co-authored works

The following co-authors have given their written permission for inclusion of their work in this dissertation: William T. Hamilton, Janna Martinek, Alexandra M. Newman, Michael J. Wagner, and Alexander J. Zolan. A copy of email correspondence indicating their permission is included in this Appendix.

Permission to use NREL copyrighted images

NREL researchers, Mark Mehos and Alexander J. Zolan, have given permission for use of NREL copyrighted images in Figures 2.1, 3.1, and 4.1. A copy of email correspondence indicating their permission is included in this Appendix.

John Cox

Subject: FW: [External] RE: Permission for Inclusion of Work in Dissertation

-----Original Message-----
From: Zolan, Alexander <Alexander.Zolan@nrel.gov>
Sent: Monday, June 13, 2022 10:35 AM
To: Martinek, Janna <Janna.Martinek@nrel.gov>; Hamilton, William <William.Hamilton@nrel.gov>; Alexandra Newman <anewman@mines.edu>; John Cox <jlcox@mines.edu>
Cc: Wagner, Michael (WISC) <mjwagner2@wisc.edu>
Subject: [External] RE: Permission for Inclusion of Work in Dissertation

Hi John,

You have my permission to include this work in your dissertation.

Best,
Alex

-----Original Message-----
From: Mike Wagner <mjwagner2@wisc.edu>
Sent: Monday, June 13, 2022 9:34 AM
To: Martinek, Janna <Janna.Martinek@nrel.gov>; Hamilton, William <William.Hamilton@nrel.gov>; Alexandra Newman <anewman@mines.edu>; John Cox <jlcox@mines.edu>
Cc: Zolan, Alexander <Alexander.Zolan@nrel.gov>
Subject: [External] RE: Permission for Inclusion of Work in Dissertation

John,

You have my permission to include this work in your dissertation.

Mike

____
Michael Wagner, Ph.D.
Assistant Professor | Mechanical Engineering University of Wisconsin-Madison

-----Original Message-----
From: Martinek, Janna <Janna.Martinek@nrel.gov>
Sent: Monday, June 13, 2022 9:20 AM
To: Hamilton, William <William.Hamilton@nrel.gov>; Alexandra M. Newman <anewman@mines.edu>; John Cox <jlcox@mines.edu>
Cc: Wagner, Michael (WISC) <mjwagner2@wisc.edu>; Zolan, Alexander <Alexander.Zolan@nrel.gov>
Subject: RE: Permission for Inclusion of Work in Dissertation

Hi John,

You have my permission to include this work in your dissertation.

Best,

Janna

-----Original Message-----
From: Hamilton, William <William.Hamilton@nrel.gov>
Sent: Monday, June 13, 2022 9:17 AM
To: Alexandra M. Newman <anewman@mines.edu>; John Cox <jlcox@mines.edu>
Cc: Wagner, Michael (WISC) <mjwagner2@wisc.edu>; Martinek, Janna <Janna.Martinek@nrel.gov>; Zolan, Alexander <Alexander.Zolan@nrel.gov>
Subject: RE: Permission for Inclusion of Work in Dissertation

Hi John,

You have my permission to include this work in your dissertation.

Thanks,

Bill

-----Original Message-----
From: Alexandra M. Newman <anewman@mines.edu>
Sent: Monday, June 13, 2022 9:16 AM
To: John Cox <jlcox@mines.edu>
Cc: Wagner, Michael (WISC) <mjwagner2@wisc.edu>; Hamilton, William <William.Hamilton@nrel.gov>; Martinek, Janna <Janna.Martinek@nrel.gov>; Zolan, Alexander <Alexander.Zolan@nrel.gov>
Subject: Re: Permission for Inclusion of Work in Dissertation

Yes, you have my permission.

Alexandra

On Mon, Jun 13, 2022 at 09:09:51AM -0600, John Cox wrote:
> All,
>
> The graduate school requires that I provide proof of permission from all co-authors to include their work in my dissertation.
>
> Please respond to this email indicate your permission for the inclusion of the following works in my dissertation:
>
> (accepted to Optimization and Engineering) Real-time Dispatch Optimization for Concentrating Solar Power with Thermal Energy Storage
> - William T. Hamilton, Michael J. Wagner, and Alex J. Zolan
>
> (submitted to Optimization and Engineering) Optimal Sizing and Dispatch of Solar Power with Storage
> - William T. Hamilton and Janna Martinek
>
> (planned for submission to Applied Energy) Parametric Analysis for Solar Power Plants with Storage
> - William T. Hamilton
>
> Thank you all for your guidance and feedback during the program!
>
> John

John Cox

From: Zolan, Alexander <Alexander.Zolan@nrel.gov>
Sent: Tuesday, April 13, 2021 5:27 PM
To: Alexandra Newman; Hamilton, William
Cc: John Cox
Subject: RE: [sahinidis@opte-journal.com: [External] Optimization and Engineering editorial manager: OPTE-2021-2022]

Hi All,

FYI, I asked Mark Mehos and he says we're definitely safe to say we have permission, and that the two co-authors working at NREL (the copyright holder) have internal permission. If they need something more specific, they should say so and we can obtain it, but I think this should be sufficient if the editor hasn't provided specific guidelines other than "obtain permission".

Thanks,
Alex

-----Original Message-----
From: Alexandra Newman <anewman@mines.edu>
Sent: Monday, April 12, 2021 1:58 PM
To: Hamilton, William <William.Hamilton@nrel.gov>
Cc: Zolan, Alexander <Alexander.Zolan@nrel.gov>; John Cox <jlcox@mymail.mines.edu>
Subject: Re: [sahinidis@opte-journal.com: [External] Optimization and Engineering editorial manager: OPTE-2021-2022]

CAUTION: This email originated from outside of NREL. Do not click links or open attachments unless you recognize the sender and know the content is safe.

All:

I know that we have been able to get these figures published before, but it sort of happened automagically and we were ont called out by the journal.
Maybe Wagner would know... but, the paper will not be sent out to referees until we get this resolved so I'd rather not delay.
We could always remove the figure but I would rather not do that.

On Mon, Apr 12, 2021 at 07:41:37PM +0000, Hamilton, William wrote:
> Hey Alex,
>
> Unfortunately, I do not know the require procedure for using that figure. Mike might know or you could try Linh Truong.
>
> Thanks,
>
> Bill
>
> -----Original Message-----
> From: Zolan, Alexander <Alexander.Zolan@nrel.gov>
> Sent: Monday, April 12, 2021 1:13 PM

> To: Hamilton, William <William.Hamilton@nrel.gov>
> Cc: John Cox <jlcox@mymail.mines.edu>; Alexandra Newman <anewman@mines.edu>
> Subject: FW: [sahinidis@opte-journal.com: [External] Optimization and Engineering editorial manager: OPTE-2021-2022]
>
> Hi Bill,
>
> Do you know the procedure you went through for your OPTE paper on the hybrid system with respect to the copyright permission on the CSP system graphic (a variation of which we're using or Fig. 1 of this paper)? I think we need to repeat that for this paper.
>
> Thanks,
> Alex
>
> -----Original Message-----
> From: Alexandra Newman <anewman@mines.edu>
> Sent: Monday, April 12, 2021 9:26 AM
> To: John Cox <jlcox@mymail.mines.edu>; Zolan, Alexander <Alexander.Zolan@nrel.gov>
> Subject: [sahinidis@opte-journal.com: [External] Optimization and Engineering editorial manager: OPTE-2021-2022]
>
> CAUTION: This email originated from outside of NREL. Do not click links or open attachments unless you recognize the sender and know the content is safe.
>
> I thought we dealt with this.
> Please confirm such that I can re-email the editor.
>
> ----- Forwarded message from Optimization and Engineering editorial manager <sahinidis@opte-journal.com> -----
>
> Date: Mon, 12 Apr 2021 14:45:16 +0000
> From: Optimization and Engineering editorial manager <sahinidis@opte-journal.com>
> To: Alexandra Newman <NEWMAN@MINES.EDU>
> Subject: [External] Optimization and Engineering editorial manager: OPTE-2021-2022
> X-Mailer: PHPMailer 6.0.2
(https://gcc02.safelinks.protection.outlook.com/?url=https%3A%2F%2Fgithub.com%2FPHPMailer%2FPHPMailer&data=04%7C01%7CAlexander.Zolan%40nrel.gov%7C039b88c0143343f80fd608d8fded5120%7Ca0f29d7e28cd4f5484427885aee7c080%7C0%7C0%7C637538543019539198%7CUnknown%7CTWFpbGZsb3d8eyJWIjoiMC4wLjAwMDAiLCJQIjoiV2luMzIiLCJBTiI6Ik1haWwiLCJXVCI6Mn0%3D%7C1000&sdata=Whb1gFKGQ6B9jiNL43pt8dJcjtej2lGYTl0exTicj5E%3D&reserved=0)
>
> Dear Dr. Alexandra Newman,
>
>
> Manuscript-ID: OPTE-2021-2022
>
> Title: Real-time Dispatch Optimization for Concentrating Solar Power with Thermal Energy Storage
>
> Figure 1 precludes us from possibly publishing your article due to copyright issues. Would you please remove or replace this figure? Alternatively, you could obtain permission to include the figure from the copyright holder.
>
> Respectfully,
> Nick Sahinidis

> Gary C. Butler Family Chair and Professor at Georgia Institute of Technology Editor-in-Chief Optimization and Engineering
>
https://gcc02.safelinks.protection.outlook.com/?url=https%3A%2F%2Fsahinidis.coe.gatech.edu%2F&data=04%7C01%7CAlexander.Zolan%40nrel.gov%7C039b88c0143343f80fd608d8fded5120%7Ca0f29d7e28cd4f5484427885aee7c080%7C0%7C0%7C637538543019539198%7CUnknown%7CTWFpbGZsb3d8eyJWIjoiMC4wLjAwMDAiLCJQIjoiV2luMzIiLCJBTiI6Ik1haWwiLCJXVCI6Mn0%3D%7C1000&sdata=WDD%2BrTgUfDUexl12Qwu%2F8131jGUWP%2BG6uhUcfSwJpOc%3D&reserved=0
>
https://gcc02.safelinks.protection.outlook.com/?url=http%3A%2F%2Fwww.springer.com%2Fmathematics%2Fjournal%2F11081&data=04%7C01%7CAlexander.Zolan%40nrel.gov%7C039b88c0143343f80fd608d8fded5120%7Ca0f29d7e28cd4f5484427885aee7c080%7C0%7C0%7C637538543019539198%7CUnknown%7CTWFpbGZsb3d8eyJWIjoiMC4wLjAwMDAiLCJQIjoiV2luMzIiLCJBTiI6Ik1haWwiLCJXVCI6Mn0%3D%7C1000&sdata=3BEnr29UOPWvFAeGod4qHmj%2B%2BbpWJt86dR80QdPyMPg%3D&reserved=0
>
> ----- End forwarded message -----